



ISSN 2959-0663 (Print)  
ISSN 2959-0671 (Online)  
ISSN-L 2959-0663

# EURASIAN JOURNAL OF CHEMISTRY

2025. Vol. 30 No. 4(120)

ISSN 2959-0663 (Print)  
ISSN 2959-0671 (Online)  
ISSN-L 2959-0663

---

# EURASIAN JOURNAL OF CHEMISTRY

---

**2025**

**Volume 30, No. 4 (120)**

Founded in 1996

Published 4 times a year

Karaganda  
2025

**Publisher: NLC “Karaganda National Research University named after academician Ye.A. Buketov”**

**Postal address:** 28, Universitetskaya Str., Karaganda, 100024, Kazakhstan

**E-mail:** [chemistry.vestnik.ksu.kz@gmail.com](mailto:chemistry.vestnik.ksu.kz@gmail.com); [ipustolaikina@gmail.com](mailto:ipustolaikina@gmail.com); **Tel./fax:** +7(7212) 34-19-40.  
**Web-site:** <https://ejc.buketov.edu.kz>

*Editor-in-Chief*

**Ye.M. Tazhbayev**, Doctor of Chemical sciences

*Executive Editor*

**I.A. Pustolaikina**, Candidate of Chemical sciences

*Editorial board*

- Z.M. Muldakhmetov**, Academician of NAS RK, Doctor of chem. sciences, Institute of Organic Synthesis and Coal Chemistry of the Republic of Kazakhstan, Karaganda (Kazakhstan);
- S.M. Adekenov**, Academician of NAS RK, Doctor of chem. sciences, International Research and Production Holding “Phytochemistry”, Karaganda (Kazakhstan);
- S.E. Kudaibergenov**, Doctor of chem. sciences, Institute of Polymer Materials and Technologies, Almaty (Kazakhstan);
- V.V. Khutoryanskiy**, Professor, University of Reading, Reading (United Kingdom);
- Fengyun Ma**, Professor, Xinjiang University, Urumqi (PRC);
- Xintai Su**, Professor, South China University of Technology, Guangzhou (PRC);
- Lijuan Zhang**, Associate Professor, South China Normal University, Guangzhou (China);
- R.R. Rakhimov**, Doctor of chem. sciences, Norfolk State University, Norfolk (USA);
- N. Nuraje**, Associate Professor, Nazarbayev University, Astana (Kazakhstan);
- S.A. Beznosyuk**, Doctor of phys.-math. sciences, Altai State University, Barnaul (Russia);
- B.F. Minaev**, Doctor of chem. sciences, Bohdan Khmelnytsky National University of Cherkasy, Cherkasy (Ukraine);
- I.V. Kulakov**, Doctor of chem. sciences, University of Tyumen (Russia);
- R.P. Bhole**, PhD, Associate Professor, Dr. D.Y. Patil Institute of Pharmaceutical Sciences and Research, Sant Tukaram Nagar, Pimpri, Pune (India);
- S.S. Gurav**, PhD, Professor, Goa College of Pharmacy, Panaji (India);
- A.A. Atakhanov**, Doctor of techn. sciences, Institute of Polymer Chemistry and Physics, Tashkent (Uzbekistan);
- I.V. Korolkov**, PhD, Associated Professor, Astana branch, Institute of Nuclear Physics of the Republic of Kazakhstan, Astana (Kazakhstan);
- A.M. Makasheva**, Doctor of techn. sciences, Zh. Abishev Chemical-Metallurgical Institute, Karaganda (Kazakhstan);
- M.I. Baikenov**, Doctor of chem. sciences, Buketov Karaganda National Research University (Kazakhstan);
- L.K. Salkeeva**, Doctor of chem. sciences, Buketov Karaganda National Research University (Kazakhstan);
- G.I. Dzhardimalieva**, Doctor of chem. sciences, Federal Research Center of Problems of Chemical Physics and Medicinal Chemistry, Russian Academy of Sciences, Chernogolovka, Moscow Region (Russia);
- S.K. Filippov**, PhD, Project Leader, DWI-Leibniz Institute for Interactive Materials, Aachen, North Rhine-Westphalia, (Germany);
- S.A. Ivasenko**, Doctor of pharm. sciences, Karaganda Medical University (Kazakhstan).

*Proofreader* I.N. Murtazina

*Computer layout* V.V. Butyaikin

**Eurasian Journal of Chemistry. — 2025. — Vol. 30, No. 4(120). — 162 p.**

**ISSN 2959-0663 (Print). ISSN 2959-0671 (Online). ISSN-L 2959-0663**

Proprietary: NLC “Karaganda National Research University named after academician Ye.A. Buketov”.

Registered by the Ministry of Culture and Information of the Republic of Kazakhstan. Re-registration certificate No. KZ02VPY00134144 dated 14.11.2025.

Signed in print 23.12.2025. Format 60×84 1/8. Offset paper. Volume 20,25 p.sh. Circulation 200 copies. Price upon request. Order № 187.

Printed in the Publishing house of NLC “Karaganda National Research University named after academician Ye.A. Buketov”.

28, University Str., Karaganda, 100024, Kazakhstan. Tel.: +7(7212) 35-63-16. E-mail: [printed@karnu-buketov.edu.kz](mailto:printed@karnu-buketov.edu.kz)

© Karaganda National Research University named after academician Ye.A. Buketov, 2025

---

# CONTENTS

## ORGANIC CHEMISTRY

<i>Filina, M.P., Bakibaev, A.A., &amp; Baiguzin, F.A.</i> Cyclopentane as an Eco-Friendly Alternative: A Review of its Properties, Industrial Applications, and Production Methods .....	4
<i>Alzhapparova, N.A., Panshina, S.Yu., Ibrayev, M.K., &amp; Babaev, E.V.</i> Features on the Way to the Synthesis of 1-Benzoyl-2-Phenyl-3a,6a-Diazapentalene and 1-Pivaloyl-2-Tert-Butyl-3a,6a-Diazapentalene .....	14
<i>Palamarchuk, I.V., Kulakov, I.V. &amp; Volkova, S.S.</i> Synthesis and Optical Properties of Substituted Derivatives of Oxazolo[5,4-b]Pyridine .....	23

## PHYSICAL AND ANALYTICAL CHEMISTRY

<i>Abdulsattar, M.A.</i> WO <sub>3</sub> Doped SnS <sub>2</sub> Gas Sensor Response to NO <sub>2</sub> : Effect of Temperature and Humidity Using Transition State Theory Formalism .....	34
<i>Milusheva, R.Yu., Nurgaliev, I.N., Abilkasimov, A.B., &amp; Rashidova, S.Sh.</i> Bioactive Chitosan/β-Tricalcium Phosphate Coatings on Titanium: Experimental Optimization and DFT Insight .....	45

## INORGANIC CHEMISTRY

<i>Soualmi, S., Henni, M., Djahnit, L., &amp; Bouzegaou, M.</i> Structural, Photocatalytic, and Antibacterial Evaluation of Cu-Doped ZnMn <sub>2</sub> O <sub>4</sub> Nanoparticles .....	66
<i>Ismayilova, S.Z., Guliyeva, L.Sh., Ismayilov, R.H., Tagiyev, D.B., Valiyev, F.F., Yalcin, B., Medjidov, A.A., Huseynova, M.T., Chien, S.Y., Lee, G.H., &amp; Peng, Sh.M.</i> Synthesis and Structure of the Novel Mononuclear Copper(II) Complex of the Unsymmetrical Pyrimidine-Modulated Long-Chain Hexapyridylpentaamine Ligand .....	79
<i>Shahid, Z.A., &amp; Tabassum, R.</i> Mn(II) and Zn(II) Complexes of a Coumarin Derivative: Synthesis, Characterization and Biological Potential .....	88

## CHEMICAL TECHNOLOGY

<i>Melikova, I.G., Efendi, A.J., Manafov, M.R., Aykan, N.F., Faradjev, G.M., Rustamova, C.T., &amp; Shikhaliyev, N.I.</i> Kinetics and Mechanism of the Oxidation Reaction of Chlorine-Containing Hydrocarbons on a Vanadium Phosphorus Catalyst .....	109
<i>Kumari, S., Gupta, P.K., Kumar, A., &amp; Kumar, R.</i> Oxidative Transformation of Ethylbenzene Utilizing Metal Bound Immobilized Catalysts .....	120
<i>Kicheeva, A.G., Sushko, E.S., Dzeranov, A.A., Bondarenko, L.S., Tropskaya N.S., Kydralieva, K.A., &amp; Kudryasheva N.S.</i> A Bacterial Enzymatic System Neutralizes the Impact of Silica-Magnetite Nanocomposites on ROS Levels .....	137
<i>Kuzieva, M.M., Urishova, F.M., Atakhanov, A.A., Ashurov, N.Sh., Rashidova, S.Sh., Shiman, D.I., Kostjuk, S.V. &amp; Kang, S.</i> Potassium Permanganate–Oxidized Nanocellulose: Structural Features and Rheological Performance for Advanced Applications .....	148
Index of articles published in “Eurasian Journal of Chemistry” in 2025 .....	160

## ORGANIC CHEMISTRY

Review

Received: 29 May 2025 | Revised: 14 September 2025|

Accepted: 24 November 2025 | Published online: 9 December 2025

UDC 661.715

<https://doi.org/10.31489/2959-0663/4-25-9>

Mariia P. Filina<sup>1\*</sup> , Abdigali A. Bakibaev<sup>1</sup> , Farkhad A. Baiguzin<sup>2</sup> 

<sup>1</sup>*Tomsk State University, Tomsk, Russia;*

<sup>2</sup>*Engineering-Promotional Center Ingehim, Kazan, Russia*

(\*Corresponding author's e-mail: [filina@ect-center.com](mailto:filina@ect-center.com))

### Cyclopentane as an Eco-Friendly Alternative: A Review of its Properties, Industrial Applications, and Production Methods

The Montreal Protocol established stringent international regulations concerning the production, consumption, and trade of ozone-depleting substances, including chlorofluorocarbons and hydrofluorocarbons, aimed at safeguarding the Earth's ozone layer. In this context, cyclopentane has emerged as an environmentally sustainable alternative owing to its zero-ozone depletion potential and low global warming potential. This review examines the physicochemical properties, industrial applications, and production methods of cyclopentane, with particular emphasis on its utilization as a refrigerant, a blowing agent in rigid polyurethane foams, and a hydrate-forming agent for seawater desalination. The primary applications are concentrated in refrigeration and thermal insulation, where cyclopentane-based foams demonstrate superior thermal conductivity and mechanical stability relative to conventional agents. However, the flammability of cyclopentane vapor presents operational challenges that necessitate the implementation of appropriate safety measures. Advances in catalytic reaction-distillation and extractive distillation processes may improve the efficiency of cyclopentane production and product purity in industrial settings. This review underscores cyclopentane's efficacy as a substitute for compounds with higher ozone depletion potentials and emphasizes the importance of ongoing research into scalable, economically viable production technologies and safe industrial integration to fully realize its environmental and practical benefits.

**Keywords:** cyclopentane, fraction C5, pyrolysis, cyclopentene, cyclopentadiene, hydrogenation, cyclopentane hydrates, eco-friendly

#### Contents

List of abbreviations  
Review Plan  
Introduction  
1 Properties  
2 Applications  
3 Methods of production  
Conclusions  
Acknowledgements  
References

#### List of Abbreviations

CPAN: cyclopentane  
CPEN: cyclopentene

CPD:	cyclopentadiene
DCPD:	dicyclopentadiene
CFC:	chlorofluorocarbons
HFCC:	hydrofluorochlorocarbons
HFC:	hydrofluorocarbons
ODP:	ozone depletion potential
GWP:	global warming potential
ORC:	Organic Rankine Cycle

### Review Plan

**Inclusion and Exclusion Criteria:** The review is devoted to properties, applications, methods of production cyclopentane.

The review data mostly cover the publications from 1959 to 2025. However, some old literature sources dated on 1925, 1949 are also cited. Articles in the relevant area were searched and analyzed using databases like Scopus, Web of Science, PubMed etc. along with other online scientific search engines (Google Scholar). The keywords used for the search were: “cyclopentane”, “blowing agent”, “fraction C<sub>5</sub>”, “pyrolysis”, “cyclopentene”, “cyclopentadiene”, “hydrogenation”, “cyclopentane hydrates”. No statistical methods were used in this review.



Mariia Filina is a research engineer at the Laboratory of Artificial Intelligence in Chemistry Materials Science at Tomsk State University, Master's degree in Technological Machines and Equipment from Kazan National Research Technological University. Throughout her scientific and engineering career, she has been involved in a wide range of research fields, including: developing technologies for the synthesis of complex organic compounds, including peroxides, glycosides, and their derivatives; creating technical documentation and engineering solutions related to chemical processing; conducting research on the synthesis and optimization of processes for producing anhydrous hydrogen fluoride and other vital chemicals. She is the author of numerous scientific articles, patents, and technical guidelines related to resource processing, synthetic chemical production, and environmentally sustainable materials.



Abdigali Bakibayev is Professor of Organic Chemistry at Tomsk State University, Doctor of Chemical Sciences. He specializes in the synthesis of biologically active nitrogen-containing compounds, development of new substances from natural raw materials, and chemistry of macro- and supramolecular systems. He has authored over 200 scientific publications, 14 monographs, and more than 50 inventions. His work is applied in industrial production across multiple regions. He actively contributes to scientific and educational communities, serving on dissertation councils and editorial boards, and collaborating internationally, including in Kazakhstan.



Farhad Baiguzin is chemical engineering scientist, PhD (2000). His research interests include applied research in chemical and biochemical engineering. His primary focus areas are heterogeneous catalytic processes, heat and mass transfer, hydrodynamics, and large-scale applications in chemical engineering. He has extensive experience working on various problems as both an employee and head of research at engineering companies. During this period, he co-authored 40 original publications in peer-reviewed journals, including those indexed in Scopus. Additionally, he holds 15 patents for inventions, some of which, when implemented in industry, have generated significant economic impact.

### Introduction

The Montreal Protocol [1], which entered into force on 1 January 1989, and its subsequent amendments, established strict measures to regulate the production, export, import, destruction and consumption of ozone-depleting substances — chlorofluorocarbons (CFC), hydrofluorochlorocarbons (HFCC), hydrofluoro-

carbons (HFC). This agreement played a key role in protecting the Earth's ozone layer and facilitated the transition to safer alternatives.

One alternative to reduce the use of CFC is cyclopentane (CPAN). This hydrocarbon has zero ozone depletion potential (ODP), making it an environmentally friendly choice for use in a variety of industries. In addition, CPAN has a global warming potential (GWP) index of only 5, which is significantly lower than conventional freons.

### *1 Properties*

CPAN is an alicyclic hydrocarbon of composition  $C_5H_{10}$  consisting of five carbon atoms joined in a ring. At room temperature it is a colorless very volatile liquid with a petrol smell, has a boiling point of 49.3 °C, melting point of minus 93.9 °C, vapor pressure at 20 °C is 45 kPa and density is 0.745 g/cm<sup>3</sup>. Flash point is minus 37 °C, autoignition temperature is 320 °C [2].

CPAN is insoluble in water but mixes well with organic solvents (ethanol, acetone, esters, Stoddard solvent or chlorinated hydrocarbons).

The cyclopentane ring can adopt a flat conformation [3, 4] with little angular strain, since the internal pentagon angle is 108°, which is close to the tetrahedral angle of 109.5°. However, in the flat state, all 10 hydrogen atoms will be shaded, leading to a significant torsional energy of 42 kJ/mol. To avoid this undesirable state, CPAN adopts a lower energy non-planar conformation known as the envelope conformation. This "torsion" occurs due to the rotation of the C–C bonds in the ring.

A few publications are devoted to the calculation of thermophysical properties of CPAN, describing the equation of state, which is expressed through the fundamental thermodynamic Helmholtz energy function. The equation of state for CPAN is presented in the book [5], and the publication [6], an evaluation of the application of the equation is presented in the publication [7], where the errors of the equation for density calculations for the liquid phase at temperatures up to 300 K and above the critical temperature are evaluated. The equation for calculation of thermodynamic properties and phase behavior of cyclic hydrocarbons in the temperature range up to 700 K and at pressures up to 100 MPa is also proposed in [8]. In works [9, 10] the possibility of application for technical calculations of thermophysical properties of CPAN of the NIST REFPROP software product, which is also based on the use of a universal equation of state, is substantiated.

### *2 Applications*

CPAN is not commonly used as a solvent or a raw material for chemical transformations [11], but its ability to efficiently absorb and release heat and minimal GWP defines use as a refrigerant. In works [12–14] the application of CPAN and its mixtures in Organic Rankine Cycle (ORC) is noted. A working fluid with a boiling point lower than water and low viscosity is used as a working body in OCR, which allows efficient conversion of low-potential heat into electricity.

The research [15] analyses efficiency and ecological impact refrigeration compression system of the CPAN in comparison with known freons: tetrafluoroethene (Freon-R134A) and HFC mixtures of R407C and R404A brands. The authors have established that at application of CPAN as a working agent the coefficient of efficiency of the refrigeration cycle made 6.485 at the evaporator temperature of 0 °C and the condenser temperature of 25 °C.

However, the main limitation of CPAN application as a working fluid in household refrigerating appliances is flammability of its vapors (explosion limits [16] from 1.4 % vol. (41 g/m<sup>3</sup>) to 8.0 % vol. (233 g/m<sup>3</sup>) that creates high level of danger arising at its leaks from the compressor system.

Polyurethane and polyisocyanurate foams using CPAN as a blowing agent are a group of rigid foams that are used as rigid insulation for pipes, inside refrigerated cabinets [17], automotive industry and other areas. Rigid polyurethane foams are most often subjected to compressive rather than tensile loads and sometimes bending or shear stresses. Strength and cell size stability for foams are important.

In Europe, CPAN and its blends have been used like blowing agent for insulation since 1993. CPAN has a lower thermal conductivity (0.0126 W/m-K) than isopentane and *n*-pentane (0.014–0.015 W/m-K) and despite initial concerns about its thermal insulation properties relative to dichlorofluoroethane (CAS 1717-00-6), European appliance manufacturers have found that CPAN-based foams perform better than expected [18].

In respect that the blowing agent capable to migrate in matrix another characteristic of the insulation is its mechanical strength under actual operating conditions. When using CPAN, there is a risk of condensation associated with its high boiling point (49.5 °C), which can reduce the pressure in the cell (up to 0.1 bar at



minus 20 °C) and compromise the stability of dimensional and strength of the insulation. These risks have been overcome by increasing the cell molding density in CPAN-based foams [19].

For thermal insulation, ageing prediction is also important, which is based on the research of the diffusion of the foaming agent under storage conditions. Over time, foaming agents migrate into the polyurethane, which affects the mechanical properties of the polymer. Hydrocarbons, including CPAN, diffuse faster than CFCs, but actual diffusion data over 15 years appear to be comparable. The condensate of CPAN in the cells maintains the gas phase concentration. Comparative researches [12] show that although some of the CPAN does dissolve into the insulation material, this does not significantly degrade the compressive strength of the insulation.

The experimental research [20] allowed us to explore the effect of the ratio of CPAN and isopentane on the properties of rigid foams used in the thermal insulation of household appliances. The thermal conductivity of the foam increased from 1.561 to 1.784 W/m-K when going from pure CPAN to a mixture of CPAN : isopentane = 60:40. The authors also noted changes in the cell size of the obtained foams, with pure CPAN forming smaller cells compared to the mixtures. There are also known works, in particular [21], that focus on the properties of modified foams obtained with the use of CPAN, during the aging period of thermal insulation.

Recently, scientific research has focused on the use of CPAN as a hydrate-forming agent for desalination seawater [22–25]. Cyclopentane hydrates are crystalline compounds formed by interaction of CPAN with water at atmospheric pressure, which makes the use of CPAN in this direction attractive. The process of desalination seawater using cyclopentane hydrates (Fig. 1) includes the following steps: mixing of cooled CPAN with salt solution, crystallization — formation of cyclopentane hydrate, separation of hydrates from concentrated solution, heating cyclopentane hydrates and reuse CPAN.

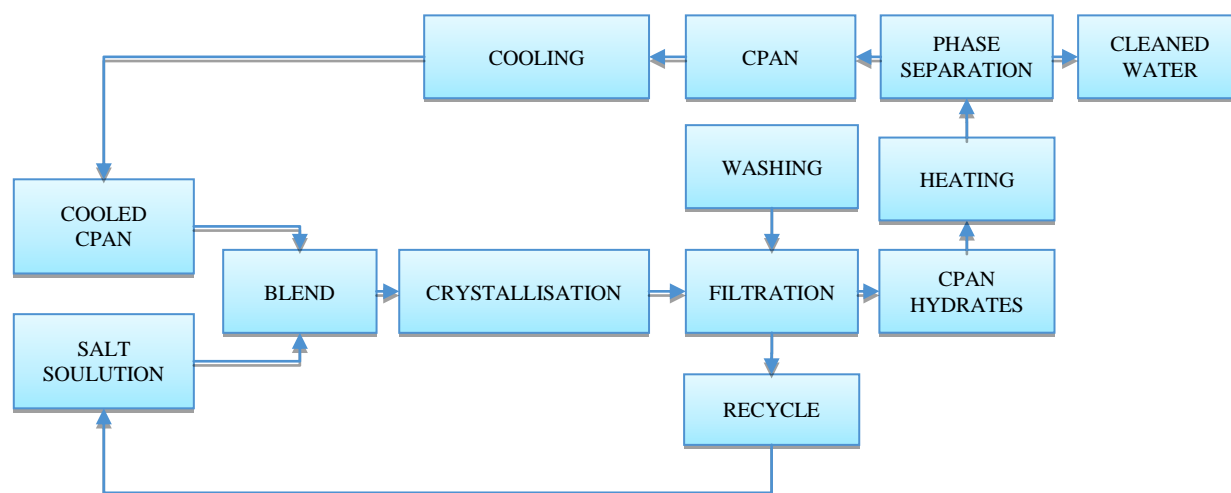


Figure 1. Process of desalination of seawater using cyclopentane hydrates

The review [26] provides a summary of data on hydrate properties, along with a diagram and a desalting process. It should be noted, however, that this process has not yet been implemented on an industrial scale.

### 3 Methods of production

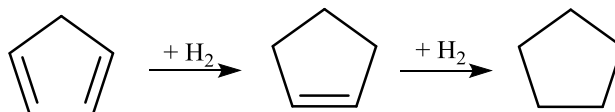
CPAN was first obtained by Connor [27] in 1967 by the action of lithium amalgam on dioxane solution of 1,5-dibromopentane in 75 % yield. This method of synthesis is still used in laboratory techniques [28, 29]. A known obsolete laboratory technique [30, 31] is the cyclisation of adipic acid to cyclopentanone which is accompanied by simultaneous dehydration and decarboxylation. To obtain cyclopentanone crystalline adipic acid is heated with barium hydroxide to 285–295 °C at the same time cyclopentanone is slowly distilled off together with a small amount of adipic acid; the ketone is separated from water by calcium chloride or ether extraction, then washed with aqueous alkali, then with water, dried with calcium chloride and distilled with a dephlegmator, collecting the fraction at 128–131 °C; the resulting cyclopentanone is reduced according to Clemmensen in CPAN with zinc amalgam.



CPAN is present in small amounts in oil and gas condensate in fractions with boiling range of 30–60 °C, but obtaining CPAN from oil fractions is hindered by neo-hexane, which has a close boiling point at atmospheric pressure. The objective of the research [32] is to develop a rapid method to select efficient solvents for the separation of CPAN and neo-hexane using extractive distillation. Dimethylformamide was found to be the most suitable of the three solvents tested. Recent research [33] suggests the use of sodium acetate additive to the above solvents to produce high purity CPAN.

The main industrial method of CPAN production is its separation from C<sub>5</sub> hydrocarbon fractions obtained during the pyrolysis process of ethylene production. Light fraction of liquid pyrolysis products contains linear isomeric and cyclic olefins, dienes, and hydrocarbons of acetylene series with the number of carbon atoms from 5 to 8 [34]. Information about the composition of the hydrocarbon fraction of pyrolysis gasoline in the C<sub>5</sub> fraction formed at industrial plants is presented in [35]. The detailed composition of the C<sub>5</sub> hydrocarbon fraction obtained from ethylene units under different reaction conditions is summarized as follows. At EP-60 ( $T = 770\text{ °C}$ ,  $\tau = 1.3\text{ s}$ ), a longer contact time at a lower temperature result in more complete conversion, with higher contents of alkanes such as isopentane and *n*-pentane, along with a significant proportion of alkenes and alkadienes. At EP-300 ( $T = 810\text{--}815\text{ °C}$ ,  $\tau = 0.5\text{--}0.6\text{ s}$ ), increased temperature and reduced contact time promote intensive dehydrogenation and cracking, decreasing overall C<sub>5</sub> yield and increasing alkynes and cyclic compounds due to extensive dealkylation and cyclization. At EP-450 ( $T = 830\text{ °C}$ ,  $\tau = 0.4\text{--}0.5\text{ s}$ ), even higher temperature and shorter residence time lead to further cracking and aromatization, reducing C<sub>5</sub> yield while increasing the fraction of alkynes and cyclic hydrocarbons. Typically, pyrolysis gasoline contains about 0.5–0.6 wt.% of acetylene hydrocarbons.

The main obstacle of separation CPAN from stream after pyrolysis is azeotrope “1,3-pentadiene-cyclopentene (CPEN)” with boiling point 43.6 °C [36]. Also, as reactive compounds like acetylenes and dienes are the source of polymer formation and limit operations heating and cooling for C<sub>5</sub> fraction of pyrolysis gasoline. Accordingly, in order to extract aromatic and cyclic hydrocarbons, the pyrolysis gasoline is subjected to step-by-step hydrogenation. One of the diolefins present in the C<sub>5</sub> fraction is capable of undergoing complete hydrogenation in CPAN is cyclopentadiene (CPD).



Separation of C<sub>5</sub> hydrocarbons from pyrolysis gasoline is one of way of processing by-products of pyrolysis, which is described in detail in [37, 38]. The generalized essence of the technology, implemented, for example, by the manufacturer Junyuan Petroleum Group [39] is shown in Figure 2.

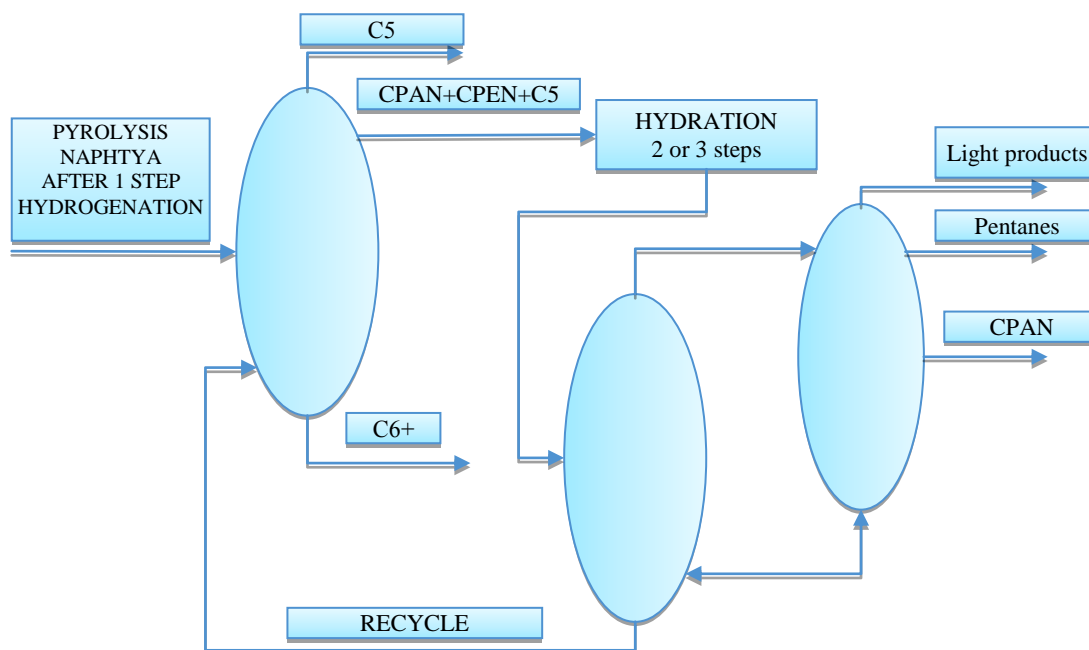


Figure 2. Scheme of CPAN production

One version of technology is also reflected in the patent of BASF AG [40]. The common process technology comprises the following stages: preliminary hydrogenation of pyrolysis naphtha to remove diene hydrocarbons and alkynes, separation of the enriched CPAN-CPEN fraction from hydrogenation naphtha, and separation of CPAN, normal and isopentanes, heavy return products and dissolved light products in rectification columns.

Haltermann Carless GmbH [41], the world's largest producer of CPAN, has an annual production capacity of approximately 100,000 tons. The unit is capable of producing hydrogenated CPAN and middle distillates, normal and isopentane. It can also produce individual hydrocarbons by separating them in the period rectification unit.

A similar approach is applied in Rosneft's patent [42] and other publications [43–47], which differ in terms of the sequence of primary and final hydrogenation stages, stream fractionation, as well as application of extractive methods of mixture separation in some cases.

An alternative way to obtain CPAN with purity up to 99 % is hydrogenation of CPD, which can be obtained from coal tar in the form of its dimer—dicyclopentadiene (DCPD) in the amount of about 10–20 g per tons of coal [48] or from the C<sub>5</sub> fraction of pyrolysis gasoline, which is treated to obtain DCPD [49]. The storage and transportation of CPD occurs in the form of a DCPD dimer.

There are a number of steps involved in the process of separating DCPD from the C<sub>5</sub> fraction. In the first step, the C<sub>5</sub> fraction is heated at normal pressure and a temperature of 30–100 °C for 5–24 hours, or at elevated pressure and a temperature of 140–150 °C, during which CPD is dimerized into DCPD. In a second step, the remaining components of the fraction with a boiling point of 28–50 °C are distilled off and 85–90 % crude DCPD is obtained at the bottom of the column. In the third step, the crude DCPD is monomerized to give cyclopentadiene with a purity of about 95 % [50]. After monomerization CPD hydrogenation yields CPEN according to the Bayer method [51] or used an alternative scheme for obtaining isoprene and CPEN from the C<sub>5</sub> fraction using extractive distillation with N-methyl pyrrolidone [52].

The review of literature devoted to methods of hydrogenation of CPD allows us to highlight several works [53–56]. It should be noted that the process of hydrogenation of CPD to CPEN is well studied and described in detail in various publications [53, 57], the interest in the research of this reaction is determined by the possibility of using CPEN as a monomer for the synthesis of frost-resistant rubbers and other polymers used for optoelectronics [58]. CPD is easily hydrogenated to CPAN on nickel catalyst in alcoholic solvents at 25 °C and atmospheric pressure [59]. The catalytic hydrogenation and isomerisation of various linear and cyclic mono- and diolefins as well as aromatic compounds using the diphenylphosphinomethylhydride compound  $[\text{Cp}_2\text{ZrH}(\text{CH}_2\text{PPh}_2)]_n$  with respect to CPD, the hydrogenation reaction to CPEN and CPAN is shown in [60].

Another way to carry out hydrogenation of CPD using the heat released during the chemical transformation of CPD into CPAN is realized in [54]. This approach is developed in [61, 62] by realizing the process of CPAN production in reaction-distillation apparatuses. Publications on the process of producing CPAN from DCPD via combined reaction-distillation processes are relatively scarce and are primarily documented in patent literature. For instance, one patent [62] describes the production of CPAN in a single catalytic distillation column, which integrates the functions of cracking DCPD, hydrogenation of CPD, and separation of hydrogenation products. In this process, DCPD and hydrocarbons are fed into the lower part of the catalytic column, where cracking to CPD occurs. Hydrogen is also introduced at the bottom of the column to hydrogenate the formed CPD during its distillation. The result is a vapor stream of CPAN, which condenses and is collected as a liquid product. Concurrently, continuous product separation takes place: CPAN is withdrawn as the top distillate, while heavy by-products remain as bottom residue.

A similar procedure for producing CPEN from DCPD is described in another patent [63]. Here, the process is carried out in a reaction-distillation apparatus with the catalytic system located directly within the packing layer of the apparatus. Thus, the primary scheme for producing CPAN from DCPD described in the literature involves feeding the raw materials into the hydrogenation zone along with a vapor stream, with continuous liquid irrigation by condensed products, as depicted in Figure 3.

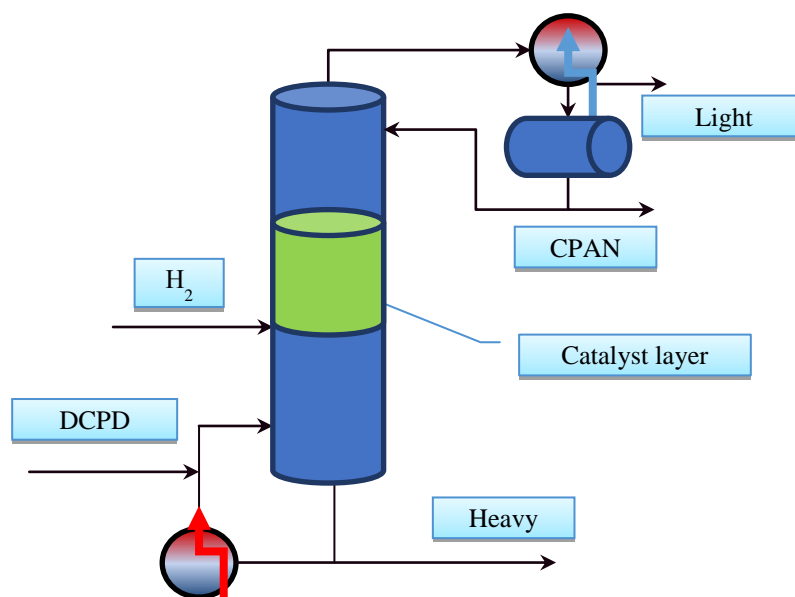


Figure 3. Scheme of CPAN production in reaction-distillation process

It should be noted that in spite of available variants of realization of technology of CPAN production and apparent efficiency of separation methods at industrial realization it is necessary to take into account a number of economic factors, often determining profitability of future production. In particular, special attention should be paid to provision of production with raw materials and possibilities of shipment of finished products. Taking into account the territorial dispersion of pyrolysis plants and, accordingly, the sources of  $C_5$  fraction required in production, in some cases it is reasonable to consider the use of concentrated dimer of CPD as a raw material for processing.

### Conclusions

The extensive industrial utilization of cyclopentane in widely manufactured products, coupled with its growing significance in innovative applications such as seawater desalination via cyclopentane hydrates, provides strong impetus for developing novel industrial production methods and identifying alternative raw material sources for large-scale cyclopentane synthesis. Presently, industrial cyclopentane production predominantly depends on the fractionation of petroleum-derived streams boiling within the 30 to 60 °C range. Advances in catalyst technology and process optimization continue to improve both yield and product purity.

Conventional hydrogenation of pyrolysis gasoline fractions yields cyclopentane; however, additional production opportunities exist through processing dicyclopentadiene from the  $C_5$  pyrolysis fraction isolating. These considerations highlight the need for ongoing research and development focused on catalyst design, integration of reaction-distillation processes, and extractive separation techniques. Such efforts are essential to establish economically viable and scalable industrial processes capable of producing cyclopentane from a variety of way.

### Author Information\*

\*The authors' names are presented in the following order: First Name, Middle Name and Last Name

**Mariia Petrovna Filina** (*corresponding author*) — Engineer, Tomsk State University, Lenin Ave., 36 634050, Tomsk, Russia; e-mail: [filina@ect-center.com](mailto:filina@ect-center.com); <https://orcid.org/0009-0001-2808-1661>

**Abdigali Abdimanapovich Bakibaev** — Doctor of Chemical Sciences, Professor, Tomsk State University, Lenin Ave., 36 634050, Tomsk, Russia; e-mail: [bakibaev@mail.ru](mailto:bakibaev@mail.ru); <https://orcid.org/0000-0002-3335-3166>

**Farkhad Abdriaufovich Baiguzin** — Candidate of Technical Sciences, Engineer, Engineering-Promotional Center Ingehim LLC, 14/83 Shalyapin Str., 420049, Kazan, Russia; e-mail: [umns\\_inform@rambler.ru](mailto:umns_inform@rambler.ru); <https://orcid.org/0009-0007-4251-9117>

### Author Contributions

The manuscript was written through contributions of all authors. All authors have given approval to the final version of the manuscript. **CRedit**: **Abdigali Abdimanapovich Bakibaev** conceptualization, methodology, validation; **Mariia Petrovna Filina** visualization, writing-original draft, writing-review & editing data curation, formal analysis; **Farkhad Abdriaufovich Baiguzin** formal analysis, validation, writing editing.

### Acknowledgments

We would like to express our sincere gratitude to *Tatneftekhiminvest-holding* for overarching research goals and aims.

### Declaration of Generative AI and AI-Assisted Technologies in the Writing Process

During the preparation of this work the authors used Grammarly in order to refine the language of the manuscript. After using this service, the authors reviewed and edited the content as needed and take full responsibility for the content of the publication.

### Conflicts of Interest

The authors declare no conflict of interest.

### References

- 1 United Nations Environment Programme. Ozone Secretariat (2006). *Handbook for the Montreal protocol on substances that deplete the ozone layer*. UNEP/Earthprint. <https://ozone.unep.org/sites/default/files/2019-09/MP-Handbook-07-en-2006.pdf>
- 2 Lide, D. R. (2020). *Basic laboratory and industrial chemicals: a CRC quick reference handbook*. CRC press. <https://doi.org/10.1201/9780429333026>
- 3 Pitzer, K. S., & Donath, W. E. (1959). Conformations and strain energy of cyclopentane and its derivatives. *Journal of the American Chemical Society*, 81(13), 3213–3218. <https://doi.org/10.1021/ja01522a014>
- 4 Ouellette, R. J., & Rawn, J. D. (2018). *Organic chemistry: structure, mechanism, synthesis*. Academic Press. <https://doi.org/10.1016/B978-0-12-812838-1.50001-3>
- 5 Span, R. (2000). *Multiparameter equations of state*. Springer Berlin, Heidelberg. <https://doi.org/10.1007/978-3-662-04092-8>
- 6 Mokbel, I., Rauzy, E., Loiseleur, H., Berro, C., & Jose, J. (1995). Vapor pressures of 12 alkylcyclohexanes, cyclopentane, butylcyclopentane and trans-decahydronaphthalene down to 0.5 Pa. Experimental results, correlation and prediction by an equation of state. *Fluid phase equilibria*, 108(1-2), 103–120. [https://doi.org/10.1016/0378-3812\(95\)02707-L](https://doi.org/10.1016/0378-3812(95)02707-L)
- 7 Gedanitz, H., Davila, M. J., & Lemmon, E. W. (2015). Speed of sound measurements and a fundamental equation of state for cyclopentane. *Journal of Chemical & Engineering Data*, 60(5), 1331–1337. <https://doi.org/10.1021/je5010164>
- 8 Grigor'ev, B., Alexandrov, I., & Gerasimov, A. (2016). Generalized equation of state for the cyclic hydrocarbons over a temperature range from the triple point to 700 K with pressures up to 100 MPa. *Fluid Phase Equilibria*, 418, 15–36. <https://doi.org/10.1016/j.fluid.2015.07.046>
- 9 Huber, M. L., Lemmon, E. W., Bell, I. H., & McLinden, M. O. (2022). The NIST REFPROP database for highly accurate properties of industrially important fluids. *Industrial & Engineering Chemistry Research*, 61(42), 15449–15472. <https://doi.org/10.1021/acs.iecr.2c01427>
- 10 Bell, I. H. (2024). Superancillary Equations for the Multiparameter Equations of State in REFPROP 10.0. *Journal of Physical and Chemical Reference Data*, 53(1). <https://doi.org/10.1063/5.0191228>
- 11 Rulhoff S. (n.d.). Cyclopentane. Haltermann Carless Group GmbH. <https://www.haltermann-carless.com/products/cyclopentane>
- 12 Lecompte, S., Huisseune, H., Van Den Broek, M., Vanslambrouck, B., & De Paepe, M. (2015). Review of organic Rankine cycle (ORC) architectures for waste heat recovery. *Renewable and sustainable energy reviews*, 47, 448–461. <https://doi.org/10.1016/j.rser.2015.03.089>
- 13 Ginosar, D. M., Petkovic, L. M., & Guillen, D. P. (2011). Thermal stability of cyclopentane as an organic Rankine cycle working fluid. *Energy & Fuels*, 25(9), 4138–4144. <https://doi.org/10.1021/ef200639r>
- 14 Minor, B. H. (2006). *Azeotropic compositions of cyclopentane* (Patent No. 7144523 B2). United States. Applicant: E. I. du Pont de Nemours and Company.
- 15 Kılıç, B., Arabacı, E., & Öz, A. (2024). Comparative Thermodynamic and Environmental Analysis of Vapor Compression Refrigeration System Using C-Pentane as Refrigerant. *Scientific Journal of Mehmet Akif Ersoy University*, 7(1), 36–42. <https://doi.org/10.70030/sjmakeu.1473745>

- 16 International Organization for Standardization (2017). *Explosive atmospheres — Part 20-1: Material characteristics for gas and vapour classification — Test methods and data* (ISO/IEC 80079-20-1:2017, including Cor 1:2018). <https://www.iso.org/standard/76568.html>
- 17 Brown, L. J., Morgan, R. E., Haworth, G. J., & Beerwart, A. (1999). Comparative evaluations of alternative blowing agent systems in appliance foams and cabinets. *Journal of cellular plastics*, 35(2), 105–117. <https://doi.org/10.1177/0021955X9903500202>
- 18 Bazzo, W., Cappella, A., & Talbot, S. (1996). Cyclopentane blown foam systems for domestic appliances application. *Journal of cellular plastics*, 32(1), 46–61. <https://doi.org/10.1177/0021955X9603200104>
- 19 Hermama, C., Bensiali, B., Lahbabi, S., & El Maliki, A. (2023). Effect of the shape and the distribution of cells on the effective thermal conductivity of polyurethane foam. *Polymer Engineering & Science*, 63(7), 2278–2294. <https://doi.org/10.1002/pen.26376>
- 20 Schilling, S. L. (2000). Appliance rigid foams blown with cyclopentane and cyclopentane/isopentane blends. *Journal of cellular plastics*, 36(3), 190–206. <https://doi.org/10.1177/0021955X0003600302>
- 21 Santiago-Calvo, M., Tirado-Mediavilla, J., Ruiz-Herrero, J. L., Villafañe, F., & Rodríguez-Pérez, M. Á. (2019). Long-term thermal conductivity of cyclopentane–water blown rigid polyurethane foams reinforced with different types of fillers. *Polymer International*, 68(10), 1826–1835. <https://doi.org/10.1002/pi.5893>
- 22 Corak, D., Barth, T., Høiland, S., Skodvin, T., Larsen, R., & Skjetne, T. (2011). Effect of subcooling and amount of hydrate former on formation of cyclopentane hydrates in brine. *Desalination*, 278(1–3), 268–274. <https://doi.org/10.1016/j.desal.2011.05.035>
- 23 Ho-Van, S., Bouillot, B., Douzet, J., Babakhani, S. M., & Herri, J. M. (2018). Implementing cyclopentane hydrates phase equilibrium data and simulations in brine solutions. *Industrial & Engineering Chemistry Research*, 57(43), 14774–14783. <https://doi.org/10.1021/acs.iecr.8b02796>
- 24 Zhang, J., Chen, S., Mao, N., & He, T. (2022). Progress and prospect of hydrate-based desalination technology. *Frontiers in Energy*, 1–15. <https://doi.org/10.1007/s11708-021-0740-5>
- 25 Mottet, B. (2019). *Method for crystallising clathrates hydrates, and method for purifying an aqueous liquid using the clathrates hydrates thus crystallised*. (Patent No. US10501339 B2). United States. Applicant: BGH.
- 26 Ho-Van, S., Bouillot, B., Douzet, J., Babakhani, S. M., & Herri, J. M. (2019). Cyclopentane hydrates — A candidate for desalination? *Journal of Environmental Chemical Engineering*, 7(5), 103359. <https://doi.org/10.1016/j.jece.2019.103359>
- 27 Connor, D. S. (1969). *Process for the preparation of cyclic alkanes*. (Patent No. 3450782 A). United States. Applicant: Procter and Gamble Co.
- 28 Ahluwalia, V. K., & Aggarwal, R. (2023). *Alicyclic Chemistry*. Springer. <https://doi.org/10.1007/978-3-031-36068-8>
- 29 Silverman, G. S., & Rakita, P. E. (1996). *Handbook of Grignard reagents*. CRC Press. <https://doi.org/10.1201/b16932>
- 30 Thorpe, G.A.R.K. (1925). Cyclopentanone. *Organic syntheses*, 5, 37. <https://doi.org/10.15227/orgsyn.005.0037>
- 31 Brewster, J. H. (1954). Reductions at metal surfaces. II. A Mechanism for the Clemmensen Reduction1. *Journal of the American Chemical Society*, 76(24), 6364–6368. <https://doi.org/10.1021/ja01653a035>
- 32 Wu, L., Pu, X., & Liu, Y. (2017). Solvent Screening for Cyclopentane Purification Based on COSMO. *International Journal of Chemical Engineering and Applications*, 8(2), 97. <https://doi.org/10.18178/ijcea.2017.8.2.637>
- 33 Ren, H., & Li, W. (2025). Study of the Salt-Adding Extractive Distillation of Cyclopentane-2, 2-dimethylbutane Using Composite Extract for the Production of High-Pure Cyclopentane. *Petroleum Chemistry*, 65(1), 82–92. <https://doi.org/10.1134/S0965544124601947>
- 34 Miki, H. (2019). Development of process for production of highly valuable chemicals derived from dicyclopentadiene for comprehensive utilization of C5 chemicals. *Journal of the Japan Petroleum Institute*, 62(6), 245–254. <https://doi.org/10.1627/jpi.62.245>
- 35 Raud, É. A., Lioznov, M. A., Yushina, E. Y., & Smidovich, E. V. (1989). Kinetics of coke deposition in pyrolysis of gasoline fractions. *Chemistry and Technology of Fuels and Oils*, 25(1), 19–23. <https://doi.org/10.1007/BF00725202>
- 36 Horsley, L. H. (1947). Table of azeotropes and nonazeotropes. *Analytical Chemistry*, 19(8), 508–600. <https://doi.org/10.1021/ac60031a022>
- 37 Yamazaki, M. (2004). Industrialization and application development of cyclo-olefin polymer. *Journal of Molecular Catalysis A: Chemical*, 213(1), 81–87. <https://doi.org/10.1016/j.molcata.2003.10.058>
- 38 Hsu, H. C., Wang, S. J., Ou, J. D. Y., & Wong, D. S. H. (2015). Simplification and intensification of a C<sub>5</sub> separation process. *Industrial & Engineering Chemistry Research*, 54(40), 9798–9804. <https://doi.org/10.1021/acs.iecr.5b01705>
- 39 Junyuan Petroleum Group. (n.d.). Junyuan Petroleum Group. Retrieved from <https://junyuanpetroleumgroup.com/>
- 40 Kanne, U., Heners, J., & Krug, T. (2000). (Patent No. 6153804 A). United States. Applicant: BASF SE.
- 41 Haltermann Carless Group GmbH. (n.d.). Hydrogenation units, Speyer. Retrieved from <https://www.haltermann-carless.com/de/hydrierung-speyer>
- 42 Arutyunov, I. A., Kulik, A. V., Khakhin, L. A., & Pominova, G. S. (2018). *Sposob polucheniia tsiklopentana* [Method for producing cyclopentane] (Patent No. 2659227 C1). Russian Federation. Applicant: Publichnoe aktsionernoe obshchestvo «Neftianaia kompaniia «Rosneft»» (PAO «NK «Rosneft»») [in Russian].
- 43 Sharifullin, I. G., Sakhabutdinov, A. G., Amirkhanov, A. T., Misbakhov, I. R., Belanogov, I. A., Shepelin, V. A., & Gilmullin, R. R. (2017). *Sposob polucheniia tsiklopentana* [Method for producing cyclopentane] (Patent No. 2618233 C1). Russian Federation. Applicant: Publichnoe aktsionernoe obshchestvo “Nizhnekamskneftekhim” [in Russian].



- 44 Wan, Sh., Wang, M., Ye, G., & Chen, Y. (2000). *Preparation method of cyclopentane*. (Patent No. 1321625 A). China. Applicant: Sinopec Research Institute of Petroleum Processing, China Petrochemical Corp [in Chinese].
- 45 Tadao, M., & Takashi, O., (2004). *Method for producing high-purity cyclopentane* (Patent No. 2004323485 A). Japan. Applicant: Idemitsu Petrochemical Co Ltd [in Japanese].
- 46 High purity production technology of Cyclopentane (2022). *Heze Sirloong Chemical*. <https://ru.sirloonggas.com/info/high-purity-production-technology-of-cyclopent-73202636.html>
- 47 Ziyatdinov, A. Sh., Maltsev, L. V., Sadrieva, F. M., Boreyko, N. P., Gavrilov, G. S., Vafina, S. F., & Elizarov, V. I. (2003). *Sposob vydeleniia tsiklopentana* [Method for isolating cyclopentane] (Patent No. 2220128 C1). Russian Federation. Applicant: Otkrytoe aktsionerное obshchestvo "Nizhnekamskneftekhim" [in Russian].
- 48 Deng, Q., Zhang, X., Wang, L., & Zou, J. J. (2015). Catalytic isomerization and oligomerization of endo-dicyclopentadiene using alkali-treated hierarchical porous HZSM-5. *Chemical Engineering Science*, 135, 540–546. <https://doi.org/10.1016/j.ces.2014.08.060>
- 49 Herink, T., Fulin, P., Krupka, J., & Pašek, J. (2022). New Technology for Production of Dicyclopentadiene and Methyl-Dicyclopentadiene. *Polymers*, 14(4), 667. <https://doi.org/10.3390/polym14040667>
- 50 Kim, H. G., Lee, H. R., Lim, C. S., & Seo, B. (2019). Separation of Dicyclopentadiene in a C5 stream using a tetraethoxydimethyl disiloxane-derived silica composite membrane. *Journal of Industrial and Engineering Chemistry*, 79, 79–86. <https://doi.org/10.1016/j.jiec.2019.05.016>
- 51 Schwerdtel, W. (1970). *Process for the preparation of cyclopentene from cyclopentadiene* (Patent No. 2025411 A1). Germany. Applicant: Bayer [in German].
- 52 Schliebs, R., Brandt, H. W., Engelhard, B., Steude, H., Scherb, H., & Schnuchel, G. (1972). *Process for recovering cyclopentene, isoprene and a diolefin stream from the C5-cut obtained by petroleum cracking*. (Patent No. 3686349 A). Germany. Applicant: Bayer AG, Erdoelchemie GmbH.
- 53 Guo, S., Zhou, F., Fan, C., & Gu, C. (2005). *Method of preparing cyclopentane by continuous hydrogenation of cyclopentadiene*. (Patent No. 1911875 A). China. Applicant: China Petroleum and Chemical Corp, Sinopec Shanghai Petrochemical Co Ltd. [in Chinese].
- 54 Lattner, J., McMullen, H., Sanchez, L., Silverberg, S., & Dennis, Wu T. (1999). *Process for forming cyclopentane from dicyclopentadiene*. (Patent No. 5998683 A). United States. Applicant: ExxonMobil Chemical Patents Inc.
- 55 Tabler, D. (1974). *Hydrogenation of cyclopentadiene*. (Patent No. 3853748 A). United States. Applicant: Phillips Petroleum Co.
- 56 GUOSHizhuo, X., & XIARonghui, Z. (2005). Kinetics on hydrogenation of cyclopentadiene over Pd/γ-Al<sub>2</sub>O<sub>3</sub> catalyst. *Chinese Journal of Chemical Engineering*, 13(5), 623. <https://cjche.cip.com.cn/EN/Y2005/V13/I5/623>
- 57 Wang, W. J., Qiao, M. H., Yang, J., Xie, S. H., & Deng, J. F. (1997). Selective hydrogenation of cyclopentadiene to cyclopentene over an amorphous NiB/SiO<sub>2</sub> catalyst. *Applied Catalysis A: General*, 163(1–2), 101–109. [https://doi.org/10.1016/S0926-860X\(97\)00125-7](https://doi.org/10.1016/S0926-860X(97)00125-7)
- 58 Kaminsky, W. (2004). Polymerisation Catalysis. In *Basic Principles in Applied Catalysis* (pp. 403–440). Berlin, Heidelberg: Springer Berlin Heidelberg. [https://doi.org/10.1007/978-3-662-05981-4\\_11](https://doi.org/10.1007/978-3-662-05981-4_11)
- 59 Nishimura, S. (2001). *Handbook of heterogeneous catalytic hydrogenation for organic synthesis* (pp. 213–215). New York: Wiley. <https://doi.org/10.1021/op0100798>
- 60 Raoult, Y., Choukroun, R., Basso-Bert, M., & Gervais, D. (1992). Hydrogenation and isomerization of olefins with diphenylphosphinomethyl hydride zirconium, [Cp<sub>2</sub>ZrH(CH<sub>2</sub>PPh<sub>2</sub>)<sub>n</sub>], a selective homogeneous catalyst. *Journal of molecular catalysis*, 72(1), 47–58. [https://doi.org/10.1016/0304-5102\(92\)80029-G](https://doi.org/10.1016/0304-5102(92)80029-G)
- 61 Silverberg, S. E., Sanchez, L. E., & Lattner, J. R. (2000). *Use of catalytic distillation to produce cyclopentane or cyclopentene*. (Patent No. 6100435 A). United States. Applicant: ExxonMobil Chemical Patents Inc.
- 62 Baiguzin, F. A., Burmistrov, D. A., Irdinkin, S. A., & Filina, M. P. (2018). Synthesis of Cyclopentane from Dicyclopentadiene under Conditions of Concurrent Downward Flow in the Catalytic Zone of a Reactive Distillation Units. *Kataliz v promyshlennosti — Catalysis in Industry*, 18(1), 6–12. <https://doi.org/10.18412/1816-0387-2018-1-6-12>
- 63 Ai, F., Yang, L., Qiao, K., Fangm, X., Xu, T., Qi, Wenbo et al. (2018). *A kind of method that high-purity cyclopentadiene is prepared by dicyclopentadiene*. (Patent No 108069813 A). China. Applicant: China Petroleum and Chemical Corp, Sinopec Fushun Research Institute of Petroleum and Petrochemicals [in Chinese].

Nazym A. Alzhapparova<sup>1\*</sup>, Svetlana Yu. Panshina<sup>1</sup>,  
Marat K. Ibrayev<sup>1</sup>, Eugene V. Babaev<sup>2</sup>

<sup>1</sup>Buketov Karaganda National Research University, Karaganda, Kazakhstan;

<sup>2</sup>Lomonosov Moscow State University, Moscow, Russia

(\*Corresponding author's e-mail: [nazym285@mail.ru](mailto:nazym285@mail.ru))

## Features on the Way to the Synthesis of 1-Benzoyl-2-Phenyl-3a, 6a-Diazapentalene and 1-Pivaloyl-2-Tert-Butyl-3a,6a-Diazapentalene

Recently discovered 1,3a,6a-triazapentalene systems are among the new fluorophores whose compact and biocompatible structures are suitable for a variety of biological applications. The wavelengths of 1,3a,6a-triazapentalenes vary depending on the nature of the substituents, allowing for the easy synthesis of yellow and red fluorescent reagents for labeling biomolecules. The prototype of the 1,3a,6a-triazapentalene system (without one aza group) is 3a,6a-diazapentalene, which, originally called pyrazolo[1,2-a]pyrazole, which may also exhibit fluorescent activity. However, their research has been limited to a few papers reporting simple and universal principles for synthesizing the 3a,6a-diazapentalene system, one of which involves double alkylation of pyrazole with  $\alpha$ -halocarbonyl compounds and treatment of the resulting products with a base. In this work, all stages of the previously performed synthesis of 1-benzoyl-2-phenyl-3a,6a-diazapentalene by the reaction of N-acylalkylation of pyrazole with  $\alpha$ -bromoketones through the stages of formation of pyrazolium cation salts are investigated. Based on the studied data, the studied synthesis conditions were first applied by us in stepwise reactions leading to the possible formation of a tert-butyl derivative of 3a,6a-diazapentalene. As a result of the studies, a new, previously undescribed adduct of 3a,6a-diazapentalene, a bicyclic aldol, was obtained. The structure of the substances of the stepwise synthesis was characterized by NMR, IR spectroscopy and mass spectrometry. The mass fragmentation of intermediate N-alkylacylpyrazoles was also considered in detail.

**Keywords:** 3a,6a-diazapentalenes, pyrazole, N-acylalkylation  $\alpha$ -bromoketones, NMR, Aldol, cyclocondensation, quaternization

### Introduction

In the chemistry of heterocyclic compounds, a special role belongs to pentalene systems [1]. Recently, a Japanese group [2] of scientists discovered 1,3a,6a-triazapentalene systems, which are among the new fluorophores (Fig. 1).

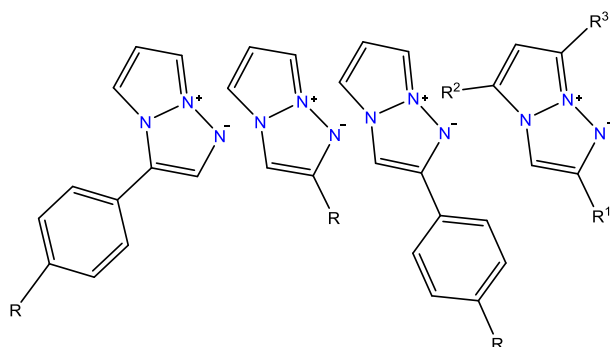


Figure 1. New 1,3a,6a-triazapentalene fluorophores

The compact and biocompatible structure (Fig. 1) of 1,3a,6a-triazapentalene systems exhibits promising spectral properties and is suitable for many biological applications [3, 4]. The wavelengths in them vary depending on the nature of the substituents, which makes it easy to synthesize yellow and red fluorescent reagents for creating labels in biomolecules [3–6].



In recent years, there has been an avalanche-like growth in work on the synthesis and use of 1,3a,6a-triazapentalenes as fluorescent labels [4–9], for example, for various thiols (and in particular, the drug captopril [9]). Methods are being developed for creating unique triazapentalene “wires” to improve the fluorescent properties of materials [10], and their combination with nanomolecular structures [11]. Publications of recent years (on 1,3a,6a-triazapentalenes and benzo- or heterocyclic derivatives) are impressive in their prospects [12–15].

It should be noted that the discovery and selection of such a popular target for fluorescent labels—the triazapentalene system was largely accidental. The prototype of the 1,3a,6a-triazapentalene system (without one aza group) is 3a,6a-diazapentalene [1]. 3a,6a-Diazapentalenes **1** are azaheterocyclic compounds consisting of two five-membered pyrazole rings fused along the N–N bond, having an aromatic 10  $\pi$ -electron system (Fig. 2), hence the alternative name—pyrazolo[1,2-a]pyrazole.

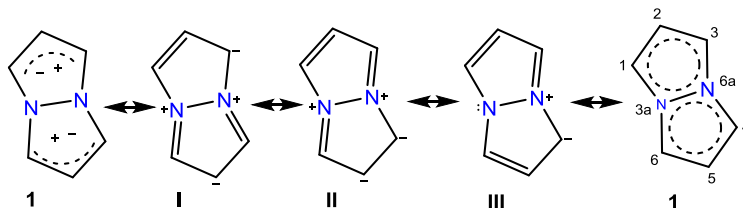


Figure 2. 3a,6a-Diazapentalene **1** and its main resonance forms

The chemistry of these substances froze in the 60–70s of the 20<sup>th</sup> century and did not develop further [16–20]. These systems are extremely easy to synthesize, but more detailed studies have not been conducted, and no studies of fluorescent properties have been reported. This aspect is undoubtedly a major gap in science that needs to be closed and developed in the scientific community, since 3a,6a-diazapentalene systems carry a huge potential for useful properties and a huge arsenal of scientific discoveries.

An interesting feature of molecule **1** is the impossibility of assigning a covalent structure to it without the participation of dipolar resonance forms, i.e. this molecule is a typical mesoionic structure or, more precisely, a mesomeric betaine [21–23]. According to a detailed analysis [24], the largest contribution (>70 %) is made by only three types of resonance forms (Fig. 2), with structures **I** and **II** with two positive and two negative charges (as well as similar ones and those obtained from them due to the symmetry of system **1**) being preferable, structure **III**, having one positive and one negative charge.

The methods for synthesizing 3a,6a-diazapentalene systems are much simpler, do not require metal catalysts, and are more flexible than those for the 1,3a,6a-triazapentalene system. The authors [16–20] first formulated simple and universal principles for the synthesis of the 3a,6a-diazapentalene system **1** from readily available pyrazoles; one of them is double alkylation of pyrazole with  $\alpha$ -halocarbonyl compounds and treatment of the resulting products with a base.

Pyrazoles **2** are five-membered  $\pi$ -electron-excess aromatic heterocyclic compounds that have two linked nitrogen atoms (N–N bond) in the ring structure [25–27], in addition, the pyrazole **2** molecules are planar and strongly associated due to hydrogen bonds [28, 29]. The acid-base properties of pyrazole **2** are due to the presence of pyrrole and pyridine type nitrogen atoms in its structure [30]. Due to the pyridine type nitrogen atom, pyrazole **2** exhibits basic properties ( $\text{pK}_b = 11.5$ ), and due to the pyrrole type nitrogen atom, it exhibits weak acidic properties ( $\text{pK}_a = 2.49$ ) [31].

One of the main ways of creating 3a,6a-diazapentalene compounds is the synthesis of quaternary pyrazolium salts. Only four examples of the synthesis of 1,2-disubstituted pyrazolium salts via repeated alkylation are known in the literature [17], which were then transformed into 3a,6a-diazapentalene structures by treatment with alkaline solutions, through the elimination of water and hydrogen halide and the closure of the second ring of 3a,6a-diazapentalene.

The authors [17] successfully synthesized 4 examples of stable pentalene systems with acceptor substituents, however, these products and their intermediate compounds were not described or characterized spectroscopically.

Taking into account the above, in this study we repeated the previously known synthesis of 3a,6a-diazapentalene, investigated the stepwise route from pyrazole **2** leading to the formation of 3a,6a-diazapentalene compound **8a** through the N-acylalkylation reaction of pyrazole **2** with  $\alpha$ -bromoketone **3a**, where a series of products were obtained and described. Based on the experience gained and understanding

of the chemistry of the reaction, we have developed and implemented for the first time a similar route aimed at the synthesis of previously unknown *tert*-butyl derivatives of 3a,6a-diazapentalene using unsubstituted pyrazole **2** and 1-bromopinacolone **3b** as starting materials.

### Experimental

#### Materials and Methods

Starting materials for the synthesis: pyrazole (98 %) purchased from Acros Organics (Cat. № 13174-0250), phenacyl bromide (98 %) purchased from Sigma-Aldrich (Cat. № 115835), 1-bromopinacolone (98 %) purchased from Sigma-Aldrich (Cat. № 414131). Solvents: dioxane (pure grade) and acetone (special purity grade) purchased from EKOS-1; aqueous ammonia solution (analytical grade) purchased from SigmaTec; NaHCO<sub>3</sub> (analytical grade) was also used. All reagents were used without further purification.

All reactions and purity were monitored by thin layer chromatography (TLC) on Silufol plates with detection by iodine vapor. Melting and boiling points were determined in open capillaries using a Buchi M560 device.

<sup>1</sup>H NMR and <sup>13</sup>C NMR spectra were obtained using Agilent 400-MR (400 MHz for <sup>1</sup>H, 100 MHz for <sup>13</sup>C) spectrometer in CDCl<sub>3</sub> (chemical shift:  $\delta$  = 7.26 for <sup>1</sup>H,  $\delta$  = 77.76 for <sup>13</sup>C) and DMSO-d<sub>6</sub> (chemical shift:  $\delta$  = 2.47 for <sup>1</sup>H,  $\delta$  = 40.03 for <sup>13</sup>C). Hexamethyldisiloxane was used as an internal standard. Splitting is reported as s = singlet, d = doublet, t = triplet, q = quartet, m = multiplet, br = broad and coupling constants are given in Hz. High resolution mass spectra were recorded on a GC-Mass analysis was performed on an Agilent 7890A gas chromatograph with an Agilent 5975C mass-selective detector on an Rtx DHA-100 column; carrier gas was helium. The samples were dissolved in 1 ml of acetone. The IR spectra were obtained using a FSM 1201 FT-IR spectrophotometer in a KBr tablet in the frequency range: 400–4000 cm<sup>-1</sup>.

#### Experimental Procedure

##### Synthesis of 1-(2-oxo-2-phenylethyl)-1H-pyrazol-2-ium bromide (**4a**)

3.4 g (0.05 mol) of pyrazole **2** and 15 ml of dioxane were placed in a 250 ml round-bottomed flask. After 5 minutes, 10 g, (0.05 mol) of phenacylbromide **3a** was added to the mixture. The reaction mixture was stirred for 48 h at room temperature. The precipitated finely dispersed white precipitate of salt **4a** was filtered off and dried in air. The yield of product **4a** is 10.8 g (81 %). Decomposition point over 230 °C (190–193 °C [16]).

##### Synthesis of 1-phenyl-2-(1H-pyrazol-1-yl)ethan-1-one (**5a**)

The salt **4a** was treated with 20 ml of aqueous ammonia solution, the precipitated yellow crystals were filtered off and dried in air. The yield of product **5a** is 8.4 g (91 %). M.p. 95 °C (89–92 °C [16]). <sup>1</sup>H NMR (CDCl<sub>3</sub>)  $\delta$  (ppm), Hz: 7.95–7.89 (m, 2H, Ph), 7.59–7.52 (m, 2H, Ph), 7.48–7.42 (m, 4H, Ph, Pyr), 6.31 (t,  $J$  = 4.4, 1H, Pyr), 5.54 (s, 2H, CH<sub>2</sub>) (Fig. S1). <sup>13</sup>C NMR (CDCl<sub>3</sub>)  $\delta$  (ppm): 192.62 (C=O), 139.98 (CH, Pyr), 134.66 (C, Ph), 134.12 (CH, Pyr), 131.03 (C, Ph), 129.03 (CH, Ph), 128.19 (CH, Ph), 106.59 (CH, Pyr), 57.75 (CH<sub>2</sub>) (Fig. S2). GC-MS Retention time 17.590 min,  $m/z$  (EI) = 186, 158, 105, 77, 51, 41, 28 (Fig. S3). IR  $\nu$ , cm<sup>-1</sup> (KBr, neat): 3013 (CH), 2986 (CH<sub>2</sub>), 1685 (C=O), 1601 (C=N) (Fig. S4).

##### Synthesis of 1,2-bis(2-oxo-2-phenylethyl)-1H-pyrazol-2-ium bromide (**6a**)

3.7 g (0.02 mol) of 1-phenyl-2-(1H-pyrazol-1-yl)ethan-1-one **5a** was dissolved in 15 ml of dry acetone in a 100 ml round-bottomed flask. After the mixture was dissolved, 3.9 g (0.02 mol) of phenacyl bromide **3b** was added. The reaction mixture was capped and stirred for 2 days. If no precipitate formed, the mixture was refluxed for three days. Then the mixture was cooled to room temperature and placed in a cold place. The thickened mass was treated with acetone, which disintegrated into a white fine precipitate **5b**. The precipitate **5b** was washed with hot acetone and isopropyl alcohol and dried in air. The yield of **6a** is 4.8 g. (63 %). M.p. 185 °C (173.5–174 °C [16]). <sup>1</sup>H NMR (DMSO-d<sub>6</sub>)  $\delta$  (ppm), Hz: 8.74 (d,  $J$  = 3.2, 2H, Ph), 8.47 (d,  $J$  = 3.1, 2H, Ph), 7.58–7.56 (m, 2H, Ph), 7.49 (t,  $J$  = 7.6, 2H, Ph), 7.32 (m, 6H, Pyr, Ph), 7.20–7.16 (m, 5H, Pyr, Ph), 6.73 (s, 1H, Pyr), 5.16 (d,  $J$  = 12.7, 2H, CH<sub>2</sub>), 4.88 (d,  $J$  = 12.8, 2H, CH<sub>2</sub>) (Fig. S5). <sup>13</sup>C NMR (D<sub>2</sub>O)  $\delta$  (ppm): 191.01 (C=O), 135.42 (Ph), 134.76 (CH, Pyr), 134.06 (Ph), 133.31 (CH, Pyr), 132.45 (Ph), 129.36, 129.21, 128.94, 128.77, 128.62, 128.46, 125.48 (Ph), 112.42 (CH, Pyr), 75.59 (CH<sub>2</sub>) (Fig. S6). IR  $\nu$ , cm<sup>-1</sup> (KBr, neat): 3078, 1597 (CH), 1693 (C=O) (Fig. S7).

##### Synthesis of 1-benzoyl-2-phenyl-3a,6a-diazapentalene (**8a**)

In 50 ml of 5 % aqueous NaHCO<sub>3</sub> solution 1 g (0.003 mol) of salt **6a** (1,2-bis(3,3-dimethyl-2-oxobutyl)-1H-pyrazol-2-ium bromide) was dissolved, the mixture was stirred and gradually heated to 50 °C. Upon reaching the temperature, copious release of orange precipitate began to be observed on the water sur-

face. The reaction was carried out with intensive stirring for 2–3 days. Control was carried out by TLC. The yellow precipitate **8a** was extracted with chloroform, dried over anhydrous sodium sulfate, then evaporated on a rotary evaporator. Precipitate **8a** was dried in air. The yield of **8a** is 0.71 g (74 %) M.p. 92 °C.  $^1\text{H}$  NMR (DMSO- $d_6$ )  $\delta$  (ppm), Hz: 7.90 (s, 1H, Pyr), 7.83 (d,  $J$  = 6.3, 1H, Pyr), 7.52 (d,  $J$  = 5.5, 4H, Ph), 7.26 (q,  $J$  = 6.8, 2H, Ph), 7.10 (dd,  $J$  = 13.3, 6.6, 4H, Ph), 6.29 (s, 1H, Pyr), 5.82 (s, 1H, CH) (Fig. S8).  $^{13}\text{C}$  NMR (DMSO- $d_6$ )  $\delta$  (ppm): 176.10 (C=O), 140.69, 132.76, 129.92 (Ph), 129.66 (CH, Pyr), 129.55 (CH, Pyr), 129.40, 128.68, 128.07, 127.61, 127.54 (Ph), 113.02 (CH), 109.36 (C=), 104.87 (CH, Pyr). (Fig. S9).

#### Synthesis of 1-(3,3-dimethyl-2-oxobutyl)-1H-pyrazol-2-iumbromide (**4b**)

2 g (0.0294 mol) of pyrazole **2** and 15 ml of dioxane were placed in a 100 ml round-bottomed flask. After 5 minutes, 3.95 ml (5.3 g, 0.0294 mol) of 1-bromopinacolone **3b** was added to the mixture. The reaction mixture was stirred for 48 h at room temperature. The formed precipitate of salt **4b** was filtered off and dried in air. The yield of product **4b** is 6 g (84 %). M.p. 175 °C.

#### Synthesis of 3,3-dimethyl-1-(1H-pyrazol-1-yl)butan-2-one (**5b**)

Then salt **4b** was treated with 20 ml of aqueous ammonia solution, the precipitated yellowish crystals **5a** were filtered off and dried in air. The yield of product **5b** is 3.2 g (65 %). M.p. 56 °C.  $^1\text{H}$  NMR (CDCl<sub>3</sub>)  $\delta$  (ppm), Hz: 8.54 (d,  $J$  = 3.0, 1H, Pyr), 8.08 (d,  $J$  = 6.8, 1H, Pyr), 6.71 (t,  $J$  = 3.0, 1H, Pyr), 4.67 (s, 2H, CH<sub>2</sub>), 1.28 (s, 9H, C(CH<sub>3</sub>)<sub>3</sub>) (Fig. S10).  $^{13}\text{C}$  NMR (CDCl<sub>3</sub>)  $\delta$  (ppm): 205.92 (C=O), 139.34 (CH, Pyr), 129.81 (CH, Pyr), 107.48 (CH, Pyr), 56.53 (CH<sub>2</sub>), 43.89 (C(CH<sub>3</sub>)<sub>3</sub>), 26.34 (C(CH<sub>3</sub>)<sub>3</sub>) (Fig. S11). GC-MS Retention time 11.759 min,  $m/z$  (EI) = 166, 151, 138, 109, 85, 81, 57, 41, 29, 28 (Fig. S12). IR  $\nu$ , cm<sup>-1</sup> (KBr, neat): 2959 (CH<sub>3</sub>), 1716 (C=O), 1597 (C=N) (Fig. S13).

#### Synthesis of 1,2-bis(3,3-dimethyl-2-oxobutyl)-1H-pyrazol-2-ium bromide (**6b**)

1.43 g (0.009 mol) of 3,3-dimethyl-1-(1H-pyrazol-1-yl)butan-2-one **5b** was dissolved in 15 ml of dry acetone in a 100 ml round-bottomed flask. After the mixture was dissolved, 1.6 g (0.009 mol) of bromopinacolone **3b** was added. The reaction mixture was capped and stirred for 2 days. If no precipitate formed, the mixture was refluxed for three days. Then the mixture was cooled to room temperature and placed in a cold place. The thickened mass was treated with acetone, which disintegrated into a white fine precipitate **6b**. The precipitate **6b** was washed with hot acetone and isopropyl alcohol and dried in air. The yield of **6b** is 2.5 g. (82 %). M.p. 190 °C.  $^1\text{H}$  NMR (D<sub>2</sub>O)  $\delta$  (ppm), Hz: 8.19 (d,  $J$  = 2.9, 1H, Pyr), 8.00 (d,  $J$  = 3.0, 1H, Pyr), 6.84 (t,  $J$  = 2.9, 1H, Pyr), 4.98 (d,  $J$  = 12.8, 2H, CH<sub>2</sub>), 4.70 (d,  $J$  = 12.8, 2H, CH<sub>2</sub>), 1.17 (s, 9H, t-Bu), 0.86 (s, 9H, t-Bu) (Fig. S14).  $^{13}\text{C}$  NMR (D<sub>2</sub>O)  $\delta$  (ppm): 212.34 (C=O), 132.01 (CH, Pyr), 130.67 (CH, Pyr), 112.58 (CH, Pyr), 45.13 (CH<sub>2</sub>), 38.23 (C, t-Bu), 24.78 (t-Bu), 23.21 (t-Bu) (Fig. S15). IR  $\nu$ , cm<sup>-1</sup> (KBr, neat): 2970 (CH<sub>3</sub>), 1724 (C=O), 1612 (C=N) (Fig. S16).

#### Synthesis of 2-(tert-butyl)-2-hydroxy-1-pivaloyl-2,3-dihydro-1H-pyrazolo[1,2-a]pyrazol-4-ium bromide (**7b**)

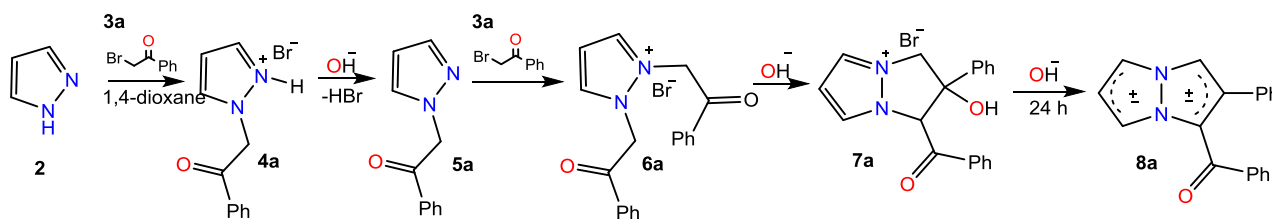
In 50 ml of 10 % aqueous NaHCO<sub>3</sub> solution 1 g (0.003 mol) of salt **6b** (1,2-bis(3,3-dimethyl-2-oxobutyl)-1H-pyrazol-2-ium bromide) was dissolved, the mixture was stirred and gradually heated to 50 °C. Upon reaching the temperature, copious release of orange precipitate began to be observed on the water surface. The reaction was carried out until the formation of precipitate **7b** ceased. Precipitate **7b** was filtered off and dried in air. The yield of **7b** is 0.71 g (74 %). M.p. 90 °C.  $^1\text{H}$  NMR (DMSO- $d_6$ )  $\delta$  (ppm), Hz: 8.36 (d,  $J$  = 2.9, 1H, Pyr), 8.21 (d,  $J$  = 2.9, 1H, Pyr), 6.89 (t,  $J$  = 2.9, 1H, Pyr), 6.54 (s, 1H, OH), 6.49 (s, 1H), 4.98 (d,  $J$  = 12.5, 1H, CH<sub>2</sub>), 4.18 (d,  $J$  = 12.5, 1H, CH<sub>2</sub>), 1.12 (s, 9H, t-Bu), 0.77 (s, 9H, t-Bu) (Fig. S17).  $^{13}\text{C}$  NMR (DMSO- $d_6$ )  $\delta$  (ppm): 210.05 (C=O), 132.59 (CH, Pyr), 131.55 (CH, Pyr), 112.54 (CH, Pyr), 90.16 (C-OH), 65.32 (CH), 53.72 (C, t-Bu), 45.14 (C, t-Bu), 39.37 (CH<sub>2</sub>), 25.97 (CH<sub>3</sub>, t-Bu), 24.25 (CH<sub>3</sub>, t-Bu) (Fig. S18).

### Results and Discussion

Thus, we obtained 1-benzoyl-2-phenyl-3a,6a-diazapentalene **8a** (74 %), the step-by-step synthesis of which is as follows: pyrazole **2** reacts with phenacyl bromide **3a** (Fig. 3) in dioxane to form salt **4a** (81 %), which, when treated with an aqueous ammonia solution, gives 1-phenacylpyrazole **5a** with a yield of 91 %.

Subsequent alkylation of compound **5a** with a second equivalent of phenacyl bromide **3a** in acetone leads to the formation of 1,2-diphenacylpyrazolium bromide **6a** in 63 % yield. The resulting dialkylated salt **6a** is a colorless crystalline water-soluble substance.

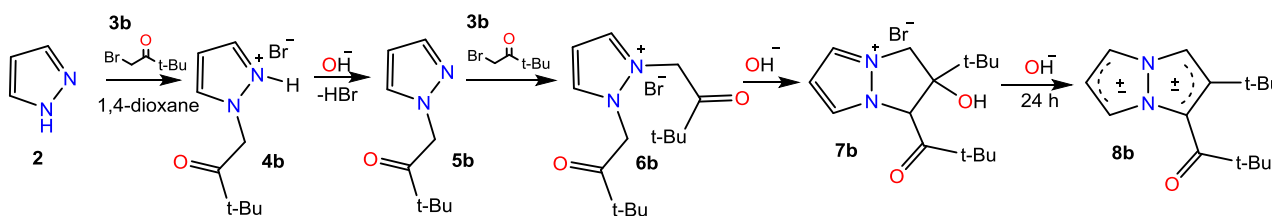
When salt **6a** was treated with 10 % aqueous NaHCO<sub>3</sub> solution upon heating to 50 °C for a long time (24 h), 1-benzoyl-2-phenyl-3a,6a-diazapentalene **8a** was formed as a yellow fine powder in good yield (74 %).

Figure 3. Scheme of the step-by-step synthesis of diaryl-3a,6a-diazapentalene **8a**

The fact that the condensation of carbonyl compounds occurs through the formation of aldols is well known [32], however, in this case, we could not quantitatively observe the formation of aldol **7a**, similar to the 4-fluoro-substituted compound that was previously also obtained and described by X-ray diffraction [33].

The structure of the stepwise synthesized products **4a**, **5a**, **6a**, **8a** was characterized by NMR, IR spectroscopy and mass spectrometry.

We repeated the studied conditions in reactions of synthesis of *tert*-butyl derivatives of pyrazole, in order to obtain a new 3a,6a-diazapentalene (Fig. 4)

Figure 4. Scheme of the step-by-step synthesis of di(*tert*-butyl)-3a,6a-diazapentalene **8b**

Thus, the N-acylalkylation reaction of unsubstituted pyrazole **2** with 1-bromopinacolone **3b** was carried out in dioxane to form salt **4b** (84 %), which is a colorless crystalline substance soluble in water and polar organic solvents. Upon further treatment of salt **4b** with a base, *tert*-butyl-1-(pyrazol-1-yl)butan-2-one **5b** is formed—low-melting light-yellow crystals, with a total yield of the final product of 65 % (Fig. 4).

The yield of product **5b** decreases due to the increased solubility of the initial salt **4b** in an aqueous medium. And it is more expedient to carry out this reaction in organic solvents, in the presence of anhydrous bases. Thus, we have experimentally established that the reaction in acetone in the presence of  $K_2CO_3$  gives product **5b** with yields of up to 90 %. The potassium carbonate used in parallel with the N-alkylation reaction “One-pot” neutralizes the released hydrobromide with the formation of inorganic salts, as well as the target product **5b**.

Next, N-pinacolone pyrazole **5b** was reacted with another equivalent of 1-bromopinacolone **3b** in acetone for a week, where colorless crystals representing the symmetrical salt **6b** were obtained (Fig. 4).

The next step was to treat salt **6b** with 10 % aqueous  $NaHCO_3$  solution by heating to 50 °C for 10 hours, which led to the formation of an orange substance in 74 % yield, NMR analysis of which showed that it was cyclic aldol **7b**. It was determined that the molecule **7b** is not dehydrated, chemical shifts of the geminal protons  $H^a$  and  $H^b$  are present as a doublet pair, as well as a chemical shift of the OH-group (Fig. 5).

To reliably establish the structure of **7b**, we used homonuclear and heteronuclear methods of 2D NMR spectroscopy, where the most convenient and informative is the  $^1H$ - $^{13}C$  HSQC spectrum. Describing this spectrum, we can compare protons connected to the corresponding carbon. As well as signals of protons that do not have direct bonds with carbons.

Thus, Figure 5 shows a pair of doublets of geminal protons  $H^a$  ( $\delta$  4.98 ppm) and  $H^b$  ( $\delta$  4.18 ppm), which are bound to carbon  $C_8$  ( $\delta$  53.72 ppm). The formation of such doublet protons of one  $CH_2$ -group indicates the formation of a cyclic structure and a hindered conformation of the methylene group, in which the rotation of the  $H^a$  and  $H^b$  protons is limited [34]. There is also a broadened chemical shift of the OH-group, the proton of which does not have a direct bond with carbons.

In addition, the chemical shifts of protons and carbons of the pyrazole fragment ( $\delta_H$  8.36 ppm –  $\delta_C$  132.59 ppm;  $\delta_H$  8.21 –  $\delta_C$  131.55 ppm;  $\delta_H$  6.89 ppm –  $\delta_C$  112.54 ppm) and *tert*-butyl groups ( $\delta_H$  1.12 ppm –  $\delta_C$  25.97 ppm;  $\delta_H$  0.77 –  $\delta_C$  24.25 ppm) are clearly distinguished; we compared the sequence in the molecule of these groups using  $^1H$ - $^{13}C$  HMBC and  $^1H$ - $^1H$  COSY spectra (Figures S19, S20).

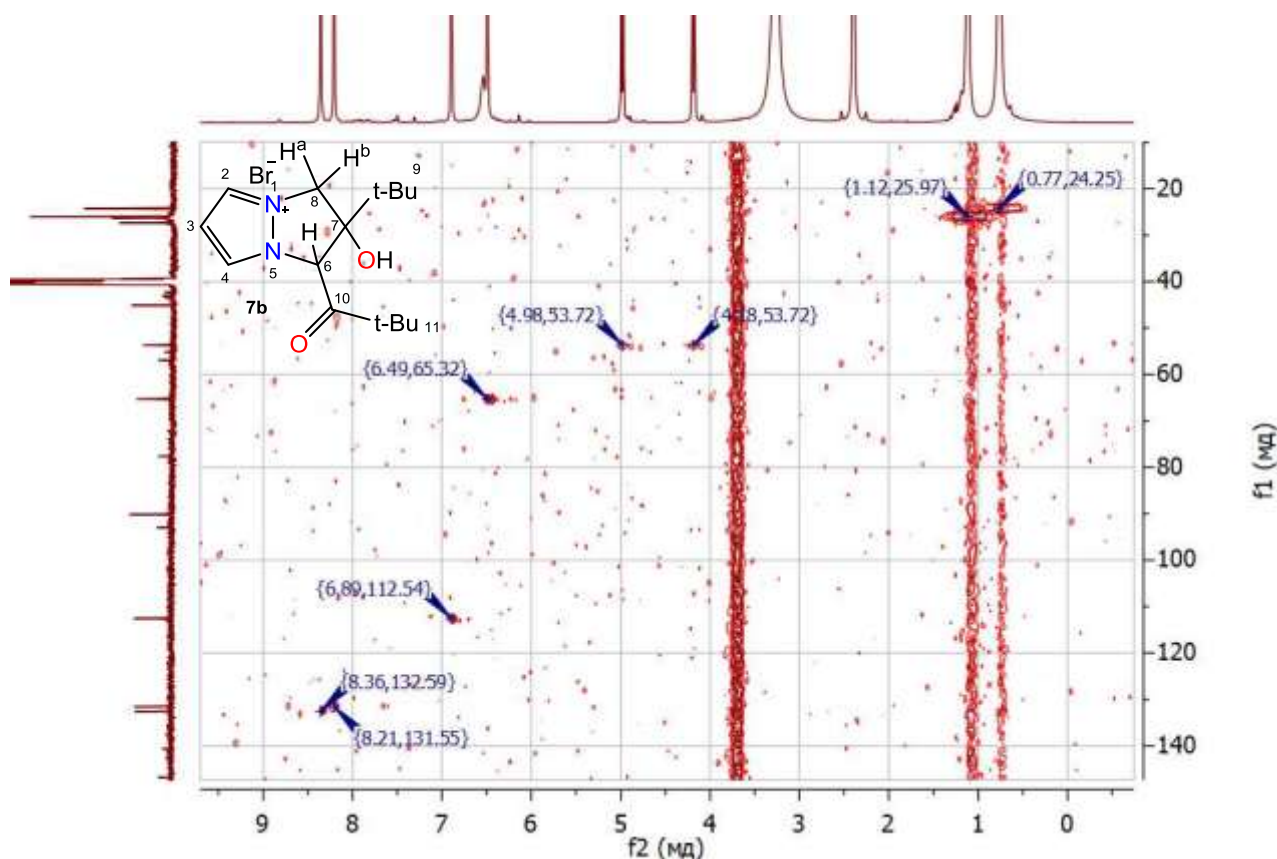


Figure 5.  $^1\text{H}$ – $^{13}\text{C}$  HSQC spectrum of aldol **7b** in  $\text{DMSO-d}_6$  ( $\delta$ : 2.50 ppm; 39.5 ppm)

It is known that if the time of treatment with the base of the obtained aldol **7b** is increased from several hours to several days, then 3a,6a-diazapentalene can be obtained [1], however, in the case of *tert*-butyl aldol **7b** we were unable to obtain any pentalene **8b**. The structures of the obtained products **4b**, **5b**, **6b**, **7b** were characterized by IR, NMR spectroscopy and mass spectrometry.

There is no information in the available literature on the features of the fragmentation of N-acylalkylpyrazoles, and therefore we examined in detail the features of the ionized decomposition of molecules **5a** and **5b**. Thus, according to the mass spectrometric analysis using Electron ionization, it was determined that the molecular ion of N-pinacolopyrazole **5b** with the value of  $M^+ = 166.1$  m/z has a noticeable intensity. The molecule disintegrates into positively charged ions by the following path (Fig. 6).

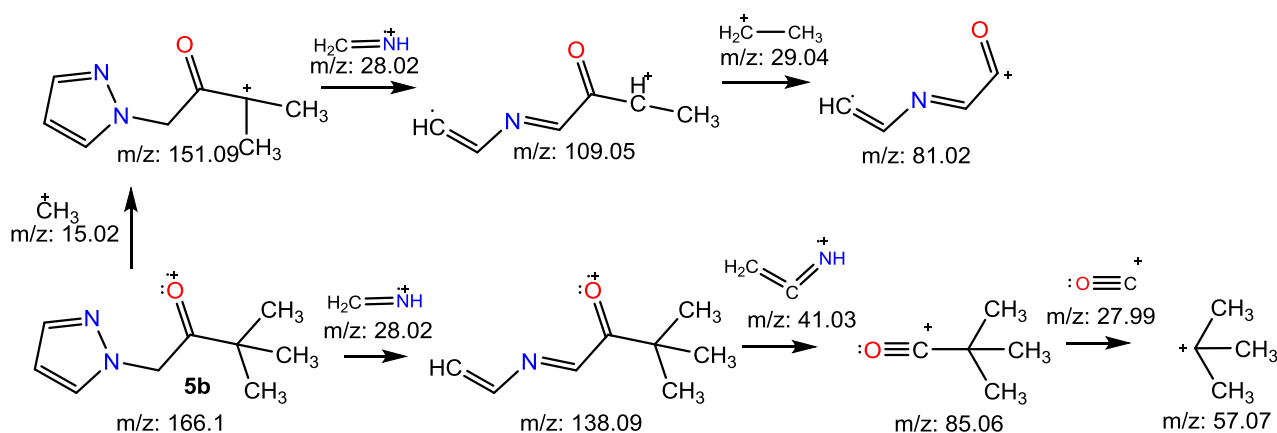


Figure 6. Molecular fragmentation of N-pinacolopyrazole **5b**

The most intense fragment peaks in the mass spectrum of compound **5b** correspond to fragment ions  $m/z = 29$ , 57, 81, which is due to the cleavage of the C–C bond adjacent to the oxygen atom, with the charge



retained on the resonance-stabilized acylium cations  $m/z = 85$  and  $81$ . In addition, the fragmentation of **5b** is due to the opening of the pyrazole ring with the detachment of ions  $m/z 28$   $\text{NH}=\text{CH}^+$  and  $m/z 41$   $\text{NH}=\text{C}=\text{CH}^+$ , which are also displayed in the mass fragmentation of N-phenacylpyrazole **5a** (Fig. 7).

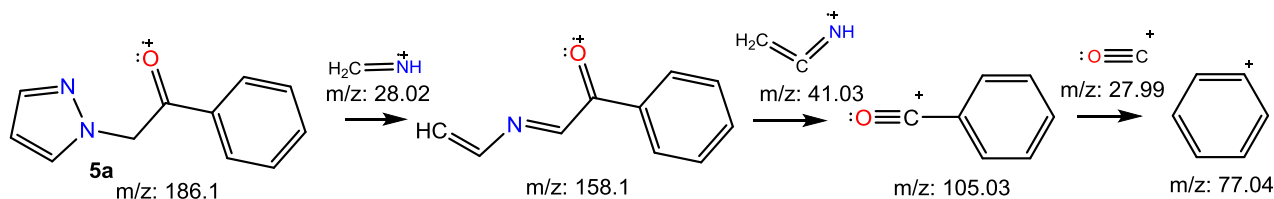


Figure 7. Molecular fragmentation of N-phenacylpyrazole **5a**

The peak of the molecular ion  $m/z$  186.1 of N-phenacylpyrazole **5a** has a noticeable intensity. First of all, the particle  $m/z$  28  $\text{NH}=\text{CH}^+$  is detached from the pyrazole ring to form a molecular ion  $m/z$  158.1, the high intensity of which is due to the formation of a stable conjugated system of alternating double bonds. Further fragmentation of the  $m/z$  158.1 ion occurs at the bond in the  $\alpha$ -position relative to the phenyl ring with the formation of the characteristic  $\text{Ph}-\text{C}=\text{O}^+$  fragment ( $m/z$  105), which exhibits maximum intensity along with the phenyl ion  $m/z$  77. The latter is formed when the  $\text{Ph}-\text{C}=\text{O}^+$  fragment subsequently loses the  $\text{C}=\text{O}^+$  particle.

Thus, N-alkylacylpyrazoles **5a** and **5b** are substances that are ketones and simultaneously substituted cyclic diamines, the identification of which in the mass spectra can be carried out by the characteristic separation of particles  $m/z$  28  $\text{NH}=\text{CH}^+$  and  $m/z$  41  $\text{NH}=\text{C}=\text{CH}^+$  and by the presence of fragmentary ions corresponding to the decomposition of aliphatic (**5b**) or aromatic ketones (**5a**).

### Conclusions

Thus, in this study, we have thoroughly studied the steps, substances and their structure in the synthesis of 1-benzoyl-2-phenyl-3a,6a-diazapentalene **8a** via the N-acylalkylation reaction of pyrazole **2** with  $\alpha$ -bromoketone **3a**. Where substance **8a** was obtained with a good yield of 74 %.

The studied chemistry of the process was used step by step to implement the synthesis route of a similar *tert*-butyl derivative of the 3a,6a-diazapentalene system **8b**. Studies have shown that this step-by-step synthesis of **8b** stopped at the formation of the aldol salt **7b**, and the target 3a,6a-diazapentalene **8b** was not obtained under the studied conditions. The structure of the aldol salt **7b** was characterized by 2D NMR spectroscopy. It is impossible not to note the peculiarity of the influence of the steric factor of phenyl and *tert*-butyl groups, which may require additional study using molecular optimization methods, since in the synthesis of the target phenyl derivative **8a**, the aldol product **7a** was not isolated by us.

The mass fragmentation of N-alkylacylpyrazoles **5a** and **5b** is also considered in detail, the consideration of which will facilitate further study of 3a,6a-diazapentalene structures.

It should be noted that the simplicity and availability of the starting reagents (**2**, **3a**, **b**) in the synthesis of 3a,6a-diazapentalene systems, high yields of intermediate products, simplicity of experiments and conditions for the isolation of target substances open up the possibility of scaling and obtaining significant quantities of derivatives of 3a,6a-diazapentalene structures for the possible creation of functional fluorophore reagents.

### Supporting Information

The Supporting Information is available free at <https://ejc.buketov.edu.kz/index.php/ejc/article/view/488/301>

### Funding

This research was funded by the Science Committee of the Ministry of Science and Higher Education of the Republic of Kazakhstan (Grant No. AP19677175) "Development of a new affordable class of fluorescent labels based on diazapentalenes" and within the framework of the State Assignment of the Lomonosov Moscow State University (Registration No. AAAA-A21-121012290046-4).

---

### Author Information\*

---

\*The authors' names are presented in the following order: First Name, Middle Name and Last Name

**Nazym Abdygazievna Alzhapparova** (*corresponding author*) — 3rd year PhD Student, Department of Organic Chemistry and Polymers, Buketov Karaganda National Research University, Universitetskaya street, 28, 100024, Karaganda, Kazakhstan; e-mail: [nazym285@mail.ru](mailto:nazym285@mail.ru); <https://orcid.org/0000-0002-0359-2350>

**Svetlana Yurievna Panshina** — Candidate of Chemical Sciences, Assistant Professor, Department of Organic Chemistry and Polymers, Buketov Karaganda National Research University, Universitetskaya street, 28, 100024, Karaganda, Kazakhstan; e-mail: [janim\\_svetatusik@mail.ru](mailto:janim_svetatusik@mail.ru); <https://orcid.org/0000-0001-6824-2645>

**Marat Kirimbayevich Ibrayev** — Doctor of Chemical Sciences, Research Professor, Department of Organic Chemistry and Polymers, Buketov Karaganda National Research University, Universitetskaya street, 28, 100024, Karaganda, Kazakhstan; e-mail: [mkibr@mail.ru](mailto:mkibr@mail.ru); <https://orcid.org/0000-0003-0798-5562>

**Eugene Veniaminovich Babaev** — Doctor of Chemical Sciences, Lomonosov Moscow State University, Leninskie Gory, 1-3, GSP-1, 119991, Moscow, Russia, e-mail: [babaev@org.chem.msu.ru](mailto:babaev@org.chem.msu.ru); <https://orcid.org/0000-0001-8727-7763>

### Author Contributions

The manuscript was written through contributions of all authors. All authors have given approval to the final version of the manuscript. **CRedit**: **Nazym Abdygazievna Alzhapparova** — writing-original draft, writing-review & editing; **Svetlana Yurievna Panshina** — writing and reviewing, editing; **Marat Kirimbayevich Ibrayev** — data curation, formal analysis, visualization, fundraising, resources, supervision, validation; **Eugene Veniaminovich Babaev** — conceptualization, data curation, research, methodology.

### Acknowledgments

We express our deep gratitude to *Lomonosov Moscow State University* for cooperation in this research.

### Conflicts of Interest

The authors declare no conflict of interest.

### References

- 1 Babaev, E.V., Panshina, S.Yu., Alzhapparova, N.A., Ibraev, M.K., & Usenova, M.S. (2025). 3a,6a-Diazapentaleny (pirazolo[1,2-a]pirazoly) [3a,6a-Diazapentalenes (pyrazolo[1,2-a]pyrazoles)]. *Izvestiia Akademii nauk. Seriya khimicheskaya — Chemical Bulletin*, 74(7), 1958–1975 [in Russian]. <https://doi.org/10.1007/s11172-025-4681-8>
- 2 Koga, H., Hirobe, M., & Okamoto T. (1978). Mesionic 1,3a,6a-triazapentalenes. *Tetrahedron Lett.*, 19(15), 1291–1294. [https://doi.org/10.1016/0040-4039\(78\)80109-9](https://doi.org/10.1016/0040-4039(78)80109-9)
- 3 Namba, K., Osawa, A., Nakayama, A., Mera, A., Tano, F., Chuman, Y., Sakuda, E., Taketsugu T., Sakaguchi, K., Kitamura, N., & Tanino, K. (2015). Synthesis of yellow and red fluorescent 1,3a,6a-triazapentalenes and the theoretical investigation of their optical properties. *Chemical Science*, 6(2), 1083–1093. <https://doi.org/10.1039/c4sc02780a>
- 4 Tsuji, D., Nakayama, A., Yamamoto, R., Nagano, S., Taniguchi, T., Sato, R., Karanjit, S., Muguruma, N., Takayama, T., Itoh, K., & Namba K. (2023). 1,3a,6a-Triazapentalene derivatives as photo-induced cytotoxic small fluorescent dyes. *Communications Chemistry*, 6(1), 37. <https://doi.org/10.1038/s42004-023-00838-0>
- 5 Chen, Y., Wang, D., Petersen, J.L., Akhmedov N.G., & Shi, X. (2010). Synthesis and characterization of organogold complexes containing an acid stable Au–C bond through triazole-yne 5-endo-dig cyclization. *Chemical Communications*, 46, 6147–6149. <https://doi.org/10.1039/C0CC01338B>
- 6 Cai, R., Wang, D., Chen, Y., Yan, W., Geise, N.R., Sharma, S., Li, H., Petersen, J.L., Li, M., & Shi., X. (2014). Facile synthesis of fluorescent active triazapentalenes through gold-catalyzed triazole-alkyne cyclization. *Chemical Communications*, 50, 7303–7305. <https://doi.org/10.1039/C4CC03175J>
- 7 Wang, Y., Opsomer, T., & Dehaen, W. (2022). Developments in the chemistry of 1,3a,6a-triazapentalenes and their fused analogs. *Advances in Heterocyclic Chemistry*, 137, 25–70. <https://doi.org/10.1016/bs.aihch.2021.10.002>
- 8 Verbelen, B. & Dehaen, W. (2016). Two-Step Synthesis of Fluorescent 3-Arylated 1,3a,6a-Triazapentalenes via a Three-Component Triazolization Reaction. *Organic Letters*, 18(24), 6412–6415. <https://doi.org/10.1021/acs.orglett.6b03309>
- 9 Nakayama, A., Otani, A., Inokuma, T., Tsuji, D., Mukaiyama, H., Nakayama A., Itoh, K., Otaka, A., Tanino, K., & Namba, K. (2020). Development of a 1,3a,6a-triazapentalene derivative as a compact and thiol-specific fluorescent labeling reagent. *Communications Chemistry*, 3(1), 6, 1–9. <https://doi.org/10.1038/s42004-019-0250-0>



- 10 Ito, M., Mera, A., Mashimo, T., Seki, T., Karanjit, S., Ohashi, E., Nakayama, A., Kitamura, K., Hamura, T., Ito, H., & Namba, K. (2018). Synthesis and Evaluation of a 1,3a,6a-Triazapentalene (TAP)-Bonded System. *Chemistry — A European Journal*, 24(67), 17727–17733. <https://doi.org/10.1002/chem.201804733>
- 11 Legentil, P., Chadeyron, G., Therias, S., Chopin, N., Sirbu, D., Suzenet, F., & Leroux, F. (2020). Luminescent N-heterocycles based molecular backbone interleaved within LDH host structure and dispersed into polymer. *Applied Clay Science*, 189, 105561. <https://doi.org/10.1016/j.clay.2020.105561>
- 12 Wang, Y., Opsomer, T., Van Meervelt, L., & Dehaen, W. (2020) Ring-Degenerate Rearrangement Resulting from the Azo Coupling Reaction of a 3-Aryl-1,3a,6a-triazapentalene. *The Journal of Organic Chemistry*, 85(14), 9434–9439. <https://doi.org/10.1021/acs.joc.0c01153>
- 13 Sirbu, D., Diharce, J., Martinić, I., Chopin, N., Eliseeva, S.V., Guillaumet, G., Petoud, S., Bonnet, P., & Suzenet, F. (2019) An original class of small sized molecules as versatile fluorescent probes for cellular imaging. *Chemical Communications*, 55(54), 7776–7779. <https://doi.org/10.1039/c9cc03765a>
- 14 Wang, Y., Pham, T. C., Huang, J., Wu, J., & Dehaen, W. (2025). Heteroaryl-Fused Triazapentalenes: Synthesis and Aggregation-Induced Emission. *Molecules*, 30(1), 156. <https://doi.org/10.3390/molecules30010156>
- 15 Wang, Y., Opsomer, T., de Jong, F., Verhaeghe, D., Mulier, M., Van Meervelt, L., Van der Auweraer, M., & Dehaen, W. (2024). Palladium-Catalyzed Arylations towards 3,6-Diaryl-1,3a,6a-triazapentalenes and Evaluation of Their Fluorescence Properties. *Molecules*, 29(10), 2229. <https://doi.org/10.3390/molecules29102229>
- 16 Solomons, T.W.G., & Voigt, C.F. (1966). The Diazapentalene System. IV. The Parent Pyrazolo[1,2- $\alpha$ ]pyrazole and Derivatives. *Journal of the American Chemical Society*, 88(1), 1992–1994. <https://doi.org/10.1021/ja00961a025>
- 17 Solomons, T.W.G., Fowler, F.W., & Calderazzo, J. (1965). The Diazapentalene System. 1-Benzoyl-2-phenylpyrazolo[1,2- $\alpha$ ]pyrazole Derivatives. *Journal of the American Chemical Society*, 87(3), 528–531. <https://doi.org/10.1021/ja01081a023>
- 18 Solomons, T.W.G., & Voigt, C.F. (1965). 4,8-Diazapentalene. *Journal of the American Chemical Society*, 87(22), 5256. <https://doi.org/10.1021/ja00950a052>
- 19 Trofimenko, S. (1966). 3a,6a-Diazapentalenes. Synthesis and Chemistry. *Journal of the American Chemical Society*, 88(23), 5588–5592. <https://doi.org/10.1021/ja00975a043>
- 20 Trofimenko, S. (1965). 3a,6a-Diazapentalene (Pyrazolo[1,2- $\alpha$ ]pyrazole). *Journal of the American Chemical Society*, 87(19), 4393–4394. <https://doi.org/10.1021/ja00947a038>
- 21 Ramsden, C.A. (1977). Mesomeric betaine derivatives of heteropentalenes. *Tetrahedron*, 33(24) 3193–3202. [https://doi.org/10.1016/0040-4020\(77\)80141-5](https://doi.org/10.1016/0040-4020(77)80141-5)
- 22 Kawase, M., Sakagami, H., & Motohashi, N. (2007). The Chemistry of Bioactive Mesoionic Heterocycles. In: Motohashi, N. (eds) *Bioactive Heterocycles VII. Topics in Heterocyclic Chemistry*, 16. Berlin, Springer, (pp. 135–152). [https://doi.org/10.1007/7081\\_2007\\_096](https://doi.org/10.1007/7081_2007_096)
- 23 Sizov, G.N. & Babaev, E.V. (2023). Criteria for a Structure to be Mesoionic. *Match*, 89(1), 5–47. <https://doi.org/10.46793/match.89-1.005S>
- 24 Alkorta, I., Blanco, F., & Elguero, J. (2009). Theoretical studies of azapentalenes. Part 4: Theoretical study of the properties of 3a,6a-diazapentalene. *Tetrahedron*, 6(29–30), 5760–5766. <https://doi.org/10.1016/j.tet.2009.05.017>
- 25 Rague, S.P., Maerker, C., Dransfeld, A., Jiao, H., & Eikema Hommes, N.J.R. (1996). Nucleus-Independent Chemical Shifts: A Simple and Efficient Aromaticity Probe. *Journal of the American Chemical Society*, 118(26), 6317–6318. <https://doi.org/10.1021/ja960582d>
- 26 Puello, J.Q., Obando, B.I., Foces-Foces, C., Infantes, L., Claramunt, R.M., Cabildo, P., Jimenez, J.A., & Elguero, J. (1997). Structure and Tautomerism of 3(5)-Amino-5(3)-arylpyrazoles in the Solid State and in Solution: an X-Ray and NMR Study. *Tetrahedron*, 53(31), 10783–10802. [https://doi.org/10.1016/s0040-4020\(97\)00678-9](https://doi.org/10.1016/s0040-4020(97)00678-9)
- 27 Stanovnik, B., & Svete, J. (2003). Product Class 1: Pyrazoles. *ChemInform*, 34(46), 15–225 <https://doi.org/10.1002/chin.200346258>
- 28 La Cour, T., Rasmussen, S.E., Hopf, H., Waisvisz, J.M., van der Hoeven, M.G., & Swahn, C. -G. (1973). The Structure of Pyrazole, C<sub>3</sub>H<sub>4</sub>N<sub>2</sub>, at 295 K and 108 K as determined by X-Ray Diffraction. *Acta Chemica Scandinavica*, 27, 1845–1854. <https://doi.org/10.3891/acta.chem.scand.27-1845>
- 29 Sikora, M., & Katrusiak, A. (2013). Pressure-Controlled Neutral–Ionic Transition and Disordering of NH···N Hydrogen Bonds in Pyrazole. *The Journal of Physical Chemistry C*, 117(20), 10661–10668. <https://doi.org/10.1021/jp401389v>
- 30 Millán, J.C., & Portilla, J. (2019). Recent advances in the synthesis of new pyrazole derivatives. *Italian Society of Chemistry*, 194–223. <https://doi.org/10.17374/targets.2019.22.194>
- 31 Perrin, D.D. (1965). Dissociation Constants of Organic Bases in Aqueous Solution. (Supplement, 1972). London: Butterworths
- 32 Smith, M.B., & March, J. (2001). March’s Advanced Organic Chemistry: Reactions, Mechanisms, and Structure. *Molecules*, 6(12), 1064–1065. <https://doi.org/10.3390/61201064>
- 33 Rybakov, V.B., Shchetinin, A.V., Babaev, E.V., Panshina, S.Yu., Alzhapparova, N.A., & Ibraev, M.K. (2024). CCDC 2393860: Experimental crystal structure determination. *CSD Communication*. <https://doi.org/10.5517/ccdc.csd.cc2lc099>
- 34 Soignet, D.M., Boudreaux, G.J., Berni, R.J., & Gonzales, E.J. (1970). Nuclear Magnetic Resonance Studies of Substituted Cyclic Ureas. *Applied Spectroscopy*, 24(2), 272–276. <https://doi.org/10.1366/000370270774371985>

Irina V. Palamarchuk<sup>\*</sup>, Ivan V. Kulakov, Svetlana S. Volkova

School of Natural Sciences, University of Tyumen, Tyumen, Russia  
(\*Corresponding author's e-mail: [ivpalamarchuk@utmn.ru](mailto:ivpalamarchuk@utmn.ru))

## Synthesis and Optical Properties of Substituted Derivatives of Oxazolo[5,4-b]Pyridine

In continuation of our work on the synthesis and study of new properties of 4-substituted 3-aminopyridin-2-(1*H*)-ones, we carried out the synthesis and subsequent cyclization of the corresponding oxalyl amides. The aminolysis reaction of diethyl oxalate with 3-aminopyridin-2-(1*H*)-ones was carried out by boiling without solvent at a temperature of 150 °C. In this case, intermediate oxalic acid monoamides with the remainder of the ester group were also recorded and separately identified. It was shown that under the action of phosphorus oxychloride the synthesized oxalic acid diamides undergo fairly smooth intramolecular cyclization into symmetrical bis-derivatives of oxazolo[5,4-b]pyridine. The photoluminescent properties of our newly obtained oxazolo[5,4-b]pyridine derivatives **5-8a-c** and 2,2'-bisoxazolo[5,4-b]pyridines **4a-c** were studied, including such parameters as maximum absorption ( $\lambda$ ), molar absorption coefficient ( $\epsilon$ ), Stokes shift, and quantum yield. All compounds were found to luminesce with a bluish-blue color and exhibit maximum absorption wavelengths in the range of 299–333 nm (in acetonitrile) and 281–317 nm (in toluene), which is associated with the  $\pi$ – $\pi^*$  electron transition. A fairly large Stokes shift (83–128 nm) is observed for all compounds. It was also found that the presence of a carboxyl linker at the C-2 position of compounds **5-8a-c** does not significantly affect the shift of the absorption band maxima and other spectral characteristics of the molecules. It should be noted that symmetrical conjugated 2,2'-bisoxazolo[5,4-b]pyridines **4a-c**, featuring two oxazolo[5,4-b]pyridine rings, exhibit fairly high quantum yield values ( $\phi \approx 0.70$ – $0.82$ ) compared to the known standard quinine sulfate ( $\phi \approx 0.55$ ), allowing their potential application as effective fluorophores.

**Keywords:** 3-aminopyridin-2(1*H*)-ones, oxazolo[5,4-b]pyridines, intramolecular heterocyclization, biological activity, UV spectroscopy, optical properties, quantum yield, Stokes shift

### Introduction

The oxazole-fused pyridine derivatives, oxazolo[5,4-b]- and oxazolo[4,5-b]pyridines, are of great interest due to their application in various fields of chemistry. The condensed pyridine fragment is acceptor and polar, thereby ensuring enhanced solubility of oxazolopyridines in water, concomitantly promoting the formation of additional interactions with the target receptor protein through a hydrogen bond with a heteroatom [1]. Oxazolopyridine derivatives have proven to serve as inhibitors of sphingomyelin synthase (SMS) (compound A, Fig. 1) [2]. The activity of this enzyme is associated with the progression of atherosclerosis, as well as inhibitors of I $\kappa$ B kinase (compound B) [3], which promotes the activation of immunoregulatory factors during inflammation.

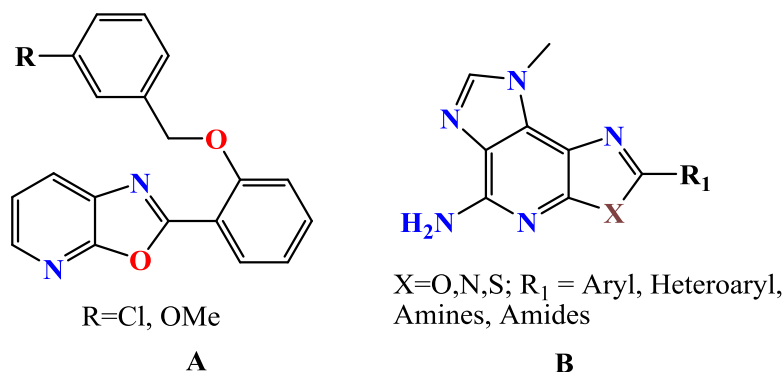
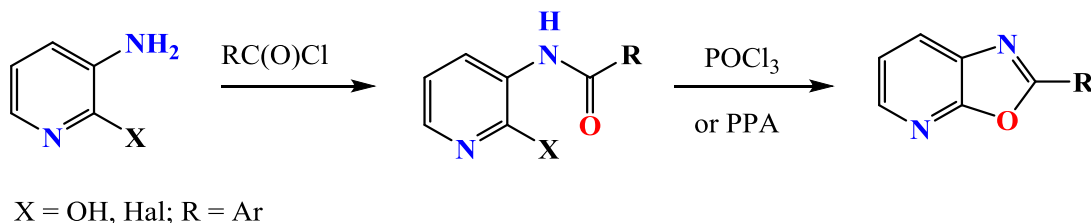


Figure 1. Inhibitors of sphingomyelin synthase (A) and inhibitors of I $\kappa$ B kinase (B)

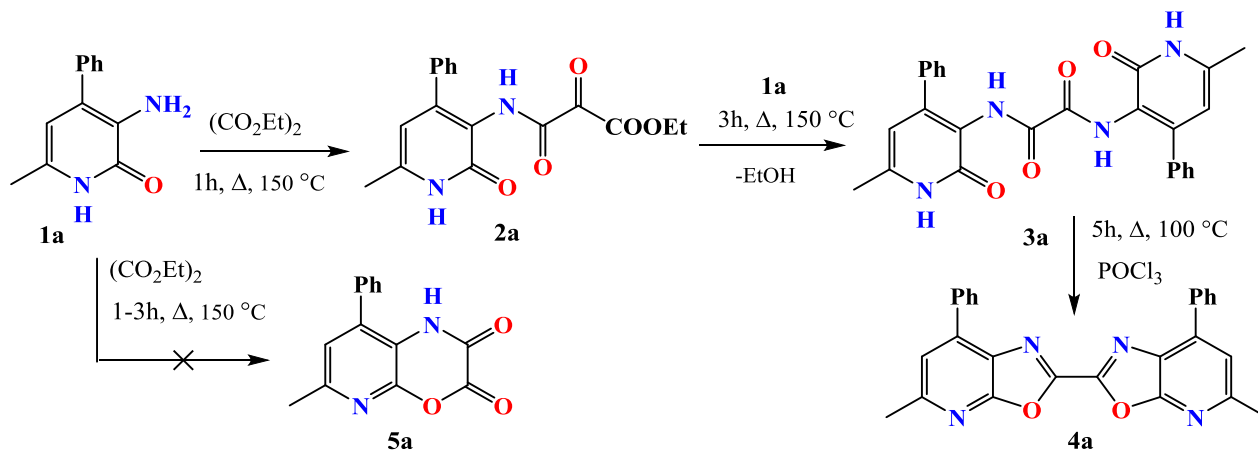
Being structural isosteres of the purine bases—adenine and guanine, these compounds exhibit a wide range of biological activity: anti-cancer, antimicrobial, antidiabetic, anti-inflammatory, etc. [4–12]. Furthermore, the potential for application as organic luminophores and biomarkers is also noteworthy [13–16]. For example, in 2011 [17], a study was conducted using oxazolopyridine derivatives as amyloid- $\beta$  ligands in positron emission tomography (PET). This analysis allows the *in vivo visualisation* of amyloid- $\beta$  fibrillary plaques, which are indicative of the pathology of Alzheimer's disease.

The most common method for synthesis of oxazolo[5,4-b]pyridines (Scheme 1) is the use of 3-amino-5-hydroxy- or 3-amino-5-halopyridines as initial compounds. The first step is the Schotten–Baumann reaction. At the second step the obtained amides cyclized into oxazolopyridines under the action of polyphosphoric acid or phosphorus oxychloride [18–20].



Scheme 1. General approach for the synthesis of oxazolo[5,4-b]pyridines

Thus, we have previously shown that that certain amides (acetamide, chloroacetamide of 3-aminopyridones) undergo cyclisation when exposed to a mixture of phosphorus oxide and phosphorus oxychloride, resulting in the formation of the corresponding oxazolo[5,4-b]pyridines [21]. Herein we report a method for the preparation of bis-oxazolopyridine **4a** was described. The first step is acylation of 3-amino-6-methyl-4-phenylpyridin-2-(1*H*)-one **1a** with a 1.5-fold excess of diethyl oxalate upon heating to 150 °C (Scheme 2). The diamide **3a** obtained in two stages, when heated with phosphorus oxychloride, forms symmetrical 5,5'-dimethyl-7,7'-diphenyl-2,2'-bis-(oxazolo[5,4-b]pyridine **4a** [22].



Scheme 2. Synthesis of 3-amino-6-methyl-4-phenylpyridin-2-(1*H*)-one **1a** [22]

It should be noted that the reaction of 3-amino-6-methyl-4-phenylpyridin-2-(1*H*)-one **1a** (which is essentially a binucleophile due to additional lactim-lactam tautomerism) with excess of diethyl oxalate we planned to obtain 1*H*-pyrido[2,3-*b*][1,4]oxazine-2,3-dione.

### Experimental

#### Materials

The obtained compounds were analyzed on an Agilent 1260 Infinity II chromatograph connected to an Agilent 6545 LC/Q-TOF high-resolution mass spectrometer equipped with an AJS ESI dual ion source operating in positive ion mode. Mass spectra with LC/MS precision were obtained in the range of 100–1000 *m/z*, at a scan rate of 1.5 spectra per second.

The  $^1\text{H}$  and  $^{13}\text{C}$  NMR spectra in DMSO- $d_6$  solutions were recorded on Bruker AVANCE 400 (400 MHz, 100 MHz) and Magritek spinsolve 80 carbon ultra (81 MHz, 20 MHz) spectrometers.

Melting points of synthetic compounds were determined on a Stuart SMP10 hot bench. All reactions were monitored by thin-layer chromatography (TLC) and identified by UV or iodine vapor.

UV-visible spectra were recorded in the range of 200–600 nm in a quartz cell with an optical path length of 1 cm using a Shimadzu UV-2600 spectrophotometer. Fluorescence spectrum of the studied compounds was recorded in the range of 300–700 nm at room temperature using a Shimadzu RF 5301 PC spectrofluorimeter. The solvents used were of analytical grade (for UV spectroscopy).

3-Aminopyridine-2(1*H*)-ones were prepared according to a similar literature procedure [28].

#### *Synthesis and Spectral Analysis of Synthesized Compounds*

The synthesis of **oxazolo[5,4-*b*]pyridine derivatives 5-8a-c** [23] involved heating a mixture of 1 mmol of 3-amino-pyridin-2-(1*H*)-one and 5 mmol of the corresponding anhydrides (succinic, maleic, glutaric, phthalic anhydrides) in 5 mL of acetic acid at reflux with vigorous stirring for 10 hours. The mixture was then cooled and poured into 25 mL of water. The resulting precipitates were filtered and recrystallized from a mixture of hexane, 2-propanol, and dichloromethane.

**N<sup>1</sup>,N<sup>2</sup>-bis(4,6-dimethyl-2-oxo-1,2-dihydropyridin-3-yl)oxalamide (3b)** 0.4 ml (3.0 mmol) of diethyl oxalate is added to 276 mg (2.0 mmol) of 3-amino-4,6-dimethylpyridin-2(1*H*)-one **1b** and the mixture is boiled for 3 hours under reflux. Then 1 ml of 2-propanol is added and the mixture is boiled for another 1 hour. The precipitate that forms upon cooling is filtered, washed with cold 2-propanol and dried. 102 mg of a finely crystalline white powder is obtained (yield 53 %). An analytically pure sample is obtained by recrystallization from a mixture of DMF and 2-propanol, m.p. = 210–211 °C. IR spectrum (KBr)  $\nu$ ,  $\text{cm}^{-1}$ : 1642–1693 (NC=O); 3466 (NH).  $^1\text{H}$  NMR spectrum (400 MHz, DMSO- $d_6$ ,  $\delta$ , ppm): 2.03 s (6H, 4,4'-CH<sub>3</sub>); 2.16 s (6H, 6,6'-CH<sub>3</sub>); 5.90 s (2H, C(5,5')-H); 9.35 br. s (2H, 3,3'-NHCO), 11.49 br. s (2H, NHCO).  $^{13}\text{C}$  NMR spectrum (101 MHz, DMSO- $d_6$ ,  $\delta$ , ppm): 17.79 (4, 21-CH<sub>3</sub>), 18.04 (6, 19-CH<sub>3</sub>), 106.33 (C-5, 20), 120.89 (C-3, 16), 141.85 (C-4, 21), 145.26 (C-6, 19), 157.93 (2, 17-CONH), 159.17 (9, 13-NHCO). Found, %: C, 58.56; H, 5.85; N, 17.38. C<sub>16</sub>H<sub>18</sub>N<sub>4</sub>O<sub>4</sub>. Calculated, %: C, 58.17; H, 5.49; N, 16.96.

**Ethyl 3-((6-methyl-2-oxo-4-(thiophen-2-yl)-1,2-dihydropyridin-3-yl)amino)-2,3-dioxopropanoate (2c)**. 200 mg (1.0 mmol) of 3-amino-4-(thiophen-2-yl)pyridin-2-one **1c** was boiled With 2 ml of diethyl oxalate (15 mmol) for about 5 hours. After cooling, the precipitated product is filtered, washed with a mixture of 2-propanol and hexane, and dried. After recrystallization, 258 mg (yield 78 %) is obtained with M.p. = 220–222 °C.

$^1\text{H}$  NMR (80 MHz, DMSO- $d_6$ ,  $\delta$ , ppm): 1.3 t (3H,  $J$  = 6.4 Hz, CH<sub>2</sub>CH<sub>3</sub>), 2.2 s (3H, 6-CH<sub>3</sub>); 4.3 q (2 H,  $J$  = 6.2 Hz, CH<sub>2</sub>CH<sub>3</sub>); 6.4 s (1H, H-5); 7.2 s (1H, H-4' thiophen); 7.7 br. s (2H, H — 3',5' thiophen); 10.1 br. s, 1H, 3-NHCO); 11.8 br. s (1H, NHCO).  $^{13}\text{C}$  NMR spectrum (21 MHz, DMSO- $d_6$ ,  $\delta$ , ppm): 14.1 (CH<sub>2</sub>CH<sub>3</sub>), 18.54 (CH<sub>3</sub>), 63.3 (OCH<sub>2</sub>), 102.9, 118.6, 127.3 (3-C thiophene), 129.1 (4-C thiophene), 130.0 (5-C thiophene), 137.1, 141.1, 143.6, 159.2 (COO), 160.3 (CONH), 161.8 (-NHCO). Found, %: C, 54.89; H, 4.61; N, 9.14. C<sub>14</sub>H<sub>14</sub>N<sub>2</sub>O<sub>4</sub>S. Calculated, %: C, 54.44; H, 4.26; N, 8.87.

**N<sup>1</sup>,N<sup>2</sup>-bis(6-methyl-2-oxo-4-(thiophen-2-yl)-1,2-dihydropyridin-3-yl)oxalamide (3c)** Obtained similarly **3b** from 200 mg (1.0 mmol) 3-amino-4-(thiophen-2-yl)pyridin-2-one **1c**, 0.2 ml (1.5 mmol) of diethyl oxalate. 225 mg (48 %) of a finely crystalline white powder are obtained. An analytically pure sample is obtained by recrystallization from a mixture of DMF and propanol-2 solvents. M.p. > 350 °C.  $^1\text{H}$  NMR spectrum (80 MHz, DMSO- $d_6$ ,  $\delta$ , ppm): 2.20 s (6H, 2 CH<sub>3</sub>); 6.37 s (2H, 2 H-5); 7.11 dd (2H,  $J$  = 4.8, 4.0 Hz, H-4' thiophen); 7.64 t (4 H,  $J$  = 4.5 Hz, 2 H-3',5' thiophen); 9.51 br. s, (2 H, 2 3-NH CO); 11.74 br. s (2H, 2NHCO).  $^{13}\text{C}$  NMR spectrum (20 MHz, DMSO- $d_6$ ,  $\delta$ , m. d.): 18.5 (2 CH<sub>3</sub>), 103.2 (2 C-5), 119.4 (2 C-3), 127.4 (2 3-C Th), 129.0 (2 4-C Th), 129.6 (2 5-C Th), 137.5 (2 C), 140.7 (2 C), 143.2 (2 C), 162.7 (2 NHCO), 166.9 (2 NHCO).

**5,5'-Dimethyl-7,7'-diphenyl-2,2'-bioxazolo[5,4-*b*]pyridine (4a)** was obtained by methodology [22]: A mixture of 0.227 g (0.5 mmol) oxalylamide **1a** and 1.0 ml POCl<sub>3</sub> heat up to 100 °C within 9 hours. Excess oxychloride phosphorus evaporate, residue are being processed ice water. The resulting precipitate was filtered off and crystallized from a mixture of 2-propanol and DMF solvents. Yield: 0.185 g (88 %), white powder, mp 263–265 °C. IR spectrum (KBr),  $\nu$ ,  $\text{cm}^{-1}$ : 1608, 1675;  $^1\text{H}$  NMR spectrum (400 MHz, DMSO- $d_6$ ,  $\delta$ , ppm): 2.71 (6H, s, 5-CH<sub>3</sub>, 5'-CH<sub>3</sub>); 7.59 (2H, d,  $^3J$  = 7.3 Hz, H-4, 4'Ph); 7.66 (4H, t,  $^3J$  = 7.3 Hz, H-3, 3',5, 5' Ph); 7.86 (2H, s, H-6,6'); 8.26 (2H, d,  $^3J$  = 7.3 Hz, H-2, 2', 6, 6' Ph).  $^{13}\text{C}$  NMR spectrum (DMSO- $d_6$ ),  $\delta$ , ppm: 24.2 (5-CH<sub>3</sub>, 5'-CH<sub>3</sub>); 119.4 (C-6, C-6'); 127.6 (C-7a, C -7a'); 128.9 (C-4,4',6,6' Ph); 130.1 (C-4,4' Ph);

129.0 (C-2, 2', 6, 6' Ph); 133.6 (C-1,1' Ph); 141.0 (C-7, C-7'); 150.2 (C-5, C-5'); 157.6 (C-3a, 3a'); 159.4 (C-2, 2'). Found, %: C 74.44; H 4.50; N 13.52.  $C_{26}H_{18}N_4O_2$ . Calculated, %: C 74.63; H 4.34; N 13.39.

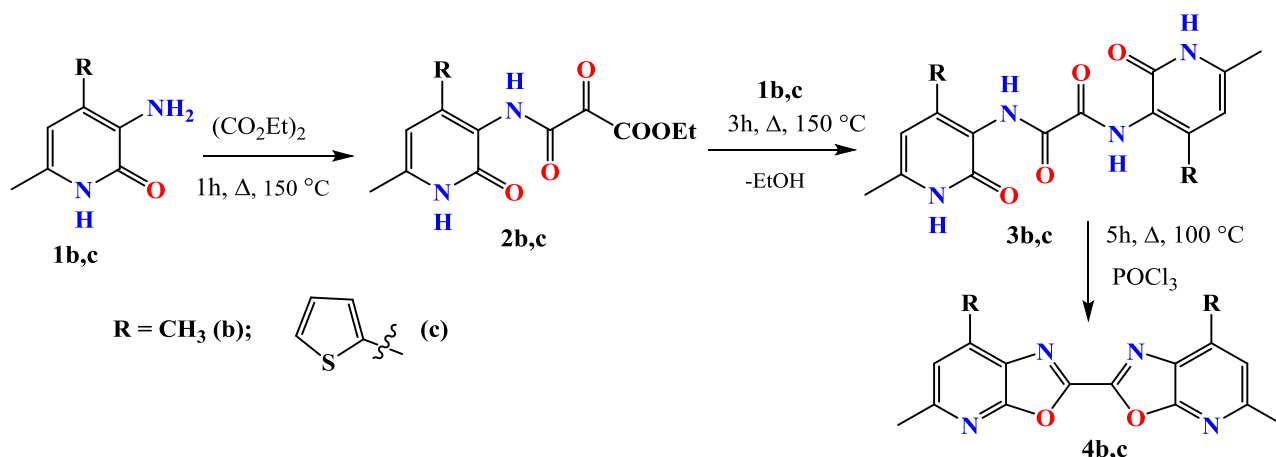
**5,5',7,7'-tetramethyl-2,2'-bioxazolo[5,4-b]pyridine (4b).** A mixture of 330.3 mg (1 mmol) of oxalylamide (**3b**) and 1.0 ml (10 mmol) of phosphorus oxychloride was heated under reflux for 9 h. The excess phosphorus oxychloride was distilled off under vacuum. The reaction mixture was treated with cold distilled water. The formed precipitate was filtered off, washed with water and air-dried. The mass of the product was 170 mg (yield 58 %) with M.p. > 330 °C.  $^1H$  NMR spectrum (80 MHz, DMSO- $d_6$ ,  $\delta$ , ppm): 2.00 s (6H, 4,4'-CH<sub>3</sub>); 2.14 s (6H, 6,6'-CH<sub>3</sub>); 7.37 s (2H, C-(7,7')-H). Mass spectrum (direct injection),  $m/z$  ( $I_{rel}$  %): 294 [M]<sup>+</sup> (100). Found, %: C, 65.30; H, 4.79; N, 19.04.  $C_{16}H_{14}N_4O_2$ . Calculated, %: C, 65.74; H, 5.01; N, 18.83.

**5,5'-dimethyl-7,7'-di(thiophen-2-yl)-2,2'-bioxazolo[5,4-b]pyridine (4c)** was obtained similar to **4**. The yield was 238 mg (51 %) with a mp > 330 °C (2-propanol-DMF).  $^1H$  NMR spectrum (80 MHz, DMSO- $d_6$ ,  $\delta$ , ppm): 2.79 s (6H, 2 CH<sub>3</sub>); 7.33 br. d (2H,  $J$  = 4.0 Hz, 2 H-4' thiophen); 7.53 s (2H, 2 H-7); 7.59 t (2H,  $J$  = 4.0 Hz, 2H-3' thiophen); 8.40 d (2H,  $J$  = 3.3 Hz, 2 H-5' thiophen).  $^{13}C$  NMR spectrum (20 MHz, DMSO- $d_6$ ,  $\delta$ , ppm): 24.7 (2 CH<sub>3</sub>), 117.5 (2 C-7), 128.8 (2 3-C Th), 129.1 (2 4-C Th), 131.3 (2 5-C Th), 136.4 (2 C), 138.7, 141.6 (2 C), 143.5, 149.8 (2 C), 158.7. Found, %: C, 61.38; H, 3.28; N, 13.01.  $C_{22}H_{14}N_4O_2S_2$ . Calculated, %: C, 61.71; H, 3.56; N, 12.84.

## Results and Discussion

### Chemistry

In order to obtain new derivatives of bis-(oxazolo[5,4-b]pyridine type **4a** with various substituents on the pyridine ring and to study their optical properties, we carried out the following similar transformations based on new 3-amino-6-methyl-4-methyl- and (2-thienyl)pyridin-2-(1*H*)-ones **1b**, **1c** (Scheme 3).

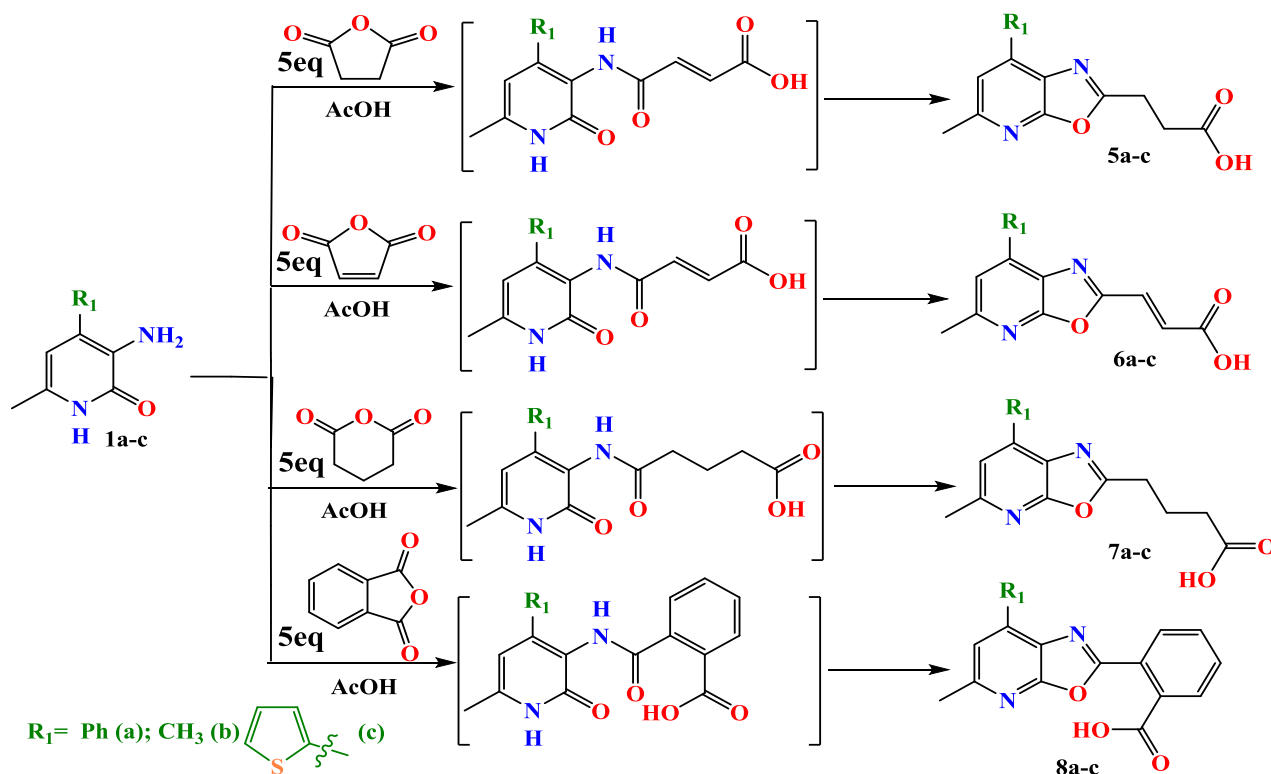


Scheme 3. Synthesis of symmetrical 5,5'-dimethyl-7,7'-diphenyl-2,2'-bis-(oxazolo[5,4-b]pyridine **4b**, **c**

Intermediate monoamides **2b**, **2c** were easily obtained by the reaction with an excess of diethyl oxalate and detected spectrally.

The characteristic chemical signals of the amide NH protons in initial diamides **3b** and **3c** (at 9.35–9.42 and 11.49–11.83 ppm) are no longer present in the  $^1H$  NMR spectra of compounds **4b** and **4c**. Furthermore, a shift of the aromatic proton to a weak field was also observed.

For possible comparison of the optical properties of bis-(oxazolo[5,4-b]pyridines, we also synthesized oxazolo[5,4-b]pyridines (**5-8 a-c**) using the previously described method [23], containing one oxazolo[5,4-b]pyridine scaffold and a carboxyl linker.

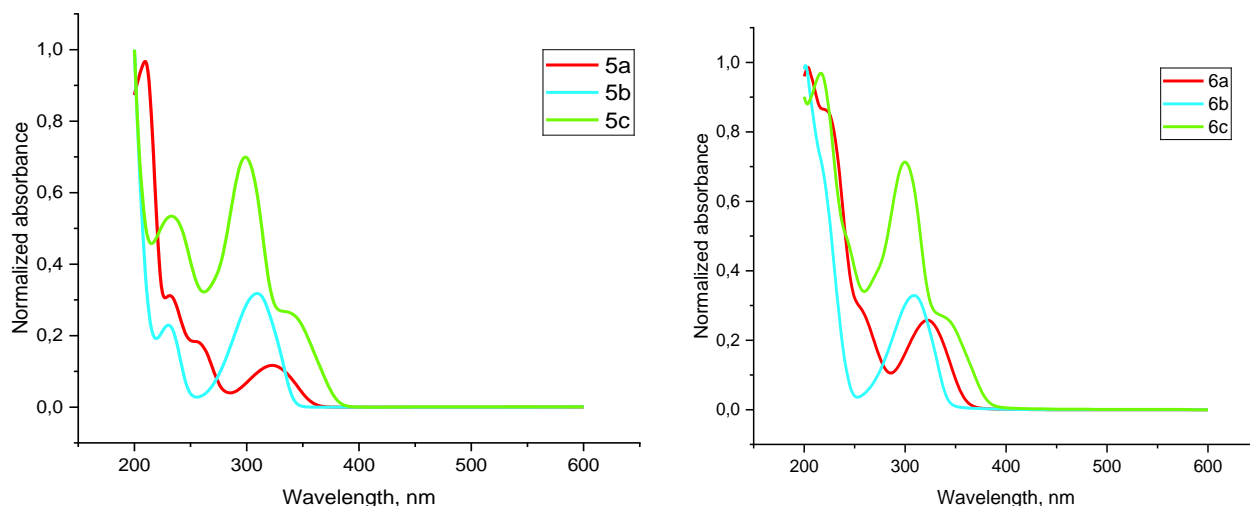


Scheme 4. Cyclization reaction of 3-aminopyridones **1a-c** with into the corresponding oxazolo[5,4-b]pyridine **5-8a-c**

#### Photophysical Properties of Compounds

Previous work by the research group of Alexander S. Fisyuk has demonstrated [24] that heterocyclic derivatives based on 3-amino-6-methyl-4-phenylpyridin-2(1*H*)-one **1a** are characterized by a high fluorescence quantum yield in the blue region of the visible spectrum ( $\phi \approx 0.76$ ), suggesting their potential as efficient fluorophores.

Within the scope of the present study, our primary objective was to investigate the photophysical properties of the synthesized 3-amino-6-methyl-4-(methyl-, aryl)pyridin-2(1*H*)-one derivatives (**1a-c**) and to elucidate the impact of linker structure on their spectral characteristics, including the absorption maximum ( $\lambda_{\text{max}}$ ), Stokes shift, and quantum yield. To initiate this, the absorption spectra of oxazolopyridine derivatives (**5-8a-c**) were recorded in two aprotic solvents—toluene (nonpolar) and acetonitrile (polar)—at a concentration of  $6 \times 10^{-4}$  M. The resulting absorption spectra are presented in Figures 2–4, while the spectral characteristics of the compounds are summarized in Table 1.





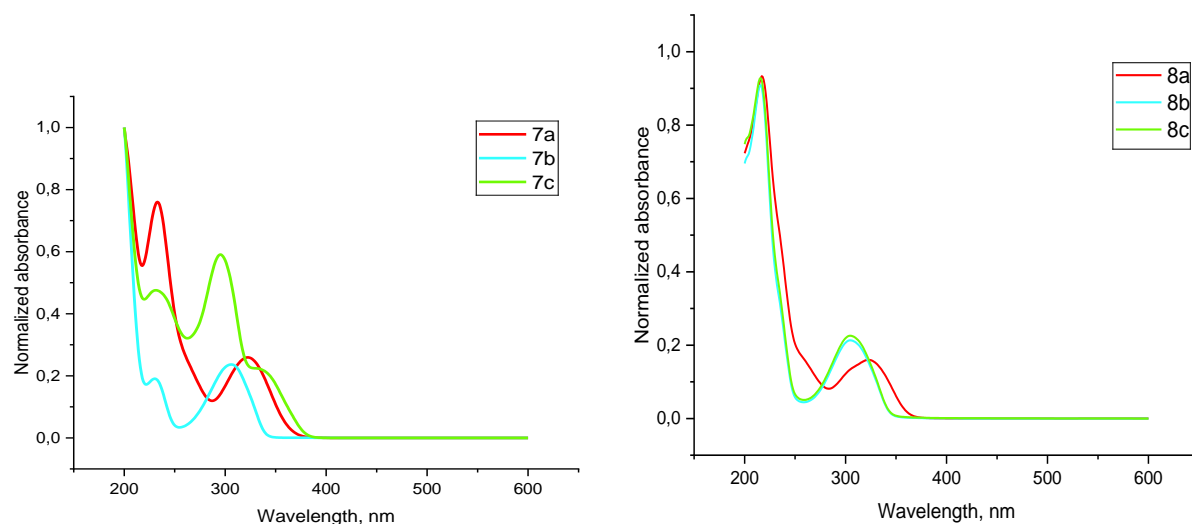


Figure 2. Normalized absorption spectra of oxazolo[5,4-b]pyridine derivatives **5-8a-c** in acetonitrile solution ( $6 \times 10^{-4}$  mol/L)

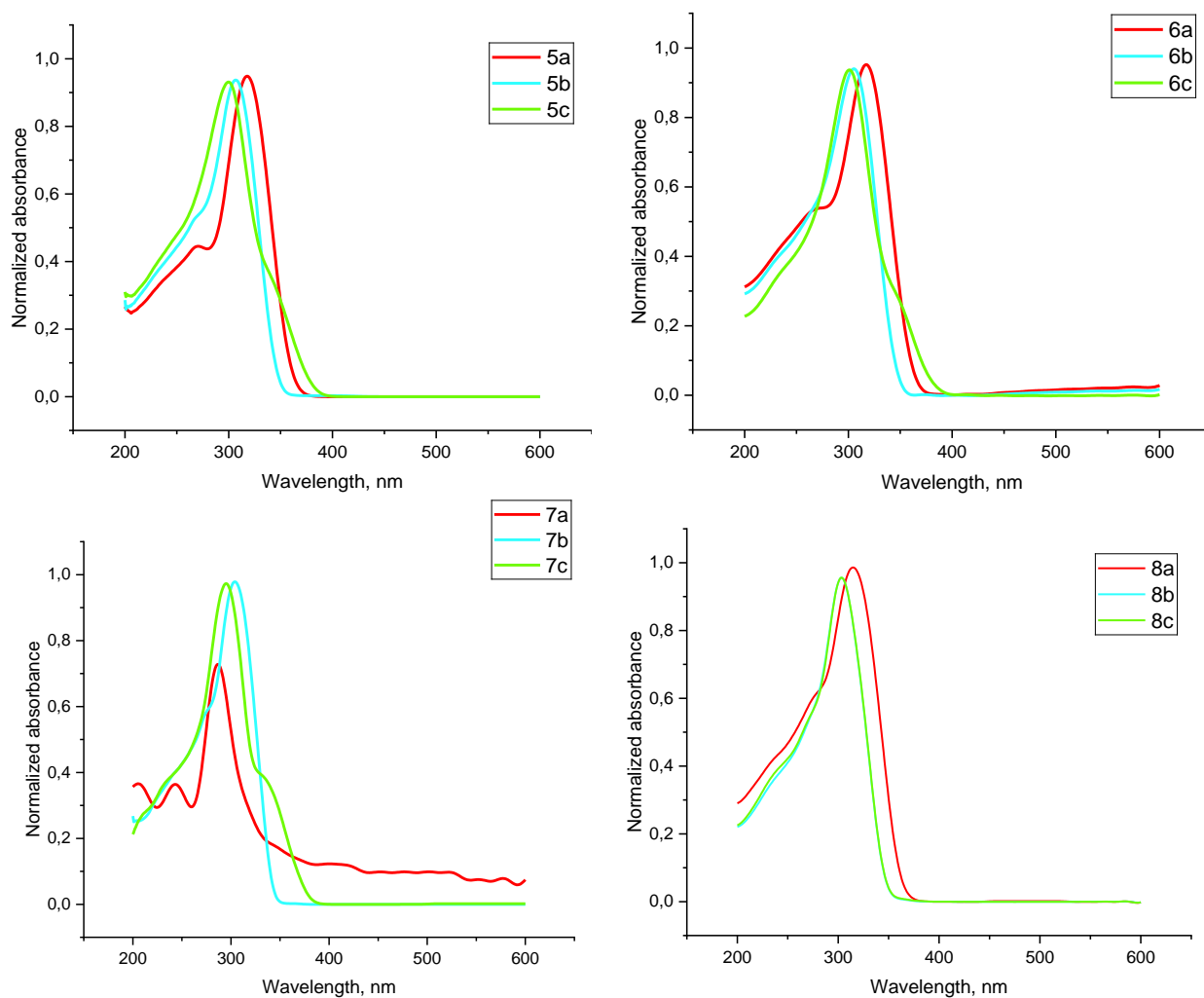


Figure 3. Normalized absorption spectra of oxazolo[5,4-b]pyridine derivatives **5-8a-c** in toluene solution ( $6 \times 10^{-4}$  mol/L)



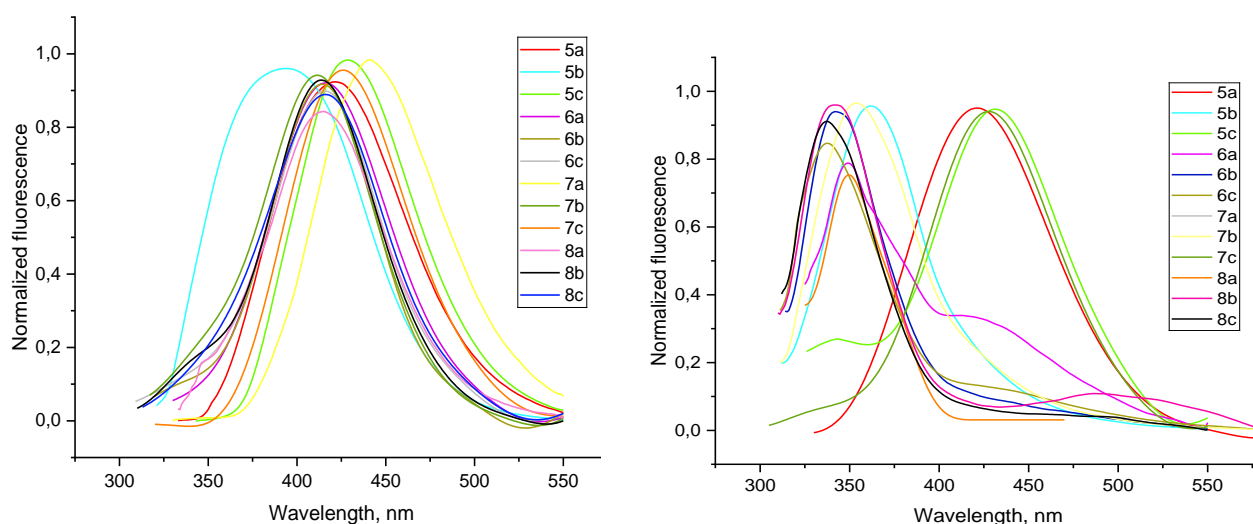


Figure 4. Normalized fluorescence spectra of oxazolo[5,4-b]pyridine derivatives **5a-8a-c** in acetonitrile (left) and toluene (right) solutions ( $6 \times 10^{-4}$  mol/L)

It was established that, for all the compounds studied, the absorption maxima fall within the range of 299–333 nm in an acetonitrile solution and in the range of 281–317 nm in a toluene solution, which is associated with the  $\pi$ - $\pi^*$  electron transition in the conjugated system of the oxazolopyridine moiety. A comparative analysis of the absorption spectra of compounds **5a-c** and **7a-c** in acetonitrile revealed that the presence of a thiophene or phenyl substituent at the C-4 position of the oxazolopyridine ring induces a slight bathochromic shift in the absorption band compared to the corresponding methyl derivative (Table 1). Moreover, the largest bathochromic shift is observed for compound **7c**. The observed bathochromic shift in the absorption bands of compounds **5a, c** and **7a, c** is attributed to the presence of the thiophene ring, which participates in p- $\pi$  conjugation, and the phenyl ring, which engages in  $\pi$ - $\pi$  conjugation with the oxazolopyridine moiety. However, within each homologous series containing an identical substituent at the C-4 position (methyl, phenyl, or thiophen-2-yl), modifications to the acidic fragment at the C-2 position had no produce a discernible effect on the shift of the absorption maxima.

Table 1

Photophysical properties of compounds **5-8a-c**

Compound	Acetonitrile				Toluene			
	UV-Vis		Photoluminescence		UV-Vis		Photoluminescence	
	$\lambda_{\text{max}}^{\text{abs}}$ , [nm]	$\epsilon$ , [l/cm <sup>2</sup> mol]	$\lambda_{\text{max}}^{\text{em}}$	Stokes shift, [nm]	$\lambda_{\text{max}}^{\text{abs}}$ , [nm]	$\epsilon$ , [l/cm <sup>2</sup> mol]	$\lambda_{\text{max}}^{\text{em}}$ , [nm]	Stokes shift, [nm]
<b>5a</b>	323	700	427	104	317	622	419	102
<b>5b</b>	311	760	394	83	306	607	362	56
<b>5c</b>	333	602	430	97	300	545	433	133
<b>6a</b>	322	694	416	94	316	560	348	32
<b>6b</b>	310	995	416	106	304	642	344	40
<b>6c</b>	299	1503	415	116	301	1222	329	28
<b>7a</b>	322	660	450	128	281	6.5	423	142
<b>7b</b>	307	810	407	100	303	735	355	52
<b>7c</b>	331	372	423	92	295	860	428	133
<b>8a</b>	323	798	414	91	315	768	347	32
<b>8b</b>	303	723	417	114	302	972	346	44
<b>8c</b>	303	1288	415	112	302	1690	342	40

The fluorescence spectra of all synthesized compounds were recorded in acetonitrile and toluene ( $6 \times 10^{-4}$  mol/L) using the absorption maximum of each compound as the excitation wavelength.

The emission maxima of the investigated compounds range from 329 to 450 nm, which corresponds to bluish-blue photoluminescence (Table 1). It should be noted that all compounds in acetonitrile solution exhibit a substantial Stokes shift (83–128 nm).

Given that the synthesized compounds **4a–c** contain two conjugated oxazolo[5,4-b]pyridine ring systems and are of significant interest as potential luminophores, we sought to determine their fluorescence quantum yield.

Upon irradiation with UV light, chloroform solutions of the bis(oxazolopyridine) derivatives **4a–c** emit intense blue-violet light (Fig. 5), indicating high-efficiency photoluminescence in the visible spectral region.

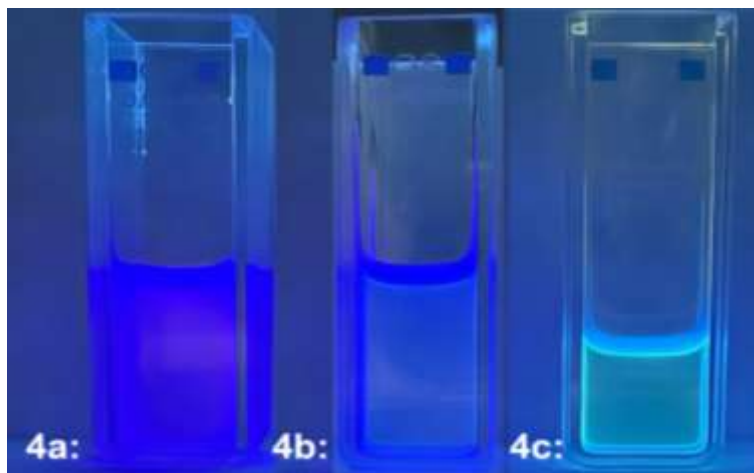


Figure 5. Photographs of compounds **4a–c** in a chloroform solution ( $2 \times 10^{-5}$  mol/L) under UV radiation ( $\lambda = 365$  nm)

To determine the quantum yield of compounds **4a–c**, their absorption and fluorescence spectra were recorded in chloroform at a concentration of  $2 \times 10^{-5}$  mol/L (Fig. 6). A quinine sulfate solution in 0.1 M  $\text{H}_2\text{SO}_4$  was utilized as an internal standard.

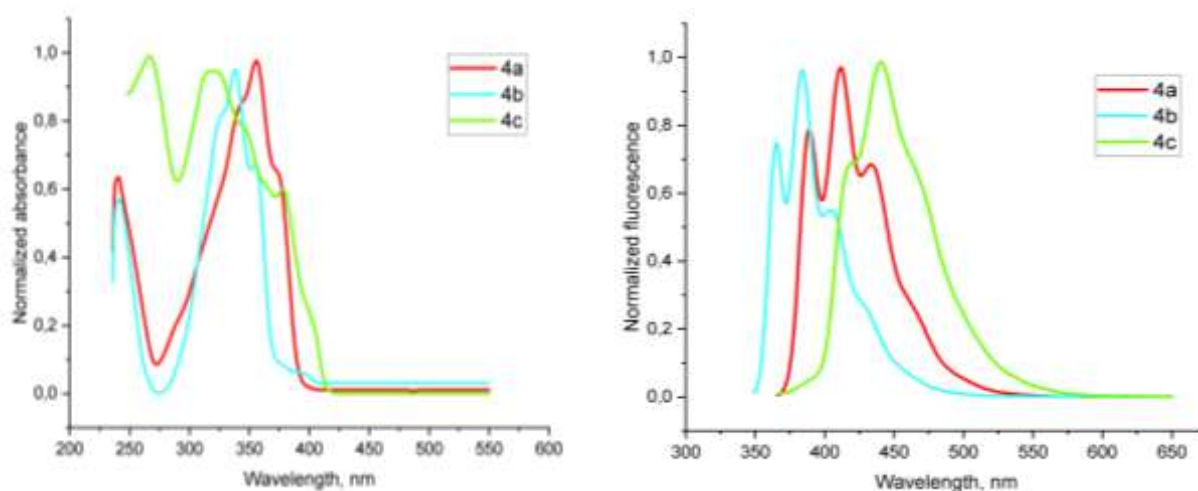


Figure 6. Normalized absorption (left) and fluorescence (right) spectra of oxazolo[5,4-b]pyridine derivatives **4a–c** in chloroform solution ( $2 \times 10^{-5}$  mol/L)

The relative quantum yield was calculated using the following formula:

$$\varphi_i = \varphi_{st} \cdot \frac{A_{st}}{A_x} \cdot \frac{F_x}{F_{st}} \cdot \frac{n_x^2}{n_{st}^2},$$

where  $\varphi_i$  is the fluorescence quantum yield of the studied compound;  $\varphi_{st}$  is the fluorescence quantum yield of the standard used (quinine sulfate);  $A_{st}$ ,  $A_x$  are the absorbances at excitation wavelength for the standard sample (st) and the studied compound (**4a–c**);  $F_{st}$ ,  $F_x$  are the areas of fluorescence spec-

trum with spectral correction for the standard sample (st) and the studied compound (**4a-c**);  $n_{st}$ ,  $n_x$  are the refractive index of the standard sample (st) and the studied compound (**4a-c**).

Table 2

Photophysical properties of compounds **4a-c**

Compound	UV-Vis		Photoluminescence		
	$\lambda_{\max}^{\text{abs}}$ , [nm]	$\epsilon$ , [l/cm <sup>2</sup> *mol]	$\lambda_{\max}^{\text{em}}$ , [nm]	Stokes shift, [nm]	Quantum yield ( $\phi_f$ ) <sup>a</sup> , %
<b>4a</b>	356	40833	389, 411, 435	79	81
<b>4b</b>	339	39583	365, 384, 405	66	82
<b>4c</b>	332	30833	418, 440	108	70

Note: <sup>a</sup>The fluorescence quantum yield was calculated relative to the standard (quinine sulfate in 0.1 M H<sub>2</sub>SO<sub>4</sub>,  $\phi_f = 0.55$ ) [25–27].

Therefore, the 2,2'-bis(oxazolo[5,4-*b*]pyridine) derivatives **4a-c** demonstrated photoluminescence quantum yields higher than that of the quinine sulfate standard ( $\phi \approx 0.55$ ).

## Conclusions

Aminolysis of diethyl oxalate with three 4-substituted 3-aminopyridin-2-(1*H*)-ones afforded the corresponding oxalylamides. Intermediate oxalic acid monoamides were also detected and separately identified. The resulting oxalic acid diamides were used in cyclization reactions to symmetrical *bis*-derivatives of oxazolo[5,4-*b*]pyridine under the action of phosphorus oxychloride. For the new oxazolo[5,4-*b*]pyridine derivatives we obtained. The photoluminescent properties of **5-8a-c** and 2,2'-bisoxazolo[5,4-*b*]pyridines **4a-c** were studied (maximum absorption  $\lambda$ , molar absorption coefficient ( $\epsilon$ ), Stokes shift, quantum yield). All compounds were found to luminesce with a bluish-blue color and have a maximum absorption length in the wavelength range of 299–333 nm (acetonitrile) and in the range of 281–317 nm (toluene), which is associated with the  $\pi$ - $\pi^*$  electron transition. A fairly large Stokes shift (83–128 nm) is observed for all compounds. It was also found that the presence of a carboxyl linker at the C-2 position of compounds **5-8a-c** does not significantly affect the shift of the absorption band maxima and other spectral characteristics of the molecules.

It should be noted that symmetrical conjugated 2,2'-bisoxazolo[5,4-*b*]pyridines **4a-c** with two oxazolo[5,4-*b*]pyridine rings have fairly high quantum yield values ( $\phi \approx 0.70$ – $0.82$ ) compared to the known standard quinine sulfate ( $\phi \approx 0.55$ ), which will allow them to find possible applications as effective fluorophores.

## Funding

The study was supported by a grant from the Russian Science Foundation (No. 24-23-00472, “Development of methods for the preparation and practical application of new derivatives of bisoxazolo[5,4-*b*]pyridine with potential luminescent, complexing and catalytic activity”, <https://rscf.ru/en/project/24-23-00472/>).

## Author Information\*

\*The authors' names are presented in the following order: First Name, Middle Name and Last Name

**Irina Valerievna Palamarchuk** (corresponding author) — Senior Lecturer, School of Natural Sciences, University of Tyumen, 15a Perekopskaya St., 625003, Tyumen, Russia; e-mail: [ivpalamarchuk@utmn.ru](mailto:ivpalamarchuk@utmn.ru); <https://orcid.org/0000-0003-3376-6953>

**Ivan Vyacheslavovich Kulakov** — Doctor of Chemical Sciences, Associated Professor, School of Natural Sciences, University of Tyumen, 15a Perekopskaya St., 625003, Tyumen, Russia; e-mail: [ivkulakov@utmn.ru](mailto:ivkulakov@utmn.ru); <https://orcid.org/0000-0001-5772-2096>

**Svetlana Stanislavovna Volkova** — Candidate of Chemical Sciences, School of Natural Sciences, University of Tyumen, 15a Perekopskaya St., 625003, Tyumen, Russia; e-mail: [s.s.volkova@utmn.ru](mailto:s.s.volkova@utmn.ru)

## Author Contributions

The manuscript was written through contributions of all authors. All authors have given approval to the final version of the manuscript. **CRedit**: **Irina Valerievna Palamarchuk** investigation, formal analysis, data

curation and writing — original draft preparation; **Ivan Vyacheslavovich Kulakov** conceptualization, methodology, validation, writing — review and editing and supervision; **Svetlana Stanislavovna Volkova** formal analysis, data curation, methodology, validation.

#### Acknowledgments

Spectrophotometric studies were carried out using the equipment of the Center for Collective Use “Rational Nature Management and Physicochemical Research” of University of Tyumen.

#### Conflicts of Interest

The authors declare no conflict of interest.

#### References

- Demmer, C. S. & Bunch, L. (2015). Benzoxazoles and oxazolopyridines in medicinal chemistry studies. *European Journal of Medicinal Chemistry*, 97, 778–785. <https://doi.org/10.1016/j.ejmech.2014.11.064>
- Qi, X. Y., Cao, Y., Li, Y. L., Mo, M. G., Zhou, L., & Ye, D. Y. (2017). Discovery of the selective sphingomyelin synthase 2 inhibitors with the novel structure of oxazolopyridine. *Bioorganic & Medicinal Chemistry Letters*, 27(15), 3511–3515. <https://doi.org/10.1016/j.bmcl.2017.05.074>
- Kempson, J., Spengel, S. H., Guo, J., Quesnelle, C., Gill, P., Belanger, D., Dyckman, A. J., Li, T., Watterson, S. H., Langevine, C. M., Das, J., Moquin, R. V., Furch, J. A., Marinier, A., Dodier, M., Martel, A., Nirschl, D., Van-Kirk, K. Burke, J.R. Pattoli, M. A., Gillooly, K., McIntyre, K. W., Chen, L., Yang, Z., Marathe, P. H., Wang-Iverson, D., Dodd, J. H., McKinnon, M., Barrish, J. C., & Pitts, W. J. (2009). Novel tricyclic inhibitors of IkB kinase. *Journal of medicinal chemistry*, 52(7), 1994–2005. <https://doi.org/10.1021/jm8015816>
- Bemis, J. E., Vu, C. B., Xie, R., Nunes, J. J., Ng, P. Y., Disch, J. S., Milne, J. C., Carney, D. P., Lynch, A. V., Jin, L., Smith, J. J., Lavu, S., Iffland, A., Jirousek, M. R., & Perni, R. B. (2009). Discovery of oxazolo[4,5-*b*]pyridines and related heterocyclic analogs as novel SIRT1 activators. *Bioorganic & Medicinal Chemistry Letters*, 19(8), 2350–2353. <https://doi.org/10.1016/j.bmcl.2008.11.106>
- Yeh, V. & Iyengar, R. (2008). Oxazoles. *Comprehensive Heterocyclic Chemistry III*, 4, 487–543. <https://doi.org/10.1016/B978-008044992-0.00404-1>
- Yalçın I. & Şener E. (1993). QSARs of some novel antibacterial benzimidazoles, benzoxazoles, and oxazolopyridines against an enteric gram-negative rod; *K. pneumoniae*. *International journal of pharmaceutics*, 98(1–3), 1–8. [https://doi.org/10.1016/0378-5173\(93\)90034-D](https://doi.org/10.1016/0378-5173(93)90034-D)
- Park, H. R., Kim, J., Kim, T., Jo, S., Yeom, M., Moon, B., Choo, I. H., Lee, J., Lim, E. J., Park, K. D., Min, S. J., Nam, G., Keum, G., Lee, C. J., & Choo, H. (2013). Oxazolopyridines and thiazolopyridines as monoamine oxidase B inhibitors for the treatment of Parkinson's disease. *Bioorganic & medicinal chemistry*, 21(17), 5480–5487. <https://doi.org/10.1016/j.bmc.2013.05.066>
- Viaud, M. C., Jamoneau, P., Flouzat, Ch., Bizot-Espiard, J. G., Pfeiffer, B., Renard, P., Caignard, D. H., Adam, G., & Guillaumet, G. (1995). N-Substituted Oxazolo[5,4-*b*]pyridin-2(1*H*)-ones: A New Class of Non-Opiate Antinociceptive Agents. *Journal of Medicinal Chemistry*, 38(8), 1278–1286. <https://doi.org/10.1021/jm00008a006>
- Huang, Z., Zhang, Y., & Song, Y. WO Patent 2011085643.
- Tekiner-Gulbas, B., Temiz-Arpaci, O., Yildiz, I., Aki-Sener, E., & Yalcin, I. (2006). 3D-QSAR study on heterocyclic topoisomerase II inhibitors using CoMSIA. *SAR and QSAR in Environmental Research*, 17(2), 121–132. <https://doi.org/10.1080/10659360600636105>
- Yildiz-Oren, I., Yalcin, I., Aki-Sener, E. & Ucarturk, N. (2004). Synthesis and structure–activity relationships of new antimicrobial active multisubstituted benzazole derivatives. *European Journal of Medicinal Chemistry*, 39(3), 291–298. <https://doi.org/10.1016/j.ejmech.2003.11.014>
- Yalçın, İ., Ören, İ., Şener, E., Akin, A., & Uçartürk, N. (1992). The synthesis and the structure-activity relationships of some substituted benzoxazoles, oxazolo(4,5-*b*)pyridines, benzothiazoles and benzimidazoles as antimicrobial agents. *European journal of medicinal chemistry*, 27(4), 401–406. [https://doi.org/10.1016/0223-5234\(92\)90154-S](https://doi.org/10.1016/0223-5234(92)90154-S)
- Shatsauskas, A. L., Zablotskii, Y. A., Chernenko, S. A., Zheleznova T. Yu., Shuvalov V. Yu., Kostyuchenko A. S., & Fisyuk A. S. (2021). Synthesis and photophysical properties of the products of the reaction of 5-methyl-7-phenyl[1,3]oxazolo[5,4-*b*]pyridin-2(1*H*)-one with amino acids. *Chemistry of Heterocyclic Compounds*, 57(12), 1212–1219. <https://doi.org/10.1007/s10593-021-03045-8>
- Mac M., Baran W., Uchacz T., Baran B., Suder M., & Leśniewski S. (2007). Fluorescence properties of the derivatives of oxazolo[4,5-*b*]pyridine. *Journal of Photochemistry and Photobiology A: Chemistry*, 192(2-3), 188–196. <https://doi.org/10.1016/j.jphotochem.2007.05.023>
- El'chaninov, M. M., Aleksandrov, A. A., & Illenzeer, E. V. (2014). Synthesis and properties of 2-(2-furyl)[1,3]oxazolo[4,5-*b*]pyridine. *Russian Journal of Organic Chemistry*, 50(12), 1826–1828. <https://doi.org/10.1134/S1070428014120197>
- Aleksandrov, A. A., & El'chaninov, M. M. (2015). Synthesis and reactivity of 2-(2-thienyl)oxazolo[4,5-*b*]pyridine. *Russian Journal of General Chemistry*, 85(4), 858–860. <https://doi.org/10.1134/S1070363215040155>

- 17 Harrison, S. T., Mulhearn, J., Wolkenberg, S. E., Miller, P. J., O'Malley, S. S., Zeng, Z., Williams, D. L., Hostetler, E. D., Sanabria-Bohórquez, S., Gammage, L., Fan, H., Sur, C., Culberson, J. C., Hargreaves, R. J., Cook, J. J., Hartman, G. D. & Barrow, J. C. (2011). Synthesis and evaluation of 5-fluoro-2-aryloxazolo[5,4-*b*]pyridines as  $\beta$ -amyloid PET ligands and identification of MK-3328. *ACS Medicinal Chemistry Letters*, 2(7), 498–502. <https://doi.org/10.1021/ml200018n>
- 18 Doise, M., Dennin, F., Blondeau, D., & Sliwa, H. (1990). Synthesis of novel heterocycles: Oxazolo[4,5-*b*]pyridines and oxazolo[4,5-*d*]pyrimidines. *Tetrahedron Letters*, 31(8), 1155–1156. [https://doi.org/10.1016/S0040-4039\(00\)88750-X](https://doi.org/10.1016/S0040-4039(00)88750-X)
- 19 Doise, M., Blondeau, D., & Sliwa, H. (1992). Syntheses of Oxazolo[4,5-*b*]pyridines and [4,5-*d*]pyrimidines. *Synthetic Communications*, 22(20), 2891–2901. <https://doi.org/10.1080/00397919208021112>
- 20 Myllymäki, M. J. & Koskinen, A. M. P. (2007). A rapid method for the preparation of 2-substituted oxazolo[4,5-*b*]pyridines using microwave-assisted direct condensation reactions. *Tetrahedron Lett.* 48(13), 2295–2298. <https://doi.org/10.1016/j.tetlet.2007.01.161>
- 21 Palamarchuk, I. V., Matsukevich, M. V., Kulakov, I. V., Seilkhanov, T. M., & Fisyuk, A. S. (2019). Synthesis of N-substituted 2-aminomethyl-5-methyl-7-phenyloxazolo[5,4-*b*]pyridines. *Chemistry of Heterocyclic Compounds*, 55(8), 788–791. <https://doi.org/10.1007/s10593-019-02537-y>
- 22 Shatsauskas, A. L., Abramov, A. A., Saibulina, E. R., Palamarchuk, I. V., Kulakov, I. V., & Fisyuk, A. S. (2017). Synthesis of 3-amino-6-methyl-4-phenylpyridin-2(1*H*)-one and its derivatives. *Chemistry of Heterocyclic Compounds*, 53(2), 186–191. <https://doi.org/10.1007/s10593-017-2038-4>
- 23 Palamarchuk, I. V. & Kulakov, I. V. (2024). A New Method for Obtaining Carboxylic Derivatives of Oxazolo[5,4-*b*]pyridine Based on 3-Aminopyridine-2(1*H*)-ones. *Eurasian Journal of Chemistry*, 29(2(114)), 32–44. <https://doi.org/10.31489/2959-0663/2-24-11>
- 24 Shatsauskas, A. L., Shatalin, Y. V., Shubina, V. S., Chernenko, S. A., Kostyuchenko, A. S., & Fisyuk, A. S. (2022). 5-Ethyl-5,6-dihydrobenzo[*c*][1,7]naphthyridin-4(3*H*)-ones — A new class of fluorescent dyes. *Dyes and Pigments*, 204, 110388. <https://doi.org/10.1016/j.dyepig.2022.110388>
- 25 Kostyuchenko, A. S., Zheleznova, T. Y., Stasyuk, A. J., Kurowska, A., Domagala, W., Pron, A., & Fisyuk, A. S. (2017). Synthesis and optical properties of new 5'-aryl-substituted 2,5-bis(3-decyl-2,2'-bithiophen-5-yl)-1,3,4-oxadiazoles. *Beilstein Journal of Organic Chemistry*, 13(1), 313–322. <https://doi.org/10.3762/bjoc.13.34>
- 26 Williams, A. T. R., Winfield, S. A., & Miller, J. N. (1983). Relative fluorescence quantum yields using a computer-controlled luminescence spectrometer. *Analyst*, 108(1290), 1067–1071. <https://doi.org/10.1039/AN9830801067>
- 27 Kurowska, A., Zassowski, P., Kostyuchenko, A. S., Zheleznova, T. Y., Andryukhova, K. V., Fisyuk, A. S., Pron, A., & Domagala, W. (2017). Effect of donor to acceptor ratio on electrochemical and spectroscopic properties of oligoalkylthiophene 1,3,4-oxadiazole derivatives. *Physical Chemistry Chemical Physics*, 19(44), 30261–30276. <https://doi.org/10.1039/C7CP05155G>
- 28 Kulakov, I. V., Matsukevich, M. V., Shulgau, Z. T., Sergazy, S., Seilkhanov, T. M., Puzari, A., & Fisyuk, A. S. (2015). Synthesis and antiradical activity of 4-aryl(hetaryl)-substituted 3-aminopyridin-2(1*H*)-ones. *Chemistry of Heterocyclic Compounds*, 51(11), 991–996. <https://doi.org/10.1007/s10593-016-1809-7>
- 29 Fisyuk, A. S., Kulakov, I. V., Goncharov, D. S., Nikitina, O. S., Bogza, Y. P., & Shatsauskas, A. L. (2014). Synthesis of 3-aminopyridin-2(1*H*)-ones and 1*H*-pyrido[2,3-*b*][1,4]oxazin-2(3*H*)-ones. *Chemistry of Heterocyclic Compounds*, 50(2), 217–224. <https://doi.org/10.1007/s10593-014-1464-9>



## PHYSICAL AND ANALYTICAL CHEMISTRY

### Article

Received: 8 July 2025 | Revised: 29 October 2025 |  
Accepted: 3 November 2025 | Published online: 15 November 2025

UDC 544.4, 544.18

<https://doi.org/10.31489/2959-0663/4-25-5>

Mudar A. Abdulsattar 

Ministry of Science and Technology, Baghdad, Iraq  
(\*Author's e-mail: [mudarahmed3@yahoo.com](mailto:mudarahmed3@yahoo.com))

### WO<sub>3</sub> Doped SnS<sub>2</sub> Gas Sensor Response to NO<sub>2</sub>: Effect of Temperature and Humidity Using Transition State Theory Formalism

Several factors frequently affect gas sensors, including sensing material, doping, temperature, detected gas properties, humidity, manufacturing method, etc. The present work studies WO<sub>3</sub> doped SnS<sub>2</sub> gas sensor response to NO<sub>2</sub>, considering the above factors using transition state theory formalism. The reaction rate equation in transition state theory was used to estimate the change in the number of vacancies in a 30 % WO<sub>3</sub>-doped SnS<sub>2</sub> sensor when NO<sub>2</sub> gas passed over its surface. Temperature dependence of Gibbs energy of adsorption and transition was evaluated at the effective temperatures. Effective temperatures were the temperatures after which NO<sub>2</sub> gas dissociates and can no longer be detected. The effect of temperature and humidity was evaluated using logistic functions. Response, response time, and NO<sub>2</sub> concentration were calculated and compared with the experiment. Interestingly, the lowest Gibbs energy of transition as a function of 30 % WO<sub>3</sub> doping percentage was very close to the highest experimental response. WO<sub>3</sub> doped SnS<sub>2</sub> gas sensor is stable for an extended period, as proved experimentally and theoretically. Transition state theory enabled the calculation of changes in the number of vacancies and various experimentally obtained quantities that cannot be evaluated using density functional theory alone.

**Keywords:** WO<sub>3</sub> Doped SnS<sub>2</sub>, NO<sub>2</sub> gas sensor, Density functional theory, Transition state theory, effecting temperature, doping, response time, Gibbs energy

### Introduction

Tin disulfide (SnS<sub>2</sub>) is a semiconductor similar to SnO<sub>2</sub> in several properties. SnS<sub>2</sub> is used in gas sensors and mosaic work. Pyramids are observed on the SnS<sub>2</sub> surface [1]. Pyramid shapes increase the gas sensitivity by increasing the surface area of the gas sensor. SnS<sub>2</sub> detects several gases, including NH<sub>3</sub>, NO<sub>2</sub>, H<sub>2</sub>S, etc. [2–4].

Tungsten trioxide (WO<sub>3</sub>) is one of the oxides with the highest number of oxygen atoms. Having a large number of oxygen atoms is beneficial in gas sensors since it can be used to exchange oxygen atoms with the detected gas. WO<sub>3</sub> gas sensors detect several gases, such as H<sub>2</sub>S, NO<sub>2</sub>, and H<sub>2</sub> [5–7].

Nitrogen dioxide (NO<sub>2</sub>) is one of several other nitrogen oxides. This oxide is poisonous for humans if its concentration becomes higher than a permissible concentration. The allowed NO<sub>2</sub> concentration is 1–5 ppm [8]. As a result, the NO<sub>2</sub> gas detector should detect NO<sub>2</sub> concentrations higher than one (1) ppm. The highest response of NO<sub>2</sub> sensors is close to its dissociation temperature but can also be detected at room temperature [9].

Density functional theory (DFT) is the usual method used in gas sensor simulation procedures [10]. However, the simulation results are limited and cannot be compared to the findings of the experimental results, such as response, response time, and effect of temperature or humidity if only DFT is used. Recently, methods that depend on reaction rate theories, such as the Arrhenius equation, collision theory, or transition state theory, have been developed to account for these deficiencies [11–13]. Transition state theory (TST) is

more sophisticated and advanced than older collision theory and the Arrhenius equation. Transition state theory relates activation energy with Gibbs free energy of transition, a valid thermodynamic quantity that is more investigated to solve current applications [12, 13].

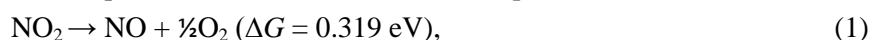
Many materials were used previously to detect NO<sub>2</sub> gas. These materials include SnO<sub>2</sub> [14], ZnO [15], WO<sub>3</sub> [16] etc. In most cases, doping increases the sensitivity of material toward gases, which is also the case with NO<sub>2</sub> sensors. Mathematically, doping increases the entropy of a material and reduces Gibbs free energy of transition or activation value for better detection, as shall be clear in the present work. Vacancies have significant roles in gas sensing. For reducing gases such as H<sub>2</sub>, CH<sub>4</sub>, H<sub>2</sub>S, etc., vacancies increase as the sensor material is exposed to the detected gas. In oxidizing gases such as present NO<sub>2</sub> gas, vacancies decrease as the detected gas passes over the detecting material.

The present work calculates WO<sub>3</sub> doped SnS<sub>2</sub> gas sensor response to NO<sub>2</sub> using transition state theory formalism. Gibbs free energy of transition is calculated at different doping percentages using pristine and WO<sub>3</sub>-doped SnS<sub>2</sub> clusters. Reaction rates are used to evaluate the change in the number of vacancies with appropriate parameters considering previous calculations of different gases. Response and response time are evaluated from the reaction rate and compared with experimental values as a function of temperature. Humidity and NO<sub>2</sub> gas properties' effects as a function of temperature are considered using a logistic function. The stability of the sensor with time is compared with the experiment. The impact of gas properties, temperature, and humidity cannot be evaluated using the DFT method alone, which is the main reason for using TST.

### Computation Details

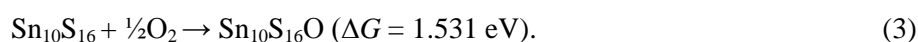
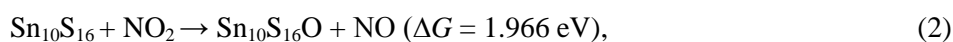
The Gaussian 09 molecular modeling program performed present DFT calculations [17]. Heavy atoms such as Sn and W cannot be described using the same basis set for light elements such as O, N, and S as a Gaussian program input. As a result, B3LYP/6-311G\*\* is used to describe light atoms, while Sn and W are described using SDD basis sets (Stuttgart/Dresden). Dispersion corrections are essential in gas sensor calculations since long-range interactions are inevitable. Dispersion corrections are added via the GD3BJ method in the Gaussian 09 program.

NO<sub>2</sub> gas is known to decompose at temperatures around 200 °C as in the equation [18]:

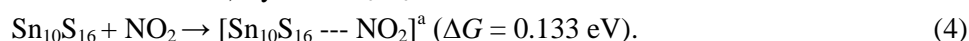


$\Delta G$  stands for the difference in Gibbs energy between reaction products and reaction reactants. The value of the Gibbs free energy ( $\Delta G$ ) of this endergonic reaction (positive value of ( $\Delta G$ )) can be supplied at temperatures around 200 °C by the thermal energy of the collision of two NO<sub>2</sub> molecules [19]. As a result, many gas sensors prefer temperatures around 200 °C to detect NO<sub>2</sub> gas [20, 21]. In fact, detecting NO<sub>2</sub> at temperatures extremely higher than 200 °C becomes more difficult as the temperature increases.

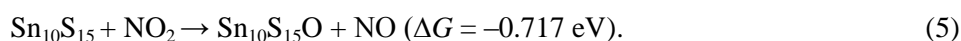
SnS<sub>2</sub> compound reacts with NO<sub>2</sub> gas at the surface pyramid structures [22]. SnS<sub>2</sub> surface pyramid structures are similar to SnO<sub>2</sub>, with many vacancies [23]. The largest possible size cluster that can be handled by theoretical calculations is used. The stable pyramid cluster with ten Sn atoms is Sn<sub>10</sub>S<sub>16</sub> [19]. The stable Sn<sub>10</sub>S<sub>16</sub> cluster is in equilibrium with a smaller number of Sn<sub>10</sub>S<sub>15</sub> (with sulfur vacancy) and Sn<sub>10</sub>S<sub>17</sub> (over sulfurized) clusters depending on the energy required to remove or add S atoms to the stable Sn<sub>10</sub>S<sub>16</sub> cluster [19]. The stable cluster Sn<sub>10</sub>S<sub>16</sub> cannot react with NO<sub>2</sub> gas or be further oxidized by oxygen as in the equations (The values of  $\Delta G$  are at standard pressure and temperature (25 °C and 1 bar) unless mentioned otherwise):



The high values of endergonic reactions make these reactions unfavorable reactions. However, NO<sub>2</sub> can still be adsorbed (by van der Waals interaction) by the Sn<sub>10</sub>S<sub>16</sub> cluster as in the reaction:

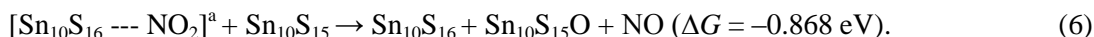


In Eq. (4), [Sn<sub>10</sub>S<sub>16</sub> ... NO<sub>2</sub>]<sup>a</sup> represents the adsorption state. Although the Gibbs free energy of the reaction is positive in the above equation, the small value of  $\Delta G$  can be supplied by the thermal energies of colliding particles. Only the Sn<sub>10</sub>S<sub>15</sub> cluster (with sulfur vacancy) can be oxidized by NO<sub>2</sub> gas (exergonic reaction) as in the equation:

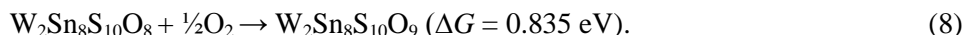
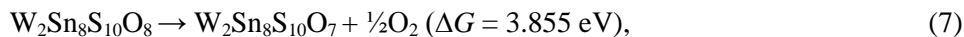




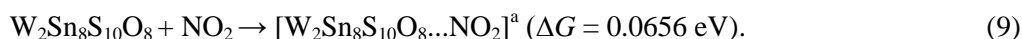
On the other hand, the reaction of the  $\text{Sn}_{10}\text{S}_{15}$  cluster with adsorbed  $\text{NO}_2$  gas is more energetically favorable, as in the equation:



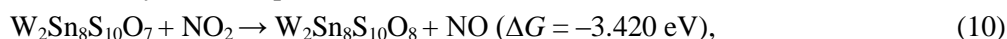
After doping  $\text{SnS}_2$  with  $\text{WO}_3$ , the reaction of  $\text{NO}_2$  gas with the doped clusters takes another trend. The nearest cluster to the available experimental doping is the  $\text{W}_2\text{Sn}_8\text{S}_{10}\text{O}_8$  cluster. The  $\text{W}_2\text{Sn}_8\text{S}_{10}\text{O}_8$  cluster is stable in an oxygen environment, i.e., the removing or adding oxygen atoms to the cluster is endergonic as in the equations:



Comparing Eq. (8) with Eq. (3), oxidizing the  $\text{W}_2\text{Sn}_8\text{S}_{10}\text{O}_8$  cluster needs approximately half the energy required to oxidize the  $\text{Sn}_{10}\text{S}_{16}$  cluster. The  $\text{W}_2\text{Sn}_8\text{S}_{10}\text{O}_8$  cluster can adsorb  $\text{NO}_2$  more efficiently than  $\text{SnS}_2$ , as in the equation:



The energy needed for the adsorption of  $\text{NO}_2$  on the doped  $\text{SnS}_2$  cluster is half of the pristine cluster. Finally, the reaction of the (oxygen-deficient or vacancy)  $\text{W}_2\text{Sn}_8\text{S}_{10}\text{O}_7$  cluster with  $\text{NO}_2$  is more vigorous than the pristine (with sulfur vacancy)  $\text{SnS}_2$  (Eqs. (5, 6)) clusters:



Several parameters are needed to apply the TST to evaluate the reaction rate of pristine and  $\text{WO}_3$ -doped  $\text{SnS}_2$  clusters with  $\text{NO}_2$  gas. The TST formula for the reaction rate of  $\text{W}_2\text{Sn}_8\text{S}_{10}\text{O}_7$  clusters (with a vacancy) with  $\text{NO}_2$  can be given by [24]:

$$\frac{d[\text{W}_2\text{Sn}_8\text{S}_{10}\text{O}_7]}{dt} = -[\text{W}_2\text{Sn}_8\text{S}_{10}\text{O}_7]^u [\text{NO}_2]_e^v k(T), \quad (12)$$

$$k(T) = AT^m \exp\left(\frac{-\Delta G^\ddagger}{k_B T}\right). \quad (13)$$

In Eqs. (12, 13),  $[\text{W}_2\text{Sn}_8\text{S}_{10}\text{O}_7]$  and  $[\text{NO}_2]$  are the concentration of doped sensor clusters and the concentration of  $\text{NO}_2$  gas, respectively. ( $u$  and  $v$ ) are concentration exponents that can be determined from experimental data. ( $u$  and  $v$ ) have a value of 1, which is also the value of some previous TST sensor calculations [25].  $k(T)$  in Eqs. (12, 13) is the temperature-dependent part of the reaction rate. ( $A$ ) is an experimental parameter that considers the sensor materials properties such as morphology, crystallinity, surface structure, and manufacturing methods. ( $m$ ) The temperature exponent in Eq. (13) is a parameter that can be determined experimentally from the response variation with gas sensor temperature.  $\Delta G^\ddagger$  is the Gibbs energy of transition (or activation), and  $k_B$  is the Boltzmann constant. The subscript (e) in the  $\text{NO}_2$  gas concentration is the effect of dissociation on  $\text{NO}_2$  concentration in Eq. (1) as given by the equation:

$$[\text{NO}_2]_d = \frac{[\text{NO}_2]}{1 + e^{k_s(T-T_0)}}, \quad (14)$$

$$[\text{NO}_2]_e = [\text{NO}_2] - \frac{[\text{NO}_2]}{1 + e^{k_s(T-T_0)}}. \quad (15)$$

In the above equations,  $[\text{NO}_2]_d$  and  $[\text{NO}_2]_e$  are the dissociated and effective  $\text{NO}_2$  gas concentrations.  $k_s$  is the rate at which  $\text{NO}_2$  dissociates, while  $T_0$  is the temperature at which  $\text{NO}_2$  concentration reaches half its original concentration. Eqs. (14, 15) does not take humidity effect into account. To consider humidity effects, Eq. (15) is modified to:

$$[\text{NO}_2]_e = [\text{NO}_2] - \frac{[\text{NO}_2]}{1 + e^{k_s(T-T_0)}} \frac{1}{1 + e^{k_h(h-h_0)}}. \quad (16)$$

In the above equation,  $h$  is the relative humidity,  $k_h$  is the rate at which  $\text{NO}_2$  effective concentration decreases due to humidity, and  $h_0$  is the humidity at which  $\text{NO}_2$  concentration reaches half of its concentration due to humidity.

Changing Eq. (12) to a difference equation, the number of clusters with a vacancy (W<sub>2</sub>Sn<sub>8</sub>S<sub>10</sub>O<sub>7</sub>) that changes to a stable cluster (W<sub>2</sub>Sn<sub>8</sub>S<sub>10</sub>O<sub>8</sub>) per unit of time can be given by:

$$\Delta[W_2Sn_8S_{10}O_8] = -\Delta[W_2Sn_8S_{10}O_7] = [NO_2]_e^v k(T) [W_2Sn_8S_{10}O_7]^u \Delta t. \quad (17)$$

The negative sign is added since the decrease of vacancies (W<sub>2</sub>Sn<sub>8</sub>S<sub>10</sub>O<sub>7</sub>) is an increase in fully oxidized clusters (W<sub>2</sub>Sn<sub>8</sub>S<sub>10</sub>O<sub>8</sub>). Using the above equation and assuming that the total number of W<sub>2</sub>Sn<sub>8</sub>S<sub>10</sub>O<sub>7</sub> clusters is nearly constant (not changing appreciably), the response can be given by:

$$\text{Response}(\text{theoretical}) = 1 + c[NO_2]_e^v k(T). \quad (18)$$

In Eq. (18), (*c*) is an experimental factor that correlates the change in the number of vacancies to the change in response, including the effective time ( $\Delta t$ ) needed to oxidize these vacancies. The theoretical response is compared to the measured experimental response given by the ratio ( $R_g/R_a$ ).  $R_g$  is the sensor resistance when the NO<sub>2</sub> gas mixed with air passes over the sensor surface, and  $R_a$  is the resistance when pure air passes over the sensor surface. Both theoretical and experimental responses reduce to 1 when the NO<sub>2</sub> gas concentration vanishes ( $R_g = R_a$ ). This ratio ( $R_g/R_a$ ) is the reciprocal of response to reducing gases ( $R_d/R_g$ ).

### Results and Discussion

Figure 1 shows the adsorption and transition states of the NO<sub>2</sub> gas molecule on the surface of the W<sub>2</sub>Sn<sub>8</sub>S<sub>10</sub>O<sub>8</sub> cluster. In the adsorption case, the negative charges in NO<sub>2</sub> are attracted to positive charges in the sensor cluster, and the positive charges in NO<sub>2</sub> are attracted to negative charges in the sensor cluster. Using NBO (natural bond order) analysis, N and O atoms in NO<sub>2</sub> have the charges 0.514 and −0.257 electronic charges, respectively. The Sn and S atoms in the pristine sensor mostly have 1.4 and −0.8 electronic charges, respectively. The same is true in the WO<sub>3</sub> doped cluster in which Sn and W have positive charges, and S and O have negative electronic charges. In the transition state case, the positive charges of the gas are nearer to the positive charges in the sensor, and the negative charges of the gas are closer to the negative charges in the sensor, resulting in higher energy. The calculated bond length of Sn–S is around 2.6 Å, which is in good agreement with previous experimental and theoretical values [26]. The W–O bond length is 1.7–1.85 Å, which agrees with previous experimental and theoretical results [27]. The calculated HOMO-LUMO gap is 3.076 eV compared to experimental 2.34–2.42 eV [28]. Being larger than the experimental value is expected because of the theoretical cluster's SnS<sub>2</sub> cluster size (or the number of atoms). After doping with WO<sub>3</sub>, the HOMO-LUMO gap is 2.417 eV.

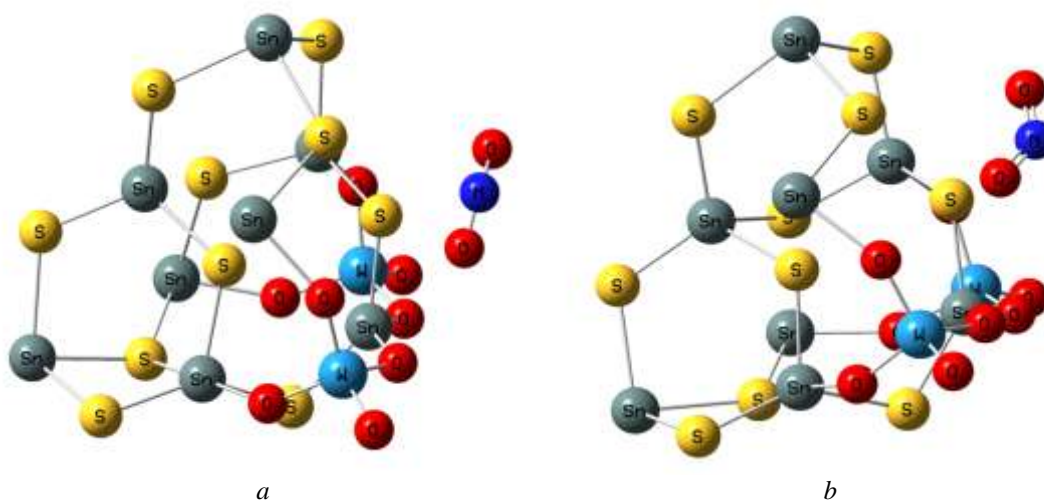


Figure 1. (a) Optimization of NO<sub>2</sub> adsorption on W<sub>2</sub>Sn<sub>8</sub>S<sub>10</sub>O<sub>8</sub> cluster and (b) the optimization of NO<sub>2</sub> transition state on W<sub>2</sub>Sn<sub>8</sub>S<sub>10</sub>O<sub>8</sub> surface cluster

Figure 2 shows the Gibbs free energy of transition as a function of doping (molar) percentage and temperature. The experimental lowest percentage of doping at 30 % molar is near the theoretically lowest determined Gibbs free energy of transition at 25 %. The pristine SnS<sub>2</sub> (zero doping percentage) sensor has very high Gibbs energy compared to doped clusters at all shown temperature ranges. The Gibbs free energy of

transition for various percentages can be calculated using the modified Evans–Polanyi principle by interpolation [29]:

$$\Delta G^\ddagger = \Delta G_0^\ddagger + \beta \Delta G_1^\ddagger \quad (19)$$

In Eq. (19),  $\Delta G_0^\ddagger$  and  $\Delta G_1^\ddagger$  are known Gibbs free energy of transition values for two different percentages, and  $\beta$  is the interpolation coefficient. The Gibbs free energy of transition is the sum of two terms, enthalpy ( $\Delta H^\ddagger$ ) and entropy ( $\Delta S^\ddagger$ ) of transition:

$$\Delta G^\ddagger = \Delta H^\ddagger - T\Delta S^\ddagger \quad (20)$$

After doping, transition entropy increases, leading to a lower transition energy, as in Eq. (20).

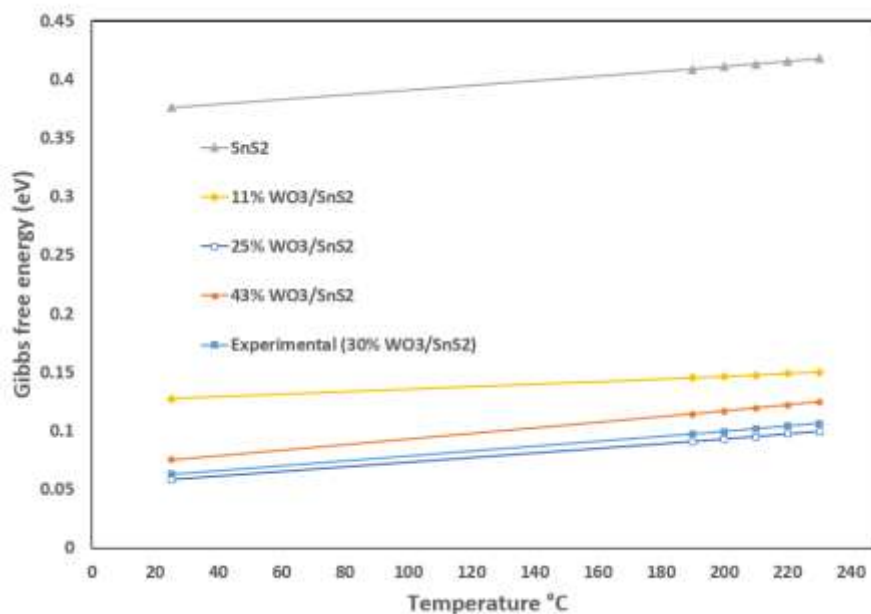


Figure 2. Gibbs energy of transition or activation of  $\text{NO}_2$  with pristine and  $\text{WO}_3$  doped  $\text{SnS}_2$  as a function of temperature for different molar percentages of the doping material  $\text{WO}_3$

Table 1 shows the parameters that are used in the present calculations. The parameters are for the 30 %  $\text{WO}_3$  doped  $\text{SnS}_2$  cluster reaction with  $\text{NO}_2$  gas. The adsorption state is designated as  $[\text{30 \% WO}_3/\text{SnS}_2 \text{ --- NO}_2]^\text{a}$ , while the transition state is designated as  $[\text{30 \% WO}_3/\text{SnS}_2 \text{ --- NO}_2]^\ddagger$ . The experimental response for the 30 %  $\text{WO}_3$  doped  $\text{SnS}_2$  to  $\text{NO}_2$  gas is available [3]. The Gibbs free energy of transition ( $\Delta G^\ddagger$ ) is calculated using the Gaussian 09 method (*ts*) as in the optimization statement ( $\text{OPT}=(\text{calcfc}, \text{ts}, \text{noeigen})$ ) to calculate the transition state. The value of  $\Delta G^\ddagger$  for the 30 %  $\text{WO}_3$  doped  $\text{SnS}_2$  cluster is 0.0629 compared to 0.376 eV for the pristine  $\text{SnS}_2$  cluster, which is six times lower.

Table 1

**Reaction parameters of 30 %  $\text{WO}_3$  doped  $\text{SnS}_2$  to  $\text{NO}_2$  gas.  $\Delta G^\ddagger$  value is at 25 °C and 1 bar**

Reaction	$\Delta G^\ddagger$ (eV)	$A$ ( $\text{s}^{-1} \cdot \text{K}^{-12}$ )	$m$	$v, u$	$k_s$ ( $^\circ\text{C}^{-1}$ )	$T_0$ ( $^\circ\text{C}$ )	$k_h$		$h_0$ (%)	$c$ (s)
$[\text{30 \% WO}_3/\text{SnS}_2 \text{ --- NO}_2]^\text{a}$ ↓	0.0629	$2.8 \times 10^{-28}$	12	1	0.15	220	0.11		100	880
$[\text{30 \% WO}_3/\text{SnS}_2 \text{ --- NO}_2]^\ddagger$										

The ( $A$ ) parameter reflects the sensor material's manufacturing method and materials properties. The properties of the materials include surface area, crystallinity, doping, electronic structure, etc. The units of this parameter are affected by the temperature exponent ( $m$ ) and the correlation parameter ( $c$ ).

The temperature exponent ( $m$ ) has a value of 12. This high value is also found in other materials' response to  $\text{NO}_2$  gas [30]. The range of  $m$  for the reaction of investigated gases with sensor materials is (1 to 12). The high value of  $m$  is a sign of a vigorous reaction between  $\text{NO}_2$  gas and doped sensor material.

The concentration exponents ( $u$ ,  $v$ ) are equal to one (1). These values are the values in the original transition state theory. The  $u$  exponent is always taken as one, while the  $v$  exponent (gas concentration exponent) can take the range  $\frac{1}{2}$  to 2 depending on the kind of gas or sensor material.

The temperature-dependent logistic function parameters of Eq. (14) are  $k_s$  and  $T_0$ . These parameters have values of  $0.15\text{ }^{\circ}\text{C}^{-1}$  and  $220\text{ }^{\circ}\text{C}$ , respectively, as in Table 1. The dissociation rate is higher than the dissociation of NO<sub>2</sub> over other materials [30]. The half concentration temperature  $T_0$  is near the NO<sub>2</sub> dissociation temperature at  $200\text{ }^{\circ}\text{C}$ .

The parameters of the humidity-dependent logistic function of Eq. (16) show the usual humidity-dependent NO<sub>2</sub> decrease rate ( $k_h$ ) value [29]. The humidity at which the effective NO<sub>2</sub> concentration is half its original concentration ( $T_h$ ) is high at 100 %, reflecting minimal humidity effects on the sensor material. These results show that the sensor material is perfect for decreasing the effect of humidity.

The last parameter is the response correlation parameter ( $c$ ). The high value of this parameter indicates the high sensitivity and response of the doped material. Comparing the value of this parameter with previous studies for various materials and doping reveals that the present 30 % WO<sub>3</sub> doped SnS<sub>2</sub> is one of the best materials to detect NO<sub>2</sub> gas [30].

Figure 3 shows a schematic diagram of Gibbs energy of adsorption and transition state of NO<sub>2</sub> with pristine and WO<sub>3</sub> doped SnS<sub>2</sub> at room temperature. The Gibbs energy of the transition state is the highest energy barrier needed to be overcome for the reaction to proceed. As shown in Figure 3, doping SnS<sub>2</sub> with WO<sub>3</sub> can reduce this barrier to more than six times. As a result, the reaction rate increases dramatically after doping.

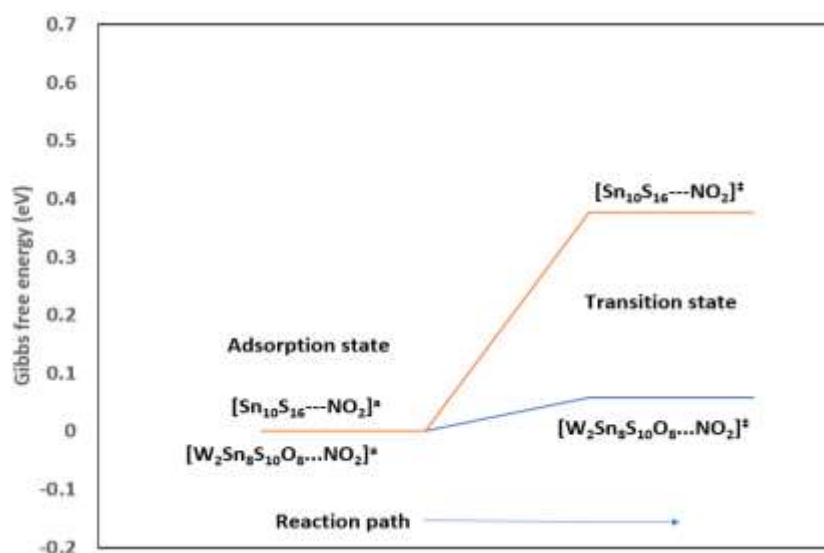


Figure 3. Schematic diagram of Gibbs energy of adsorption and transition state of NO<sub>2</sub> with pristine and 30 % WO<sub>3</sub> doped SnS<sub>2</sub> at room temperature. All energies are taken with reference to adsorption state energy

Figure 4 compares the theoretical response of 30 % WO<sub>3</sub> doped SnS<sub>2</sub> as a function of temperature and experimental results ( $R_g/R_a$ ) [3] to 20 ppm of NO<sub>2</sub> at low humidity. The comparison shows acceptable results for temperatures higher than  $210\text{ }^{\circ}\text{C}$  and less matching for temperatures lower than  $210\text{ }^{\circ}\text{C}$ . Both theoretical and experimental results peak at  $210\text{ }^{\circ}\text{C}$ ; however, experimental results have relatively sharper peak that are less pronounced theoretically.

Figure 5 shows the theoretical response of 30 % WO<sub>3</sub> doped SnS<sub>2</sub> as a function of NO<sub>2</sub> concentration at temperature  $210\text{ }^{\circ}\text{C}$  compared with experimental results ( $R_g/R_a$ ). The linear theoretical response, as established by Eq. (18) ( $v = 1$ ), is close and generally lower than the experimental values. As the introduction mentions, the detected concentration can be lower than the allowed NO<sub>2</sub> concentration in the range 1–5 ppm range.

Figure 6 shows the 90 % response time to 20 ppm NO<sub>2</sub> of 30 % WO<sub>3</sub> doped SnS<sub>2</sub> as a function of temperature in comparison with experiment [3] at low humidity. The 90 % response time can be obtained by integrating Eq. (12), resulting in the equation:

$$t_{res(90\%)} = \frac{\ln(10)}{[\text{NO}_2]_e^v AT^m \exp\left(\frac{-\Delta G^\ddagger}{k_B T}\right)} \quad (21)$$

90 % response time is the duration for a sensor to reach 90 % of its final, stable reading after exposure to the detected gas. A good agreement between theory and experiment is obtained in Figure 6.

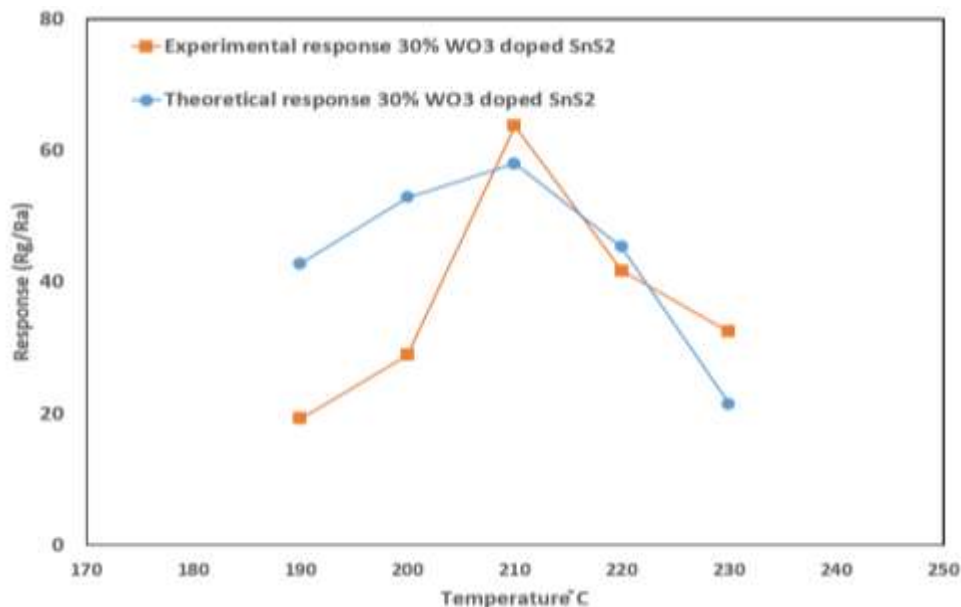


Figure 4. Theoretical response of 30 % WO<sub>3</sub> doped SnS<sub>2</sub> as a function of temperature compared with experimental results ( $R_g/R_a$ ) [3] to 20 ppm of NO<sub>2</sub> at low humidity

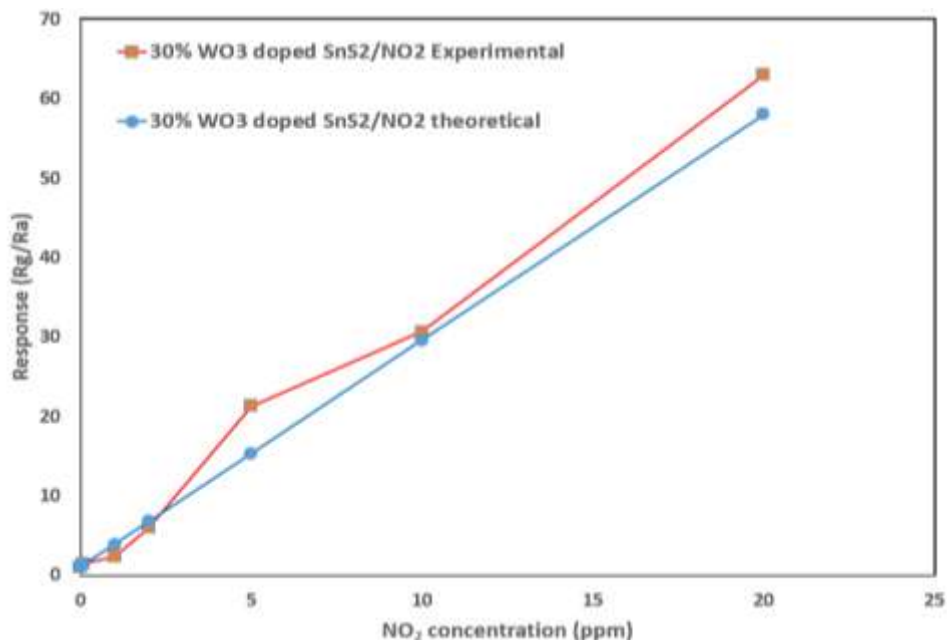


Figure 5. Theoretical response of 30 % WO<sub>3</sub> doped SnS<sub>2</sub> as a function of NO<sub>2</sub> concentration at temperature 210 °C compared with experimental results ( $R_g/R_a$ ) [3] at low humidity

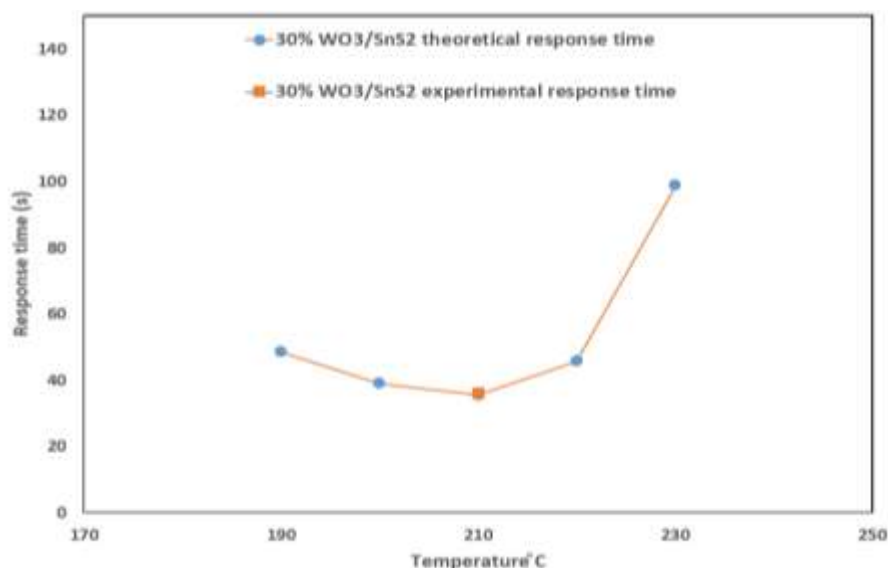


Figure 6. 90 % response time to 20 ppm NO<sub>2</sub> of 30 % WO<sub>3</sub> doped SnS<sub>2</sub> as a function of temperature in comparison with experiment [3] at low humidity

Figure 7 shows the effect of relative humidity on 30 % WO<sub>3</sub> doped SnS<sub>2</sub> response to 20 ppm of NO<sub>2</sub> gas at 210 °C temperature compared with the experiment [3]. Relative humidity affects response mainly in high humidity only, which can also be deduced from humidity parameters in Table 1. This indicates good response at relatively low to medium humidity.

Figure 8 shows the response stability after 30 days of 20 ppm NO<sub>2</sub> of 30 % WO<sub>3</sub> doped SnS<sub>2</sub> at 210 °C temperature compared to the experiment [3]. The theoretical response is equal to or lower than the experimental response, as shown in Figure 5 for higher NO<sub>2</sub> concentrations. As time passes (several months), it is expected for the detected response to be reduced further, and the experimental response becomes nearer to the theoretical response in Figure 8. Material degradation that includes changes in material crystallinity, doping, and electronic structure can all decrease the sensitivity. Dust, temperature fluctuations, and even pressure fluctuations affect sensor readings.

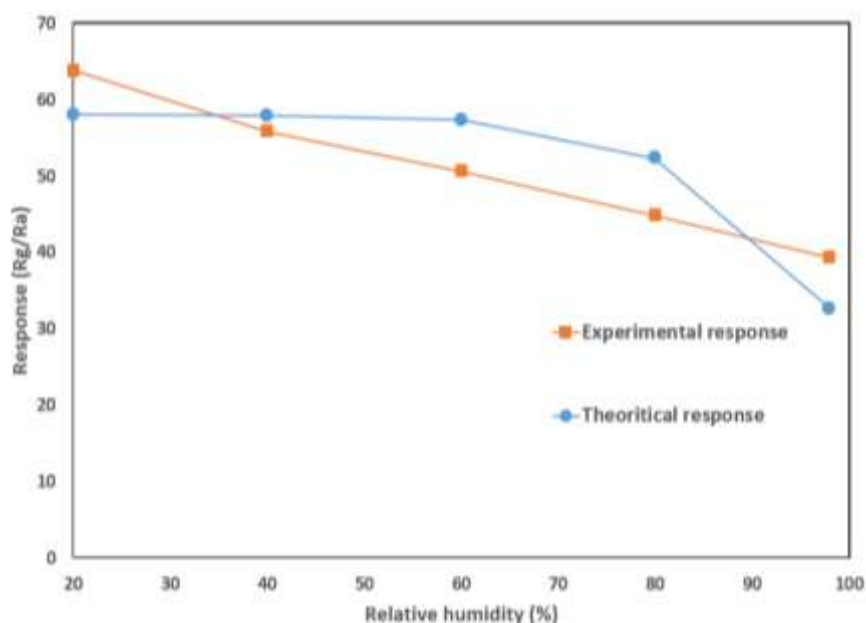


Figure 7. The effect of relative humidity on 30 % WO<sub>3</sub> doped SnS<sub>2</sub> response to 20 ppm of NO<sub>2</sub> gas at 210 °C temperature compared with experiment [3]



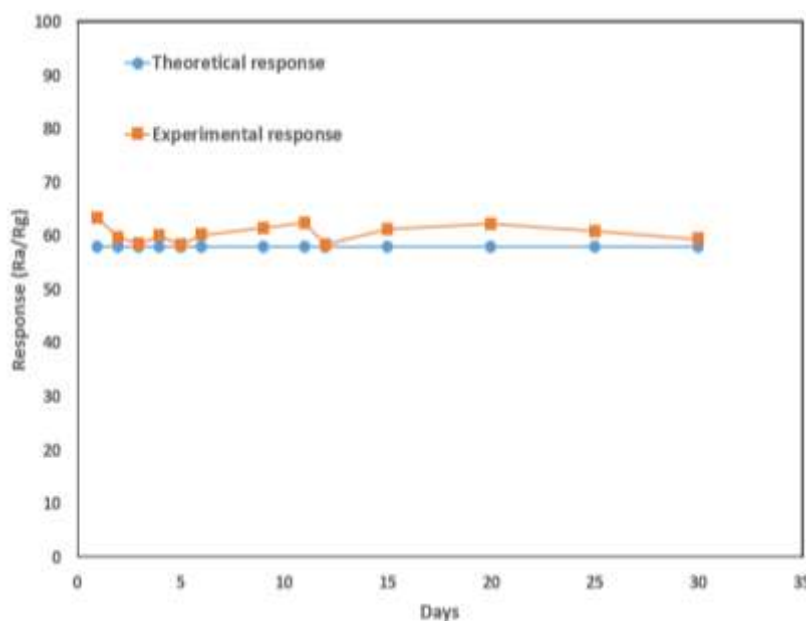


Figure 8. The stability of response after 30 days of 20 ppm  $\text{NO}_2$  of 30 %  $\text{WO}_3$  doped  $\text{SnS}_2$  at 210 °C temperature compared to experiment [3]

Figure 9 summarizes the  $\text{NO}_2$  dissociation in air and reaction with the sensor material.

As the  $\text{NO}_2$  molecule approaches the sensor material, its temperature rises to reach the sensor temperature (210 °C for the present sensor).  $\text{NO}_2$  begins to dissociate as it passes its dissociation temperature. Other  $\text{NO}_2$  molecules that reach the sensor material might get adsorbed. Some of the  $\text{NO}_2$ -adsorbed molecules might oxidize an oxygen vacancy in the sensor material, increasing the sensor's resistance and getting detected by the electronic circuit connected to the sensor material.

The present theoretical method adds new methods to distinguish between detected gases and response values at a given temperature [3]. The distinguishing method depends on the temperature at which the detected gas dissociates (such as  $\text{NO}_2$  in the present work at 200 °C) or reaches its autoignition temperature such as ethanol at 368 °C [24]. After the dissociation or autoignition temperatures, the gas concentration and response drop rapidly. Scanning the temperature-response profile of a detected gas can add information that differentiates between several gases.

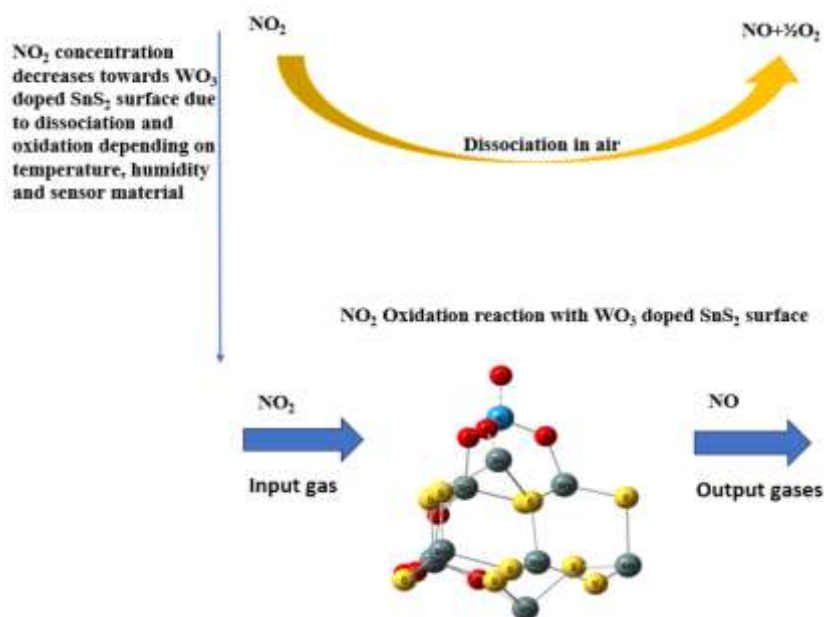


Figure 9. Summarizing the  $\text{NO}_2$  dissociation in air and reactions with the sensor material

### Conclusions

The reaction rate equation in transition state theory was used to evaluate the change in the number of vacancies in a 30 % WO<sub>3</sub> doped SnS<sub>2</sub> sensor as NO<sub>2</sub> gas passes over its surface. The change in number of vacancies was correlated to the change in response and response time. The Gibbs free energy of transition was evaluated to calculate the change of response with temperature and gas concentration. Gibbs free energy of transition showed low values of activation barrier near the highest response of experimentally determined doping ratio, indicating the quality of the used theory. The calculated response variation with temperature and NO<sub>2</sub> concentration agrees with the experimental response ( $R_g/R_a$ ) variation. The response time is also in good agreement with the experiment. The effect of humidity was also considered and compared to the experiment. The sensor material shows good stability for long-term use and nearly stays around a specific value with some fluctuations for a month. The present theory can distinguish different gases by the gas properties, such as dissociation temperature for NO<sub>2</sub> gas or autoignition temperature for other gases. The use of reaction rate methods such as the TST in the present work is the only available method in literature to simultaneously calculate response, response time, temperature effect, and humidity effect.

### Author Information\*

*\*The authors' names are presented in the following order: First Name, Middle Name and Last Name*

**Mudar Ahmed Abdulsattar** — Chief Scientific Researcher, Head of Solid-State Department, Ministry of Science and Technology, Rusafa Street, 52, 10045, Baghdad, Iraq, e-mail: [mudarahmed3@yahoo.com](mailto:mudarahmed3@yahoo.com); <https://orcid.org/0000-0001-8234-6686>

### Author Contributions

The manuscript was written through contributions of all authors. All authors have given approval to the final version of the manuscript. **CRedit**: **Mudar Ahmed Abdulsattar** — supervision, data curation, methodology, review & editing.





### Conflicts of Interest

The authors declare no conflict of interest.

### References

- 1 Lin, G., Zheng, T., Zhan, L., Lu, J., Huang, J., Wang, H., Zhou, Y., Zhang, X., & Cai, W. (2020). Tunable Structure and Optical Properties of Single Crystal SnS<sub>2</sub> Flakes. *Applied Physics Express*, 13. <https://doi.org/10.35848/1882-0786/ab7443>
- 2 Zhang, L., Xu, J., Lei, X., Sun, H., Ai, T., Ma, F., & Chu, P.K. (2025). Edge-Enriched SnS<sub>2</sub> Nanosheets on Graphene for Chemiresistive Room Temperature NH<sub>3</sub> Sensors. *Sensors and Actuators B: Chemical*, 433. <https://doi.org/10.1016/j.snb.2025.137565>
- 3 Zhao, H., Lv, J., Ma, X., Huang, B., Han, L., Kang, X., Wang, D., & Fang, H. (2025). Highly Responsive WO<sub>3</sub>/SnS<sub>2</sub> Sensor with Humidity Compensation: NO<sub>2</sub> Real-Time Detection System in Soil Surface Layer. *Sensors and Actuators B: Chemical*, 429. <https://doi.org/10.1016/j.snb.2025.137318>
- 4 Lee, S.M., Kim, Y.J., Park, S.J., Cheon, W.S., Kim, J., Nam, G.B., Kim, Y., & Jang, H.W. (2025). In-Situ Growth of 2D MOFs as a Molecular Sieving Layer on SnS<sub>2</sub> Nanoflakes for Realizing Ultrasensitive H<sub>2</sub>S Detection. *Advanced Functional Materials*, 35. <https://doi.org/10.1002/adfm.202417019>
- 5 Wang, Y., Li, J., Zhang, D., Zhou, T., Sun, M., Chen, S., & Sun, M. (2025). Hydrothermal Synthesis of Ag-Doped WO<sub>3</sub>-Based H<sub>2</sub>S Room Temperature Sensors: Unprecedented High and Fast Response. *Sensors and Actuators B: Chemical*, 438. <https://doi.org/10.1016/j.snb.2025.137811>
- 6 Liaqat, M.J., Hussain, S., Shahid, A., Amu-Darko, J.N.O., Ibrahim, T.K., Ibrahim, S.M., Manavalan, R.K., Zhang, X., Qiao, G., & Liu, G. (2025). Hydrothermally Grown WO<sub>3</sub>-SnO<sub>2</sub> Nanocomposites for Efficient NO<sub>2</sub> Detection at Low Concentration. *Sensors and Actuators B: Chemical*, 436. <https://doi.org/10.1016/j.snb.2025.137711>
- 7 An, B., Yang, Y., Yan, J., Wang, Y., Li, R., Wu, Z., Zhang, T., Han, R., Cheng, X., Wang, Q., & Xie, E. (2025). Oxygen Vacancies Engineering and Palladium Quantum Dots Sensitized WO<sub>3</sub> Nanosheet for Highly Efficiently H<sub>2</sub> Detection. *Applied Surface Science*, 692. <https://doi.org/10.1016/j.apsusc.2025.162722>
- 8 Airgas. (2018). Safety Data Sheet Nitrogen Dioxide (NO<sub>2</sub>). Pennsylvania. chrome-extension://efaidnbmnnnnibpcajpcglclefindmkaj/https://www.airgas.com/msds/001041.pdf

- 9 Chen, X., Chen, X., Han, Y., Su, C., Zeng, M., Hu, N., Su, Y., Zhou, Z., Wei, H., & Yang, Z. (2019). Two-Dimensional MoSe<sub>2</sub> Nanosheets via Liquid-Phase Exfoliation for High-Performance Room Temperature NO<sub>2</sub> Gas Sensors. *Nanotechnology*, 30. <https://doi.org/10.1088/1361-6528/ab35ec>
- 10 Sobrinho, H.H. de O., Eising, R., & Wrasse, E.O. (2025). Nanomaterials as Medicinal Gas Sensors Described by Density Functional Theory: A Comprehensive Review. *Medical Gas Research*, 15, 435–441. <https://doi.org/10.4103/mgr.MEDGASRES-D-24-00121>
- 11 Abdulsattar, M.A. & Mahmood, T.H. (2023). Enhancement of SnO<sub>2</sub> Sensitivity to Acetone by Au Loading: An Application of Evans–Polanyi Principle in Gas Sensing. *Optik*, 275, 170604. <https://doi.org/10.1016/j.ijleo.2023.170604>
- 12 Abdulsattar, M.A. (2024). Effect of Acetylene Properties on Its Gas Sensing by NiO Doped ZnO Clusters: A Transition State Theory Model. *Eurasian Journal of Chemistry*, 29, 35–43. <https://doi.org/10.31489/2959-0663/4-24-8>
- 13 Abdulsattar, M. A., & Almaroof, S. M. (2025). H<sub>2</sub>S Properties and Temperature Effects on the Response of Pristine and Al-Doped ZnO Gas Sensor. *Eurasian Journal of Chemistry*, 30(1(117)), 40–49. <https://doi.org/10.31489/2959-0663/1-25-10>
- 14 Sun, S., Li, X., Wang, N., Huang, B., & Li, X. (2025). A Sensitive Ppb-Level NO<sub>2</sub> Sensor Based on SnO<sub>2</sub> Decorated Te Nanotubes. *Sensors and Actuators B: Chemical*, 428. <https://doi.org/10.1016/j.snb.2025.137238>
- 15 Kim, T., Kim, W., Kim, S., & Lee, W. (2025). Sensitive and Stable NO<sub>2</sub> Sensor in a Wide Range Based on RGO/ZnO via Simple Spray Coating. *Microchemical Journal*, 212. <https://doi.org/10.1016/j.microc.2025.113250>
- 16 Rani, S., Dahiya, R., Kumar, V., Berwal, P., & Sihag, S. (2024). Hydrothermally Engineered WO<sub>3</sub> Nanosheets as Potential NO<sub>2</sub> Gas Sensor. *Ionics*, 31, 993–1002. <https://doi.org/10.1007/s11581-024-05934-2>
- 17 Frisch, M.J., Trucks, G.W., Schlegel, H.B., Scuseria, G.E., Robb, M.A., Cheeseman, J.R., Scalmani, G., Barone, V., Mennucci, B., Petersson, G.A., Nakatsuji, H., Caricato, M., Li, X., Hratchian, H.P., Izmaylov, A.F., Bloino, J., Zheng, G., Sonnenberg, J.L., Hada, M., Ehara, M., Toyota, K., Fukuda, R., Hasegawa, J., Ishida, M., Nakajima, T., Honda, Y., Kitao, O., Nakai, H., Vreven, T., Montgomery, J.A.J., Peralta, J.E., Ogliaro, F., Bearpark, M., Heyd, J.J., Brothers, E., Kudin, K.N., Staroverov, V.N., Kobayashi, R., Normand, J., Raghavachari, K., Rendell, A., Burant, J.C., Iyengar, S.S., Tomasi, J., Cossi, M., Rega, N., Millam, J.M., Klene, M., Knox, J.E., Cross, J.B., Bakken, V., Adamo, C., Jaramillo, J., Gomperts, R., Stratmann, R.E., Yazyev, O., Austin, A.J., Cammi, R., Pomelli, C., Ochterski, J.W., Martin, R.L., Morokuma, K., Zakrzewski, V.G., Voth, G.A., Salvador, P., Dannenberg, J.J., Dapprich, S., Daniels, A.D., Farkas, Ö., Foresman, J.B., Ortiz, J. V., Cioslowski, J., & Fox, D.J. (2013). Gaussian 09, Revision D.01. Gaussian, Inc., Wallingford CT.
- 18 Cai, J., Hao, S., Zhang, Y., Wu, X., Li, Z., & Zhao, H. (2024). Co<sub>3</sub>O<sub>4</sub> as an Efficient Passive NO<sub>x</sub> Adsorber for Emission Control during Cold-Start of Diesel Engines. *Chinese Journal of Chemical Engineering*, 66, 1–7. <https://doi.org/10.1016/j.cjche.2023.10.013>
- 19 Abdulsattar, M.A. (2024). NO<sub>2</sub> Properties That Affect Its Reaction with Pristine and Pt-Doped SnS<sub>2</sub>: A Gas Sensor Study. *Journal of Molecular Modeling*, 30. <https://doi.org/10.1007/s00894-024-06223-5>
- 20 Ambi, R.R., Mali, R.A., Pawar, A.B., Mulla, M.M., & Pittala, R.K. (2025). NiO Nanosheet-Assembled Chemiresistive Sensor for NO<sub>2</sub> Detection. *Applied Physics A: Materials Science and Processing*, 131. <https://doi.org/10.1007/s00339-025-08320-5>
- 21 Nikam, S.M., Patil, T.S., Nimbalkar, N.A., Kothavale, V.P., Kamble, R.S., Gaikwad, G.A., Mane, S.M., Lee, J., & Mane, R.D. (2025). Nickel Ion-Doped Vertical Nanorod Array Network of ZnO Engineered by Chemical Bath Deposition for Versatile NO<sub>2</sub> Gas Sensor. *Journal of the Korean Ceramic Society*, 62, 330–349. <https://doi.org/10.1007/s43207-024-00469-8>
- 22 Hu, Y., Chen, T., Wang, X., Ma, L., Chen, R., Zhu, H., Yuan, X., Yan, C., Zhu, G., Lv, H., Liang, J., Jin, Z., & Liu, J. (2017). Controlled Growth and Photoconductive Properties of Hexagonal SnS<sub>2</sub> Nanoflakes with Mesa-Shaped Atomic Steps. *Nano Research*, 10, 1434–1447. <https://doi.org/10.1007/s12274-017-1525-3>
- 23 Wang, M., Chen, J., Zhang, C., Ding, H., Wu, H.H., Li, X., Huai, S., Tang, Z., Zhao, X., Liu, H., & Wang, X. (2025). Engineering Surface Defect Active Sites in SnS<sub>2</sub> Nanosheets with Electron-Donating Groups for Efficient Photoelectrochemical Water Splitting. *Journal of Catalysis*, 446. <https://doi.org/10.1016/j.jcat.2025.116087>
- 24 Abdulsattar, M.A., Jabbar, R.H., & Al-Seady, M.A. (2024). Ethanol Properties Effects on Its Reaction with Mo-Doped SnO<sub>2</sub> Clusters: A Gas Sensor Model. *Results in Surfaces and Interfaces*, 17. <https://doi.org/10.1016/j.rsufi.2024.100291>
- 25 Abdulsattar, M.A., Jabbar, R.H., Abed, H.H., & Abduljalil, H.M. (2021). The Sensitivity of Pristine and Pt Doped ZnO Nanoclusters to NH<sub>3</sub> Gas: A Transition State Theory Study. *Optik*, 242. <https://doi.org/10.1016/j.ijleo.2021.167158>
- 26 Khan, W., & Reshak, A.H. (2015). Electronic Properties of Orthorhombic BaSn<sub>2</sub>S<sub>5</sub> Single Crystal. *Indian Journal of Physics*, 89, 437–443. <https://doi.org/10.1007/s12648-014-0605-4>
- 27 Zhang, B.F., Lin, J.Z., Wang, Y.X., Zhao, Y., & Zhang, Y.F. (2023). Theoretical Studies on the G-Factors and the Local Structure of W<sup>5+</sup> Ions in Tungsten Phosphate Glasses. *Revista Mexicana de Fisica*, 69. <https://doi.org/10.31349/RevMexFis.69.040402>
- 28 Sawini, Singh, K., Kumar, A., Kumar, D., Kumar, A., Kumar, A., Mahatha, S.K., & Praveenkumar, S. (2025). Unveiling the Role of Temperature on Structural, Compositional, Morphological, Thermal and Optical Properties of Hydrothermally Synthesized SnS<sub>2</sub> Nanostructures. *Inorganic Chemistry Communications*, 171. <https://doi.org/10.1016/j.inoche.2024.113548>
- 29 Abdulsattar, M.A., Almaroof, H.M., & Al-Saraf, W.J. (2025). Cl<sub>2</sub> Gas Properties, Temperature, and Humidity Effects on SnO<sub>2</sub> Sensor Response: Transition State Theory Study. *Journal of Molecular Modeling*, 31. <https://doi.org/10.1007/s00894-025-06368-x>
- 30 Abdulsattar, M.A. (2025). Pristine and Ni-Doped In<sub>2</sub>O<sub>3</sub> Pyramids Response to NO<sub>2</sub> Gas: A Transition State Theory Study. *Interactions*, 246. <https://doi.org/10.1007/s10751-025-02282-z>

Rakiya Yu. Milusheva<sup>1</sup> , Ilnar N. Nurgaliev<sup>1\*</sup> ,  
Akmal B. Abilkasimov<sup>2</sup> , Sayora Sh. Rashidova<sup>1</sup> 

<sup>1</sup>*Institute of Polymer Chemistry and Physics of the Academy of Sciences of the Republic of Uzbekistan, Tashkent, Uzbekistan;*

<sup>2</sup>*Kimyo International University in Tashkent, Tashkent, Uzbekistan*

(\*Corresponding author's e-mail: [ilnarvodnik@gmail.com](mailto:ilnarvodnik@gmail.com))

## Bioactive Chitosan/ $\beta$ -Tricalcium Phosphate Coatings on Titanium: Experimental Optimization and DFT Insight

The development of bioactive coatings combining biopolymers and calcium phosphate ceramics offers an effective strategy to improve osseointegration and functional performance of titanium-based implants. In this study, highly purified Bombyx mori chitosan (CS-BM) and  $\beta$ -tricalcium phosphate ( $\beta$ -TCP) were used to fabricate hybrid coatings on titanium substrates via electrochemical deposition under optimized conditions (52 °C, pH 6.6–7.0, 2.0–4.0 mA·cm<sup>-2</sup>). SEM and AFM analyses revealed uniform, strongly adherent two-layer structures with microtopography (1–10  $\mu$ m roughness) favorable for bone ingrowth, while elemental analysis confirmed complete Ca- and P-rich coverage. Density functional theory (DFT) modeling confirmed the cooperative role of Ca<sup>2+</sup> and PO<sub>4</sub><sup>3-</sup> in bridging CS-BM to TiO<sub>2</sub>, contributing to coating stability. In vivo studies demonstrated that CS-BM/TCP-coated implants accelerated early contact osteogenesis, dense trabecular bone formation, and stable bone-implant integration compared to uncoated controls. In an experimental osteoporosis model, intramuscular administration of CS-BM with active calcium or calcium–vitamin D<sub>3</sub> significantly enhanced fibroblast-to-osteoblast differentiation, stimulated osteoid synthesis, and led to complete restoration of bone microarchitecture within 21 days. These findings highlight CS-BM/TCP coatings as a sustainable, locally sourced, and highly effective platform for orthopedic and dental implant applications, with additional therapeutic potential in osteoporosis management.

**Keywords:** chitosan, Bombyx mori, DFT modeling, chitosan coating,  $\beta$ -tricalcium phosphate, TiO<sub>2</sub>(110), electrochemical deposition, implant, osteogenesis

### Introduction

The design of bioactive surfaces for titanium-based implants remains a pivotal objective in contemporary biomedical materials research. Titanium and its alloys are extensively employed in orthopedic and dental applications owing to their excellent mechanical performance, corrosion resistance, and intrinsic biocompatibility. Nevertheless, the inherently bioinert nature of their surfaces restricts direct bonding with bone tissue, thereby limiting long-term clinical performance. To overcome this limitation, extensive efforts have been directed toward surface functionalization strategies that integrate biopolymers with calcium phosphate ceramics, aiming to enhance osseointegration and biological activity [1–10].

One of the key challenges in biomedical materials science is enhancing the physico-mechanical and biological performance of implants to improve their long-term biocompatibility. A widely adopted approach to achieving this goal is the surface modification of the underlying implant material. Among the diverse materials investigated for such applications, chitosan (CS), a  $\beta$ -(1→4)-linked D-glucosamine polysaccharide, has garnered considerable attention due to its intrinsic biocompatibility, biodegradability, and strong affinity for biological molecules via its amino and hydroxyl functional groups. These characteristics make CS a particularly promising candidate for advanced prosthetic applications, positioning it at the forefront of bioactive surface engineering strategies [11–14].

Globally, the production of chitin and its derivative, CS, is predominantly based on shellfish exoskeletons as the primary raw material source. However, this approach is constrained by seasonal and geographic limitations in shellfish harvesting, which restrict large-scale and consistent supply. In Uzbekistan, where sericulture has been historically well-developed, an alternative and underutilized resource is available in the form of Bombyx mori silkworm pupae—by-products of the silk production process. These pupae represent a sustainable source of chitin that can be chemically processed into CS, a polymer of equally high industrial and biomedical value [15–21].

Tricalcium phosphate (TCP), particularly in its  $\beta$ -phase, is a well-recognized osteoconductive material extensively applied in bone regeneration owing to its close compositional resemblance to the mineral phase of natural bone. Compared with hydroxyapatite,  $\beta$ -tricalcium phosphate demonstrates more favorable resorption kinetics and pronounced osteoinductive potential, which makes it especially suitable for use in coating systems designed to enable controlled ion release and facilitate progressive bone remodeling [22, 23].

Recent research has increasingly focused on combining CS with TCP to develop composite materials that provide both structural reinforcement and enhanced biological functionality. Among the various deposition techniques, electrochemical methods are particularly attractive for producing uniform, strongly adherent coatings under low-temperature conditions [24]. Literature reports indicate that promising coating components include phosphate, calcium, copper, and gold ions, as well as macromolecular bioactive polymers such as CS, fibroin, and TCP [25–32]. Comprehensive investigations into the use of these constituents in implant coatings are regarded as highly promising, with the potential to markedly improve both the mechanical performance and the biological activity of dental implant surfaces.

Given the high incidence and increasing frequency of bone fractures—driven in part by technological progress and industrialization—post-traumatic osteoporosis has become increasingly prevalent. Recent studies have emphasized the important role of CS in bone tissue metabolism and in the treatment of osteoporosis of various etiologies [33–36]. Composite coatings combining chitosan with calcium phosphate significantly enhance cell adhesion and osteoblastic differentiation (e.g., MG-63, MC3T3-E1), while increasing surface hydrophilicity—key properties for improved osseointegration [37]. CS is of particular interest as a potential therapeutic agent for osteoporosis due to its ability to enhance calcium absorption, stimulate bone formation, and provide targeted drug delivery. CS-calcium complexes for osteoporosis treatment are especially promising owing to their biocompatibility, drug delivery potential, and osteogenic properties. An underexplored alternative to conventional marine-sourced chitosan is *Bombyx mori* chitosan, which, due to its lower crystallinity, high purity, and enhanced solubility, offers unique advantages for biomedical coatings; given the growing demand for sustainable, locally available biomaterials and the complete absence of studies applying CS-BM in implant surface engineering, its investigation is both timely and scientifically relevant. Despite promising experimental advances, a detailed understanding of the interactions at the atomic level between coating components and titanium dioxide surfaces remains limited. Density functional theory (DFT) and atomistic modeling can provide insights into surface binding, charge redistribution, and electronic effects, offering valuable guidance for experimental design.

This study aims to develop and optimize electrochemically deposited chitosan *Bombyx mori*/ $\beta$ -tricalcium phosphate (CS-BM/TCP) hybrid coatings on titanium substrates, elucidating their interfacial binding mechanisms and evaluating their potential to enhance osseointegration and bone regeneration. The experimental approach is complemented by DFT simulations of the rutile  $\text{TiO}_2(110)$  surface, focusing on its interactions with individual and cooperative adsorbates, including a chitosan dimer,  $\text{Ca}^{2+}$ , and  $\text{PO}_4^{3-}$  ions. This combined methodology aims to elucidate the underlying binding mechanisms responsible for improved coating adhesion and enhanced bioactivity.

## Experimental

### *Isolation of Chitin from Bombyx mori and Synthesis of Chitosan.*

The first stage of chitin production involves multiple extractions of oil using organic solvents, including ethanol, at elevated temperature. Chitin was extracted from *Bombyx mori* silkworm pupae using 5–7 % NaOH or KOH solutions (1:10 ratio) at 90 °C for 3 hours, followed by extensive washing and drying. Proteins are removed by treating the defatted raw material with an alkali solution. Chitosan *Bombyx mori* (CS-BM) was obtained by deacetylating chitin in 50 % NaOH (1:10 ratio) at 120 °C for 3 h. The resulting product was washed to neutrality, lyophilized at –50 °C under 0.5 mbar pressure, yielding a yellowish powder readily soluble in 2 % acetic acid. Purification involved dissolving crude CS-BM in 2 % acetic acid, coagulating at controlled pH, washing with ethanol, centrifugation, and subsequent lyophilization, as described previously.

### *Characterization Techniques*

The characterization of the obtained samples was carried out using a set of complementary analytical techniques. Fourier transform infrared (FTIR) spectra were acquired with a Shimadzu 84005 spectrometer (Japan) in the range of 4000–400  $\text{cm}^{-1}$  using KBr pellet preparation. The phase composition was analyzed by



X-ray diffraction (XRD) on a Rigaku Miniflex 600 diffractometer (Japan) employing Cu K $\alpha$  radiation ( $\lambda = 1.5406 \text{ \AA}$ ). The elemental composition was determined with a Flash Smart elemental analyzer (Thermo Scientific, USA). Surface topography was examined by atomic force microscopy (AFM) using an Agilent Technologies 5500 system (USA), while morphological features were observed by scanning electron microscopy (SEM) on an EVO MA10 instrument (ZEISS, Germany).

#### *Preparation of Electrolyte Solutions and Coating Deposition*

The electrolyte solution was prepared by dissolving chitosan derived from CS-BM,  $0.5 \text{ g L}^{-1}$  in 2 % acetic acid, followed by mixing with a saturated 0.2 M TCP solution. Titanium plates ( $30 \times 10 \times 1 \text{ mm}$ , surface roughness  $4.0 \text{ }\mu\text{m}$ ) were thoroughly cleaned and subsequently immersed in the prepared electrolyte. Electrochemical deposition was carried out at  $52 \text{ }^\circ\text{C}$  for 15 h under a constant current density of  $2.0\text{--}4.0 \text{ mA}\cdot\text{cm}^{-2}$  in a pH 6.6–6.7 buffer solution. Previous studies have demonstrated that lower pH values ( $<6.5$ ) negatively impact the adhesion strength of calcium phosphate coatings, primarily due to the accelerated dissolution of precursor species and reduced nucleation efficiency on titanium substrates [37, 38]. After electrolytic deposition, the titanium plates were rinsed thoroughly with demineralized water and dried in an oven at  $50 \text{ }^\circ\text{C}$  for 12 h.

#### *Biomedical Studies of Titanium Implantation in Vivo*

The in vivo biomedical study was conducted on 18 clinically healthy, non-breed rabbits weighing 4200–4300 g. The animals were maintained under standard vivarium conditions at the Interuniversity Scientific Research Laboratory of the Tashkent Medical Academy and provided with a standard diet. All experimental procedures were performed in strict compliance with the international guidelines for the ethical treatment of laboratory animals, as outlined in the European Communities Council Directive 86/609/EEC of 24 November 1986.

Titanium dental implants coated with a bioactive TCP/CS-BM composite, as well as uncoated titanium implants, were surgically placed under general anesthesia. The animals were randomly assigned to three experimental groups:

- Group 1 — Intact control;
- Group 2 — Implant without bioactive coating;
- Group 3 — Implant with bioactive coating.

General anesthesia was induced via intravenous injection of a freshly prepared sodium ethaminal solution ( $40 \text{ mg}\cdot\text{kg}^{-1}$ ) into the auricular vein. Upon achieving deep anesthesia, 0.5 % novocaine solution was administered subcutaneously at the surgical site. Osteoplastic surgery for implant insertion was performed using a 1 mm diameter drill operating at 1000 rpm under continuous saline irrigation. Implant placement was completed using a rotating torque key to ensure controlled insertion.

Postoperative monitoring of the animals' general condition was carried out hourly during the first 24 hours and subsequently once daily over a 90-day period. Radiographic assessments of the implant sites were performed at 1, 2, and 3 months post-surgery to evaluate the progression of osseointegration.

#### *Biomedical Evaluation of Modified Chitosan for Osteoporosis Treatment*

The biomedical evaluation of modified chitosan for osteoporosis treatment was conducted on 50 healthy female Chinchilla rabbits weighing 2.0–2.5 kg. Osteoporosis was experimentally induced by performing an osteotomy of the right femur, followed by immobilization of the limb. After 40–50 days, radiographic examinations confirmed the development of osteoporosis, and the animals were divided into three experimental groups. The first group ( $n = 10$ ) served as the control and, after removal of immobilization, was kept under standard conditions without treatment. The second group ( $n = 15$ ) received intramuscular injections of CS-BM combined with active calcium for 20 days, while the third group ( $n = 15$ ) received CS-BM in combination with “Calcium-D3 Nycomed” for the same duration. At the end of the treatment period, all animals were euthanized, and samples from the femoral epiphysis and diaphysis were collected for micromorphological analysis. The specimens were fixed in 10 % neutral buffered formalin and decalcified in 5 % nitric acid in preparation for histological examination.

#### *Statistical Analysis*

The experimental data were processed statistically using Microsoft Excel software. Calculated parameters included the arithmetic mean ( $M$ ), standard deviation ( $\sigma$ ), standard error of the mean ( $m$ ), and relative values expressed as percentages. Differences between mean values were evaluated for statistical significance



using Student's *t*-test, with a threshold of  $p \leq 0.05$  considered significant. All statistical analyses were performed in accordance with established guidelines for the processing of clinical and laboratory research data.

### Computational Details

Density functional theory (DFT) calculations were performed using the Vienna Ab-initio Simulation Package (VASP) [39–42]. The Perdew–Burke–Ernzerhof (PBE) generalized gradient approximation (GGA) [43] was used for the exchange–correlation functional, and projector augmented-wave (PAW) pseudopotentials [44] were employed.

A kinetic energy cutoff of 500 eV was chosen after convergence tests, ensuring total energy variation below  $10^{-5}$  eV/atom. Brillouin zone sampling was performed using a Monkhorst–Pack grid [45] of  $2 \times 2 \times 1$  for the slab models. Atomic structures were fully optimized until the residual forces on each atom were less than  $0.02 \text{ eV } \text{\AA}^{-1}$ .

The rutile  $\text{TiO}_2$  structure was obtained from the Materials Project (mp-2657) and used as the model for the  $\text{TiO}_2(110)$  surface. The rutile  $\text{TiO}_2(110)$  surface was modeled as a  $2 \times 2$  supercell slab composed of four atomic layers separated by a vacuum region of  $20 \text{ \AA}$  along the surface normal ( $z$ -axis). The bottom two layers were fixed to represent the bulk structure, while the top layers were relaxed. Dipole corrections were applied along the  $z$ -direction (LDIPOL = TRUE, IDIPOL = 3) to eliminate artificial electrostatic interactions caused by asymmetry in the slab geometry.

The chitosan repeating unit was represented by the protonated glucosamine monomer ( $[\text{GlcNH}_3]^+$ ), optimized separately in the gas phase. To maintain overall charge neutrality in periodic boundary conditions, a uniform compensating background charge was applied, following standard procedures for charged adsorbates [46]. This approach enables reliable estimation of local binding energetics and charge redistribution while avoiding long-range Coulomb artifacts.

Adsorption models included: (i) isolated  $[\text{GlcNH}_3]^+$  interacting with  $\text{TiO}_2(110)$ ; (ii) single  $\text{Ca}^{2+}$  and  $\text{PO}_4^{3-}$  ions; and (iii) a cooperative  $\text{CS-Ca}^{2+}\text{-PO}_4^{3-}$  composite cluster.  $\beta$ -Tricalcium phosphate ( $\beta$ -TCP) was modeled in its rhombohedral R3c phase (space group No. 161) using crystallographic parameters from the ICSD database, cross-validated with data from the Materials Project (mp-3487).

The adsorption energy ( $E_{\text{ads}}$ ) was calculated using:

$$E_{\text{ads}} = E_{(\text{surface} + \text{adsorbate})} - E_{(\text{surface})} - E_{(\text{adsorbate})},$$

where  $E_{(\text{surface} + \text{adsorbate})}$  is the total energy of the adsorption system, and  $E_{(\text{surface})}$  and  $E_{(\text{adsorbate})}$  correspond to the isolated surface and molecule/ion, respectively.

Charge transfer analysis was performed using the Bader method [47, 48]. The chosen DFT-PBE/PAW level of theory provides a good balance between accuracy and computational efficiency for describing oxide–biomolecule interfaces and has been widely validated for  $\text{TiO}_2$  and calcium phosphate systems [49]. Charge transfer was estimated using Bader charge analysis.

### Results and Discussion

#### Physicochemical Properties of CS and TCP

For the purposes of this study—given the intended biomedical application—highly purified CS-BM was required. CS-BM purification was carried out according to a previously developed method [15, 16]. The physicochemical properties of the starting material were characterized using elemental analysis, IR spectroscopy, and X-ray diffraction. Additionally, the degree of deacetylation (DDA) and viscosity-average molecular weight ( $M_v$ ) of the CS-BM samples were determined. Purified CS-BM exhibited high nitrogen content (8.52 %), low ash content (1.43 %), and high solubility in acetic acid (98.85 %). TCP powder displayed limited solubility in water but dissolved well in acetic acid, forming hydrophosphates.

FTIR spectra confirmed characteristic CS-BM functional groups (OH,  $\text{NH}_2$ , and C–O–C) and complete deacetylation. TCP spectra showed strong phosphate group vibrations, while XRD confirmed the crystalline phase of single-phase tricalcium phosphate. The broad and intense absorption band observed in the  $3500\text{--}3100 \text{ cm}^{-1}$  region corresponds to the stretching vibrations of hydroxyl (OH) and amino (NH) groups involved in hydrogen bonding. The stretching vibrations of the C–H and  $\text{CH}_2$  groups were observed at  $2917$  and  $2873 \text{ cm}^{-1}$ , respectively. The absorption bands within  $900\text{--}1150 \text{ cm}^{-1}$  are associated with various deformation vibrations of C–O–C, NH, and C–C groups (Figure S1 of the Supplementary Materials file). The spectrum lacked the absorption peak of the acetamide group characteristic of chitin, while the amide II band appeared as a distinct single peak at  $1578 \text{ cm}^{-1}$ . The nitrogen content and solubility of the purified CS-BM

reached 8.52 % and 98.8 %, respectively. A low ash content (1.43 %) also confirmed the high purity of the obtained material (Table 1).

TCP powder was used as the calcium-containing component of the coating. TCP belongs to the group of bioactive materials capable of participating in ion exchange and metabolic processes within the bone matrix, being partially or completely replaced by bone tissue during regeneration. Due to its osteoconductive properties, TCP serves as a scaffold that is gradually substituted by newly formed bone.

Table 1

Physicochemical characteristics of CS-BM and TCP

Sample	Nitrogen content, %	Ash content, %	Solubility in 2 % acetic acid, %	Solubility in water, %	pH of 1 % aqueous suspension	Intrinsic viscosity, dl/g	Moisture content, %
<i>Bombyx mori</i> chitosan	8.52	1.43	98.85	1.15	7.5	2.5	3.17
TCP — $\text{Ca}_3(\text{PO}_4)_2$	—	58.40	96.10	43.68	—	—	1.68

One of its most valuable characteristics is its osteoinductivity, which makes it widely applicable as a biomaterial for bone defect repair. However, osteoinductivity alone is insufficient to ensure complete bone regeneration and remodeling in composite materials based solely on tricalcium phosphate [50, 51]. Successful bone growth also requires additional factors, such as bioactive scaffolding materials (e.g., CS) and specific growth factors capable of inducing cellular differentiation toward bone tissue. Therefore, the bone-regenerative potential of TCP can be significantly enhanced by the incorporation of osteoinductive growth factors stimulating osteoblast differentiation [52–54]. Tricalcium phosphate is a tertiary calcium phosphate, also referred to as bone ash, serving as a rich and bioavailable source of calcium and phosphorus for cells.

The TCP used in this study was a grayish powder with a molecular weight of 310.18 g/mol and a density of 2.81 g/cm<sup>3</sup>, measured under standard conditions (25 °C, 100 kPa). The physicochemical characteristics of purified CS-BM and TCP used for implant coatings are summarized in Table 1.

The purified CS-BM was subsequently utilized for the fabrication of composite coatings on titanium substrates in combination with TCP. The TCP employed in this study was characterized by a high content of ash-forming elements (~60 %). While TCP demonstrated low solubility in water, it readily dissolved in 2 % acetic acid, resulting in the formation of hydrophosphate species. Structural characterization of the TCP powder was performed using Fourier-transform infrared (FTIR) spectroscopy and X-ray diffraction (XRD) (Figure S2 of the Supplementary Materials file).

The FTIR spectrum of  $\text{Ca}_3(\text{PO}_4)_2$  confirmed the presence of phosphate anions, as evidenced by a broad, intense absorption band centered at 1452 cm<sup>-1</sup>, accompanied by shoulders at 1138 cm<sup>-1</sup> and 1065 cm<sup>-1</sup>, corresponding to the antisymmetric stretching vibrations of the phosphate group. Additionally, a deformation vibration was observed at 528 cm<sup>-1</sup> (Figure S2, a of the Supplementary Materials file).

The XRD pattern of the TCP sample (Figure S2, b) displayed distinct diffraction peaks characteristic of single-phase tricalcium phosphate, with prominent reflections at  $2\theta = 30.0^\circ$ ,  $34.2^\circ$ , and  $36.5^\circ$ . The peak at  $2\theta = 30.0^\circ$  serves as a definitive marker for TCP, in agreement with previously reported crystallographic data [55, 56].

#### Preparation of Calcium Phosphate/Chitosan Coatings

Titanium plates were prepared according to the procedure described in Experimental section. A deposition setup was assembled, consisting of a thermostated electrochemical cell equipped with a temperature sensor, two electrodes (a reference electrode and a counter electrode), and a cathode onto which the titanium plate was fixed (Fig. 1).

The electrochemical deposition parameters for bioactive coatings were systematically optimized, with the following key factors identified: applied current density (0.1–10 mA), temperature range (30–70 °C), solution and bioactive mixture concentrations (0.1–10 %), and deposition time (1–20 h). Prior to electrolysis, all raw materials, solutions, and mixtures were carefully prepared and purified. Special emphasis was placed on the physical surface characteristics of the titanium substrates, particularly smoothness and roughness, as micro-scale surface irregularities were found to be critical for effective electrolytic deposition and stable fixation of the bioactive layer. This effect is attributed to the enhanced reduction of ions and macroions during electrochemical processing.

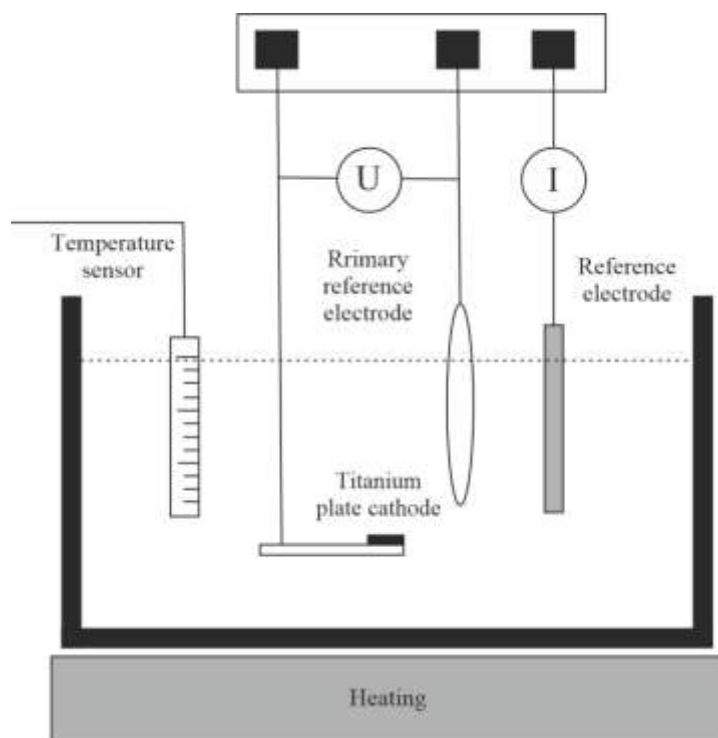


Figure 1. Schematic diagram of the installation for electrolytic deposition of coatings on titanium plates

Titanium plates were mechanically treated to achieve the desired roughness. Previous studies have shown that increasing surface roughness significantly improves the primary mechanical stability of implants and supports their long-term performance [57–59]. While roughness enhances the bone–implant contact area, thereby facilitating osseointegration, it is not the sole determinant of success. Surface chemistry, particularly the incorporation of bioactive ions, plays an equally important role during the initial stages of reparative osteogenesis by promoting osteogenic activity.

Surface roughness of the plates was measured using an atomic force microscope (Agilent Technologies 5500, USA) (Figure S3 of the Supplementary Materials file).

A developed surface topography facilitates mechanical interlocking between the newly formed bone tissue and the implant surface. A robust process of reparative regeneration is a key factor determining the mechanical integrity of the bone–implant interface. The microscopic level of roughness reflects the microgeometry of the implant surface, with surface irregularities in the range of 1 to 10  $\mu\text{m}$ .

The obtained surface roughness range was found to provide optimal adhesion between the implant and mineralized bone tissue. According to literature data, the most favorable topography for osseointegration includes hemispherical pores approximately 1.5  $\mu\text{m}$  deep and 4  $\mu\text{m}$  in diameter.

SEM analysis confirmed the successful formation of TCP coatings on titanium substrates, with thicknesses ranging from 10 to 14  $\mu\text{m}$  (Fig. 2). Under optimized electrolytic deposition conditions—CS-BM concentration of 0.41 g/dL, TCP in a supersaturated solution at pH 7.0, temperature of 52  $^{\circ}\text{C}$ , deposition time of 15 h, and applied current density of 2.0  $\text{mA}/\text{cm}^2$ —the resulting composite coating reached a total thickness of 58  $\mu\text{m}$ , of which 16  $\mu\text{m}$  corresponded to the CS-BM layer.

Surface roughness measurements, performed using an atomic force microscope (Agilent Technologies 5500, USA), are presented in Figure S3 of the Supplementary Materials file. The resulting microtopography enables mechanical interlocking between the implant and the newly formed bone tissue, which is a decisive factor for the long-term integrity of the bone–implant interface. At the microscopic scale, the implant surface exhibited irregularities in the 1–10  $\mu\text{m}$  range, corresponding to the optimal geometry for enhanced osteointegration.

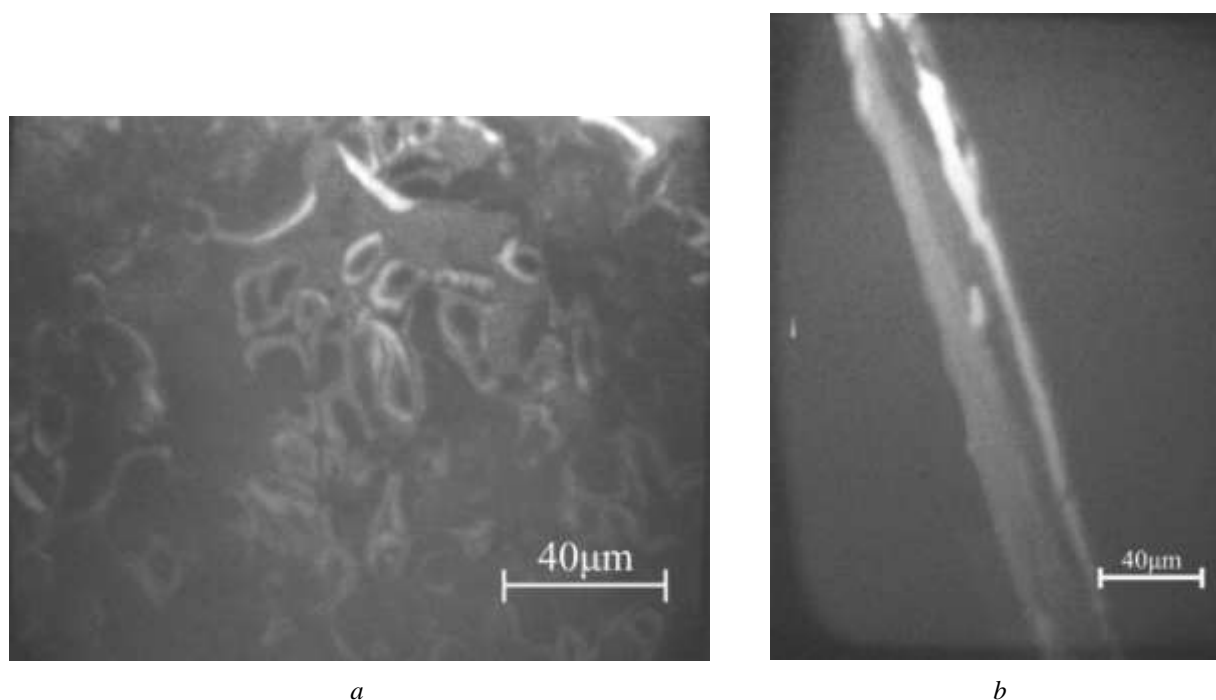


Figure 2. Electrolytically deposited two-layer coating based on CS-BM and TCP on a titanium plate:  
 (a) SEM image of the coating surface at 250 $\times$  magnification. CS-BM concentration:  $C = 0.41$  g/dL;  $T = 52$   $^{\circ}\text{C}$ ; deposition time: 15 h; in supersaturated TCP solution (buffer pH 7.0); current density:  $I = 2.0$  mA/cm $^2$ ;  
 (b) SEM image of the coating cross-section at 250 $\times$  magnification. Outer layer: TCP; inner (darker) layer: CS-BM; intermediate connecting layer: TCP; layer thicknesses: 1 — 32  $\mu\text{m}$ , 2 — 16  $\mu\text{m}$ , 3 — 8  $\mu\text{m}$

A moderate increase in CS-BM concentration to 0.46 g/dL, while keeping all other deposition parameters unchanged, resulted in a pronounced reduction in total coating thickness to 24  $\mu\text{m}$ . Correspondingly, the CS-BM layer thickness decreased to 10  $\mu\text{m}$  (Fig. 3).

These results align with previous reports [60, 61], which also documented a progressive reduction in coating thickness with increasing CS-BM concentration in the electrolyte. Experimental data demonstrated that raising the CS-BM concentration to 0.48 g/dL, while simultaneously shortening the deposition time and increasing the current density to 4.0 mA/cm $^2$ , yielded a total coating thickness of 30  $\mu\text{m}$ , with the CS-BM layer reduced to 6  $\mu\text{m}$  (Fig. 4). Both the overall coating thickness and surface roughness exhibited a consistent downward trend with higher CS-BM concentrations. Importantly, the combination of reduced processing time and elevated current density produced coatings comparable in quality to those formed under prolonged deposition, offering a more cost-effective and time-efficient manufacturing approach.

Experimental results confirmed that the developed bioactive coating comprises three structurally distinct layers: a CS-BM matrix, an intermediate TCP layer, and an outer TCP layer. Each layer fulfills a specific function in enhancing implant performance. The CS-BM matrix acts as a reservoir for the sustained release of bioactive molecules, supporting local therapeutic action.

The outer TCP layer promotes bone tissue ingrowth, while the intermediate TCP layer ensures robust adhesion between the matrix and the implant surface. Owing to the ionic exchange capacity of TCP in combination with CS-BM, the coating undergoes gradual resorption, facilitating its replacement by newly formed bone tissue during the regenerative process.

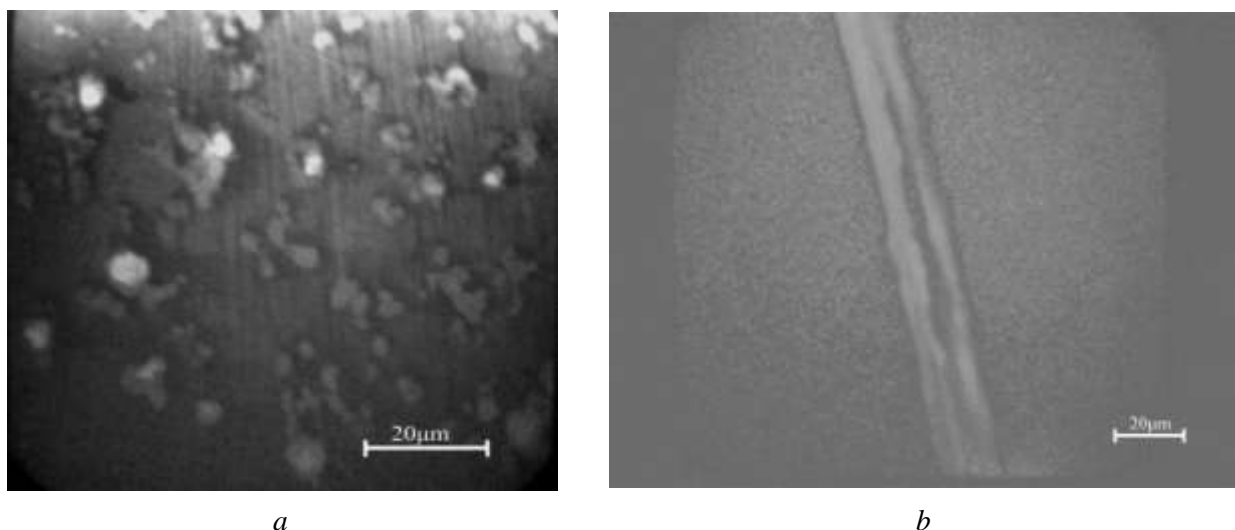


Figure 3. Electrolytically deposited two-layer coating based on CS-BM and TCP on a titanium plate:  
 (a) SEM image of the coating surface at 500× magnification. CS-BM concentration:  $C = 0.46$  g/dL;  $T = 52$  °C; deposition time: 15 h; in supersaturated TCP solution (buffer pH 6.6); current density:  $I = 2.0$  mA/cm<sup>2</sup>;  
 (b) SEM image of the coating cross-section at 500× magnification. Outer layer: TCP; inner (darker) layer: CS-BM; layer thicknesses: 1 — 10 μm, 2 — 10 μm, 3 — 4 μm

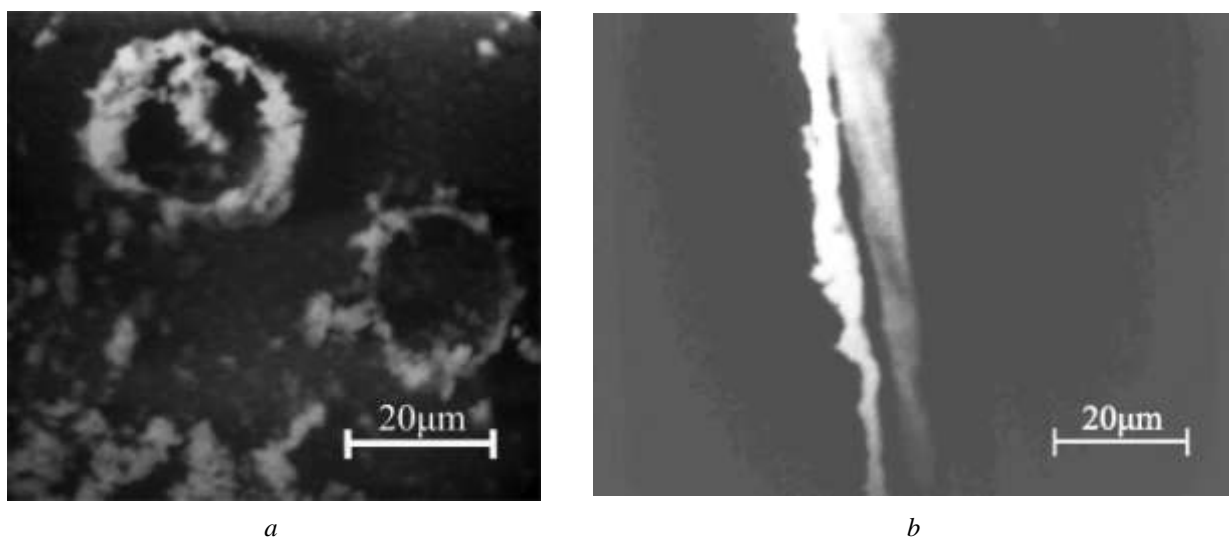


Figure 4. Electrolytically deposited two-layer coating based on CS-BM and TCP on a titanium plate:  
 (a) SEM image of the coating surface at 500× magnification. CS-BM concentration:  $C = 0.48$  g/dL;  $T = 52$  °C; deposition time: 7 h; in supersaturated TCP solution (buffer pH 6.65); current density:  $I = 4.0$  mA/cm<sup>2</sup>;  
 (b) SEM image of the coating cross-section at 500× magnification. Outer layer: TCP; inner (darker) layer: CS-BM; layer thicknesses: 1 — 10 μm, 2 — 6 μm, 3 — 14 μm

#### Optimization of Titanium Surface

Surface roughness significantly affects osseointegration. AFM revealed optimal roughness values of ~4.0 μm after progressive processing, enhancing implant stability and bone integration. The microstructural characteristics of the coating were further examined using scanning electron microscopy (SEM, EVO MA10, ZEISS, Germany) at varying magnifications (Fig. 5, *a*, *b*), providing detailed visualization of surface morphology and coating uniformity.

As shown in Figure 5, *a* the untreated titanium plate surface displays distinct roughness characterized by pronounced scratches. After coating, the surface is covered with TCP microspheres ranging from 10 to 30 μm in diameter (Fig. 5, *b*), around which the CS-BM film aggregates. These CS-BM domains are integrated with both the calcium phosphate spheres and each other, forming cross-linked structural networks.

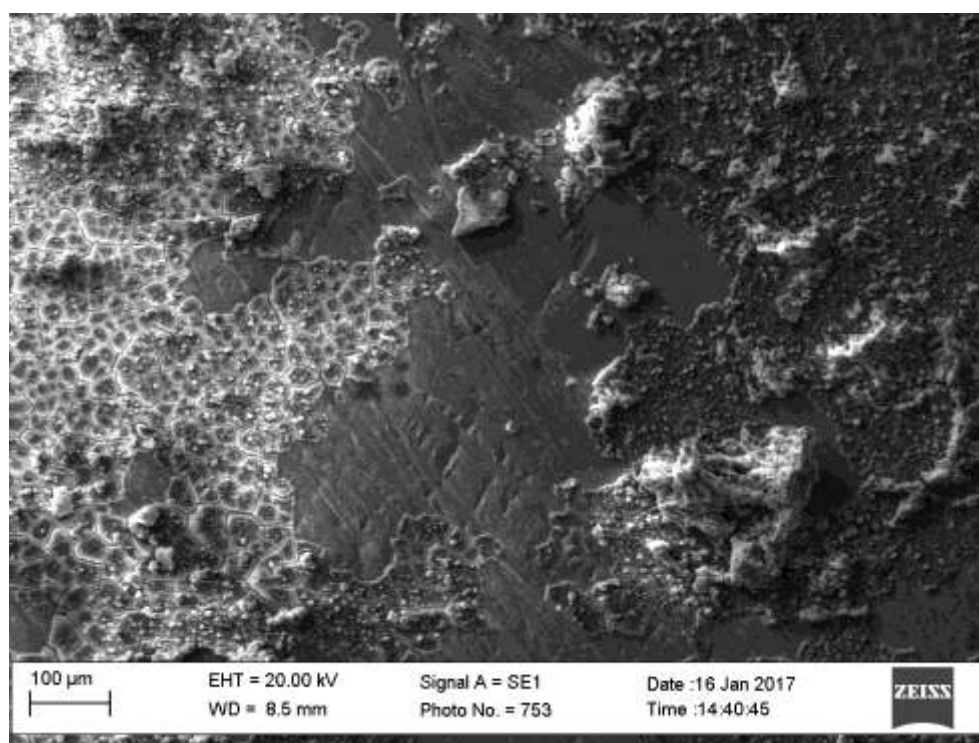
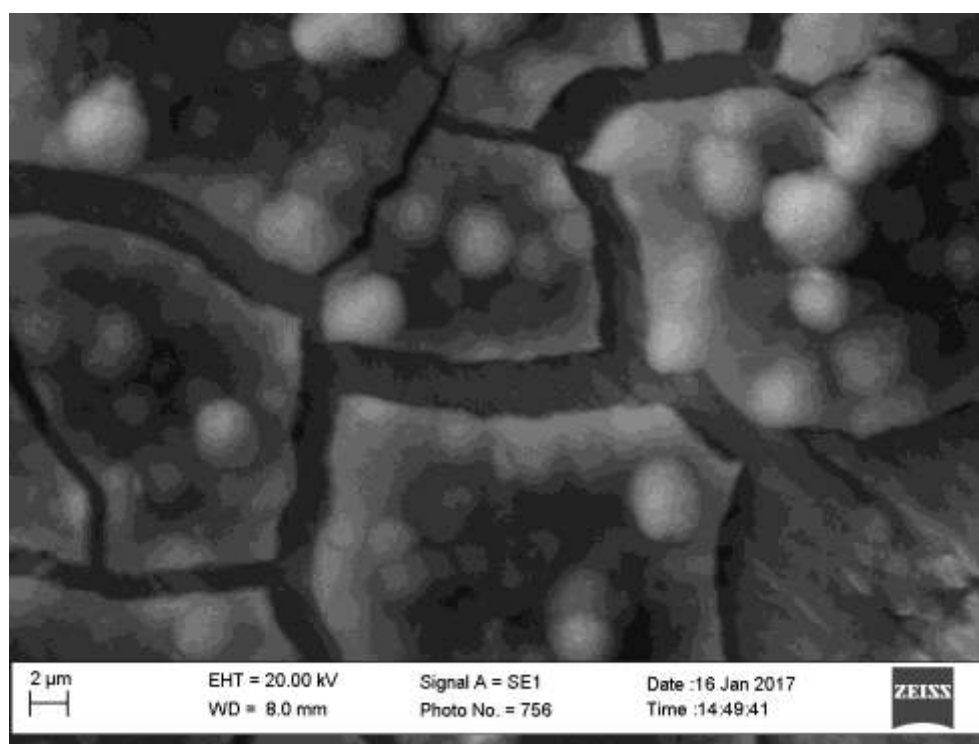
*a**b*

Figure 5. (a) Image of the CS-BM/TCP coating on a titanium plate, scale bar: 100  $\mu$ m;  
(b) Image of the CS-BM-TCP coating on a titanium plate, scale bar: 10  $\mu$ m

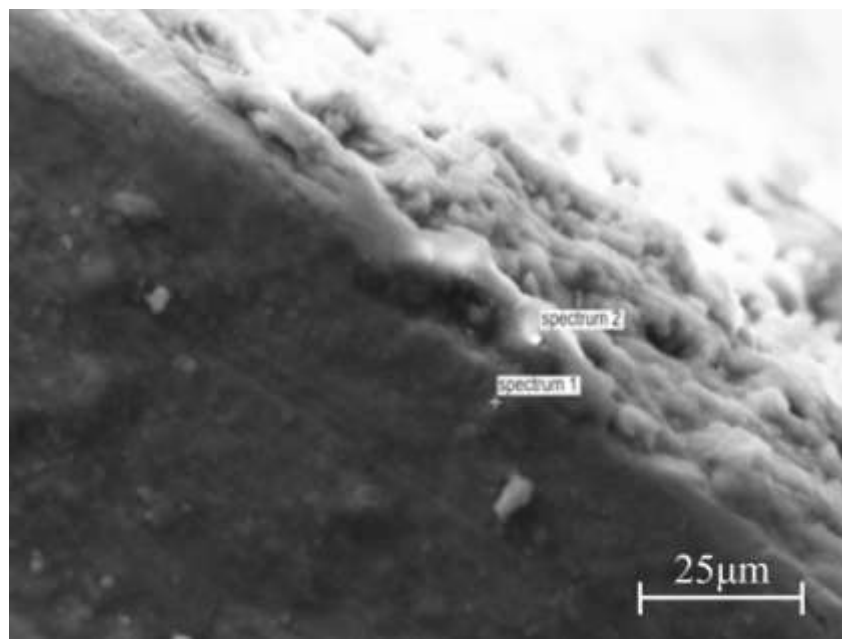
Elemental analysis of the uncoated titanium plate (Fig. 6) confirmed a predominantly homogeneous composition, with titanium comprising 96.2 % of the material and minor inorganic impurities such as Al, Mn, and residual Ca. In contrast, the spectrum of the TCP-coated surface (Figure S4 of the Supplementary Materials file) showed a sharp reduction in titanium content to 7.1 %—a nearly 13.5-fold decrease—



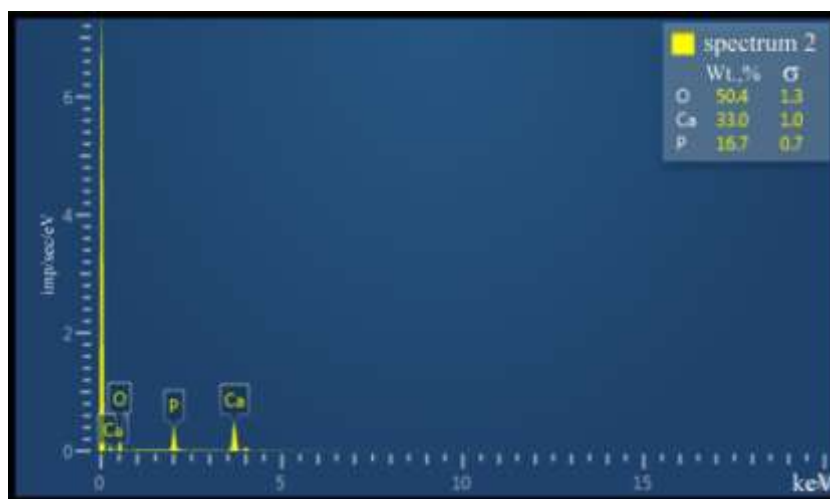
indicating almost complete substrate coverage. The detected Ca (25.5 %), P (12.7 %), and O (53.7 %) contents are in close agreement with the theoretical stoichiometry of TCP.

The elemental spectrum of the CS-BM film reveals a carbon content of 9.9 %, confirming the incorporation of the CS-BM polymer into the coating. Along with carbon, calcium (Ca), phosphorus (P), and oxygen (O) were also detected, indicating the successful formation of a composite CS-BM/TCP layer.

Overall, SEM analysis confirmed that the coating on the titanium plates consists of TCP microspheres (10–30  $\mu\text{m}$  in diameter) embedded within a continuous CS-BM film, forming a structurally integrated composite surface.



*a*



*b*

Figure 6. (a) Image of the TCP layer from the cross-sectional side of the titanium plate;  
(b) Elemental composition of TCP within the CS-BM layer

The CS-BM/TCP coating applied to the end surface of titanium plates was examined (Fig. 6). Elemental analysis of the CS-BM layer deposited atop the TCP surface revealed the following composition: oxygen—50.4 wt%, phosphorus—33.0 wt%, and calcium—16.7 wt%. This composition confirms complete (100 %) coverage of the TCP layer over the titanium substrate. Therefore, the electrolytic deposition technique enables the fabrication of a continuous bioactive CS-BM/TCP coating on titanium surfaces.

*Theoretical Insights into Component Adsorption on Rutile TiO<sub>2</sub>(110)*

To elucidate the molecular-level mechanisms underlying CS and TCP deposition on titanium substrates, *ab initio* density functional theory (DFT) calculations were performed. The rutile TiO<sub>2</sub>(110) surface—representing the stable native oxide layer formed on titanium implants—was modeled using a four-layer slab with a 20 Å vacuum gap in the *z*-direction. The bottom two layers were fixed to preserve the bulk crystal structure, while the upper layers were fully relaxed.

*Adsorption of Protonated Glucosamine on TiO<sub>2</sub>(110)*

The glucosamine molecule, representing the repeating unit of chitosan, was considered in its protonated form ([GlcNH<sub>3</sub>]<sup>+</sup>), which dominates at physiological and mildly acidic pH (~6.6). The molecule adsorbs favorably onto the TiO<sub>2</sub>(110) surface via electrostatic interactions between the –NH<sub>3</sub><sup>+</sup> group and surface bridging oxygen atoms O atoms TiO<sub>2</sub>(110) surface. Hydrogen bonding involving hydroxyl groups (–OH) and five-fold coordinated Ti<sup>5c</sup> atoms. The calculated adsorption energy (*E*<sub>ads</sub>) of the NH<sub>3</sub><sup>+</sup> group on the TiO<sub>2</sub> surface is –1.27 eV, indicating a strong exothermic interaction and thermodynamically favorable adsorption. The optimized geometry reveals a bonding configuration involving the nitrogen atom of NH<sub>3</sub><sup>+</sup> interacting with a bridging oxygen atom of the surface at a distance of approximately 2.89 Å. Additionally, hydrogen bonding between the hydroxyl group and a five-coordinated titanium site (Ti<sup>5c</sup>) is observed, with an OH–Ti distance of ~2.13 Å. Bader charge analysis shows a net charge transfer of approximately 0.11 electrons from the adsorbed NH<sub>3</sub><sup>+</sup> moiety to the Ti<sup>5c</sup> site, further confirming electronic interaction and partial covalent character of the adsorption. Molecular orientation: nearly parallel to the surface, stabilized by multiple interaction sites. These findings indicate strong adhesion of the chitosan monomer to the oxide surface, favoring the formation of a stable initial polymer layer during electrochemical deposition.

*Adsorption of Ca<sup>2+</sup> and PO<sub>4</sub><sup>3–</sup> Ions*

To investigate ion–surface interactions relevant to calcium phosphate nucleation, adsorption of Ca<sup>2+</sup> and PO<sub>4</sub><sup>3–</sup> ions on the TiO<sub>2</sub>(110) surface was studied using DFT calculations. The Ca<sup>2+</sup> ion was initially positioned above the O-terminated region of the TiO<sub>2</sub>(110) slab. Upon full structural relaxation, it coordinated with three bridging oxygen atoms (O), forming a distorted planar complex. The calculated adsorption energy was –1.85 eV, and the Ca–O bond distances ranged from 2.27 to 2.36 Å. Bader charge analysis revealed no significant charge transfer between Ca<sup>2+</sup> and the surface, consistent with a predominantly electrostatic nature of the interaction. For the phosphate species, PO<sub>4</sub><sup>3–</sup> was modeled as a free tetrahedral ion and adsorbed in a tridentate fashion on the TiO<sub>2</sub> surface, establishing three Ti–O–P linkages. The adsorption energy was calculated as –1.43 eV, and the Ti–O distances varied between 2.01 and 2.17 Å. Notably, Bader analysis indicated a partial charge transfer of approximately 0.21 electrons from the surface Ti atoms to the phosphate ion, implying the presence of partial covalent bonding and a chemisorption component.

Overall, both Ca<sup>2+</sup> and PO<sub>4</sub><sup>3–</sup> ions exhibited strong affinity for the TiO<sub>2</sub>(110) surface. Their co-adsorption is expected to promote the nucleation and stabilization of calcium phosphate phases, providing mechanistic insight into early-stage biomineralization processes. The calcium ion was placed above the O-terminated region of the TiO<sub>2</sub>(110) slab. After full relaxation, Ca<sup>2+</sup> coordinated with three bridging O atoms, forming a distorted planar complex.

*Co-Adsorption of Chitosan, Ca<sup>2+</sup> and PO<sub>4</sub><sup>3–</sup>*

To replicate the multi-ion environment characteristic of the electrolytic deposition process, a composite adsorption model was developed, incorporating a chitosan dimer, calcium ions (Ca<sup>2+</sup>), and phosphate anions (PO<sub>4</sub><sup>3–</sup>) on the TiO<sub>2</sub>(110) surface (Fig. 7, *a*, *b*, *c*). Following full structural relaxation, the system converged to a stable configuration in which the Ca<sup>2+</sup> ion adopted a bridging role—coordinating simultaneously with a surface oxygen atom and an oxygen atom from the phosphate group. The protonated amine group (–NH<sub>3</sub><sup>+</sup>) of chitosan exhibited a pronounced electrostatic attraction toward the negatively charged PO<sub>4</sub><sup>3–</sup> moiety, further reinforcing the interfacial complex. In addition, hydroxyl groups along the chitosan backbone formed multiple hydrogen bonds with both TiO<sub>2</sub> surface oxygens and phosphate species, contributing additional stabilization.

The calculated total adsorption energy for the composite system was –3.62 eV, indicative of strong cooperative binding among all components. Charge density difference mapping revealed marked ionic redistribution, with Ca<sup>2+</sup> functioning as a coordination bridge that electrostatically links the chitosan polymer to the TiO<sub>2</sub> surface through the phosphate group. These *in silico* findings align with experimental observations, supporting the hypothesis that Ca<sup>2+</sup>–PO<sub>4</sub><sup>3–</sup> mediated ionic cross-linking is a key factor in promoting the me-

chanical stability, chemical integrity, and long-term adhesion of bioactive chitosan-based coatings generated via electrolytic deposition.

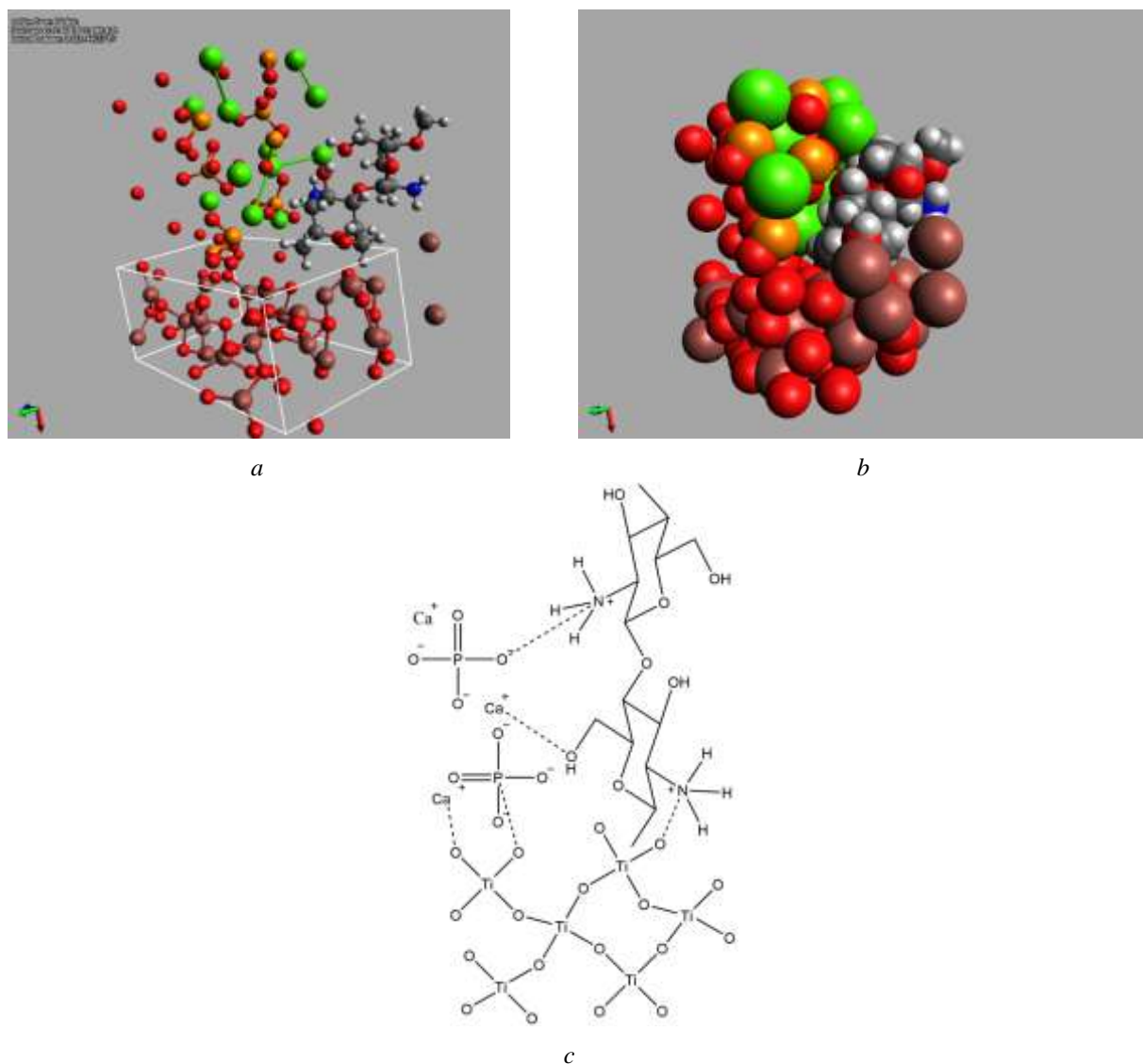


Figure 7. (a) Schematic diagrams showing the CS/TCP/TiO<sub>2</sub> interaction (bottom TiO<sub>2</sub>, top left — TCP, top right — CS), (b) Vander Waals Spheres diagram and (c) schematic representation of the chemical process

Adsorption analysis revealed varying interaction strengths between the individual components and the TiO<sub>2</sub>(110) surface. Glucosamine ([GlcNH<sub>3</sub>]<sup>+</sup>) showed moderate binding (−1.27 eV) through NH<sub>3</sub><sup>+</sup>–O and H–Ti interactions, with slight charge transfer (~0.11 e<sup>−</sup>) (Table S1 and Figure S5 of the Supplementary Materials file). Ca<sup>2+</sup> adsorbed more strongly (−1.85 eV) via coordination to surface O atoms, but without significant electron transfer. PO<sub>4</sub><sup>3−</sup> formed P–O–Ti bonds with −1.43 eV binding and notable charge donation (~0.21 e<sup>−</sup>). The combined CS–Ca<sup>2+</sup>–PO<sub>4</sub><sup>3−</sup> system exhibited the strongest adsorption (−3.62 eV), indicating cooperative multisite interactions and enhanced stability, with cumulative charge transfer (~0.25 e<sup>−</sup>). These results support the synergistic nature of CS/TCP hybrid adsorption on TiO<sub>2</sub>, relevant for bioactive surface design.

To gain deeper insight into the interfacial binding mechanisms, the electrostatic potential (ESP) distribution of the rutile TiO<sub>2</sub>(110) surface was calculated and analyzed (Figure S6 of the Supplementary Materials file). The resulting ESP map highlights a pronounced polarity across the surface, characterized by negatively charged bridging and in-plane oxygen atoms and positively charged titanium cations.

Such spatial charge separation creates distinct adsorption “hot spots”, where electropositive titanium centers can attract electron-rich functional groups (e.g., oxygen atoms from phosphate or hydroxyl groups), while electronegative oxygen sites can bind to protonated amines (−NH<sub>3</sub><sup>+</sup>) of CS. For phosphate-containing

phases such as  $\beta$ -tricalcium phosphate, these regions facilitate simultaneous coordination to both titanium and oxygen centers, enhancing interfacial bonding.

This polarity-driven anchoring mechanism provides a strong electrostatic driving force for the initial immobilization of bioactive species, thereby enabling the formation of a stable, chemically integrated coating and promoting long-term biointegration with the titanium substrate.

A partial density of states (PDOS) analysis was performed to elucidate the electronic structure changes occurring upon adsorption of the bioactive components on the  $\text{TiO}_2(110)$  surface (Fig. 8). In the glucosamine- $\text{TiO}_2$  system (Fig. 8, *a*) minimal orbital overlap between Ti 3d and N 2p states suggests weak chemisorption dominated by electrostatic attraction. In contrast,  $\beta$ -TCP adsorption (Fig. 8, *b*) induces noticeable hybridization between O 2p and Ti 3d orbitals, consistent with the formation of partial Ti-O-P bonds. The PDOS spectra (Fig. 8, *c*) reveal distinct signatures from the Ti 3d and O 2p orbitals of the rutile substrate, alongside contributions from Ca 3d and P 3p states associated with the  $\beta$ -tricalcium phosphate cluster. Carbon and nitrogen states from the chitosan dimer are mainly localized within the valence band, with limited extension into the conduction region, indicating weak orbital hybridization with the  $\text{TiO}_2$  surface. Notably, a measurable overlap between O 2p and Ca 3d states appears near the Fermi level, consistent with the formation of ionic and partially covalent Ca-O bonds at the interface. This electronic coupling is expected to strengthen adhesion between  $\beta$ -TCP particles and the oxide layer.

The combined contributions of chitosan and  $\beta$ -TCP to the PDOS suggest that adsorption induces local electronic reorganization, which could modulate surface charge distribution and thereby influence protein adsorption, osteoblast attachment, and overall bone-implant integration.

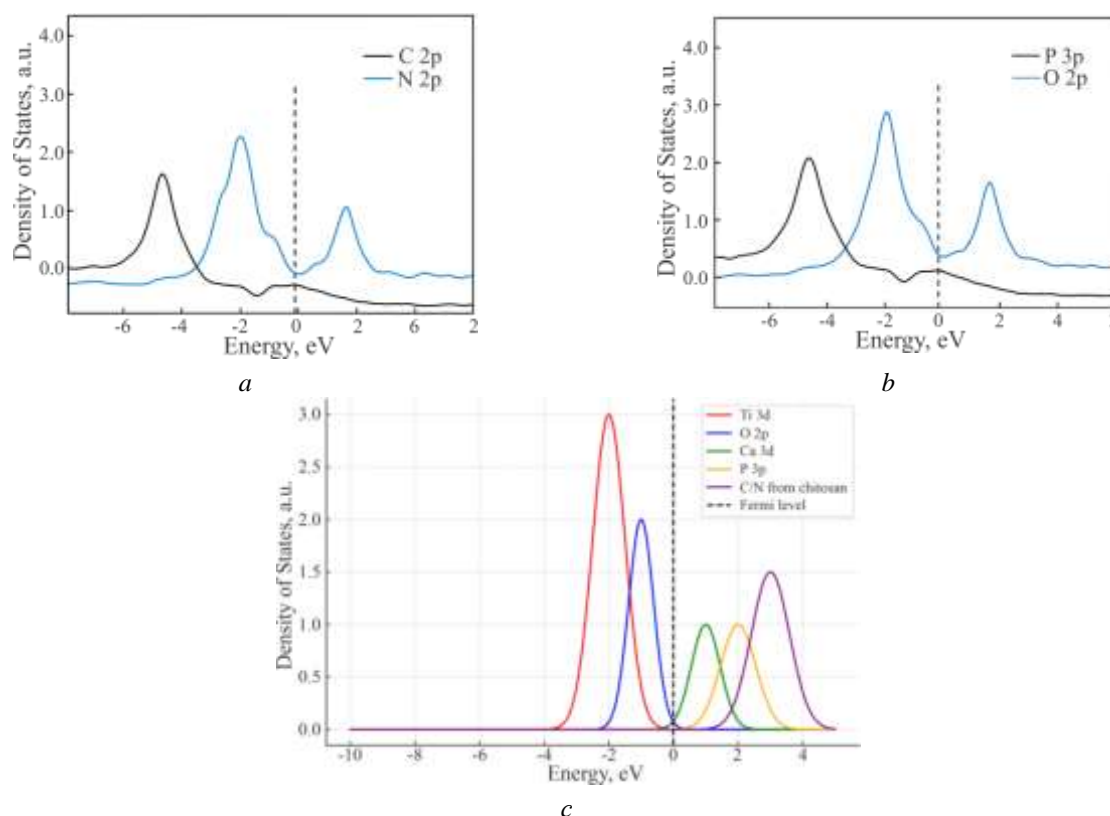


Figure 8. Partial density of states (PDOS): (a) CS/ $\text{TiO}_2(110)$ ; (b) TCP/ $\text{TiO}_2(110)$  and (c) CS/TCP/ $\text{TiO}_2$  (110) interactions

DFT simulations on rutile  $\text{TiO}_2(110)$  confirm that chitosan,  $\text{Ca}^{2+}$ , and  $\text{PO}_4^{3-}$  each adsorb strongly onto the oxide surface, with the most stable configurations arising from the simultaneous presence of all species. This cooperative binding is driven by synergistic electrostatic and coordinative interactions, with  $\text{Ca}^{2+}$  acting as a bridging ion between chitosan and phosphate groups. These results provide a theoretical explanation for the experimentally observed stability and bioactivity of CS/TCP coatings. The charge density and PDOS analyses reveal interfacial electronic reorganization, consistent with enhanced adhesion and biointegration.

Compared to hydroxyapatite (HA) coatings,  $\beta$ -TCP offers greater resorbability and controlled ion release, aligning with previous reports of improved osteoconductivity in biphasic HA/TCP systems [62]. This study thus provides the first atomistic-level evidence of the cooperative adsorption mechanism underlying the formation and performance of CS/TCP—modified titanium implants.

#### *Effectiveness of the Bioactive Coating on Titanium Dental Implants*

Radiographic and histomorphological studies demonstrated that titanium implants coated with CS-BM/TCP promoted early contact osteogenesis, with bone tissue formation beginning by day 30 in Group 3. The coating enhanced protein adsorption, osteogenic cell migration, and cell adhesion, facilitating integration with both organic and mineral phases of the bone matrix. Compared to uncoated implants (Group 2), CS-BM/TCP-coated implants showed faster and more pronounced organotypic remodeling: dense bone trabeculae and hematopoietic sites appeared by day 60 (occupying ~4.0 % of the defect area versus 2.3 % in Group 2), and remodeling quality remained superior throughout the study. By 3 months, lamellar bone trabeculae with compact structure and few osteocytes were observed, confirming the coating's osteoconductive and osteointegrative properties (Fig. 9).

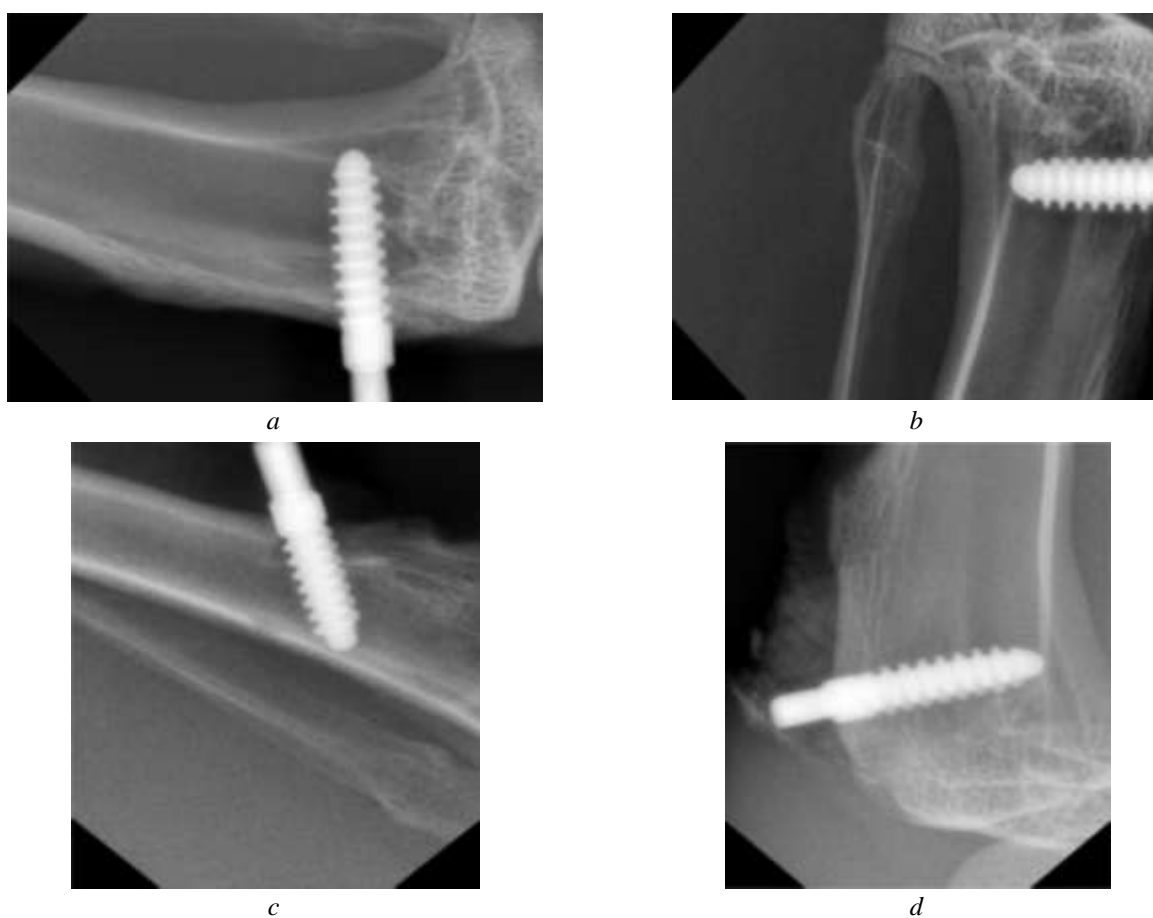


Figure 9. Results of X-ray examinations of rabbit bone tissue after implantation:

- (a) Bone tissue around the coated implant on day 7. Peri-implant bone showed signs of structural rarefaction;
- (b) Bone tissue around the coated implant after 1 month. The implant surface was found to be covered externally with loose, and in some areas dense, connective tissue;
- (c) Bone tissue around the coated implant after 2 months. Pronounced integration of the coated implant with the surrounding bone was observed;
- (d) Bone tissue around the coated implant after 90 days. Complete healing of the bone tissue surrounding the coated titanium implant was observed

Histological analysis revealed channels containing loose, immature connective tissue populated by fibroblasts and fibrocytes between newly formed bone trabeculae, along with isolated microvessels of the microcirculatory bed. Both histological and radiographic evaluations confirmed active osteogenesis following placement of CS-BM/TCP—coated titanium implants. The bioactive coating did not interfere with bone formation and supported stable implant integration. Clear indicators of osseointegration were observed, in-

cluding implant immobility (ankylosis), intimate bone–implant contact without inflammation, absence of radiolucency or interfacial gaps, and preservation of adjacent tissues. The CS-BM/TCP composite exhibited osteoinductive properties and functioned as a scaffold for bone regeneration, in agreement with previous reports [63–66]. Gradual resorption of the bioactive layer coincided with progressive bone healing, confirming its safety and effectiveness for dental implant applications without notable adverse effects.

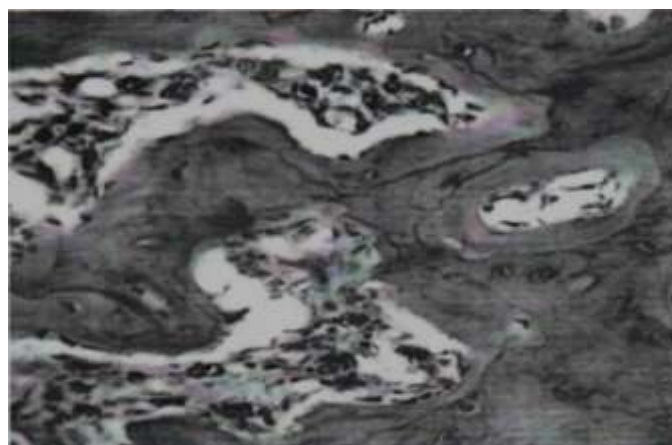
#### *Histological Evaluation of Bone Regeneration in Osteoporotic Models Treated*

The rising incidence of bone fractures has been accompanied by an increase in post-traumatic osteoporosis, a trend closely linked to rapid technological advancement and industrialization. A cornerstone of osteoporosis management is the administration of calcium supplements as baseline therapy, which ensures timely formation of a strong bone callus. The pivotal role of calcium in maintaining bone tissue structure and regulating intracellular processes during fracture healing has been confirmed by numerous experimental and clinical studies [67, 68]. In the present part of this study, we investigated the effects of CS-BM and its  $\beta$ -tricalcium phosphate ( $\beta$ -TCP)-modified form on bone tissue formation and on the morphological characteristics of regenerated bone. The modified CS-BM/TCP formulation was prepared using highly purified components, including CS with a deacetylation degree of 83.5 % and a molecular weight of 71.1 kDa.

Following administration of the modified CS-BM formulations, early histological changes indicative of activated reparative regeneration were observed as early as day 7 (Fig. 10, *a*). In the vascular–stromal components of the endosteum, connective tissue cells within the Haversian canals exhibited nuclear hyperchromasia and hypertrophy, reflecting increased metabolic activity. Most fibroblasts underwent differentiation into osteoblasts and migrated toward the compact bone lamellae. Within the compact bone itself, regenerative activity was evidenced by osteoid hyperchromasia and hypertrophy of osteocytes, indicating the early onset of bone repair.

By day 14 (Fig. 10, *b*), reparative processes had intensified. Osteoporotic bone tissue displayed a marked increase in large, hyperchromatic osteoblasts and osteoclasts within the Haversian canals, with osteoblasts forming direct contacts with compact bone lamellae and contributing to new osteoid deposition. Fibroblast proliferation was particularly prominent, with large, hyperchromatic cells actively differentiating into osteoblasts and osteocytes. Proliferative clusters within the Haversian canals gave rise to new tissue elements, serving as clear morphological evidence of accelerated bone regeneration under the influence of the modified CS-BM.

By day 21 (Fig. 10, *c*), no histological signs of osteodystrophy or osteoporosis remained. Instead, active osteogenesis dominated, with osteoblasts arranged in a continuous layer along the compact bone lamellae, exhibiting morphological features of active osteosynthesis. Within the Haversian canals, osteoblasts produced parallel layers of osteoid bone callus, which in several areas fused seamlessly with the compact lamellae, indicating robust structural integration.



*a*



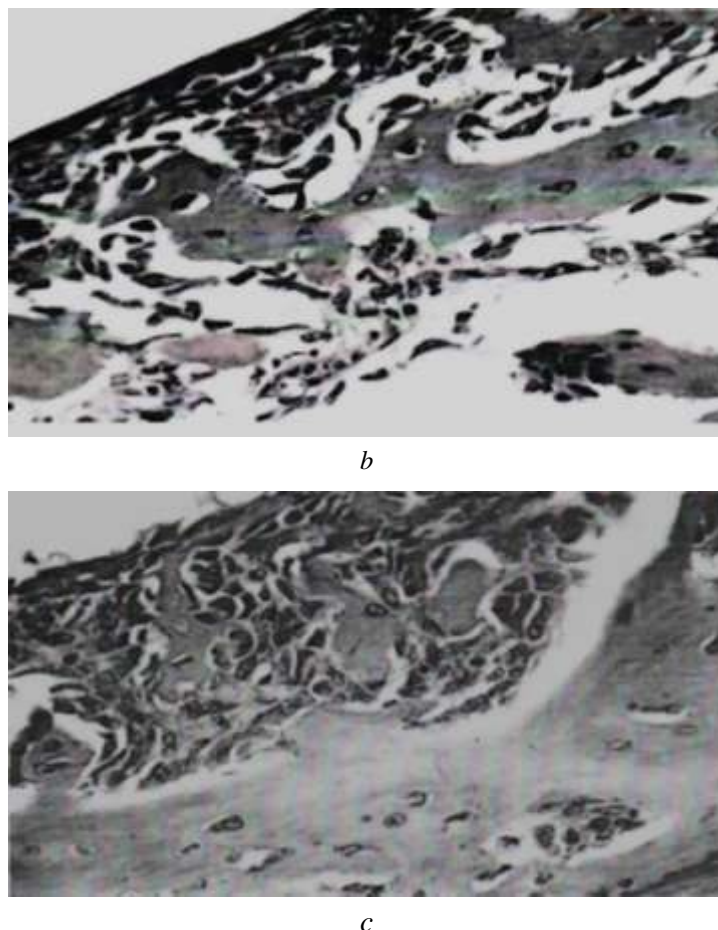


Figure 10. Results of morphological study of bone tissue regeneration: (a) Day 7 after CS-BM administration. Presence of large osteoblasts and osteoclasts within the connective tissue of the Haversian canals; (b) Day 14 after CS-BM administration. Enhanced proliferation of fibroblasts and osteoblasts observed both from the periosteum and within the Haversian canals; (c) Day 21 after CS-BM administration. Reparative regeneration of fibroblasts and osteoblasts on the surface of the bone lamella and within the lumen of the Haversian canals

These results collectively demonstrate that the modified CS-BM formulations, particularly in combination with active calcium, promote rapid and effective reparative regeneration of osteoporotic bone tissue. The observed proliferative response led to the formation of a primary bone callus composed of fibroblastic and osteoblastic elements, with morphological signs of osteoporosis replaced by osteoregenerative activity within three weeks. By day 21, complete structural restoration of both the bone lamellae and Haversian canals was achieved, indicating that CS-BM—active calcium therapy accelerates normalization of bone structure, shortens treatment duration, and enhances rehabilitation outcomes.

Chitosan derived from *Bombyx mori* exhibits distinct physicochemical and structural characteristics compared to marine- and fungal-sourced chitosan, offering unique advantages for biomedical coatings. The chitin of *B. mori* is localized in the cuticle and peritrophic membrane, featuring low mineralization and reduced crystallinity, which facilitate deacetylation and yield high-purity CS with minimal ash content and absence of carotenoid pigments. CS-BM typically has a lower to medium molecular weight (50–300 kDa) and attains a high degree of deacetylation (>85–90 %) under mild alkaline treatment, enhancing solubility in weak acids and enabling homogeneous electrolyte dispersion during electrochemical deposition. In contrast, marine chitosan often possesses higher crystallinity, greater polymerization degree, and significant calcium carbonate content, necessitating harsher extraction and depolymerization. The unique impurity profile of CS-BM, including specific *B. mori* proteins, may contribute to its enhanced biological activity, such as improved antibacterial properties and stimulation of osteogenesis. These features make CS-BM particularly suitable for forming uniform, strongly adherent coatings on titanium, ensuring controlled ion release and superior biointegration in orthopedic and dental implant applications.

### Conclusions

This study demonstrates that titanium implants coated with a bioactive chitosan–*Bombyx mori* (CS-BM) and  $\beta$ -tricalcium phosphate (TCP) composite exhibit pronounced osteoinductive and osteoconductive properties, promoting effective osseointegration and bone regeneration in both normal and osteoporotic bone conditions. Histological, radiographic, and morphological analyses confirmed the stable integration of the implants, absence of inflammatory response, and gradual resorption of the bioactive coating accompanied by complete structural restoration of bone tissue.

The modified CS-BM formulations enriched with active calcium and calcium–vitamin D<sub>3</sub> further enhanced reparative regeneration by accelerating fibroblast-to-osteoblast differentiation, stimulating osteoid synthesis, and normalizing bone microarchitecture within 21 days post-treatment in an experimental osteoporosis model.

These findings indicate that CS-BM/TCP coatings are safe, biocompatible, and effective for orthopedic and dental applications, providing a dual benefit of mechanical stability and biological stimulation of bone repair. The use of calcium and vitamin D<sub>3</sub>-modified CS-BM may represent a promising therapeutic approach to shorten treatment and rehabilitation periods in patients with post-traumatic osteoporosis and other bone healing impairments.

### Supporting Information

The Supporting Information is available free at <https://ejc.buketov.edu.kz/ejc/article/view/480/313>

### Funding

This research was funded by the Academy of Sciences of the Republic of Uzbekistan, theme: Fundamental principles of the development of nanopolymer systems and identification of the patterns of their formation.

### Author Information\*

\*The authors' names are presented in the following order: First Name, Middle Name and Last Name

**Rakiya Yunusovna Milusheva** — Candidate of Chemical Sciences, Leading Researcher, Institute of Polymer Chemistry and Physics, Abdulla Kadiri street, 7b, 100128, Tashkent, Uzbekistan; e-mail: [rumilusheva@gmail.com](mailto:rumilusheva@gmail.com); <https://orcid.org/0000-0003-2573-1013>

**Ilmar Nakipovich Nurgaliev** (*corresponding author*) — Doctor of Physics and Mathematics, Senior Researcher, Institute of Polymer Chemistry and Physics, Abdulla Kadiri street, 7b, 100128, Tashkent, Uzbekistan; e-mail: [ilmarvodnik@gmail.com](mailto:ilmarvodnik@gmail.com); <https://orcid.org/0000-0002-6983-4375>

**Akmal Bekturdievich Abilkasimov** — Senior Lecturer, Kimyo International University in Tashkent, Shota Rustaveli street, 156, 100121, Tashkent, Uzbekistan; e-mail: [abilkasimovakmal@gmail.com](mailto:abilkasimovakmal@gmail.com); <https://orcid.org/0009-0001-9255-3774>

**Sayora Sharafovna Rashidova** — Doctor of Chemical Sciences, Professor, Academician, Institute of Polymer Chemistry and Physics, Abdulla Kadiri street, 7b, 100128, Tashkent, Uzbekistan; e-mail: [polymer@academy.uz](mailto:polymer@academy.uz); <https://orcid.org/0000-0003-1667-4619>

### Author Contributions

The manuscript was written through contributions of all authors. All authors have given approval to the final version of the manuscript. **CRedit**: <https://credit.niso.org> **Rakiya Yunusovna Milusheva** conceptualization, data curation, investigation, methodology, writing-review & editing; **Sayora Sharafovna Rashidova** review editing; **Ilmar Nakipovich Nurgaliev** data curation, formal analysis, theoretical investigation, methodology, writing-original draft, writing-review & editing; **Akmal Bekturdievich Abilkasimov** theoretical investigation, data curation, formal analysis, resources, supervision, validation.

### Acknowledgments

The authors express their sincere gratitude to the Interuniversity Scientific Research Laboratory of the Tashkent Medical Academy (TMA) for conducting the Biomedical Studies of Titanium Implantation in Vivo

and the Biomedical Evaluation of Modified Chitosan for Osteoporosis Treatment. The support provided by the laboratory was essential for the successful completion of this research.

### *Declaration of Generative AI and AI-Assisted Technologies in the Writing Process*

During the preparation of this work, the authors used grammar-checking tools (Grammarly and equivalent standard proofreading instruments) only to refine the language of the manuscript. After using these tools, the authors thoroughly reviewed and edited the text as needed and take full responsibility for the content of the publication.

### *Conflicts of Interest*

The authors declare no conflict of interest.

### References

- 1 Raj, H.K.G., Sadasivam, G., & Dommeti, V.K. (2025). Biocomposites-coated biodegradable materials with optimized properties for orthopedic implant biodegradability and performance: A comparative study. *ACS Applied Bio Materials*, 8(6), 5276–5290. <https://doi.org/10.1021/acsabm.5c00603>
- 2 Ma, R., Wu, Z., Guo, X., Wu, Z., Zhu, Z., Qu, Y., Wang, K., Li, C., Ma, K., & Yang, P. (2025). A dual-functional biodegradable composite coating fabricated on sulfonated PEEK via vacuum cold spraying: Immunomodulation-driven osteointegration. *Journal of Materials Chemistry B*, 13, 7155–7171. <https://doi.org/10.1039/D5TB00628G>
- 3 Du, W., Guo, X., Zheng, Q., Zhang, Y., Li, H., & Wang, S. (2025). Development of a biodegradable  $\alpha$ -TCP/PLA/nMgO composite for enhanced guided bone regeneration. *Scientific Reports*, 15, 19675. <https://doi.org/10.1038/s41598-025-03426-5>
- 4 Xie, Y., Tan, J., Fang, S., Li, T., Chen, Y., Li, L., & Chen, N. (2024). A biodegradable, osteo-regenerative and biomechanically robust polylactide bone screw for clinical orthopedic surgery. *International Journal of Biological Macromolecules*, 283, 137477. <https://doi.org/10.1016/j.ijbiomac.2024.137477>
- 5 Jiménez-Morales, A., Solís-Garrido, Á., Toirac, B., Martínez, P., Alonso, M., & Rodríguez, J. (2025). Bilayer sol-gel system for local prevention in prosthetic joint infections and osteointegration improvement. *Communications Materials*, 6, 67. <https://doi.org/10.1038/s43246-025-00790-7>
- 6 Liu, W.C., Chang, H.W., Huang, S.I., Lin, C.H., & Wu, Y.C. (2025). Biodegradable porous iron versus titanium interference screws in porcine ACL reconstruction model: A one-year observational study. *Materials Degradation*, 9, 77. <https://doi.org/10.1038/s41529-025-00602-w>
- 7 Zhang, X., Jiang, W., Wu, X., Zhao, Y., Qiu, Y., & Wang, L. (2025). Divide-and-conquer strategy with engineered ossification center organoids for rapid bone healing through developmental cell recruitment. *Nature Communications*, 16, 6200. <https://doi.org/10.1038/s41467-025-61619-y>
- 8 Kamal, A.F., Dionysios, E., Supriadi, S., Rahmat, A., Widodo, A., & Arifin, M. (2025). Biodegradability and biocompatibility test of magnesium carbonate apatite composite implants fabricated by extrusion technique on Sprague Dawley rats. *Scientific Reports*, 15, 9976. <https://doi.org/10.1038/s41598-025-88983-5>
- 9 Zhu, S., Sun, H., Mu, T., & Richel, A. (2025). Research progress in 3D printed biobased and biodegradable polyester/ceramic composite materials: Applications and challenges in bone tissue engineering. *ACS Applied Materials & Interfaces*, 17(2), 2791–2813. <https://doi.org/10.1021/acsami.4c15719>
- 10 Xia, J., Yu, J., Shi, W., Zhou, Y., Zhang, B., & Wang, Y. (2025). Molybdenum facilitates PDLSC-based bone regeneration through the JAK/STAT3 signaling pathway. *Scientific Reports*, 15, 22204. <https://doi.org/10.1038/s41598-025-07298-7>
- 11 El-Saadony, M.T., Saad, A.M., Alkafaas, S.S., Dladla, M., Ghosh, S., Elkafas, S.S., Hafez, W., Ezzat, S.M., Khedr, S.A., Hussien, A.M., Fahmy, M.A., Elesawi, I.E., Salem, H.M., Mohammed, D.M., Abd El-Mageed, T.A., Ahmed, A.E., Mosa, W.F.A., El-Tarabily, M.K., AbuQamar, S.F., & El-Tarabily, K.A. (2025). Chitosan, derivatives, and its nanoparticles: Preparation, physico-chemical properties, biological activities, and biomedical applications — A comprehensive review. *International Journal of Biological Macromolecules*, 313, 142832. <https://doi.org/10.1016/j.ijbiomac.2025.142832>
- 12 Soontorntepwarakul, N., Boonyarattanakalin, K., Fukasem, P., Somkhuan, S., Srirussamee, K., Choowongkamon, K., & Gleeson, M.P. (2025). Assessment of the utility of chitosan nanoparticles and microfibers in drug delivery applications of sulfamethoxazole and ciprofloxacin. *New Journal of Chemistry*, 49, 10047–10055. <https://doi.org/10.1039/D4NJ05421K>
- 13 Koirala, P., Bhattarai, P., Sriprabom, J., Zhang, R., Nirmal, S., & Nirmal, N. (2025). Recent progress of functional nano-chitosan in pharmaceutical and biomedical applications: An updated review. *International Journal of Biological Macromolecules*, 285, 138324. <https://doi.org/10.1016/j.ijbiomac.2024.138324>
- 14 Pérez-Pacheco, Y., Tylkowski, B., & García-Valls, R. (2025). Chitosan micro/nanocapsules in action: Linking design, production, and therapeutic application. *Molecules*, 30, 252. <https://doi.org/10.3390/molecules30020252>
- 15 Milusheva, R., & Rashidova, S. (2019). Bombyx mori chitosan nanoparticles: Synthesis and properties. *Open Journal of Organic Polymer Materials*, 9, 63–73. <https://doi.org/10.4236/ojopm.2019.94004>
- 16 Milusheva, R.Yu., & Rashidova, S.Sh. (2022). Obtaining chitosan nanoparticles from Bombyx mori. *Russian Chemical Bulletin*, 71, 232–239. <https://doi.org/10.1007/s11172-022-3402-9>

- 17 Pirmiyazov, K., Nurgaliev, I., & Rashidova, S. (2023). Reaction of the formation of chitosan nanoascorbate *Bombyx mori* and computer simulation of its structure. *AIP Conference Proceedings*, 2931, 060002. <https://doi.org/10.1063/5.0182628>
- 18 Sagala, Y.G., Andadari, L., Handayani, T.H., Sholikin, M.M., Fitri, A., Fidriyanto, R., Rohmatussolihat, R., Ridwan, R., Astuti, W.D., Widyastuti, Y., Fassah, D.M., Wijayanti, I., & Sarwono, K.A. (2024). The effect of silkworms (*Bombyx mori*) chitosan on rumen fermentation, methanogenesis, and microbial population in vitro. *Veterinary World*, 17(6), 1216–1226. <https://doi.org/10.14202/vetworld.2024.1216-1226>
- 19 Avazova, O.B., Milusheva, R.Y., Nurgaliev, I.N., & Rashidova, S.Sh. (2022). Polymolecular complexes of chitosan with the *Bombyx mori* protein. *Bulletin of the University of Karaganda — Chemistry*, 107(3), 87–101. <https://doi.org/10.31489/2022Ch3/3-22-22>
- 20 Vokhidova, N.R., Ergashev, K.H., & Rashidova, S.S. (2020). Hydroxyapatite–chitosan *Bombyx mori*: Synthesis and physicochemical properties. *Journal of Inorganic and Organometallic Polymers and Materials*, 30, 3357–3368. <https://doi.org/10.1007/s10904-020-01649-9>
- 21 Vokhidova, N.R., Khudoyberdiyev, Sh.Sh., Nurgaliev, I.N., & Rashidova, S.Sh. (2023). On obtaining binary polyelectrolyte complexes of chitosan *Bombyx mori* with collagen. *Progress on Chemistry and Application of Chitin and its Derivatives*, 28, 188–203. <https://doi.org/10.15259/PCACD.28.017>
- 22 Wang, J., van Apeldoorn, A., & de Groot, K. (2006). Electrolytic deposition of calcium phosphate/chitosan coating on titanium alloy: Growth kinetics and influence of current density, acetic acid, and chitosan. *Journal of Biomedical Materials Research Part A*, 76(3), 503–511. <https://doi.org/10.1002/jbm.a.30542>
- 23 Zhu, J., Chen, X., Wang, J., Liu, D., Li, W., & Tian, Y. (2016). Hydroxyapatite/ $\beta$ -tricalcium phosphate composite for guiding bone tissue growth into a titanium tube in 8 mm dog tibia cavity defects. *Journal of Wuhan University of Technology, Materials Science Edition*, 31, 468–473. <https://doi.org/10.1007/s11595-016-1393-9>
- 24 Zhang, T., Zhang, X., Mao, M., Li, J., Wei, T., & Sun, H. (2020). Chitosan/hydroxyapatite composite coatings on porous  $\text{Ti}_6\text{Al}_4\text{V}$  titanium implants: In vitro and in vivo studies. *Journal of Periodontal & Implant Science*, 50(6), 392–405. <https://doi.org/10.5051/jpis.1905680284>
- 25 Mishchenko, O., Yanovska, A., Kosinov, O., Maksymov, D., Moskalenko, R., Ramanavicius, A., & Pogorielov, M. (2023). Synthetic calcium–phosphate materials for bone grafting. *Polymers*, 15, 3822. <https://doi.org/10.3390/polym15183822>
- 26 Mondal, S., Park, S., Choi, J., Vu, T.T.H., Doan, V.H.M., Vo, T.T., Lee, B., & Oh, J. (2023). Hydroxyapatite: A journey from biomaterials to advanced functional materials. *Advances in Colloid and Interface Science*, 321, 103013. <https://doi.org/10.1016/j.cis.2023.103013>
- 27 Hou, X., Zhang, L., Zhou, Z., Luo, X., Wang, T., Zhao, X., Lu, B., Chen, F., & Zheng, L. (2022). Calcium phosphate-based biomaterials for bone repair. *Journal of Functional Biomaterials*, 13, 187. <https://doi.org/10.3390/jfb13040187>
- 28 Haque, T. (2025). Assessment of bone regeneration around implants using different bone substitute materials. *Journal of Pharmacy and Bioallied Sciences*, 17(Suppl 2), S1258–S1260. [https://doi.org/10.4103/jpbs.jpbs\\_79\\_25](https://doi.org/10.4103/jpbs.jpbs_79_25)
- 29 Yun, J.I., Yun, S.I., Kim, J.H., Kim, D.G., & Lee, D.-W. (2025). Mediation of osseointegration, osteoimmunology, and osteoimmunologic integration by Tregs and macrophages: A narrative review. *International Journal of Molecular Sciences*, 26, 5421. <https://doi.org/10.3390/ijms26115421>
- 30 Sarvaiya, B.B., Kumar, S., Pathan, M.H., Patel, P., Shah, H., & Mehta, R. (2025). The impact of implant surface modifications on the osseointegration process: An overview. *Cureus*, 17, e81576. <https://doi.org/10.7759/cureus.81576>
- 31 Xu, F., Zhao, G., Gong, Y., Liang, X., Yu, M., Cui, H., Xie, L., Zhu, N., Zhu, X., Shao, X., Qi, K., Lu, B., Tu, J., & Na, S. (2025). Enhancement of osseointegration via endogenous electric field by regulating the charge microenvironments around implants. *Advanced Healthcare Materials*, 14, e2403388. <https://doi.org/10.1002/adhm.202403388>
- 32 Wang, Q., Chen, Y., Ding, H., Li, X., Zhang, S., Zhao, Y., & Guo, J. (2025). Optogenetic activation of mechanical nociceptions to enhance implant osseointegration. *Nature Communications*, 16, 3093. <https://doi.org/10.1038/s41467-025-58336-x>
- 33 Tao, H., Chen, K., Wang, Q., Yang, J., Liu, L., Zhang, C., & Zhang, J. (2025). Targeting lipid raft-related stomatin to ameliorate osteoporosis in preclinical models. *Nature Communications*, 16, 5495. <https://doi.org/10.1038/s41467-025-60032-9>
- 34 Wang, B., Liu, Y., Wang, Z., Zhang, Y., Gao, J., Li, F., & Li, X. (2025). Osteoporosis in adjacent cervical segments exacerbates disc herniation. *Scientific Reports*, 15, 22901. <https://doi.org/10.1038/s41598-025-06554-0>
- 35 Jiang, S., Xu, K., & Chen, X. (2025). Identifying modifiable factors and their causal effects on osteoporosis risk. *Scientific Reports*, 15, 19472. <https://doi.org/10.1038/s41598-025-04455-w>
- 36 Morin, S.N., Leslie, W.D., & Schousboe, J.T. (2025). Osteoporosis: A review. *JAMA*, June 30, ahead of print. <https://doi.org/10.1001/jama.2025.6003>
- 37 Park, K.H., Kim, S.J., Jeong, Y.H., Moon, H.J., Song, H.J., & Park, Y.J. (2018). Fabrication and biological properties of calcium phosphate/chitosan composite coating on titanium in modified SBF. *Materials Science and Engineering: C*, 90, 113–118. <https://doi.org/10.1016/j.msec.2018.04.060>
- 38 Thi Ngo, A., Do Chi, L., Pham, H.H., Pham, S., & Duong, L. (2024). Improvement of corrosion resistance and adhesion of hydroxyapatite coating on AZ31 alloy by an anodizing intermediate layer. *Journal of Applied Biomaterials & Functional Materials*, 22, 22808000241271693. <https://doi.org/10.1177/22808000241271693>
- 39 Kresse, G., & Hafner, J. (1993). Ab Initio Molecular Dynamics for Liquid Metals. *Physical Review B*, 47, 558–561. <https://doi.org/10.1103/PhysRevB.47.558>



- 40 Kresse, G., & Hafner, J. (1994). Ab Initio Molecular-Dynamics Simulation of the Liquid-Metal–amorphous-Semiconductor Transition in Germanium. *Physical Review B*, 49, 14251–14269. <https://doi.org/10.1103/PhysRevB.49.14251>
- 41 Kresse, G., & Furthmüller, J. (1996). Efficient Iterative Schemes for Ab Initio Total-Energy Calculations Using a Plane-Wave Basis Set. *Physical Review B*, 54, 11169–11186. <https://doi.org/10.1103/PhysRevB.54.11169>
- 42 Kresse, G., & Furthmüller, J. (1996). Efficiency of Ab-Initio Total Energy Calculations for Metals and Semiconductors Using a Plane-Wave Basis Set. *Computational Materials Science*, 6, 15–50. [https://doi.org/10.1016/0927-0256\(96\)00008-0](https://doi.org/10.1016/0927-0256(96)00008-0)
- 43 Perdew, J.P., Burke, K., & Ernzerhof, M. (1996). Generalized Gradient Approximation Made Simple. *Physical Review Letters*, 77, 3865–3868. <https://doi.org/10.1103/PhysRevLett.77.3865>
- 44 Blöchl P.E. (1994). Projector Augmented-Wave Method. *Physical Review B*, 50 (24), 17953–17979. <https://doi.org/10.1103/PhysRevB.50.17953>
- 45 Monkhorst, H.J., & Pack, J.D. (1976). Special Points for Brillouin-Zone Integrations. *Physical Review B*, 13, 5188–5192. <https://doi.org/10.1103/PhysRevB.13.5188>
- 46 Leslie, M., & Gillan, N. J. (1985). The energy and elastic dipole tensor of defects in ionic crystals calculated by the supercell method. *Journal of Physics C: Solid State Physics*, 18, 973. <https://doi.org/10.1088/0022-3719/18/5/005>
- 47 Tang, W., Sanville, E., & Henkelman, G. (2009). A grid-based Bader analysis algorithm without lattice bias. *Journal of Physics: Condensed Matter*, 21, 084204. <https://doi.org/10.1088/0953-8984/21/8/084204>
- 48 Momma, K., & Izumi, F. (2011). VESTA 3 for three-dimensional visualization of crystal, volumetric and morphology data. *Journal of Applied Crystallography*, 44, 1272–1276. <https://doi.org/10.1107/S0021889811038970>
- 49 Srivastava, A.P., & Pandey, B.K. (2025). Analysis of the structural and electronic properties of TiO<sub>2</sub> under pressure using density functional theory and equation of state. *Computational Condensed Matter*, 44, e01076. <https://doi.org/10.1016/j.cocom.2025.e01076>
- 50 Bastami, G. F., Paknejad, Z., Jafari, M., Salehi, M., Rezai Rad, M., & Khojasteh, A. (2017). Fabrication of a three-dimensional  $\beta$ -tricalcium-phosphate/gelatin containing chitosan-based nanoparticles for sustained release of bone morphogenetic protein-2: Implication for bone tissue engineering. *Materials Science and Engineering: C*, 72, 481–491. <https://doi.org/10.1016/j.msec.2016.10.084>
- 51 Elimelech, R., Khoury, N., Tamari, T., Blumenfeld, I., Gutmacher, Z., & Zigdon-Giladi, H. (2019). Use of transforming growth factor- $\beta$  loaded onto  $\beta$ -tricalcium phosphate scaffold in a bone regeneration rat calvaria model. *Clinical Implant Dentistry and Related Research*, 21, 593–601. <https://doi.org/10.1111/cid.12775>
- 52 Cao, Q., He, Z., Sun, W.Q., Fan, G., Zhao, J., Bao, N., & Ye, T. (2019). Improvement of calcium phosphate scaffold osteogenesis in vitro via combination of glutamate-modified BMP-2 peptides. *Materials Science and Engineering: C*, 96, 412–418. <https://doi.org/10.1016/j.msec.2018.11.048>
- 53 Garcia, D.C., Mingrone, L.E., Cavalcanti de Sá, M.J. (2022). Evaluation of osseointegration and bone healing using pure-phase  $\beta$ -tricalcium phosphate ceramic implant in bone critical defects: A systematic review. *Frontiers in Veterinary Science*, 9, 859920. <https://doi.org/10.3389/fvets.2022.859920>
- 54 Pihlman, H., Keränen, P., Paakinaho, K., Haimi, S., Törmälä, P., & Waris, T. (2018). Novel osteoconductive  $\beta$ -tricalcium phosphate/poly(L-lactide-co- $\epsilon$ -caprolactone) scaffold for bone regeneration: A study in a rabbit calvarial defect. *Journal of Materials Science: Materials in Medicine*, 29, 156. <https://doi.org/10.1007/s10856-018-6159-9>
- 55 Xie, L., Yang, Y., Fu, Z., Li, Y., Shi, J., Ma, D., Liu, S., & Luo, D. (2019). Fe/Zn-modified tricalcium phosphate (TCP) biomaterials: Preparation and biological properties. *RSC Advances*, 9, 781–789. <https://doi.org/10.1039/C8RA08453J>
- 56 Kim, S.-M., Yoo, K.-H., Kim, H., Kim, Y.-I., & Yoon, S.-Y. (2022). Simultaneous substitution of Fe and Sr in beta-tricalcium phosphate: Synthesis, structural, magnetic, degradation, and cell adhesion properties. *Materials*, 15, 4702. <https://doi.org/10.3390/ma15134702>
- 57 Kumar, P.S., KS, S.K., Grandhi, V.V., & Gupta, V. (2019). The effects of titanium implant surface topography on osseointegration: Literature review. *JMIR Biomedical Engineering*, 4(1), e13237. <https://doi.org/10.2196/13237>
- 58 Jahani, B., & Wang, X. (2021). The effects of surface roughness on the functionality of Ti<sub>13</sub>Nb<sub>13</sub>Zr orthopedic implants. *Biomedical Journal of Scientific & Technical Research*, 38(1), 30058–30067. <https://doi.org/10.26717/BJSTR.2021.38.006104>
- 59 Romero-Serrano, M., Romero-Ruiz, M.-M., Herrero-Climent, M., Rios-Carrasco, B., & Gil-Mur, J. (2024). Correlation between implant surface roughness and implant stability: A systematic review. *Dentistry Journal*, 12, 276. <https://doi.org/10.3390/dj12090276>
- 60 Xing, Y., Xu, Q., Yang, S.X., Chen, C., Tang, Y., Sun, S., Zhang, L., Che, Z., & Li, X. (2016). Preservation mechanism of chitosan-based coating with cinnamon oil for fruits storage based on sensor data. *Sensors*, 16(7), 1111. <https://doi.org/10.3390/s16071111>
- 61 Singh, T.P., Chatli, M.K., & Sahoo, J. (2015). Development of chitosan-based edible films: Process optimization using response surface methodology. *Journal of Food Science and Technology*, 52(5), 2530–2543. <https://doi.org/10.1007/s13197-014-1318-6>
- 62 Jinno, T., Davy, D.T., & Goldberg, V.M. (2002). Comparison of hydroxyapatite and hydroxyapatite tricalcium-phosphate coatings. *Journal of Arthroplasty*, 17(7), 902–909. <https://doi.org/10.1054/arth.2002.34821>
- 63 Gutiérrez-Sánchez, M., Flores-Rocha, S., Pozos-Guillén, A., Flores, H., Escobar-Barrios, V., Palestino-Escobedo, A.G., & Escobar-García, D.M. (2025). Design, characterization, and biocompatibility of chitosan–nano-hydroxyapatite/tricalcium phosphate sponges. *Tissue and Cell*, 94, 102804. <https://doi.org/10.1016/j.tice.2025.102804>

- 64 Zhou, J., Ma, R., Shi, W., Lei, S., Zhang, X., Jiang, N., Lin, Y., Li, Z., & Nie, M. (2024). Zinc and chitosan-enhanced  $\beta$ -tricalcium phosphate from calcined fetal bovine bone for mandible reconstruction. *Frontiers in Bioengineering and Biotechnology*, 12, 1355493. <https://doi.org/10.3389/fbioe.2024.1355493>
- 65 Karimipour, A., Shahgholi, M., Attaeyan, A., Viet, P.H.H., Asiri, S.A., Alfawaz, K.M., & Alogla, A.F. (2024). The effect of initial temperature on the mechanical strength of tricalcium phosphate/chitosan/silica aerogels nanocomposites using molecular dynamics simulation. *Journal of the Taiwan Institute of Chemical Engineers*, 164, 105682. <https://doi.org/10.1016/j.jtice.2024.105682>
- 66 Senthil, R. (2024). Preparation of bioscaffold supported by chitosan and nanocurcumin to promote tissue engineering. *Regenerative Engineering and Translational Medicine*, 10, 553–563. <https://doi.org/10.1007/s40883-024-00344-2>
- 67 Fischer, V., Haffner-Luntzer, M., Prystaz, K., Vom Scheidt, A., Busse, B., Schinke, T., Amling, M., & Ignatius, A. (2017). Calcium and vitamin D deficiency marginally impairs fracture healing but aggravates posttraumatic bone loss in osteoporotic mice. *Scientific Reports*, 7, 7223. <https://doi.org/10.1038/s41598-017-07511-2>
- 68 Saul, D., & Khosla, S. (2022). Fracture healing in the setting of endocrine diseases, aging, and cellular senescence. *Endocrine Reviews*, 43, 984–1002. <https://doi.org/10.1210/endrev/bnac008>



## INORGANIC CHEMISTRY

### Article

Received: 6 June 2025 | Revised: 27 October 2025 |

Accepted: 10 November 2025 | Published online: 26 November 2025

UDC 546.02+544.42

<https://doi.org/10.31489/2959-0663/4-25-3>

Saida Soualmi<sup>1\*</sup>, Meriem Henni<sup>1</sup>, Leila Djahnit<sup>2,3</sup>, Maroua Bouzegaou<sup>1</sup>

<sup>1</sup>Laboratory of Synthesis and Catalysis, University of Ibn Khaldoun Tiaret, Tiaret, Algeria;

<sup>2</sup>Chemistry Department, Faculty of Exact Sciences and Informatics, University Hassiba Benbouali Chlef (UHBC), Chlef, Algeria;

<sup>3</sup>Renewable Energy and Materials Laboratory, University of Medea, Medea, Algeria

(\*Corresponding author's e-mail: [saida.soualmi@univ-tiaret.dz](mailto:saida.soualmi@univ-tiaret.dz))

### Structural, Photocatalytic, and Antibacterial Evaluation of Cu-Doped ZnMn<sub>2</sub>O<sub>4</sub> Nanoparticles

In this study, the impact of doping ZnMn<sub>2</sub>O<sub>4</sub> spinel nanoparticles with different proportions of copper (Cu) was investigated for the first time. The nanomaterials were synthesized via sol-gel method and characterized structurally, optically, and morphologically. X-ray diffraction (XRD) confirmed the formation of a pure tetragonal spinel phase, with no secondary phases detected. Successful incorporation of Cu<sup>2+</sup> ions into the ZnMn<sub>2</sub>O<sub>4</sub> lattice was confirmed by shifts in peak positions and intensities. FTIR analysis revealed distinct Zn–O and Mn–O vibrations, confirming the structural integrity of the spinel. The optical band gap, estimated via Tauc plots, decreased from 2.61 eV for undoped ZnMn<sub>2</sub>O<sub>4</sub> to 1.58 eV for 3 % Cu-doped samples, indicating improved light absorption properties. SEM analysis showed that Cu doping induced increased porosity and particle agglomeration. Photocatalytic activity was evaluated through the degradation of Methylene Blue under visible light; notably, the sample with 1 % Cu achieved an efficiency of 87.7 %. Furthermore, the doped nanoparticles exhibited strong antibacterial activity against both Gram-positive and Gram-negative bacteria, with pronounced inhibition observed against *E. coli*. These findings highlight the multifunctionality of Cu-doped ZnMn<sub>2</sub>O<sub>4</sub> for environmental and biomedical applications.

**Keywords:** spinel, synthesis, nanomaterials, photocatalysis, doping, antibacterial, sol-gel, copper

### Introduction

Nanoparticles have become an interesting research focus in various environmental fields. Their effectiveness has been demonstrated in drug delivery, antibacterial activity [1, 3], and gas sensors [4]. Among these nanomaterials, nickel-and copper-doped ZnMn<sub>2</sub>O<sub>4</sub>, which can address current energy, health, and environmental challenges. ZnMn<sub>2</sub>O<sub>4</sub> is a promising material due to its electrical, optical, and catalytic properties. These intrinsic characteristics can be further improved by the incorporation of dopants such as Bi, Al, and Mg. In a study conducted by Heiba et al. [5], Sn-doped ZnMn<sub>2</sub>O<sub>4</sub> showed notable improvements in structural and optical properties. According to Heiba [6], spinels based on ZnMn<sub>2</sub>O<sub>4</sub> were synthesized using the sol-gel method and doped with Bi<sup>3+</sup> ions. They successfully enhanced the material's functional properties for applications in optoelectronics. A recent study on the influence of aluminum doping on the structural, optical, and electrical characteristics of ZnMn<sub>2</sub>O<sub>4</sub> was conducted by Heiba et al. [7]. They found that aluminum doping significantly alters the structural, optical, and electrical properties of ZnMn<sub>2</sub>O<sub>4</sub>. The Zn<sub>1-x</sub>Al<sub>x</sub>Mn<sub>2</sub>O<sub>4</sub> compounds were synthesized through an atomic layer drying thermal treatment. The effect of doping with Al<sup>3+</sup> ions on the crystalline structure and electrochemical properties was studied [8].

Rajesh et al. [9] demonstrated that doping the spinel CdAlO<sub>4</sub> with Zn increases its photocatalytic efficiency. To examine the effect of doping, Ma et al. [10] synthesized ZnMn<sub>2</sub>O<sub>4</sub> nanocrystals doped with Co<sup>2+</sup> using a hydrothermal technique. They found that the photocatalytic activity of doped Zn<sub>1-x</sub>Co<sub>x</sub>Mn<sub>2</sub>O<sub>4</sub> sam-

ples was significantly higher than that of pure  $\text{ZnMn}_2\text{O}_4$  samples for the photodegradation of methyl orange (MO) under visible light irradiation.

This study aims to investigate the photocatalysis of Methylene Blue (MB) using pure and doped  $\text{ZnMn}_2\text{O}_4$  nanoparticles with Cu and their antibacterial activity against *E. coli* and *S. aureus* bacteria. This research introduces, for the first time, Cu-doped  $\text{ZnMn}_2\text{O}_4$  Nanoparticles to study their photocatalytic Performance, and Antibacterial Properties.

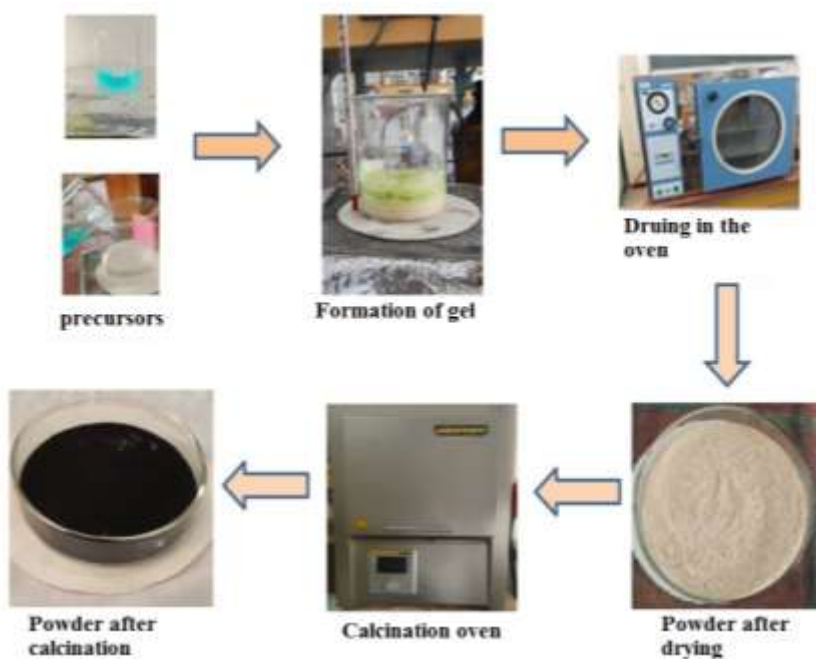
### Experimental

#### Materials

Zinc nitrate hexahydrate ( $\text{Zn}(\text{NO}_3)_2 \cdot 6\text{H}_2\text{O}$ ) was purchased from Panreac, 99 % purity. Manganese (II) nitrate  $\text{Mn}(\text{NO}_3)_2 \cdot 4\text{H}_2\text{O}$  obtained from Fluka  $\geq 98$  % purity. Copper (II) nitrate trihydrate  $\text{Cu}(\text{NO}_3)_2 \cdot 3\text{H}_2\text{O}$  obtained from Biochem, Citric acid  $\text{C}_6\text{H}_8\text{O}_7$  obtained from Biochem and Methylene blue (Merck chemicals).

#### Synthesis of Copper doped $\text{ZnMn}_2\text{O}_4$ Nanoparticles

A facile sol–gel method was used to synthesize pure and Cu-doped  $\text{ZnMn}_2\text{O}_4$  nanoparticles. A mixture 0.0052 mol of zinc nitrate hexahydrate ( $\text{Zn}(\text{NO}_3)_2 \cdot 6\text{H}_2\text{O}$ ) and 0.01 mol of manganese (II) nitrate tetrahydrate ( $\text{Mn}(\text{NO}_3)_2 \cdot 4\text{H}_2\text{O}$ ) were dissolved in 100 mL of deionized water. The two solutions were then mixed with vigorous agitation at room temperature for 30 minutes to ensure homogeneity. Citric acid, used as a complexing agent, as well as  $\text{Cu}(\text{NO}_3)_2 \cdot 3\text{H}_2\text{O}$  (0.0376 g) dissolved in ethanol, were successively added to the reaction mixture. The solution was then heated and stirred at 90 °C until the gel was formed then converted into a powder, which was dried in an oven at 70 °C for 24 hours. Finally, the dried powder was calcined at 600 °C for 4 hours, resulting in the formation of  $\text{ZnMn}_2\text{O}_4$  nanocomposites, as illustrated in Scheme 1.



Scheme 1. Spinel synthesis protocol

#### Antibacterial Activity

##### Preparation of the Bacterial Suspension

The evaluation of the antibacterial activity of the prepared nanoparticles was carried out on both Gram-negative and Gram-positive bacteria, namely *Escherichia coli* ATCC 25922, *Bacillus subtilis* ATCC 6633, *Staphylococcus aureus* ATCC 25925, and *Bacillus cereus* ATCC 10876. The strains were cultured at 37 °C in Mueller Hinton medium for 24 hours. The bacterial culture was adjusted to 0.5 McFarland standard using a spectrophotometer set at a wavelength of 625 nm, with an optical density (OD) ranging between 0.08 and 0.1, corresponding to approximately  $1 \times 10^8$  CFU/mL [11].

### Agar Well Diffusion Method

The agar well diffusion method, adapted from Imran et al. [12], was used to evaluate the antimicrobial activity of the oxide nanoparticles, with some modifications. Culture plates were prepared using sterilized Mueller-Hinton agar. One milliliter of the bacterial suspension was evenly spread over the agar surface. Each Petri dish was perforated with four wells, each 6 mm in diameter. Then, 100  $\mu\text{L}$  of each nanoparticle (NP) concentration (10 mg/mL, 15 mg/mL) was added to the wells. The positive control was performed using the antibiotic Piperacillin PRL100 (100  $\mu\text{g}$ ). The plates were incubated at 37  $^{\circ}\text{C}$  for 24 hours. Finally, antimicrobial potency was determined by measuring the inhibition zones in millimeters using a caliper.

### Characterization

Characterization of the synthesized nanocomposites' properties was carried out using X-ray diffraction (XRD, Rigaku MINIFLEX 600) using Cu K $\alpha$  radiation ( $\lambda = 1.5406$ ) and a scanning rate of 5 $^{\circ}$  min $^{-1}$ . Perkin Elmer Spectrum One FTIR was used to analyze the samples following KBr pellets, in the range of 4000–400  $\text{cm}^{-1}$ . A QUANTA 650 FEI scanning electron microscopy (SEM) was used to examine the morphology of the produced spinel oxides.

## Results and Discussion

### FT-IR Spectra

FTIR spectra of  $\text{ZnMn}_2\text{O}_4$  samples (Fig. 1), whether undoped or doped with 1 % and 3 % copper (Cu) were analyzed. Strong signals were detected from 400 to 600  $\text{cm}^{-1}$  related to the vibrations of the metal-oxygen M–O bond. Bands of the octahedral Zn–O and tetrahedral Mn–O groups were observed around 400 and 600  $\text{cm}^{-1}$ , respectively.

These observations, in line with those of Roy et al. [13], confirm that the inverse spinel structure of  $\text{ZnMn}_2\text{O}_4$ , with  $\text{Zn}^{2+}$  in the tetrahedral sites and  $\text{Mn}^{3+}$  in the octahedral sites, has indeed been achieved. The O–H stretching vibration peaks between 3400 to 3200  $\text{cm}^{-1}$  were detected in the spectrum due to surface water and hydroxyl group presence. A band present at 1630  $\text{cm}^{-1}$  indicates either H–O–H bending or C=O stretching although it points toward the existence of surface water or hydroxyl groups typical for aqueous precipitation materials. A band at 1380  $\text{cm}^{-1}$ , probably due to symmetric deformation vibrations of  $\text{CH}_3$  groups, indicated the presence of organic residues, likely from citric acid used as a chelating agent. Moreover, bands at 995  $\text{cm}^{-1}$  ( $\nu(\text{C–O})$  vibrations or  $\text{NO}_3^-$  nitrates) and 878  $\text{cm}^{-1}$  (out-of-plane deformation of  $\text{COO}^-$  carboxylates) revealed that an incomplete calcination of the precursors occurred.

FTIR analysis clearly demonstrates that doping significantly affects the intensity of the bands. When copper is added up to 3 %, there is a notable increase in intensity, indicating that  $\text{Cu}^{2+}$  ions are properly integrated into the crystal lattice. On the other hand, the intensity decreases when the content reaches 6 %, indicating that the structure begins to be disturbed or saturated. This destabilization may be related to the fact that the radius of ionized  $\text{Cu}^{2+}$  (0.73) is marginally larger than that of  $\text{Mn}^{2+}$  (0.65), which leads to internal stresses in the highly concentrated lattice. This may be due to the slightly larger ionic radius of  $\text{Cu}^{2+}$  compared to that of  $\text{Mn}^{2+}$ , which introduces high concentration stresses in the lattice.

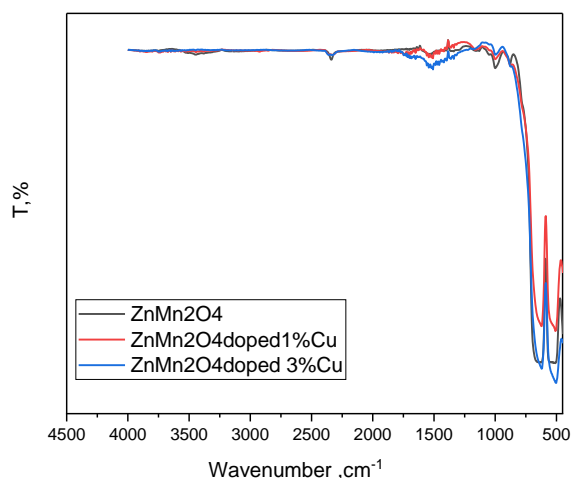


Figure 1. FTIR absorption spectra of all Cu-doped  $\text{ZnMn}_2\text{O}_4$  compounds

### XRD Measurements

X-ray diffraction (XRD) analysis (Fig. 2) confirmed the formation of the  $\text{ZnMn}_2\text{O}_4$  spinel structure (heterolite) for all samples, both doped and undoped, in accordance with JCPDS card no. 96-901-2843. The diffraction peaks observed at  $2\theta$  values of  $18.224^\circ$ ,  $29.39^\circ$ ,  $31.23^\circ$ ,  $33.09^\circ$ ,  $36.40^\circ$ ,  $50.58^\circ$ ,  $52.11^\circ$ ,  $54.41^\circ$ ,  $59.1^\circ$ ,  $60.82^\circ$ , and  $65.16^\circ$  correspond well to the (011), (112), (020), (013), (121), (220), (015), (132), (231), (224), and (040) crystallographic planes, respectively. The undoped sample exhibited no additional or secondary peaks, confirming its phase purity and high crystallinity.

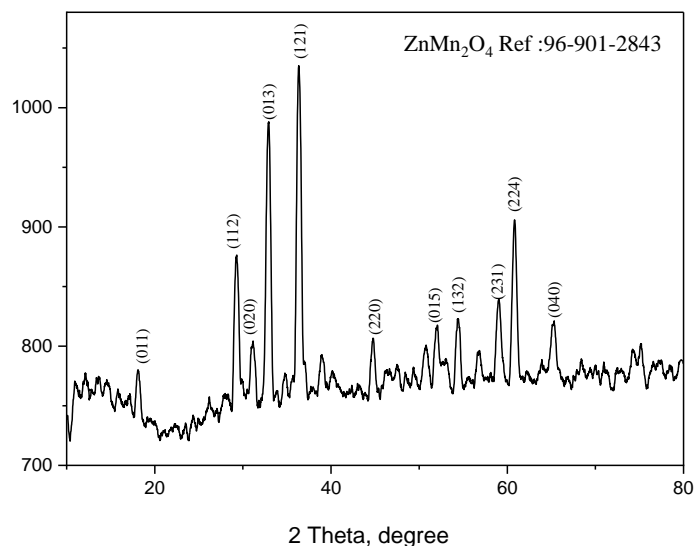


Figure 2. XRD spectrum of  $\text{ZnMn}_2\text{O}_4$  nanocomposite

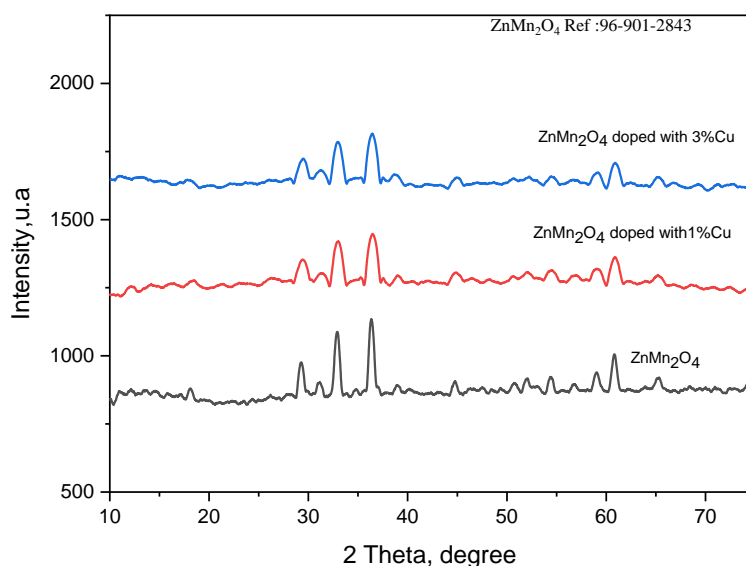


Figure 3. XRD spectrum of Cu-doped  $\text{ZnMn}_2\text{O}_4$  nanocomposite

The diffraction peaks are perfectly indexed to the  $\text{ZnMn}_2\text{O}_4$  phase of inverse spinel type (heterolite structure), referenced to the data of JCPDS card no. 96-901-2843. As shown in Figure 3, increasing the Cu doping level from 1 % to 3 % induces noticeable changes in peak positions and intensities. In comparison with the undoped material, the sample containing 1 % Cu. However, when the Cu content is increased to 3 %, the structural changes become more evident. This suggests that a higher Cu concentration leads to increased lattice strain and possible distortions within the crystal framework, likely due to the integration of  $\text{Cu}^{2+}$  ions into the lattice. Alongside these effects, a gradual rise in crystallite size was also noticed with increasing Cu levels, indicating that  $\text{Cu}^{2+}$  may play a role in promoting or facilitating crystal growth.

The average crystallite size of spinel grains (Table I) was calculated by the Debye–Scherrer equation applied to the most intense diffraction line [14]:

$$D_c = \frac{K\lambda}{\beta \cos \theta},$$

where  $K = 0.9$ ;  $D$  is the catalyst's crystallite size;  $\lambda$  is the X-ray wavelength;  $\beta$  is the "Full Width at Half Maximum (FWHM)";  $\theta$  is the diffraction angle.

Table 1

**The average crystallite size of the synthesized spinels**

Sample	Crystallite size D (nm)
ZnMn <sub>2</sub> O <sub>4</sub>	24.82
ZnMn <sub>2</sub> O <sub>4</sub> doped with 1 % Cu	30.21
ZnMn <sub>2</sub> O <sub>4</sub> doped with 3 % Cu	32.82

#### *Optical Band Gap of the Synthesized Spinel*s

The optical band gap is a physical property that corresponds to the energy difference between the valence band and the conduction band. The determination of the band gap energy was carried out using a reflectance method based on Tauc's theory [15].

The calculation of  $E_g$  was performed using Tauc's equation.

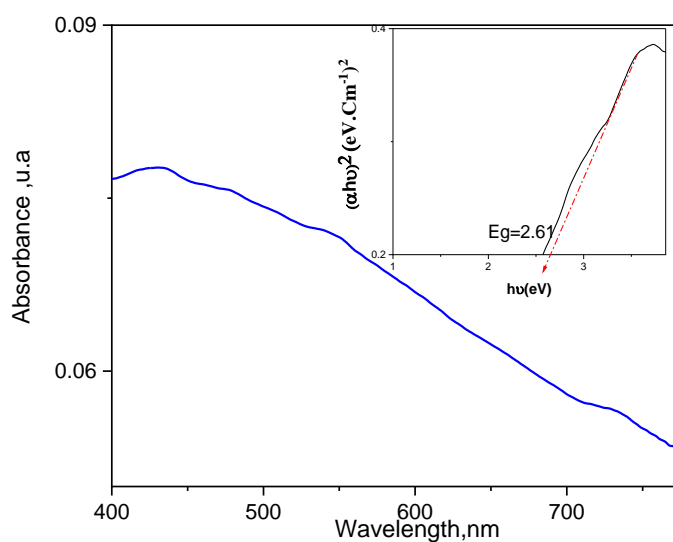
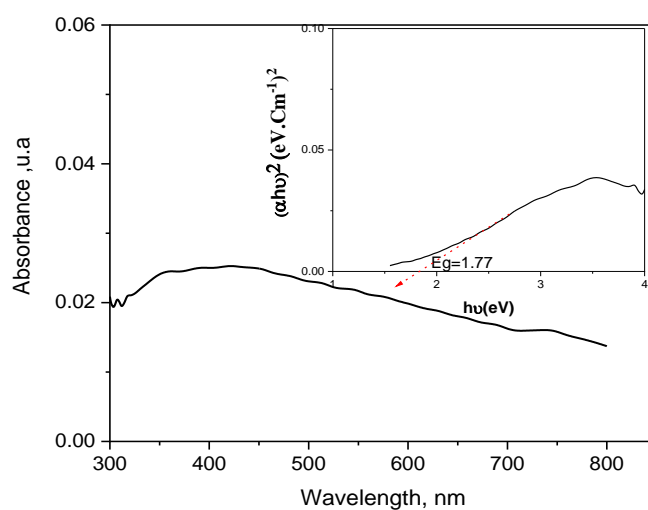
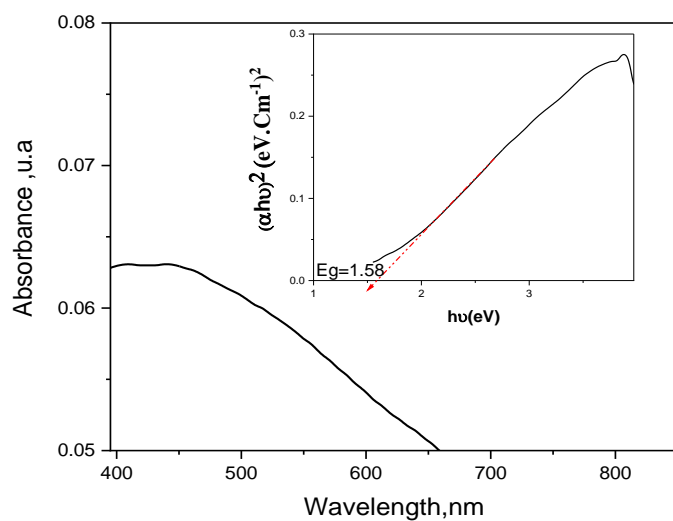
$$\alpha_{hv} = \alpha_0(hv - E_g)^{1/2},$$

where  $\alpha_0$  is a constant,  $E_g$  is the band gap energy,  $\alpha$  is the absorption coefficient given by  $\alpha = 2.303 A/d$ ; there  $d$  is the thickness of the sample (in our case, the cuvette thickness  $d$  is 1 cm),  $A$  is the absorbance,  $h\nu$  is the photon energy, hence:  $h\nu(\text{eV}) = 1240/\lambda$ , where  $\lambda$  is the incident wavelength (nm).

In the course of this study, the optical band gap was estimated to be around 2.61 eV (Fig. 4). This value is fairly consistent with what has been previously reported in the literature — 2.49 eV in reference [16] with only a slight difference of 0.12 eV, which falls within the expected margin of experimental error. Similarly, the absorption wavelength recorded here (475 nm) is close to the previously cited value of 498 nm [16], supporting the idea that the material absorbs within the UV-visible range. Figures 4 to 6 show the Tauc plots corresponding to both the undoped and Cu-doped ZnMn<sub>2</sub>O<sub>4</sub> samples. A clear reduction in the band gap is observed as more copper is introduced: it drops from 2.61 eV in the pure sample to 1.77 eV and 1.58 eV for the 1 % and 3 % Cu-doped materials, respectively.

This trend agrees with what has been highlighted in earlier works [17], where doping is known to affect the electronic structure of metal oxides often by narrowing the band gap due to the introduction of new energy levels or changes within the lattice.

The band gap narrows mainly because copper ions create new energy levels within it. These extra levels let electrons move between states more easily, requiring less energy and thus reducing the overall optical band gap. This phenomenon comes from the interaction between the Cu 3d orbitals and the electronic structure of the host oxide—a mechanism that has been widely observed in other transition metal oxides like ZnO and CuO [18]. Additionally, the narrowing of the band gap in Cu-doped ZnMn<sub>2</sub>O<sub>4</sub> can also be influenced by structural defects and the interactions between copper and manganese ions, which together modify the electronic environment of the material. Similar patterns have been reported in copper-doped ZnO, TiO<sub>2</sub> [19], and other spinel oxides doped with Cu [20]. Interestingly, the band gap reduction is more noticeable in ZnMn<sub>2</sub>O<sub>4</sub>, likely because of the distinctive electronic characteristics of manganese-based spinels.

Figure 4. Tauc plots of  $\text{ZnMn}_2\text{O}_4$  nanoparticlesFigure 5. Tauc plots of  $\text{ZnMn}_2\text{O}_4$  NPs doped with 1 % CuFigure 6. Tauc plots of  $\text{ZnMn}_2\text{O}_4$  NPs doped with 3 % Cu



### Scanning Electron Microscopy (SEM)

The morphology of the 3 % Cu-doped  $\text{ZnMn}_2\text{O}_4$  nanoparticles, observed by scanning electron microscopy (SEM) and shown in Figure 7, reveals a heterogeneous porous structure. The pore sizes range roughly from 50 to 200 nm, as estimated using the 2  $\mu\text{m}$  scale bar. The morphology consists of a complex three-dimensional network formed by spheroidal or irregular particles that tend to agglomerate into porous assemblies. Such elevated porosity is characteristic of materials engineered for applications requiring a high specific surface area, including gas sensing and battery electrodes. In the first case (Fig. 7a), the surface is rough and porous, characterized by irregular aggregates of angular particles, indicating a marked influence of Cu doping on pore density and distribution. In contrast, in Figure 7b, the texture appears more homogeneous, with regularly distributed spheroidal or lamellar particles, suggesting a structured organization in layers or stacking. Finally, Figure 7c highlights a complex mixed morphology, dominated by well-developed porosity.

The pronounced porosity and clustering in the Cu-doped samples probably result from copper's impact on how the crystals grow, causing the particles to stick together more easily. Since the ionic sizes of  $\text{Cu}^{2+}$  (73 pm),  $\text{Zn}^{2+}$  (74 pm), and  $\text{Mn}^{3+}$  (65 pm) are quite close, copper ions can replace either zinc or manganese in the crystal lattice. When copper ions take the place of others in the lattice, they can create defects that promote the formation of a porous structure. In contrast, doping with tin usually leads to dense, angular particles with very little porosity [21], making it quite different from the more open, porous structure seen with copper doping. Cobalt doping falls somewhere in between, leading to particles that are mostly round with less porosity [9]. These differences clearly show how important the choice of dopant is in shaping  $\text{ZnMn}_2\text{O}_4$  nanoparticles: copper encourages a highly porous structure, cobalt results in moderate aggregation with smoother particles, and tin creates a denser, more compact material.

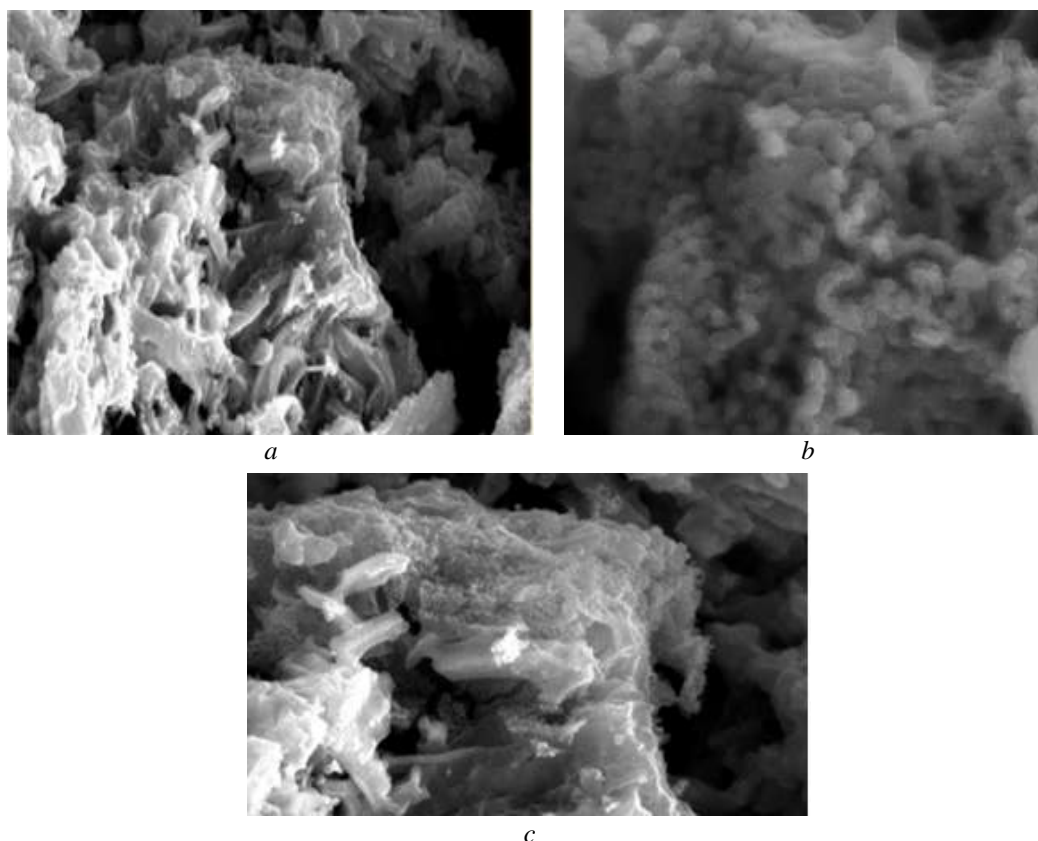


Figure 7. SEM micrographs profile of Cu-doped  $\text{ZnMn}_2\text{O}_4$ . The images show (a) rough, porous surface with irregular angular aggregates; (b) a more homogeneous texture with regularly distributed spheroidal or lamellar particles suggesting structured layering; (c) a complex mixed morphology with high overall porosity (pore sizes ranging from 50 to 200 nm, scale bar = 2  $\mu\text{m}$ )

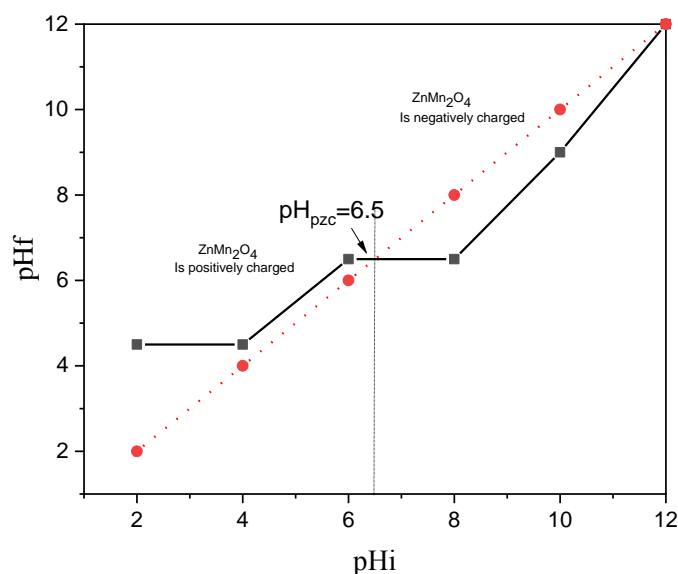


Figure 8. Determination of the  $\text{pH}_{\text{pzc}}$  for  $\text{ZnMn}_2\text{O}_4$

### Photocatalysis

The point of zero charge ( $\text{pH}_{\text{pzc}}$ ) was determined using the pH drift method [22]. The  $\text{pH}_{\text{pzc}}$  is equal to 6.5 (Fig. 8) was identified as the intersection point between the final pH versus initial pH curve and the line  $\text{pH}_{\text{final}} = \text{pH}_{\text{initial}}$ .

The photodegradation of Methylene Blue (MB) dye by synthesized  $\text{ZnMn}_2\text{O}_4$  spinels, both undoped and copper-doped, using a 30 W visible light source, was investigated. Figure 9 shows the photocatalytic degradation of MB by  $\text{ZnMn}_2\text{O}_4$  synthesized at pH 12, where a significant adsorption of the dye is observed over time (adsorption equilibrium reached before irradiation). After irradiation, a gradual decrease in the intensity of the absorption peak at 664 nm is observed over time (from 30 to 180 minutes), with a degradation rate of 71.71 %, which is a good yield, especially for a dye that is difficult to degrade. As shown in Figure 10,  $\text{ZnMn}_2\text{O}_4$  doped with 3 % Cu reached a degradation efficiency of 78.21 %. Notably, the sample doped with 1 % Cu exhibited the highest photocatalytic performance, with a degradation rate of 87.7 % (Fig. 11). This enhancement can be attributed to the beneficial role of copper in promoting charge carrier separation and introducing favorable structural defects.

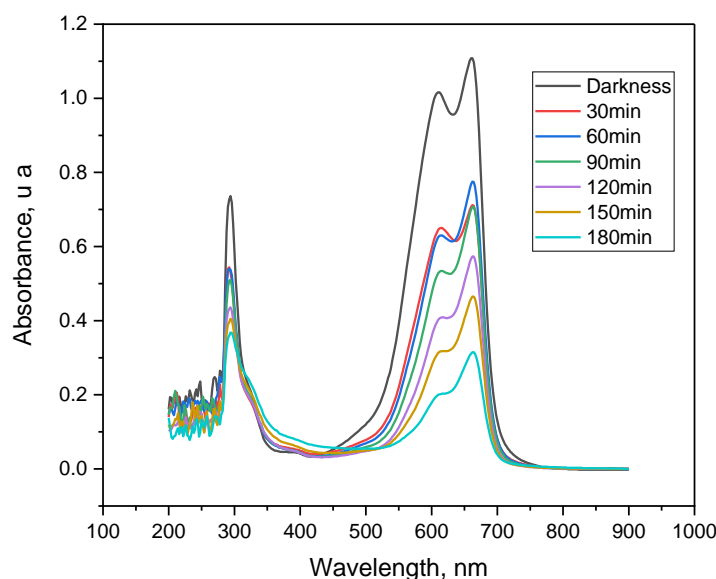


Figure 9. Photocatalytic degradation of Methylene Blue (MB) by synthesized  $\text{ZnMn}_2\text{O}_4$ , with MB concentration of 0.01 g/L and  $\text{ZnMn}_2\text{O}_4$  concentration of 0.1 g/L

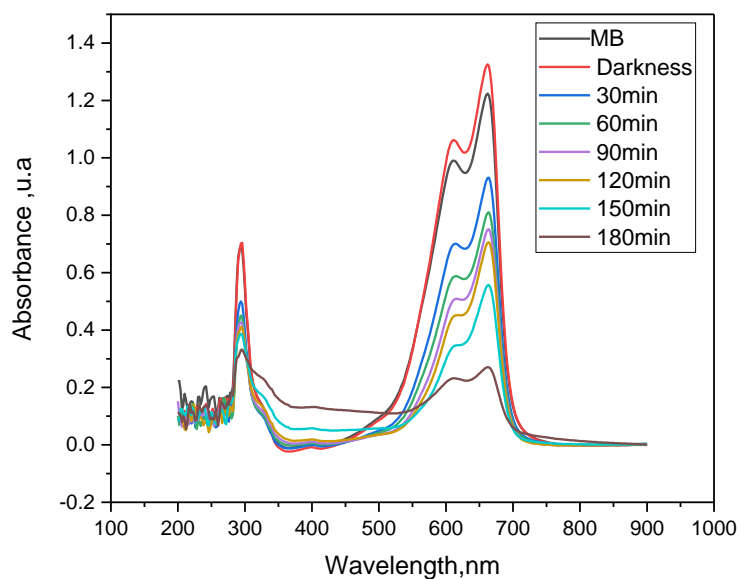


Figure 10. Photocatalytic degradation of Methylene Blue (MB) by 3 % Cu-doped  $\text{ZnMn}_2\text{O}_4$ , synthesized with an MB concentration of 10 mg/L and a 1 % Cu-doped  $\text{ZnMn}_2\text{O}_4$  concentration of 0.1 g/L

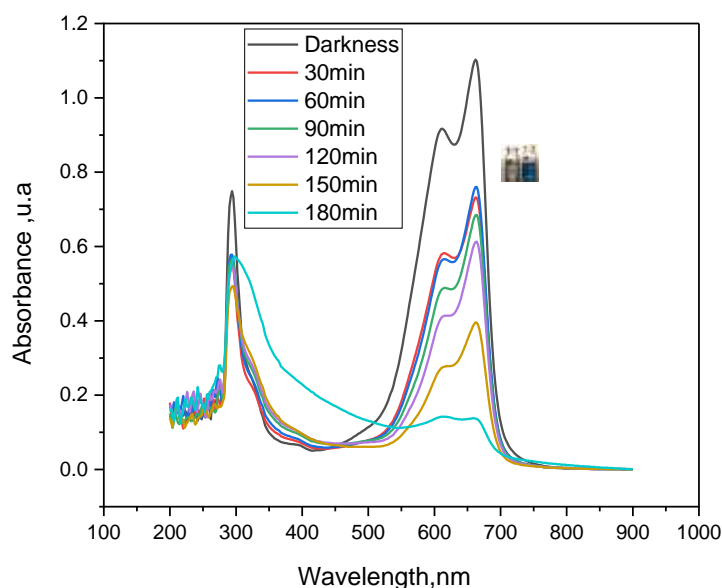


Figure 11. Photocatalytic degradation of Methylene Blue (MB) by 1 % Cu-doped  $\text{ZnMn}_2\text{O}_4$ , synthesized with an MB concentration of 0.01g/L and a 1 % Cu-doped  $\text{ZnMn}_2\text{O}_4$  concentration of 0.1 g/L

### Antibacterial Activity

The antibacterial activity results of the synthesized  $\text{ZnMn}_2\text{O}_4$  nanoparticles, both doped and undoped, revealed notable antibacterial effects against all tested strains. The inhibition zones around the wells are shown in Figures 12, 13, 14, and 15, and the measured inhibition values are presented in Table 2.

It was observed that the antibacterial activity of Cu-doped nanoparticles is higher compared to undoped nanoparticles. Figure 12 confirms that the synthesized nanoparticles effectively inhibit the growth of *Bacillus subtilis*, producing inhibition zones ranging from 10 to 14 mm. In contrast, the standard antibiotic showed a considerable inhibition zone of 27 mm.

Each sample exhibited a moderate inhibition zone against the *S. aureus* strain, with diameters ranging from 11 to 15 mm, similar to that of the antibiotic (Fig. 13). However, the various nanoparticles demonstrated significant antibacterial properties against the *Bacillus cereus* strain, with inhibition zones ranging from 10 to 14 mm (Fig. 14). In comparison, the standard antibiotic exhibited a strong inhibition zone of

29 mm. These findings confirm that increasing the concentration of pure and doped nanoparticles is associated with enhanced inhibition of bacterial growth.

Regarding *E. coli* bacteria, as shown in Figure 15, all nanoparticles demonstrated notable antibacterial activity, with inhibition zones ranging from 10 to 16 mm. In contrast, the standard antibiotic showed a significant inhibition zone of 25 mm. Figure 16 clearly shows the expansion of the inhibition zone with the increase in nanoparticle concentration and doping percentage.

In other studies, Soualmi al. also confirmed that  $\text{ZnMn}_2\text{O}_4$  nanoparticles showed strong antibacterial activity against *E. coli*, *S. aureus*, *B. cereus*, and *B. subtilis* [2].

However, the Cu-doped nanoparticles exhibited a notable inhibitory effect against all strains, with a particularly large inhibition zone observed against *E. coli*. Therefore, doping with copper proved to be more effective against *E. coli* (Gram-negative) than against *S. aureus* (Gram-positive). These results are consistent with the findings of Bogdanovi et al., who demonstrated that *E. coli* strains are generally more sensitive to copper nanoparticles compared to *S. aureus* [22].

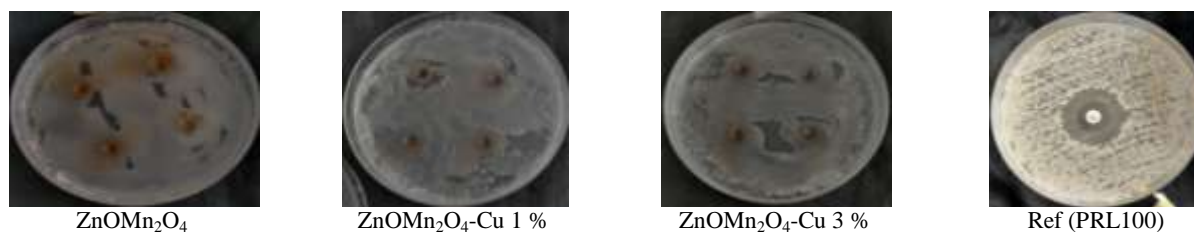
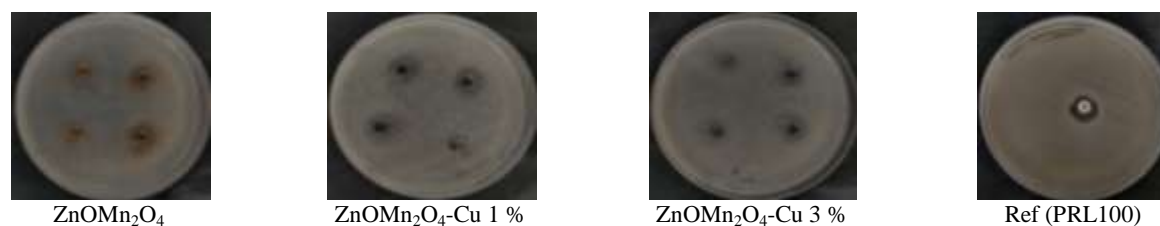
According to Giannousi et al., copper nanoparticles (Cu-NPs) and copper oxide ( $\text{Cu}_2\text{O}$ ) exhibit strong antibacterial properties, notably by inducing plasmid DNA degradation in a dose-dependent manner across both Gram-positive and Gram-negative bacteria [23]. In addition, the antibacterial action of ZnO and CuO nanoparticles is generally thought to result from the release of  $\text{Cu}^{2+}$  and  $\text{Zn}^{2+}$  ions, which tend to bind to the negatively charged surfaces of bacterial cells [24].

This interaction may disrupt biochemical processes and damage cell membranes. Additionally, the small size of the nanoparticles facilitates their attachment to the bacterial cell wall, leading to cell destruction. Nanoparticles capable of damaging essential bacterial enzymes may also penetrate the cell membrane [25, 26].

Table 2

Diameter of inhibition zones against microorganisms

Bacteria	Zone of inhibition (mm)						
	Control	$\text{ZnOMn}_2\text{O}_4$		$\text{ZnOMn}_2\text{O}_4\text{-Cu 1 \%}$		$\text{ZnOMn}_2\text{O}_4\text{-Cu 3 \%}$	
		10 mg/ml	15 mg/ml	10 mg/ml	15 mg/ml	10 mg/ml	15 mg/ml
<i>Bacillus cerus</i>	25	10	12	12	13	13.5	14
<i>Escherichia coli</i>	23	10	11.5	11	14.5	14	16
<i>Staphylococcus aureus</i>	13	11	12	12	14	13	15
<i>Bacillus subtilis</i>	27	11.5	13	12	13	12.5	14

Figure 12. Results of antibacterial activity against *Bacillus subtilis*Figure 13. Results of antibacterial activity against *S. Aureus*

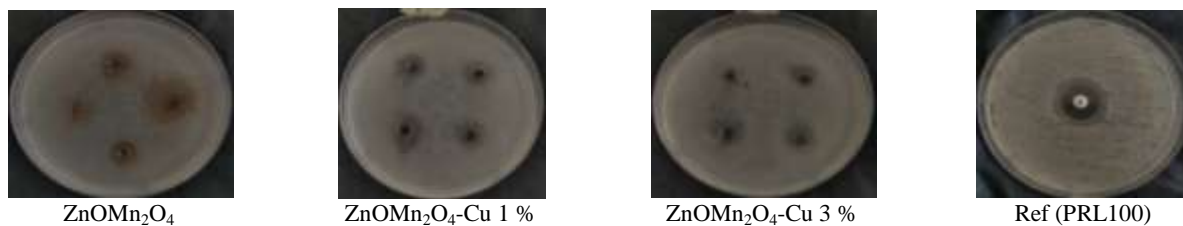


Figure 14. Results of antibacterial activity against *Bacillus Cereus*

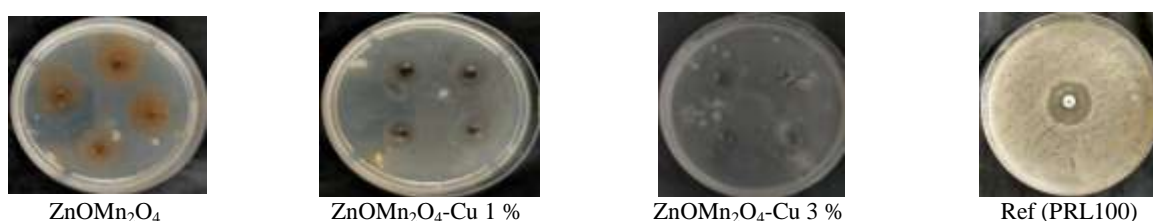


Figure 15. Results of antibacterial activity against *E. Coli*

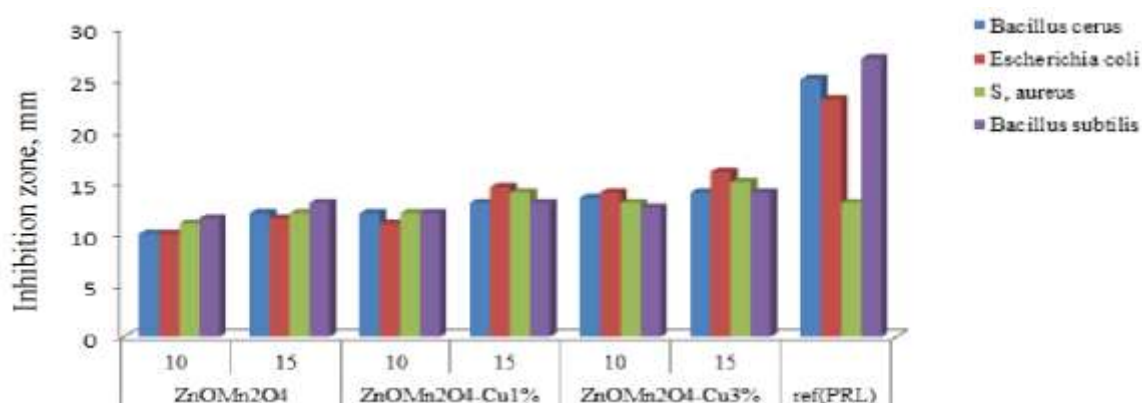


Figure 16. Antibacterial effects of nanoparticles

### Conclusions

The effect of incorporating different amounts of copper (Cu) into  $\text{ZnMn}_2\text{O}_4$  spinel nanoparticles was investigated in this study for the first time. A sol-gel method was used to synthesize the nanoparticles, followed by their structural, optical, and morphological characterization. FTIR results confirmed that the material possesses a spinel structure, as evidenced by bands located between  $400$  and  $600\text{ cm}^{-1}$ . Copper doping increased band intensity, indicating successful incorporation without altering the main structure. The results of SEM are typical of materials produced through methods like co-precipitation or hydrothermal synthesis [27].

The presence of copper seemed to promote noticeable particle agglomeration and increased surface roughness features often associated with crystalline imperfections which could enhance performance in applications requiring a large specific surface area. The best photocatalytic performance was shown by  $\text{ZnMn}_2\text{O}_4$  doped with 1 % copper, which achieved 87.7 % MB degradation, attributed to improved charge separation and structural defects.  $\text{ZnMn}_2\text{O}_4$  nanoparticles exhibit notable antibacterial activity against *B. cereus*, *E. coli*, *S. aureus* and *B. subtilis* strains. However, copper-doped nanoparticles, specifically  $\text{ZnMn}_2\text{O}_4$ , 3 %, exhibit better antibacterial properties. Overall, these results demonstrate that controlled copper doping not only preserves the spinel structure of  $\text{ZnMn}_2\text{O}_4$  nanoparticles but also enhances their photocatalytic and antibacterial activity, highlighting their potential for environmental and biomedical applications.



### Author Information\*

\*The authors' names are presented in the following order: First Name, Middle Name and Last Name

**Saida Soualmi** (*corresponding author*) — Doctor and Researcher, Laboratory of Synthesis and Catalysis, University of Ibn Khaldoun Tiaret, 14000, Tiaret, Algeria; e-mail: [saida.soualmi@univ-tiaret.dz](mailto:saida.soualmi@univ-tiaret.dz); <https://orcid.org/0009-0009-4858-8695>

**Meriem Henni** — Doctor and Researcher, Laboratory of Synthesis and Catalysis, University of Ibn Khaldoun Tiaret, 14000, Tiaret, Algeria; e-mail: [hanan1112@yahoo.fr](mailto:hanan1112@yahoo.fr), <https://orcid.org/0009-0005-5378-0674>

**Leila Djahnit** — Doctor and Researcher, Chemistry Department, Faculty of Exact Sciences and Informatics, University Hassiba Benbouali Chlef (UHBC), 02000, Chlef, Algeria; Renewable Energy and Materials Laboratory, University of Medea, 26000, Medea, Algeria; e-mail: [Leila\\_djahnit@yahoo.fr](mailto:Leila_djahnit@yahoo.fr), <https://orcid.org/0000-0001-5834-8024>

**Maroua Bouzegaou** — Master Student, Chemistry Department, Laboratory of Synthesis and Catalysis, University of Ibn Khaldoun Tiaret, 14000, Tiaret, Algeria; e-mail: [bouzegaoumaroua3@gmail.com](mailto:bouzegaoumaroua3@gmail.com)

### Author Contributions

The manuscript was written through contributions of all authors. All authors have given approval to the final version of the manuscript. **CRedit**: **Saida Soualmi** conceptualization, data curation, investigation, methodology, validation, visualization, writing-review & editing, interpreted the results, plotted the graphs, and wrote the manuscript performed the photocatalytic degradation of methylene blue under visible light. **Meriem Henni** application of the antibacterial activity of the synthesized materials; **Leila Djahnit** conservation of antibacterial activity data. **Maroua Bouzegaou** synthesis of material.

### Conflicts of Interest

The authors declare no conflict of interest.

### References

- 1 Maksud, T. M. A., El-Sayed, H. A., & Ahmed, H. B. (2019). Antibacterial activity of metal oxide nanoparticles: A review. *Journal of Nanomaterials and Molecular Nanotechnology*, 8(2), 1–12. <https://doi.org/10.4172/2324-8777.1000178>
- 2 Soualmi, S., Djahnit, L., Henni, M., & Douar, R. (2025). Green synthesis of ZnMn<sub>2</sub>O<sub>4</sub> nanoparticles using tragacanth gel for antibacterial effects. *Chemical Papers*, 1–14. <https://doi.org/10.1007/s11696-025-04065-w>.
- 3 Soualmi, S., Henni, M., Djahnit, L., & Hamdani, H. (2024). Sol-gel synthesized ZnO–SrMn<sub>2</sub>O<sub>4</sub> nanocomposite and its antibacterial properties. *Eurasian Journal of Chemistry*, 29(4), 71–81. <https://doi.org/10.31489/2959-0663/4-24-12>
- 4 Fort, S., Hu, H., & Lakshminarayanan, B. (2019). Deep ensembles: A loss landscape perspective. *arXiv*. <https://doi.org/10.48550/arXiv.1912.02757>.
- 5 Heiba, Z. K., Ghannam, M. M., Badawi, A., & Mohamed, M. B. (2024). Tailoring the structure, optical and shielding characteristics of ZnMn<sub>2</sub>O<sub>4</sub> nanostructures through Sn-doping. *ECS Journal of Solid State Science and Technology*, 13(7), 077001. doi: [10.1149/2162-8777/ad5b86](https://doi.org/10.1149/2162-8777/ad5b86).
- 6 Heiba, Z. K., Ghannam, M. M., Mohamed, M. B., Sanad, M. M. S., Abdel-Kader, M. H., El-Naggar, A. M., & Lakshminarayana, G. (2023). Impact of Bi doping on the structural, optical, and dielectric features of nano ZnMn<sub>2</sub>O<sub>4</sub>. *Ceramics International*, 11, 303. <https://doi.org/10.1016/j.ceramint.2023.11.303>.
- 7 Heiba, Z. K., Ghannam, M. M., Mohamed, M. B., Sanad, M. M., El-Naggar, A. M., & Shaltout, A. A. (2024). Influence of Al doping on the structural, optical, and electrical characteristics of ZnMn<sub>2</sub>O<sub>4</sub>. *ECS Journal of Solid State Science and Technology*, 13(2), 023008. <https://doi.org/10.1149/2162-8777/ad28ca>
- 8 Zhu, X., Quan, J., Huang, J., Ma, Z., Chen, Y., Zhu, D., & Li, D. (2018). A new approach to improve the electrochemical performance of ZnMn<sub>2</sub>O<sub>4</sub> through a charge compensation mechanism using the substitution of Al<sup>3+</sup> for Zn<sup>2+</sup>. *RSC Advances*, 8(14), 7361–7368. <https://doi.org/10.1039/c8ra00310f>
- 9 Rajesh, G., Kumar, P. S., Alanazi, A. K., Rangasamy, G., & Abo-Dief, H. M. (2023). Development of lattice defects and oxygen vacancies in Zn-doped CdAl<sub>2</sub>O<sub>4</sub> nanoparticles for improving the photocatalytic efficiencies of brilliant green and brilliant blue dyes under visible illumination. *Catalysis Communications*, 183, 106762. <https://doi.org/10.1016/j.catcom.2023.106762>
- 10 Ma, L., Wei, Z., Zhu, X., Liang, J., & Zhang, X. (2019). Synthesis and photocatalytic properties of Co-doped Zn<sub>1-x</sub>Co<sub>x</sub>Mn<sub>2</sub>O hollow nanospheres. *Journal of Nanomaterials*, 2019, 4257270. <https://doi.org/10.1155/2019/4257270>



- 11 Ramon, M. V., Stoeckli, F., Moreno-Castilla, C., & Carrasco-Marin, F. (1999). On the characterization of acidic and basic surface sites on carbons by various techniques. *Carbon*, 37, 1215–1221. [https://doi.org/10.1016/S0008-6223\(98\)00317-0](https://doi.org/10.1016/S0008-6223(98)00317-0)
- 12 Imran, M., Riaz, S., Sanaullah, I., Khan, U., Sabri, A. N., & Naseem, S. (2019). Microwave assisted synthesis and antimicrobial activity of Fe<sub>3</sub>O<sub>4</sub>-doped ZrO<sub>2</sub> nanoparticles. *Ceramics International*, 45(8), 10106–10113. <https://doi.org/10.1016/j.ceramint.2019.02.057>
- 13 Roy, A., Ghosh, M., Ramos Ramón, J. A., Saha, S., Pal, U., & Das, S. (2019). Study on charge storage mechanism in working electrodes fabricated by sol-gel derived spinel NiMn<sub>2</sub>O<sub>4</sub> nanoparticles for supercapacitor application. *Applied Surface Science*, 463, 513–525. <https://doi.org/10.1016/j.apsusc.2018.08.259>
- 14 Bond, G. C. (2005). Small metal particles and supported metal catalysts. In *Metal Catalysed Reactions of Hydrocarbons* (pp. 35–91). Elsevier. [https://doi.org/10.1007/0-387-26111-7\\_2](https://doi.org/10.1007/0-387-26111-7_2)
- 15 Heiba, Z. K., Mohamed, M. B., & Badawi, A. (2022). Structural and optical properties of (1-x)ZnMn<sub>2</sub>O<sub>4</sub>/xPbS. *Journal of Materials Science: Materials in Electronics*, 33(14), 11354–11364.
- 16 Ma, Z., Ren, F., Ming, X., Long, Y., & Volinsky, A. A. (2019). Cu-doped ZnO electronic structure and optical properties studied by first principles calculations and experiments. *Materials*, 12(1), 196. <https://doi.org/10.3390/ma12010196>
- 17 Khalid, A., Ahmad, P., Alharthi, A. I., Muhammad, S., Khandaker, M. U., Rehman, M., & Bradley, D. A. (2021). Structural, optical, and antibacterial efficacy of pure and zinc doped copper oxide against pathogenic bacteria. *Nanomaterials*, 11(2), 293. <https://doi.org/10.3390/nano11020451>
- 18 Yıldırım, M. (2019). Characterization of the framework of Cu-doped TiO<sub>2</sub> layers: An insight into optical, electrical and photodiode parameters. *Journal of Alloys and Compounds*, 773, 890–904. <https://doi.org/10.1016/j.jallcom.2018.09.276>
- 19 Ali, B. M., Siddig, M. A., Alsabab, Y. A., Elbadawi, A. A., & Ahmed, A. I. (2018). Effect of Cu<sup>2+</sup> doping on structural and optical properties of synthetic Zn<sub>0.5</sub>Cu<sub>x</sub>Mg<sub>0.5-x</sub>Fe<sub>2</sub>O<sub>4</sub> (x = 0.0–0.4) nano ferrites. *Advances in Nanoparticles*, 7(1), 1–13. <https://doi.org/10.4236/anp.2018.71001>
- 20 Gherbi, R., Bessekhouad, Y., & Trari, M. (2016). Optical and transport properties of Sn-doped ZnMn<sub>2</sub>O<sub>4</sub> prepared by sol-gel method. *Journal of Physics and Chemistry of Solids*, 89, 69–77. <https://doi.org/10.1016/j.jpcs.2015.10.019>
- 21 Lima, D. S., Gullon, B., Cardelle-Cobas, A., Brito, L. M., Rodrigues, K. A., Quelemes, P. V., ... & Batziou, K. (2017). Chitosan-based silver nanoparticles: A study of the antibacterial, antileishmanial and cytotoxic effects. *Journal of Bioactive and Compatible Polymers*, 32(4), 397–410. <https://doi.org/10.1177/0883911516681329>
- 22 Bogdanović, U., Lazić, V., Vodnik, V., Budimir, M., Marković, Z., & Dimitrijević, S. (2014). Copper nanoparticles with high antimicrobial activity. *Materials Letters*, 128, 75–78. <https://doi.org/10.1016/j.matlet.2014.04.106>
- 23 Giannousi, K., Lafazanis, K., Arvanitidis, J., Pantazaki, A., & Dendrinou-Samara, C. (2014). Hydrothermal synthesis of copper-based nanoparticles: Antimicrobial screening and interaction with DNA. *Journal of Inorganic Biochemistry*, 133, 24–32. <https://doi.org/10.1016/j.jinorgbio.2013.12.009>
- 24 Cai, Y., Stromme, M., Melhus, A., Engqvist, H., & Welch, K. (2013). Photocatalytic inactivation of biofilms on bioactive dental adhesives. *Journal of Biomedical Materials Research Part B: Applied Biomaterials*, 102, 62–67. <https://doi.org/10.1002/jbm.b.32980>
- 25 Kim, J., Cho, H., Ryu, S., & Choi, M. (2000). Effects of metal ions on the activity of protein tyrosine phosphatase VHR: Highly potent and reversible oxidative inactivation by Cu<sup>2+</sup> ion. *Archives of Biochemistry and Biophysics*, 382, 72–80. <https://doi.org/10.1006/abbi.2000.1996>
- 26 Stohs, S. J., & Bagchi, D. (1995). Oxidative mechanisms in the toxicity of metal ions. *Free Radical Biology and Medicine*, 18, 321–336. [https://doi.org/10.1016/0891-5849\(94\)00159-h](https://doi.org/10.1016/0891-5849(94)00159-h)
- 27 Park, G. D., Kang, Y. C., & Cho, J. S. (2022). Morphological and electrochemical properties of ZnMn<sub>2</sub>O<sub>4</sub> nanopowders and their aggregated microspheres prepared by simple spray drying process. *Nanomaterials*, 12(4), 680. <https://doi.org/10.3390/nano12040680>

Sabina Z. Ismayilova<sup>1</sup>, Lala Sh. Guliyeva<sup>1</sup>, Rayyat H. Ismayilov<sup>1\*</sup>,  
Dilgam B. Tagiyev<sup>1</sup>, Fuad F. Valiyev<sup>2</sup>, Bahattin Yalcin<sup>3</sup>, Ajdar A. Medjidov<sup>1</sup>,  
Mansura T. Huseynova<sup>4</sup>, Su Y. Chien<sup>5</sup>, Gene H. Lee<sup>6</sup>, Shie M. Peng<sup>6</sup>

<sup>1</sup>*Institute of Catalysis and Inorganic Chemistry named after acad. M. Nagiyev,  
Ministry of Science and Education of the Republic of Azerbaijan, Baku, Azerbaijan;*

<sup>2</sup>*“OilGasScientificResearchProject” Institute, SOCAR, Baku, Azerbaijan;*

<sup>3</sup>*Department of Chemistry, Marmara University, Kadiköy, Istanbul, Türkiye;*

<sup>4</sup>*Institute of Chemistry and Additives, Ministry of Science and Education of the Republic of Azerbaijan, Baku, Azerbaijan;*

<sup>5</sup>*X-Ray Laboratory, Institute of Chemistry, Academia Sinica, Taiwan, China;*

<sup>6</sup>*Department of Chemistry, National Taiwan University, Taipei, Taiwan, China*

(\*Corresponding author's e-mail: [ismayilov.rayyat@gmail.com](mailto:ismayilov.rayyat@gmail.com))

## Synthesis and Structure of the Novel Mononuclear Copper(II) Complex of the Unsymmetrical Pyrimidine-Modulated Long-Chain Hexapyridylpentaamine Ligand

Through the pyrimidine-modulated hexapyridylpentaamine ligand N<sup>2</sup>-(pyridin-2-yl)-N<sup>6</sup>-(6-(((6-(pyrimidin-2-ylamino)pyridin-2-yl)amino)pyridin-2-yl)amino)pyridine-2,6-diamine (H<sub>5</sub>N<sub>11</sub>-tpm), a new mononuclear copper(II) complex [Cu(H<sub>5</sub>N<sub>11</sub>-tpm)](ClO<sub>4</sub>)<sub>2</sub> (**1**) were synthesized and structurally characterized. The single crystal X-ray analysis showed distorted trigonal bipyramidal geometry (Addison parameter value  $\tau = 0.69$ ) of the complex (**1**), which is well consistent with the “inverted type” of ESR spectra ( $g_{\parallel} < g_{\perp}$ ), measured magnetic susceptibility, and electronic spectroscopy studies. The equatorial copper-nitrogen distances (Cu–N(1) = 2.094(9) Å; Cu–N(5) = 2.045(9) Å; Cu–N(9) = 2.214(9) Å), along with the axial Cu–N distances (Cu–N(3) = 1.999(9) Å and Cu–N(7) = 2.001(9) Å), fall well within the range typically reported for Cu(II) complexes that incorporate this type of ligand. All Cu–N distances are short, ranging from 1.999(9) to 2.094(9) Å, which suggests a strong binding affinity of the chelating ligand. The monohelical H<sub>5</sub>N<sub>11</sub>-tpm ligand coordinates with the metal atom, exhibiting an all-anti conformation. The extensive hydrogen bonds were observed between the amino groups and uncoordinated perchlorate anions, resulting in the formation of a three-dimensional network (3D) of the complex. The synthesized complex has high potential for the creation of novel cholinesterase inhibitors since it contains a number of pyridine and pyrimidine rings.

**Keywords:** modulated oligo- $\alpha$ -aminopyridine ligand, long-chain ligand, copper complex, crystal structure, addison parameter, hydrogen bonds, spectroscopy, magnetic measurement

### Introduction

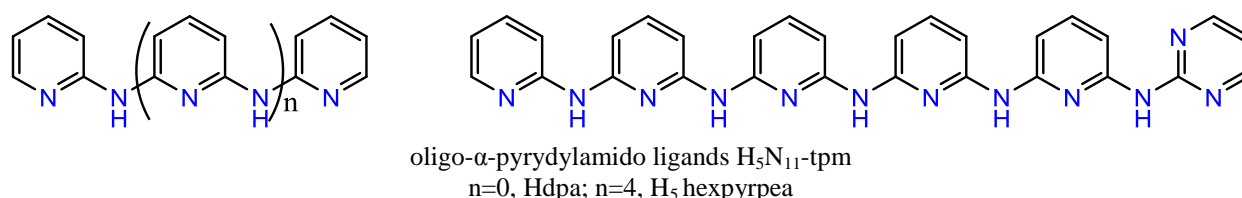
Oligo- $\alpha$ -pyridylamine ligands (Scheme 1) have garnered increasing interest over the past three decades due to their ability to synthesize metal string complexes, commonly referred to as “Extended Metal Atom Chain complexes” (EMACs), which have potential molecular electronic device applications, such as single-molecule transistors and molecular wires [1–4]. There are several ways that oligo- $\alpha$ -pyridylamido ligands coordinate with metal atoms. The supporting ligands in EMACs are coordinated to the metal in an all-syn form, while mononuclear complexes were shown to be coordinated in an all-anti form [5–7]. And anti-syn conformation was only observed in the dimers of free ligands [8]. The synthesis of long-chain metal string complexes is very important. This is directly related to their use as molecular wires. It is believed that if a metal-string complex contains 17 metal atoms, it can be described as a 1D (one-dimensional) infinite molecule [9]. However, the synthesis of long-chain metal strings based on traditional oligo- $\alpha$ -aminopyridine ligands is characterized by low yields and instability because of their oxidative decompositions [10].

For the development of oxidative degradation-resistant and extended metal chains, we have recently created a series of modulated oligo- $\alpha$ -pyridylamido ligands. This was achieved by substituting the pyridine rings with nitrogen-rich alternatives such as pyrazine, pyrimidine, and naphthyridine within the oligo- $\alpha$ -pyridylamine ligands (Scheme 1). Using pyrazine-modulated oligo- $\alpha$ -pyridylamine ligands, successfully syn-

thesized heptacobalt and nonachromium EMACs, which are the longest Co(II) and Cr(II) EMAC molecules obtained to date [9, 11].

The introduction of nitrogen-rich aromatic pyrazine rings has enabled ligand molecules to exhibit a variety of coordination modes, making them particularly versatile for the construction of coordination polymers. A series of one-dimensional (1D), two-dimensional (2D), and three-dimensional (3D) copper(II) coordination polymers using pyrazine-modulated N, N'-bis(a-pyridyl)-2,6-diaminopyridine ligands has been synthesized and studied [12]. Furthermore, our recent studies have demonstrated that the string complexes of nickel (II), mononuclear complexes, and coordination polymers of copper (II) with pyrazine/pyrimidine-modulated oligo- $\alpha$ -pyridylamino ligands exhibit significant biological activity [4, 7]. Therefore, it is of great interest to synthesize and determine the structure and characteristics of novel copper complexes with pyrazine/pyrimidine-modulated oligo- $\alpha$ -pyridylamine ligands.

In this paper, we present our latest findings in this area. We report, for the first time, the synthesis and characterization of the new mononuclear copper(II) complex,  $[\text{Cu}(\text{H}_5\text{N}_{11}\text{-tpm})](\text{ClO}_4)_2$  (**1**). This complex is derived from the unsymmetrical pyrimidine-modulated long-chain oligo- $\alpha$ -pyridylamino ligand  $\text{N}^2$ -(pyridin-2-yl)- $\text{N}^6$ -(6-((6-(pyrimidin-2-ylamino)pyridin-2-yl)amino)pyridin-2-yl)amino)pyridin-2-yl)pyridine-2,6-diamine ( $\text{H}_5\text{N}_{11}\text{-tpm}$ ). The inhibition effect of synthesized complex **1** against AChE and BChE enzymes, as well as the molecular docking and molecular dynamic simulation studies, will be the subject of an upcoming paper.



Scheme 1. Oligo- $\alpha$ -pyridylamines and their modulated analogues

## Experimental

### Materials and measurements

Commercially obtained chemicals and solvents were used without further purification unless otherwise noted. IR spectra were recorded on a Bruker Alpha FTIR spectrometer in the range of 400–4000  $\text{cm}^{-1}$ . Electronic spectra were recorded on a SPECORD 50 plus spectrophotometer in MeOH using cuvettes of 1 cm path length, and collected data were reported in  $\lambda_{\text{max}}/\text{nm}$ . The EPR spectrum of the copper complex was recorded in the solid state on a Bruker BioSpin GmbH spectrometer at room temperature. Elemental analyses were carried out on FlashEA 1112 Series CHNS-O Analyzer. Molar magnetic susceptibility was recorded on a SQUID system with 2 kOe external magnetic field.

### Preparation of Compounds

$\text{N}^2$ -(pyridin-2-yl)- $\text{N}^6$ -(6-((6-(pyrimidin-2-ylamino)pyridin-2-yl)amino)pyridin-2-yl)amino) pyridin-2-yl)pyridine-2,6-diamine ( $\text{H}_5\text{N}_{11}\text{-tpm}$ ) was synthesized by the palladium-catalysed cross-coupling of 2-aminopyrimidine and  $\text{N}^2$ -(6-bromopyridin-2-yl)- $\text{N}^6$ -(6-((6-(pyridin-2-ylamino)pyridin-2-yl)amino)pyridin-2-yl)pyridine-2,6-diamine in the presence of catalysts  $[\text{Pd}_2(\text{dba})_3]$ , BINAP,  $\text{Bu}^t\text{ONa}$  in refluxing benzene under argon, as described in our previously reported work [13, 14]. The work [14] also provides stages for obtaining  $\text{N}^2$ -(6-bromopyridin-2-yl)- $\text{N}^6$ -(6-((6-(pyridin-2-ylamino)pyridin-2-yl)amino)pyridin-2-yl)pyridine-2,6-diamine (Scheme 1S).

$[\text{Cu}(\text{H}_5\text{N}_{11}\text{-tpm})](\text{ClO}_4)_2$  (**1**). A mixture of  $\text{H}_5\text{N}_{11}\text{-tpm}$  (0.200 g, 0.37 mmol) and  $\text{Cu}(\text{ClO}_4)_2 \cdot 6\text{H}_2\text{O}$  (0.160 g, 0.43 mmol) in methanol (50 mL) was stirred overnight. The solution was then filtered to remove insoluble impurities and concentrated under vacuum. Diffusing ether into the  $\text{CH}_3\text{OH}$  solution provided blue single crystals suitable for X-ray analysis (0.382 g, 47 % yield). IR (KBr)  $\nu/\text{cm}^{-1}$ : 3440 w, 3310 w, 3249 w, 3206 w, 3075 s, 1652 s, 1564 s, 1533 m, 1490 s, 1467 s, 1448 s, 1409 s, 1426 m, 1211 m, 1140 s, 1041 s, 795 m, 498 w, 431; UV/Vis UV/Vis ( $\text{CH}_3\text{OH}$ )  $\lambda_{\text{max}}/\text{nm}$  ( $\epsilon/\text{dm}^3 \text{ mol}^{-1} \text{ cm}^{-1}$ ): 206 ( $1.23 \times 10^4$ ), 272 ( $3.37 \times 10^4$ ), 330 ( $3.10 \times 10^4$ ), 475 ( $1.05 \times 10^2$ ), 635 (54.5), 850 (47.8); Elemental analysis (%)  $\text{C}_{29}\text{H}_{24}\text{Cl}_2\text{CuN}_{12}\text{O}_8$ : calc. C 43.38, H 3.01, N 20.93; found: C 43.52, H 3.10, N 20.84.

### Crystal Structure Determinations

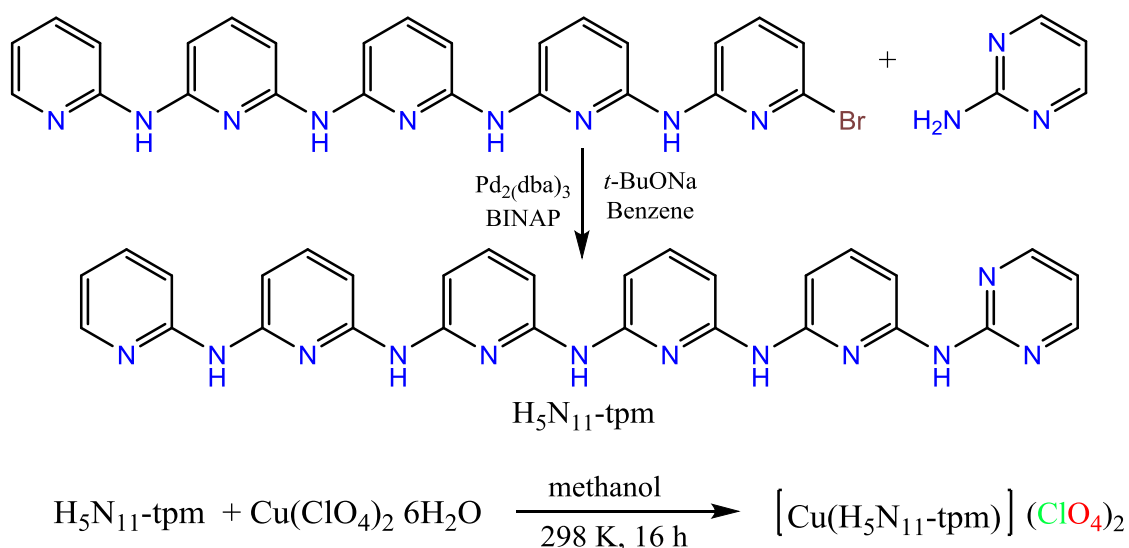
The suitable crystals of  $[\text{Cu}(\text{H}_5\text{N}_{11}\text{-tpm})](\text{ClO}_4)_2$  (**1**) was selected for data collection, which was performed on a NONIUS Kappa CCD diffractometer at 293 K using Mo-K $\alpha$  radiation ( $\lambda = 0.71073 \text{ \AA}$ ). The structure was solved by direct methods using SHELXS-2013 [15] and refined by full-matrix least-squares methods on  $F^2$  using SHELXL-2018 [16]. All non-hydrogen atoms were refined with anisotropic parameters. The hydrogen atoms were located from different maps and then refined as riding atoms with a C-H distance of 0.95 Å and a N-H distance of 0.88 Å. The other H atoms were located in a difference map refined freely. Molecular graphics were created using MERCURY programs. Below are the specifics of the X-ray diffraction experiment and a summary of the crystallographic data for the copper(II) complex **1**:

Empirical formula  $\text{C}_{29}\text{H}_{24}\text{Cl}_2\text{CuN}_{12}\text{O}_8$ ; formula weight = 803.4; crystal system—orthorhombic; space group—*Pbcn*;  $a = 11.8184(3)$ ,  $b = 20.8835(2)$ ,  $c = 26.3509(7) \text{ \AA}$ ;  $\alpha = \beta = 90^\circ$ ; volume =  $6503.7(3) \text{ \AA}^3$ ,  $Z = 8$ ; density (calculated) =  $1.640 \text{ g/cm}^3$ ; absorption coefficient =  $0.908 \text{ mm}^{-1}$ ; crystal size:  $0.17 \times 0.15 \times 0.08 \text{ mm}^3$ ;  $\theta$  range for data collection  $1.546\text{--}24.122^\circ$ ; reflection collected—18457, independent reflection—4878 [ $R(\text{int}) = 0.0804$ ];  $R_1 = 0.1114$ ,  $wR_2 = 0.2711$ ;  $R_1(\text{all data}) = 0.1465$ ,  $wR_2(\text{all data}) = 0.2879$ ; GOF = 1.152.

### Results and Discussion

#### Syntheses and Structures

$\text{N}^2$ -(pyridin-2-yl)- $\text{N}^6$ -(6-((6-((6-(pyrimidin-2-ylamino)pyridin-2-yl)amino)pyridin-2-yl)amino)pyridin-2-yl)pyridine-2,6-diamine ( $\text{H}_5\text{N}_{11}\text{-tpm}$ ) was synthesized according to our previously reported work [13].



Scheme 2. The synthesis of  $\text{H}_5\text{N}_{11}\text{-tpm}$  and its copper(II) complex **1**

The Cu(II) complex **1** was synthesized by treating of pyrimidine-modulated long-chain  $\text{H}_5\text{N}_{11}\text{-tpm}$  ligand and  $\text{Cu}(\text{ClO}_4)_2 \cdot 6\text{H}_2\text{O}$  in methanol. Slow diffusion of the solution with ether gave light blue single crystals suitable for X-ray diffraction. The structure of complex **1** is established by various spectroscopic methods (IR, UV-Vis, ESR) and the single X-ray crystallography. The obtained complex was found to be stable in air and dissolved well in common polar solvents like methanol, dimethyl sulfoxide (DMSO), and dimethylformamide (DMF). According to X-ray diffraction studies complex **1** crystallizes in the orthorhombic crystal system with the *Pbcn* space group. An ORTEP diagram of **1** including the atomic numbering scheme is depicted in Figure 1, and the important bond lengths and angles in the structure are given in Table 1.

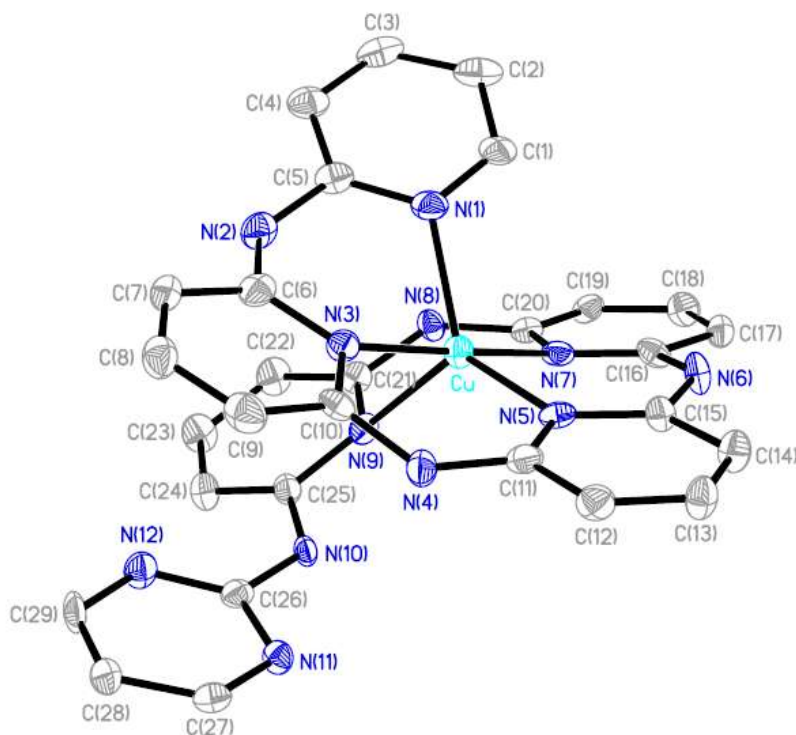


Figure 1. The molecular structure of  $[\text{Cu}(\text{H}_5\text{N}_{11}\text{-tpm})](\text{ClO}_4)_2$  **1**. Atoms are drawn at the 50 % probability level and hydrogen atoms are omitted for clarity

Table 1

Selected bond distances (Å) and bond angles (°) for complex **1**

Bond lengths for complex 1, Å		
Cu–N(1)	2.094(9)	Cu–N(7) 2.001(9)
Cu–N(3)	1.999(9)	Cu–N(9) 2.214(9)
Cu–N(5)	2.045(9)	
Bond angles for complex 1, °		
N(3)–Cu–N(7)	173.6(4)	N(3)–Cu–N(1) 88.7(4)
N(1)–Cu–N(5)	132.3(4)	N(3)–Cu–N(5) 93.5(4)
N(1)–Cu–N(9)	100.3(3)	N(3)–Cu–N(9) 89.6(4)
N(5)–Cu–N(9)	127.4(4)	N(7)–Cu–N(5) 92.8(4)

In this complex the nitrogen atoms of the amino groups are uncoordinated to Cu(II) center. It is noticeable that the uncoordinated amine nitrogen atoms are more characteristic for the coordination polymers and mononuclear Cu(II) complexes of the modulated oligo- $\alpha$ -pyridylamine ligands with perchlorate, nitrate, and chloride anions [4, 12, 17]. However, in all cases known to us, the deprotonation of oligo- $\alpha$ -pyridyl amido ligands modulated with nitrogen-containing heterocycles occurs when they interact with copper(II) acetate. In the process of creating the tetranuclear copper(II) complex  $[\text{Cu}_4(\text{Hdpzpd})_2(\text{CH}_3\text{COO})_6]$  with the  $\text{H}_2\text{dpzpd}$  ligand and the copper(II) coordination polymer  $\{\text{Cu}(\text{mpmpza})(\text{CH}_3\text{COO})(\text{H}_2\text{O})\}$  with the  $\text{Hmpmpza}$  ligand, we have previously seen deprotonation of the pyrazine-modulated oligo- $\alpha$ -aminopyridine ligands [6, 7].

The Cu(II) center in complex **1** is five-coordinated and adopts a distorted trigonal bipyramidal geometry by coordinating five pyridine ring nitrogen atoms of  $\text{H}_5\text{N}_{11}\text{-tpm}$ . The equatorial plane of complex **1** consists of three pyridyl nitrogen atoms (N1, N5, N9), while the axial positions are occupied by two nitrogen atoms (N3 and N7) from the pyridyl rings of the  $\text{H}_5\text{N}_{11}\text{-tpm}$  ligand (Fig. 2). This arrangement results in an overall distorted trigonal bipyramidal stereochemistry. The trigonality index  $\tau$  is calculated by analysing  $\alpha$  and  $\beta$  (the largest angles around the Cu(II) ion), and it was found to be  $\tau = 0.69$  for complex **1**. Since the observed  $\tau = 0$  and 1 have been assigned to perfectly square pyramidal and trigonal bipyramidal geometries, the geometry



around the Cu(II) center in complex **1** could be described as distorted trigonal bipyramidal. The equatorial copper-nitrogen distances (Cu–N(1) = 2.094(9) Å; Cu–N(5) = 2.045(9) Å; Cu–N(9) = 2.214(9) Å), as well as axial Cu–N distances (Cu–N(3) = 1.999(9) Å and Cu–N(7) = 2.001(9) Å), are well within the range reported for Cu(II) complexes with this type of nitrogen-containing heterocyclic ligand [4, 12, 17, 18]. In complex **1**, except for the Cu–N(9) distance (2.214(9) Å), all Cu–N distances are short, ranging from 1.999(9) to 2.094(9) Å, indicating a strong binding of the chelating ligand.

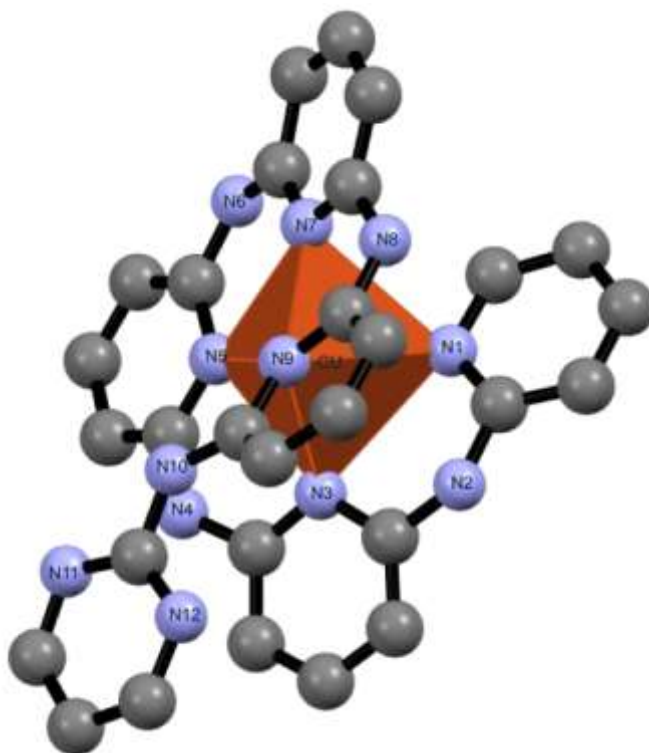


Figure 2. The distorted trigonal bipyramidal geometry environment of Cu(II) in  $[\text{Cu}(\text{H}_5\text{N}_{11}\text{-tpm})]^{2+}$

In complex **1**, the monohelical hexadentate ligand  $\text{H}_5\text{N}_{11}\text{-tpm}$  coordinates with the metal atom, adopting an all-anti conformation. The pyridyl groups of the ligand are planar, and the dihedral angles between planes Py(N1)-Py(N3), Py(N3)-Py(N5), Py(N5)-Py(N7), Py(N7)-Py(N9), and Py(N9)-Py(N11) are  $25.6(5)^\circ$ ,  $20.4(5)^\circ$ ,  $11.6(3)^\circ$ ,  $27.7(4)^\circ$ , and  $31.9(4)^\circ$ , respectively. The crystal lattice of compound **1** contains no solvent molecules. Non-coordinated perchlorate ions act as counter-ions within its crystal structure. Complex **1** was found to have extensive intra- (N(3)⋯N(10) = 3.076 Å, N(1)⋯N(8) = 2.960 Å) and intermolecular hydrogen bonding. Intermolecular hydrogen bonds (HBs) between the amino group and uncoordinated perchlorate anions (N(6)⋯O(4) = 2.988 Å and N(8)⋯O(10) = 2.957 Å) create complex **1**'s three-dimensional network. These hydrogen bonds are essential for maintaining the system's overall stability.

#### IR, UV-Vis, EPR Spectroscopy and Magnetic Properties

The IR bands associated with the C=C and C=N vibrations in aromatic rings for complex **1** were observed in the range of  $1650\text{--}1422\text{ cm}^{-1}$ . Complex **1** exhibited a series of absorption bands within the range of  $3448\text{--}3111\text{ cm}^{-1}$ , which are characteristic of the N–H bonds present in the amine groups (Fig. 1S and Fig. 2S). The strong bands observed at  $1040\text{--}1148\text{ cm}^{-1}$  are attributed to the  $\text{ClO}_4^-$  anions. The Far-IR spectra of compound **1** displayed a band at  $431\text{ cm}^{-1}$ , which was assigned to the  $\nu(\text{Cu}\text{--}\text{N})$  vibration.

The assignment of electronic spectra for Cu(II) complexes has been thoroughly examined in the literature [19–21]. The electronic spectra of complex **1** were recorded at room temperature in a methanol solution, revealing six bands at wavelengths of 206, 272, 330, 475, 635, and 850 nm (Fig. 3). Compared to  $\text{H}_5\text{N}_{11}\text{-tpm}$ , which exhibited absorption at 210, 260, and 310 nm, the band observed at 475 nm for compound **1**, within the visible region of the electronic spectra, can be attributed to a charge transfer between the ligand and the metal center. Weak, broad bands centered at 635 nm and 850 nm in the electronic spectra of **1** were related to d–d transitions [19]. The result obtained is consistent with a trigonal-bipyramidal ligand environment for



Cu(II) ions in **1**, which is further corroborated by X-ray structural analysis. By comparing the electronic spectra of the complexes in methanol solution and Nujol suspension (in the solid state), it was discovered that their structure remained unaltered (Fig. 3S). Using absorbance spectroscopy, similar findings have already been reached for other Cu(II) complexes [7, 22].

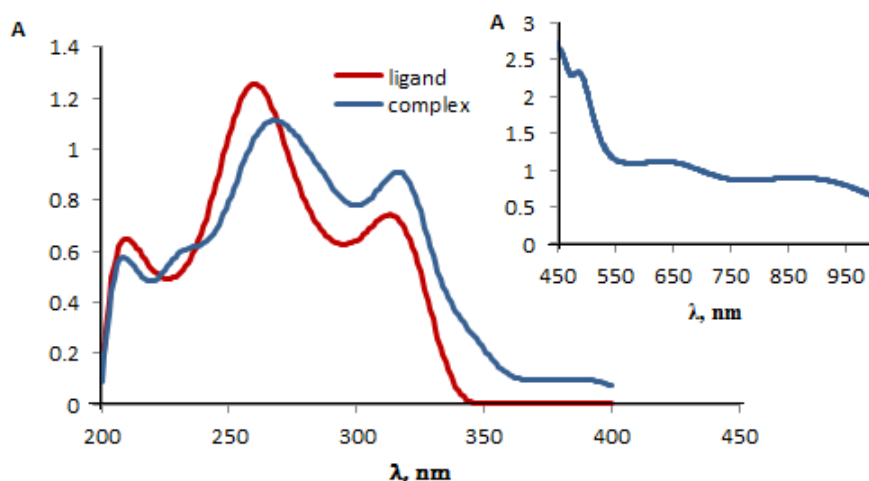


Figure 3. Electronic spectra of the  $H_5N_{11}$ -tpm ligand and its Cu(II) complex —  $[Cu(H_5N_{11}\text{-tpm})](ClO_4)_2$  **1** in methanol solution

The EPR spectra of complex **1** were recorded at room temperature in the polycrystalline state to analyze the coordination environment surrounding the Cu(II) ion and to determine the geometry of the complex (Fig. 4).

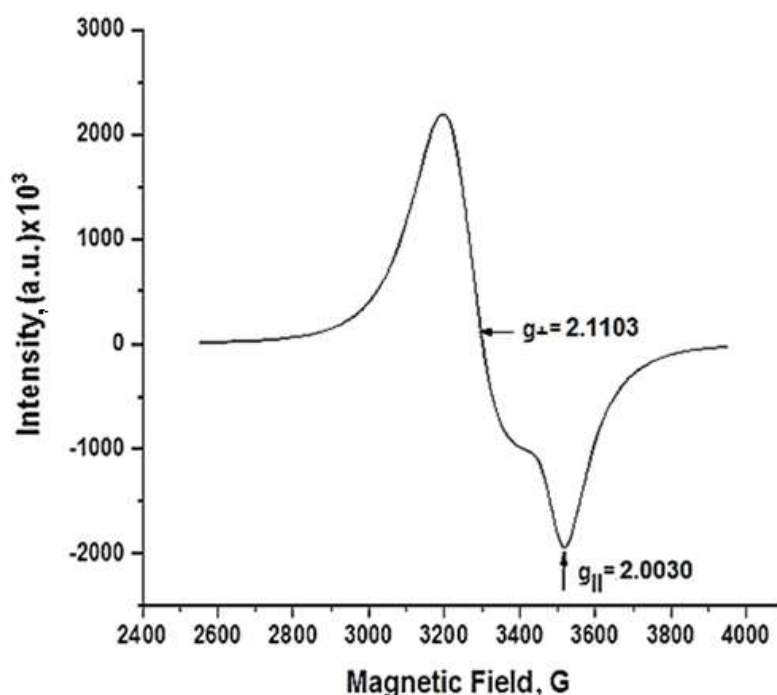


Figure 4. EPR spectrum of powder sample of the Cu(II) complex **1** at room temperature

The EPR spectra of complex **1** displayed a broad signal, with  $g_{\parallel}$  recorded at 2.0030 and  $g_{\perp}$  at 2.1103, suggesting pentacoordinate geometry around the metal atom. The  $g$  parameters indicate that the paramagnetic center shows axial symmetry, characterized by “inverted type” EPR spectra, where  $g_{\parallel} < g_{\perp}$ . It is well known that for  $Cu(II)N_5$  polyhedrons, two different geometric arrangements, the trigonal bipyramidal geometry (TBP) (symmetry  $D_{3h}$ ) and the square pyramidal geometry (SP) (symmetry  $D_{4v}$ ), are possible. Square

pyramidal geometry is ruled out for pentacoordinate complexes with  $g_{\perp}$  values bigger than  $g_{\parallel}$ , which are suggestive of distorted trigonal bipyramidal geometry [23, 24]. So, from the order of  $g_{\perp} > g_{\parallel} \sim g_e$  (free electron  $g$  value,  $g_e = 2.0023$ ), it can be concluded that Cu(II) ion in complex **1** is located in the distorted triangular bipyramid arrangement and the ground state of the unpaired electron is  $d_{z^2}$ . The results obtained from EPR are in excellent agreement with the single crystal analysis data for complex **1**. The  $\mu_{\text{eff}}$  value of complex **1** at room temperature (300 K) was 1.80 B.M., slightly higher than the expected spin-only value for a non-interacting Cu(II) ion (1.73 B.M.).

### Conclusions

The pyrimidine-modulated long-chain oligo- $\alpha$ -pyridylamino ligand  $N^2$ -(pyridin-2-yl)- $N^6$ -(6-(((6-((6-(pyrimidin-2-ylamino)pyridin-2-yl)amino)pyridin-2-yl)amino)pyridine-2,6-diamine ( $H_5N_{11}$ -tpm) has been used to synthesize and structurally characterize the novel mononuclear Cu(II) complex. In Cu(II) complex  $[Cu(H_5N_{11}\text{-tpm})](ClO_4)_2$  (**1**),  $H_5N_{11}$ -tpm functions as a pentadentate ligand and coordinates to a metal atom in an all-anti mode as a monohelix. The amino groups' nitrogen atoms are not coordinated to the metal center. The computed Addison parameter value of  $\tau = 0.69$  for Cu(II) establishes the distorted trigonal bipyramidal geometry of the copper (II) core in complex **1**. Complex **1** builds extensive hydrogen bonds to construct 3D networks. The synthesized complex has high potential for the creation of novel cholinesterase inhibitors and medications to treat particular illnesses since it contains a number of nitrogen-containing heterocycles, such as pyridine and pyrimidine.

### Supporting Information

The Supporting Information is available free at <https://ejc.buketov.edu.kz/ejc/article/view/420/320>

CCDC 2443681 contains the supplementary crystallographic data for compound **1**. These data can be obtained free of charge from the Cambridge Crystallographic Data Centre via [www.ccdc.cam.ac.uk/data\\_request/cif](http://www.ccdc.cam.ac.uk/data_request/cif), or from the Cambridge Crystallographic Data Centre, 12 Union Road, Cambridge CB2 EZ, UK; fax: (+44) 1223-336-033; or e-mail: [deposit@ccdc.cam.ac.uk](mailto:deposit@ccdc.cam.ac.uk)

### Author Information\*

\*The authors' names are presented in the following order: First Name, Middle Name and Last Name

**Sabina Zahid Ismayilova** — Candidate of Chemical Sciences, Senior Researcher, Acad. M. Nagiyev Institute of Catalysis and Inorganic Chemistry, Ministry of Science and Education of the Republic of Azerbaijan, H. Javid ave., 113, AZ 1143 Baku, Azerbaijan; e-mail: [sabina.chemistry.1986@mail.ru](mailto:sabina.chemistry.1986@mail.ru); <https://orcid.org/0000-0002-3957-7996>

**Lala Shahin Guliyeva** — PhD student, Junior Researcher, Acad. M. Nagiyev Institute of Catalysis and Inorganic Chemistry, Ministry of Science and Education of the Republic of Azerbaijan, H. Javid ave., 113, AZ 1143 Baku, Azerbaijan; e-mail: [lalasabili92@gmail.com](mailto:lalasabili92@gmail.com); <https://orcid.org/0009-0000-8477-916X>

**Rayyat Huseyn Ismayilov** (*corresponding author*) — Doctor of Chemical Sciences, Senior Researcher, Acad. M. Nagiyev Institute of Catalysis and Inorganic Chemistry, Ministry of Science and Education of the Republic of Azerbaijan, H. Javid ave., 113, AZ 1143 Baku, Azerbaijan; e-mail: [ismayilov.rayyat@gmail.com](mailto:ismayilov.rayyat@gmail.com); <https://orcid.org/0009-0004-7753-6468>

**Dilgam Babir Tagiyev** — Doctor of Chemical Sciences, Director, Acad. M. Nagiyev Institute of Catalysis and Inorganic Chemistry, Ministry of Science and Education of the Republic of Azerbaijan, H. Javid ave., 113, AZ 1143 Baku, Azerbaijan; e-mail: [dtagiyev@rambler.ru](mailto:dtagiyev@rambler.ru); <https://orcid.org/0000-0002-8312-2980>

**Fuad Famil Valiyev** — Candidate of Chemical Sciences, Leading Researcher, "OilGasScientific-ResearchProject" Institute, SOCAR, AZ 1122 Baku, Azerbaijan; e-mail: [fuadfamilvaliyev@gmail.com](mailto:fuadfamilvaliyev@gmail.com); <https://orcid.org/0009-0004-1120-8728>

**Bahattin Yalcin** — Doctor of Chemical Sciences, Professor, Department of Chemistry, Marmara University, 34722 / Kadiköy -Istanbul, Türkiye; e-mail: [byalcin@marmara.edu.tr](mailto:byalcin@marmara.edu.tr); <https://orcid.org/0000-0003-4448-1101>

**Ajdar Akber Medjidov** — Doctor of Chemical Sciences, Head of Laboratory, Acad. M. Nagiyev Institute of Catalysis and Inorganic Chemistry, Ministry of Science and Education of the Republic of Azerbaijan,

H. Javid ave., 113, AZ 1143 Baku, Azerbaijan; e-mail: [ajdarmedjidov@gmail.com](mailto:ajdarmedjidov@gmail.com); <https://orcid.org/0000-0002-1766-5450>

**Mansura Teyfur Huseynova** — Candidate of Chemical Sciences, Head of Laboratory, Institute of Chemistry and Additives, Ministry of Science and Education of the Republic of Azerbaijan, AZ 1029 Baku, Azerbaijan; e-mail: [huseynovamansura@gmail.com](mailto:huseynovamansura@gmail.com); <https://orcid.org/0000-0002-1534-6819>

**Su-Ying Chien** — Candidate of Chemical Sciences, Postdoc at Single Crystal XRD Lab, X-Ray Laboratory, Institute of Chemistry, Academia Sinica, 128 Academia Road, Section 2, Nankang, Taipei 115201, Taiwan, China; e-mail: [suyingchien@as.edu.tw](mailto:suyingchien@as.edu.tw); <https://orcid.org/0009-0008-0931-3149>

**Gene-Hsiatig Lee** — Candidate of Chemical Sciences, Project Research Fellow Instrumentation Center, Department of Chemistry, National Taiwan University, 10617 Taipei, Taiwan, China; e-mail: [ghlee@ntu.edu.tw](mailto:ghlee@ntu.edu.tw); <https://orcid.org/0000-0003-1218-8082>

**Shie-Ming Peng** — Doctor of Chemical Sciences, Distinguished Chair Professor for Research, Department of Chemistry, National Taiwan University, 10617 Taipei, Taiwan, China; e-mail: [smpeng@ntu.edu.tw](mailto:smpeng@ntu.edu.tw); <https://orcid.org/0000-0003-1412-5018>

#### Author Contributions

The manuscript was written through contributions of all authors. All authors have given approval to the final version of the manuscript. **CRedit**: **Sabina Zahid Ismayilova** data curation, validation, writing-original draft; **Lala Shahin Guliyeva** data curation, formal analysis, visualization; **Rayyat Huseyn Ismayilov** data curation, conceptualization, visualization, writing-review & editing; **Dilgam Babir Tagiyev** conceptualization, supervision, validation; **Fuad Famil Valiyev** data curation, formal analysis; **Bahattin Yalcin** supervision, validation; **Ajdar Akber Medjidov** methodology, supervision; **Mansura Teyfur Huseynova** data curation, validation; **Su-Ying Chien** data curation, formal analysis, investigation; **Gene-Hsiatig Lee** data curation, formal analysis; **Shie-Ming Peng** conceptualization, supervision.

#### Conflicts of Interest

The authors declare no conflict of interest.

#### References

- 1 Berry, J.F., Cotton, F.A., Daniels, L.M., & Murillo, C.A. (2002). Trinickel Dipyriddydamido Complex with Metal-Metal Bonding Interaction: Prelude to Polynickel Molecular Wires and Devices. *J. Am. Chem. Soc.*, 124, 3212–3213. <https://doi.org/10.1021/ja025543i>
- 2 Ting, T.C., Hsu, L.Y., Huang, M.J., Horng, E.C., Lu, H.C., Hsu, C.H., Jiang, C.H., Jin, B.Y., Peng, S.M., & Chen, C.H. (2015). Energy-Level Alignment for Single-Molecule Conductance of Extended Metal-Atom Chains. *Angew. Chem. Int. Ed.*, 54, 15734–15738. <https://doi.org/10.1002/anie.201508199>
- 3 Ismayilov, R.H., Ismayilova, S.Z., Tagiyev, D.B., Medjidov, A.A., Jafarov, Y.I., Wang, W.Z., Yeh, C.Y., Chien, S.Y., Lee, G.H., & Peng, S.M. (2025). Linear nonanuclear chromium(II) complex with pyrazine-modulated pentapyridyltetraamine ligand: Synthesis, structure and properties. *J. Mol. Struct.* 1331, 141592. <https://doi.org/10.1016/j.molstruc.2025.141592>
- 4 Ismayilov, R.H., Valiyev, F.F., Tagiyev, D.B., Song, Y., Medjidov, A.A., Fatullayeva, P.A., Tüzün, B., Taslimi, P., Peng, C.H., Chien, S.Y., Lee, G.H., & Peng, S.M. (2024). Trinuclear nickel (II) string complexes and copper (II) coordination polymer with pyrazine modulated unsymmetrical dipyriddydamino ligand: Synthesis, structure and bioactivity properties with molecular docking. *J. Mol. Struct.*, 1307, 137966. <https://doi.org/10.1016/j.molstruc.2024.137966>
- 5 Chae, D.H., Berry, J.F., Jung, S., Cotton, F.A., Murillo, C.A., & Yao, Z. (2006). Vibrational Excitations in Single Trimetal-Molecule Transistors. *Nano Lett.*, 6, 165–168. <https://doi.org/10.1021/nl0519027>
- 6 Ismayilov, R.H., Valiyev, F.F., Tagiyev, D.B., Song, Y., Israfilov, N.V., Wang, W.-Z., Lee, G.-H., Peng, S.-M., & Suleimanov, B.A. (2018). Linear pentanuclear nickel(II) and tetranuclear copper(II) complexes with pyrazine-modulated tripyridyldiamine ligand: Synthesis, structure and properties. *Inorganica Chimica Acta* 483, 386–391. <https://doi.org/10.1016/j.ica.2018.08.045>
- 7 Abbasova, G.G., Ismayilov, R.H., Tagiyev, D.B., Şenol, H., Song, Y., Medjidov, A.A., Huseynova, M.T., Fatullaeva, P.A., Taslimi, P., Sadeghian, N., Lee, G.H., & Peng, S.M. (2024). Synthesis, characterization, crystal structure, molecular dynamics simulations, MM-GBSA analysis, and bioactivity studies of pyrazine- and pyrimidine-modulated unsymmetrical dipyriddydamide complexes. *J. Mol. Struct.*, 1315, 138896. <https://doi.org/10.1016/j.molstruc.2024.138896>
- 8 Brogden, D.W. & Berry, J.F. (2015). Coordination Chemistry of 2,2'-Dipyridylamine: The Gift That Keeps on Giving. *Comments Inorg. Chem.*, 17–37. <https://doi.org/10.1080/02603594.2015.1079522>

- 9 Ismayilov, R.H., Wang, W.Z., Wang, R.R., Yeh, C.Y., Lee, G.H., & Peng, S.M. (2007). Four quadruple metal–metal bonds lined up: linear nonachromium(II) metal string complexes. *Chem. Commun.* 1121–1123. <https://doi.org/10.1039/B614597C>
- 10 Yeh, C.Y., Wang, C.C., Chen, Y.H., & Peng, S.M. (2006). *Redox Systems Under Nano-Space Control*. Springer Berlin Heidelberg. <https://doi.org/10.1007/3-540-29580-1>
- 11 Wang, W.Z., Ismayilov, R.H., Lee, G.H., Liu, I.P.C., Yeh, C.Y., & Peng, S.M. (2007). The nano-scale molecule with the longest delocalized metal–metal bonds: linear heptacobalt(II) metal string complexes  $[\text{Co}_7(\mu_7\text{-L})_4\text{X}_2]$ . *Dalton Trans.*, 830–839. <https://doi.org/10.1039/B614661A>
- 12 Ismayilov, R.H., Wang, W.Z., Lee, G.H., & Peng, S.M. (2006). One-, two- and three-dimensional Cu(II) complexes built via new oligopyrazinediamine ligands: from antiferromagnetic to ferromagnetic coupling. *Dalton Trans.*, 478–491. <https://doi.org/10.1039/B507485A>
- 13 Guliyeva, L.Sh., Ismayilova, S.Z., Ismayilov, R.H., Tagiyev, D.B., Yalcin, B., Medjidov, A.A., Peng, C.H., Chien, S.Y., & Lee, G.H. (2025, June 3–5). Copper(II) monohelix complex with pyrimidine-modulated long-chain oligo- $\alpha$ -aminopyridine ligand: Synthesis and crystal structure. In *International UFAZ Conference: Chemistry, Process, Materials* (pp. 42–43).
- 14 Hasanov, H., Tan, U.K., Wang, R.R., Lee, G.H., & Peng, S.M. (2004). Synthesis of long-chained oligo- $\alpha$ -aminopyridines by tandem Pd-catalyzed cross-coupling aminations and their helical dinuclear complexes. *Tetrahedron Letters*, 7765–7769. <https://doi.org/10.1016/j.tetlet.2004.08.066>
- 15 Sheldrick, G.M. (2008). A short history of SHELX. *Acta Cryst.*, A64, 112. <http://dx.doi.org/10.1107/S0108767307043930>
- 16 Sheldrick, G.M. (2015). Crystal structure refinement with SHELXL. *Acta Cryst.* C71, 3–8. <http://dx.doi.org/10.1107/S2053229614024218>
- 17 Ismayilova, S.Z., Ismayilov, R.H., Tagiyev, D.B., Yalcin, B., Şahin, O., Medjidov, A.A., Huseynova, M.T., Guliyeva, L.Sh., Gasimov, R.J., & Peng, S.M. (2025). Copper(II) complex of the pyrazine-modulated oligo- $\alpha$ -aminopyridine as a coordination polymers' promising building block. *Chem. Probl.*, 4(23), 476–482. <https://doi.org/10.32737/2221-8688-2025-4-476-482>
- 18 Ismayilova, S.Z., Huseynova, M.T., Ismayilov, R.H., & Medjidov, A.A. (2024). Synthesis and properties of Cu<sup>II</sup> complex of benzidine-N,N,N',N'-tetraacetic acid. *Azerbaijan Chem. J.*, 3, 69–75. <https://doi.org/10.32737/0005-2531-2024-3-69-75>
- 19 Vicente, M., Bastida, R., Macías, A., Valencia, L., Geraldes, C.F.G.C., & Brondino, C.D. (2005). Copper complexes with new oxaza-pendant-armed macrocyclic ligands: X-ray crystal structure of a macrocyclic copper(II) complex. *Inorg. Chim. Acta*, 358, 1141–1150. <https://doi.org/10.1016/j.ica.2004.11.006>
- 20 Aljahdali, M., & EL-Sherif, A.A. (2013). Synthesis, characterization, molecular modeling and biological activity of mixed ligand complexes of Cu(II), Ni(II) and Co(II) based on 1,10-phenanthroline and novel thiosemicarbazone. *Inorg. Chim. Acta*, 407, 58–68. <https://doi.org/10.1016/j.ica.2013.06.040>
- 21 Chandra, S., & Gupta, L.K. (2005). EPR, mass, IR, electronic, and magnetic studies on copper(II) complexes of semicarbazones and thiosemicarbazones. *Spectrochimica Acta Part A*, 61, 269–275. <https://doi.org/10.1016/j.saa.2004.03.040>
- 22 Jozefikova, F., Perontsis, S., Konarikova, K., Svorc, L., Mazúr, M., Psomas, G., & Moncol, J. (2022). *In vitro* biological activity of copper(II) complexes with NSAIDs and nicotinamide: Characterization, DNA- and BSA-interaction study and anticancer activity. *J. Inorg. Biochem.*, 228, 111696. <https://doi.org/10.1016/j.jinorgbio.2021.111696>
- 23 Valko, M., Pelikán, P., Biskupič, S., & Mazúr, M. (1990). ESR spectra of copper(II) complexes in the solids. *Chem. Papers*, 44, 805–813.
- 24 Korkmaz, Ş.A., Karadağ, A., Yerli Y., & Soylu, M.S. (2014). Synthesis and characterization of new heterometallic cyanido complexes based on  $[\text{Co}(\text{CN})_6]^{3-}$  building blocks: crystal structure of  $[\text{Cu}_2(\text{N-bishydeten})_2\text{Co}(\text{CN})_6] \cdot 3\text{H}_2\text{O}$  having a strong antiferromagnetic exchange. *New. Chem.* 38, 5402–5410. <https://doi.org/10.1039/C4NJ00737A>

Zulfiqar Ali Shahid<sup>ib</sup>, Rukhsana Tabassum<sup>id\*</sup>

*Institute of Chemistry, Islamia University of Bahawalpur, Bahawalpur, Pakistan*  
(\*Corresponding author's e-mail: [rukhsana.tabassum@iub.edu.pk](mailto:rukhsana.tabassum@iub.edu.pk))

## Mn(II) and Zn(II) Complexes of a Coumarin Derivative: Synthesis, Characterization and Biological Potential

This study focused on the synthesis, characterization and biological evaluation of coumarin derivatives and their metal complexes. The synthesized compounds were characterized using spectroscopic techniques, including FTIR, <sup>1</sup>H NMR, <sup>13</sup>C NMR, X-ray diffraction (XRD), and thermal analysis, with mass spectrometry confirming their molecular weights. Notably, the XRD analysis revealed crystal sizes of 4.092 nm for ZL16, 4.34 nm for ZL16Mn, and 1.57 nm for ZL16Zn. FTIR analysis confirmed the presence of the –N=N– group, and comparative UV-Visible spectra validated the successful synthesis of new coumarin compounds. Antibacterial activity of synthesized compounds was evaluated against gram-negative and gram-positive bacteria using the disc diffusion method, with inhibition zones ranging from 7–31 mm, compared to the standard drug Amikacin, which had a zone of 15 mm. Antioxidant activity was assessed with IC<sub>50</sub> values between 5.65–11.84 µg/mL for DPPH and 5.89–11.20 µg/mL for NO, compared to ascorbic acid. Molecular Docking analysis revealed strong binding interactions between the synthesized compounds and the Mannosyl-oligosaccharide glucosidase and Oligo-1,6-glucosidase enzymes, with binding energies ranging from –9.8 to –10.9 kcal/mol. These findings contribute to the field of medicinal chemistry, highlighting the potential of these compounds as therapeutic agents. Further investigations are required at molecular level to explore their full therapeutic potential.

**Keywords:** coumarin derivatives, manganese, zinc metal complexes, antioxidant activity, antibacterial activity, molecular docking, X-ray diffraction, thermal analysis, antidiabetic

### Introduction

The term *coumarins* comes from the French word *coumarou*, meaning “tonka bean”. The study of coumarin began in 1820 when Vogel first extracted it from tonka beans [1]. Coumarins are basically known for its vanilla-like or freshly-mowed hay-like fragrance. It is white crystalline powder with a sweet aromatic odour with certain nutty shadings [2]. Coumarin derivatives are gaining significant attention in the field of medicine due to their physiological activity [3]. These compounds have shown promising potential in metal-based drug chemistry for the treatment of sensitive cancers [4]. Coumarin, a type of heterocyclic organic compound, is widely utilized in analytical and biological fields [5]. It contains a benzopyrone ring with an oxygen functional group, making it an effective donor. It also have a wide range of applications, including being used as anticoagulants, spasmolytic, anticancer drugs, antibacterial, antithrombotic, vasodilatory, antioxidant effects, and plant growth regulators as given in Figure 1 [6]. Based on these findings, a Schiff base ligand containing coumarin moieties was synthesized, along with its metal complexes, and their antimicrobial and antioxidant activities were studied [7]. Metal complexes of coumarins have been extensively studied for their medicinal applications and have shown greater biological activity compared to their ligands [8]. The chelating ability of coumarin derivatives, enhances their biological activity [9]. Additionally, synthetic coumarins have found applications as fluorescent brightening agents [10]. In a specific study, bivalent metal complexes of a coumarin derivatives were synthesized and evaluated spectroscopically and biologically [11]. Schiff bases, another class of ligands, have interesting coordination modes towards various metals and have been studied for their biological applications [12]. Coumarin derivatives, particularly hydroxycoumarins, exhibit antioxidant properties and metal chelating abilities [13]. The antioxidant activity of metal complexes is influenced by both the metal and the ligands [14].



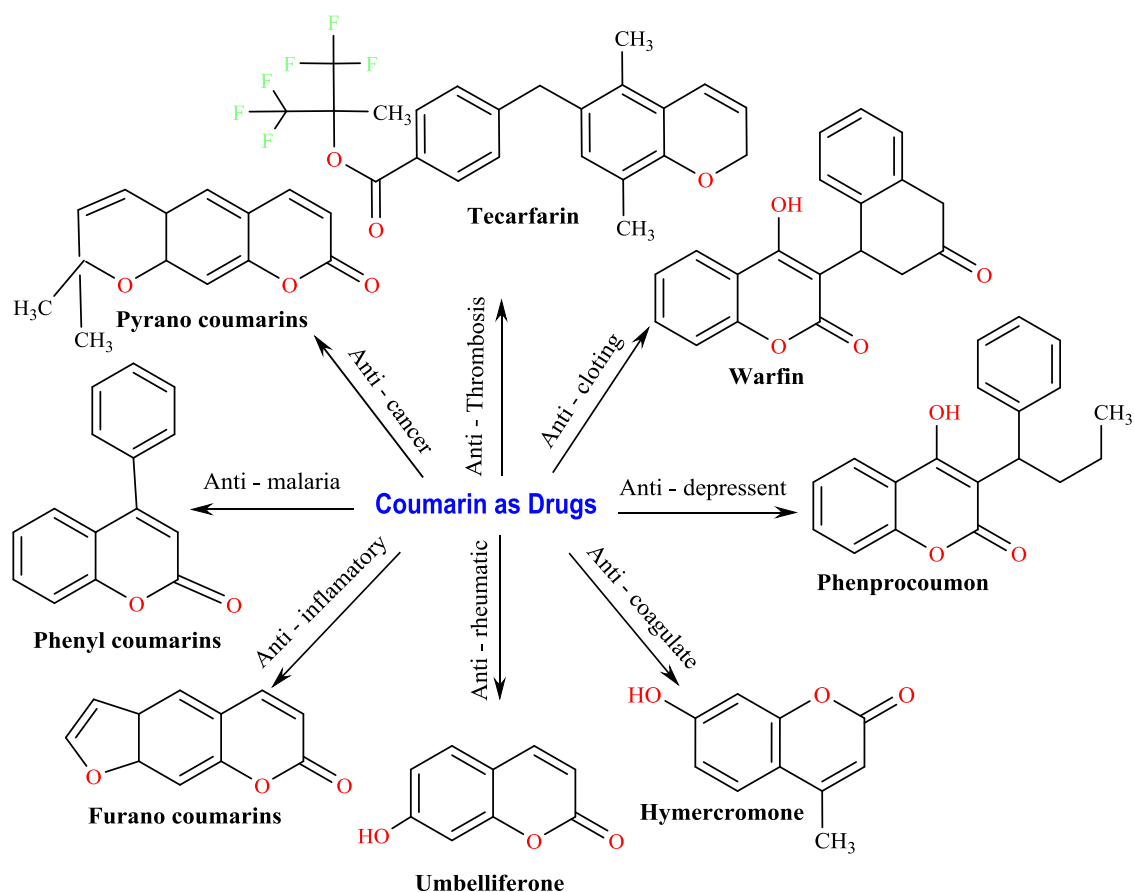


Figure 1 Some commercially available coumarin derivatives

Overall, the research discussed highlights the importance of heterocyclic compounds with nitrogen atoms, specifically coumarin derivatives, in various medicinal applications [15]. The synthesis and evaluation of metal complexes and the exploration of their biological activities contribute to the understanding of their potential in drug development and disease treatment [16]. In this paper we are reported an efficient route for the synthesis of new Mn(II), and Zn(II) complexes obtained from (4-Hydroxy coumarin) coumarin [17]. The thermal decomposition of their complexes is also used to infer the structure and the different thermodynamic activation parameters are calculated [18]. Synthetic coumarins have been used as fluorescent brightening agents in textiles, paper, detergents and dyes [19].

Furthermore, the aim for studying the interaction between synthesized ligands and  $\alpha$ -glucosidase using molecular docking is to explore alternative strategies for managing type 2 diabetes (T2DM).  $\alpha$ -Glucosidase inhibitors (AGIs), such as acarbose, are effective in controlling postprandial blood glucose levels but come with gastrointestinal side effects. First-row transition metal complexes, particularly those involving zinc and other metals, have shown promise as  $\alpha$ -glucosidase inhibitors, potentially offering advantages like lower toxicity and novel mechanisms of action [20]. Molecular docking studies help predict the binding affinities and interaction modes of these complexes with the enzyme, aiding in the design of more effective inhibitors. This approach aims to overcome the limitations of traditional AGIs, offering a promising alternative for T2DM treatment with potentially fewer side effects and improved efficacy.

### Experimental

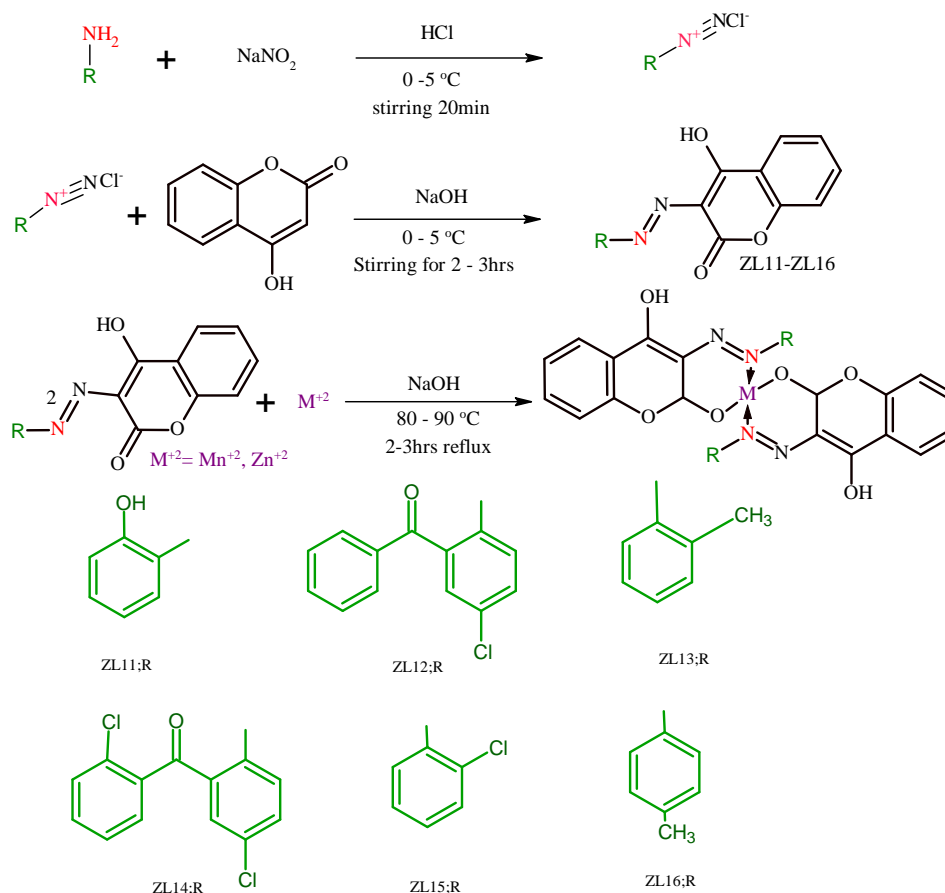
#### Chemicals and Solvents

All chemicals like 4-hydroxycoumarin, 2-aminophenol, 2-amino-5-chlorobenzophenone, o-toluidine, 2'-amino-2,5-dichlorobenzophenone, 2-chloroaniline, p-toluidine, sodium nitrite ( $\text{NaNO}_2$ ), HCl, NaOH (base) and solvents; ethanol, methanol, distilled water, dimethylsulfoxide (DMSO), tetrahydrofuran (THF), carbon tetrachloride ( $\text{CCl}_4$ ), acetone, benzene, n-hexane, chloroform, dimethylformamide (DMF) were purchased from sigma Aldrich, Merck, Alfa Aesar and BDH and were used without further purification.



### Instruments

Silica gel plates were used to monitor the progress of reaction by thin layer chromatography technique which was visualized under UV. Melting points were recorded by open capillary method on Stuart SMP10 and are uncorrected. The FTIR spectra were obtained using a BRUKER Tensor 27 (M15E-PS/09) FTIR spectrophotometer, using KBr discs. The spectral range was covered from 4000 to 400  $\text{cm}^{-1}$ . The  $^{13}\text{C}$  NMR and  $^1\text{H}$  NMR spectra were acquired using a Bruker-300 MHz spectrometer. The DPPH and NO scavenging activity were assessed using an Optima SP300-spectrophotometer. UV-visible spectra were recorded using ELISA reader. Powdered XRD data was obtained using BRUKER D8 X-ray diffractometer. The molecular mass of compounds was measured using JEOL 600H-1mass spectrometer. TGA analysis was recorded on a Shimadzu TGA-50H.



Scheme 1. Synthetic route for coumarin derivatives and their metal complexes

### Preparation of Ligands

#### General Procedure for the Synthesis of Coumarin Derivatives ZL11-ZL16

A 10 mL solution of 3 M hydrochloric acid ( $\text{HCl}$ ) was prepared and combined with a substituted aniline compound. Gradually, an aqueous solution of sodium nitrite ( $\text{NaNO}_2$ ) was added, resulting in the formation of a diazonium salt. Then, a solution of 4-hydroxycoumarin was introduced to the reaction mixture, which was placed in an ice bath for 20 minutes to maintain the optimal temperature of  $0-5\text{ }^\circ\text{C}$ . The coupling between the diazonium salt and 4-hydroxycoumarin occurred under these conditions. Neutralization was achieved by adding 3 M sodium hydroxide ( $\text{NaOH}$ ) to the mixture, and the reaction was stirred for 2-3 hours at  $0-5\text{ }^\circ\text{C}$ , facilitating the formation of the coumarin ligand (ZL). The synthesized product was collected by filtration and purified through recrystallization in ether, yielding up to 87 %. The reaction completion and purity of the compound were assessed using thin-layer chromatography (TLC) analysis (Scheme 1).

*Metallization of Metal Complexes of Ligands ZL11-ZL16*

To synthesize the  $\text{Mn}^{2+}$  and  $\text{Zn}^{2+}$  metal complexes, a 0.5 mmol solution of the coumarin derivative was prepared in ethanol and stirred continuously for 5 minutes. An ethanolic solution of the metal salts ( $\text{Zn}^{2+}$  or  $\text{Mn}^{2+}$ ) was then added in a 1:2 metal-to-ligand ratio, and the mixture was stirred for 20 minutes. Sodium hydroxide was added dropwise under reflux conditions to adjust the pH to approximately 8, creating a basic environment. A visible color change occurred, indicating the formation of the metal complex (MZL). The reaction was allowed to proceed under reflux at a temperature range of 80–90 °C for 2 hours. The product was collected, washed with distilled water, and dried for further use.

**4-hydroxy-3-[(E)-(2-hydroxyphenyl)diazenyl]-2H-chromen-2-one (ZL11).** Brown solid, yield: 79.28 %, Rf: 0.56 (acetone: $\text{CCl}_4$  (1:1)), soluble in THF, DMF, DMSO, acetone, ethanol, methanol, chloroform, n-hexane, and benzene m.p.: 182 °C, FTIR (KBr disc,  $\text{cm}^{-1}$ ): 3080.72 (NH stretch, O–H stretch), 1741.87 (C=O), 1610.11 (N=N stretch), 1645.43 (C=C stretch), 1525.03 (C–C stretch), 1346.60 (C–N stretch), 1190.63 (C–O stretch), UV-Visible,  $\lambda_{\text{max}}$  (DMSO, nm): 590,  $^1\text{H}$  NMR (300 MHz, DMSO- $\text{D}_6$ )  $\delta$  15.9 (s, OH), 8.03 (d,  $J$  = 7.8 Hz, Hd), 7.92 (s, Hb, Hg), 7.79 (s, Hc), 7.66 (s, He), 7.56 (s, Ha), 5.59 (s, Hh).  $^{13}\text{C}$  NMR (100 MHz, DMSO)  $\delta$  178.5 (C4), 163.7 (C2), 154.1 (C6), 151.9 (C14), 137.2 (C17), 130.1 (C15, C16), 129.1 (C19), 128.7 (C18), 124.7 (C9), 124.0 (C10), 117.7 (C7), 116.7 (C5), 102.3 (C3), 19.3 (C21). EI-MS m/z: Required for  $\text{C}_{15}\text{H}_{10}\text{N}_2\text{O}_4^+$ : 282.25 found 282.2.

**3-[(E)-(2-benzoyl-4-chlorophenyl)diazenyl]-4-hydroxy-2H-chromen-2-one (ZL12).** Yellowish Orange solid, yield: 79.81 %, Rf: 0.72 ( $\text{CCl}_4$ :chloroform (2:8)), soluble in THF, DMF, DMSO, acetone, ethanol, methanol, chloroform, n-hexane, and benzene m.p: 290 °C, FTIR (KBr disc,  $\text{cm}^{-1}$ ): 3008.02 (NH stretch, O–H stretch), 1738.65 (C=O), 1625.81 (N=N stretch), 1661.61 (C=C stretch), 1396.68 (C–C stretch), 1290.64 (C–N stretch), 1067.10 (C–O stretch) UV-Visible,  $\lambda_{\text{max}}$  (DMSO, nm):380,  $^1\text{H}$  NMR (300 MHz, DMSO- $\text{D}_6$ )  $\delta$  7.77–7.68 (m, He), 7.59 (d,  $J$  = 6.5 Hz, Hg), 7.54 (d,  $J$  = 5.5 Hz, Hk, Hi), 7.52 (s, Ha, Hc), 7.48–7.38 (m, Hb, Hj), 7.32 (s, Hi, Hh), 7.12 (s, Hf), 6.88 (s, Hh, Hd).  $^{13}\text{C}$  NMR (100 MHz, DMSO)  $\delta$  196.7 (C21), 150.5 (C4), 139.1 (C2), 1133.9 (C24, C6), 132.6 (C27, C18, C15), 131.2 (C17), 128.4 (C29, C25, C16), 120.0 (C7, C5), 116.9 (C3). EI-MS m/z: Required for  $\text{C}_{22}\text{H}_{13}\text{ClN}_2\text{O}_4^+$ : 404.80 found 404.0.

**4-hydroxy-3-[(E)-(2-methylphenyl) diazenyl]-2H-chromen-2-on (ZL13).** Light Greenish solid, Yield: 89.28 %, Rf: 0.63 ( $\text{CCl}_4$ :chloroform (2:8)), soluble in THF, DMF, DMSO, acetone, ethanol, methanol, chloroform, n-hexane, and benzene, m.p: 196 °C, FTIR (KBr disc,  $\text{cm}^{-1}$ ): 3350.62 (NH stretch, O–H stretch), 1735.97 (C=O), 1599.37 (N=N stretch), 1544.49 (C=C stretch), 1328.21 (C–N stretch), 1234.68 (C–O stretch) UV-Visible,  $\lambda_{\text{max}}$  (DMSO, nm): 660,  $^1\text{H}$  NMR (300 MHz, DMSO- $\text{D}_6$ )  $\delta$  12.53 (s, OH), 7.82 (d,  $J$  = 1.7 Hz, Ha, Hd), 7.80 (d,  $J$  = 1.7 Hz, He), 7.53 (s, Hf), 7.33 (d,  $J$  = 1.1 Hz, Hb, Hc, Hh), 5.59 (s, Hg), 3.37 (s,  $\text{CH}_3$ ).  $^{13}\text{C}$  NMR (100 MHz, DMSO)  $\delta$ : 177.6 (C4), 166.5 (C2), 162.5 (C6), 154.0 (C15), 151.9 (C16), 136.4 (C8), 132.3 (C17), 131.1 (C19), 130.1 (C9), 123.8 (C5), 102.3 (C7), 90.9 (C3). EI-MS m/z: Required for  $\text{C}_{16}\text{H}_{12}\text{N}_2\text{O}_3^+$ : 280.87 found 280.87.

**3-[(E)-[4-chloro-2-(2-chlorobenzoyl) phenyl] diazenyl]-4-hydroxy-2H-chromen-2-one (ZL14).** Dark Orange solid, Yield: 79.81 %, Rf: 0.65 ( $\text{CCl}_4$ :ethanol (3:7)), soluble in THF, DMF, DMSO, acetone, ethanol, methanol, chloroform, n-hexane, and benzene m.p: 226 °C, FTIR (KBr disc,  $\text{cm}^{-1}$ ): 3399.49 (NH stretch, O–H stretch), 1739.99 (C=O), 1596.09 (N=N stretch), 1465.96 (C=C stretch), 1403.68 (C–N stretch), 712.75 (C–Cl stretch), 1067.88 (C–O stretch) UV-Visible,  $\lambda_{\text{max}}$  (DMSO, nm): 660,  $^1\text{H}$  NMR (300 MHz, DMSO- $\text{D}_6$ )  $\delta$ : 16.36 (s, OH), 7.84–7.78 (m, He), 7.66 (s, Hb, Hj), 7.58 (d,  $J$  = 7.9 Hz, Ha, Hc, Hg), 7.58–7.52 (m, Hi, Hk), 7.49–7.46 (m, Hh, Hf), 7.43 (d,  $J$  = 7.4 Hz, Hh).  $^{13}\text{C}$  NMR (100 MHz, DMSO)  $\delta$ : 194.9 (C21), 164.4 (C4), 138.3 (C2), 133.9 (C25, C15), 132.6 (C27, C17, C24), 131.2 (C8, C16), 128.4 (C29, C18), 120.0 (C9, C10), 117.1 (C5) 116.1 (C7), 90.9 (C3). EI-MS m/z: Required for  $\text{C}_{22}\text{H}_{12}\text{Cl}_2\text{N}_2\text{O}_4^+$ : 439.24 found 439.3.

**3-[(E)-(2-chlorophenyl) diazenyl]-4-hydroxy-2H-chromen-2-one (ZL15).** Brown solid, Yield: 83.33 %, Rf: 0.63 ( $\text{CCl}_4$ :benzene (3:7)), soluble in THF, DMF, DMSO, acetone, ethanol, methanol, chloroform, n-hexane, and benzene m.p: 172 °C, FTIR (KBr disc,  $\text{cm}^{-1}$ ): 3366.65 (NH stretch, O–H stretch), 1739.98 (C=O), 1607.69 (N=N stretch), 1571.03 (C=C stretch), 1394.26 (C–N stretch), 742.93 (C–Cl stretch), 1081.74 (C–O stretch); UV-Visible,  $\lambda_{\text{max}}$  (DMSO, nm): 660,  $^1\text{H}$  NMR (300 MHz, DMSO- $\text{D}_6$ )  $\delta$ : 15.98 (s, OH), 8.03 (d,  $J$  = 7.8 Hz, He), 7.92 (d,  $J$  = 8.3 Hz, Ha, Hd), 7.79 (t,  $J$  = 7.7 Hz, Hh), 7.66 (d,  $J$  = 7.9 Hz, Hb, Hc), 7.56 (d,  $J$  = 7.7 Hz, Hf), 7.37 (d,  $J$  = 2.5 Hz, Hg).  $^{13}\text{C}$  NMR (100 MHz, DMSO)  $\delta$ : 165.4 (C4), 161.8 (C2), 153.5 (C6), 132.9 (C15), 123.9 (C19, C17), 116.7 (C5), 116.4 (C7), 91.7 (C3). EI-MS m/z: Required for  $\text{C}_{15}\text{H}_9\text{ClN}_2\text{O}_3^+$ : 300.69 found 300.1.

**4-hydroxy-3-[(E)-(4-methylphenyl)diazenyl]-2H-chromen-2-one (ZL16).** Light yellow solid, yield: 89.84 %, Rf: 0.73 (methanol:CCl<sub>4</sub> (3:7)), soluble in THF, DMF, DMSO, acetone, ethanol, methanol, chloroform, n-hexane, and benzene, m.p.: 211 °C, FTIR (KBr disc, cm<sup>-1</sup>): 3352.50 (NH stretch, O–H stretch), 1740.31 (C=O), 1647.46 (N=N stretch), 1543.45 (C=C stretch), 1328.16 (C–N stretch), 1236.66 (C–O stretch), UV-Visible,  $\lambda_{\text{max}}$  (DMSO, nm): 620; <sup>1</sup>H NMR (300 MHz, DMSO-D<sub>6</sub>)  $\delta$ : 15.51 (s, OH), 7.82–7.80 (m, Hd, Ha), 7.65–7.63 (m, He, Hf), 7.36 (d, J = 1.4 Hz, Hb, Hc), 5.58 (s, Hg, Hh), 2.49 (s, Hi, Hj, Hk). <sup>13</sup>C NMR (100 MHz, DMSO)  $\delta$ : 178.5 (C4), 163.7 (C2), 154.1 (C6), 151.9 (C14), 137.2 (C17), 130.1 (C15, C16), 129.1 (C19), 128.7 (C18), 124.7 (C9), 124.0 (C10), 117.7 (C7), 116.7 (C5), 102.3 (C3), 19.3 (C21). EI-MS m/z: Required for C<sub>16</sub>H<sub>12</sub>N<sub>2</sub>O<sub>3</sub><sup>+</sup>: 280.27 found 280.2

**4-hydroxy-3-[(E)-(4-methylphenyl) diazenyl]-2H-chromen-2-one Manganese complex (ZL16Mn).** Pale yellow solid, m.p.: >300 °C, yield: 89.53 %, soluble in chloroform, THF, acetone, DMSO, benzene, CCl<sub>4</sub>, ethanol, methanol, DMF and n-hexane, FTIR (KBr disc, cm<sup>-1</sup>): 1632.76 (N=N stretch), 1414.64 (C–N stretch), 1321.97 (C–O stretch), 577.02 (Mn–O), 516.37 (Mn–N), UV-Visible  $\lambda_{\text{max}}$  (DMSO, nm): 660.

**4-hydroxy-3-[(E)-(4-methylphenyl) diazenyl]-2H-chromen-2-one Zinc complex (ZL16Zn).** Dark yellow solid, m.p.: >300 °C, yield: 86.49 %, soluble in acetone, ethanol, methanol DMSO, benzene, CCl<sub>4</sub>, chloroform, THF, DMF and n-hexane, FTIR (KBr disc, cm<sup>-1</sup>): 3391.93 (NH stretch, O–H stretch), 1513.02 (N=N stretch), 1650.25 (C=C stretch), 1561.28 (C–C stretch), 1342.96 (N=O stretch), 1350.20 (C–N stretch), 1058.16 (C–O stretch), 761.28 (C–Cl stretch), 669.83 (Zn–O), 521.04 (Zn–N), UV-Visible  $\lambda_{\text{max}}$  (DMSO, nm): 380.

#### *Anti-Oxidant Scavenging Assay*

Antioxidant compounds found in food are crucial for maintaining good health and reducing the risk of chronic diseases like heart disease and cancer. These antioxidants are primarily found in fruits, whole grains, and vegetables. Plant-based antioxidants, such as vitamin E, vitamin C, carotenes, phytoestrogens, phytate, and phenolic acids, have been recognized for their potential to lower disease risk. The diverse range of antioxidant compounds in our diet have varying levels of antioxidant activity, with some being strong antioxidants, like gallates, and others being weaker, like mono-phenols. The main function of antioxidants is to neutralize free radicals by donating hydrogen atoms, thereby reducing them to non-reactive species. By removing the odd electron feature responsible for radical reactivity, antioxidants help protect against the harmful effects of free radicals. Free radicals have garnered significant attention from scientists due to their wide-ranging impact on biological systems, including their involvement in disease development and aging. It has been established that oxidative stress, caused by an imbalance between antioxidants and free radicals, contributes to the pathogenesis of certain diseases. Therefore, there is evidence supporting the use of antioxidant supplementation to reduce oxidative stress levels and potentially slow down or prevent disease-related complications. While synthetic antioxidant components have been found to have toxic and mutagenic effects, natural antioxidants have gained attention due to their safer profile [21].

#### *Diphenyl-2-Picrylhydrazide (DPPH) Free Radical Scavenging Assay*

The antioxidant activity of the synthesized compounds against 2,2-diphenyl-2-picrylhydrazide (DPPH) were evaluated [22]. The standard used was ascorbic acid and various concentration (5, 10, 15, 20, and 25 µg/ml) of the compounds were measured using Optima SP300-spectrophotometer at 517 nm [23].

The experiment was triplicates and % scavenging was calculated by using formula.

$$\% \text{Scavenging} = ((A_o - A_s)/A_o) \times 100,$$

where A<sub>o</sub> is the absorbance of blank; A<sub>s</sub> is the absorbance of sample.

Absorbance of sample was calculated by using formula:

$$A_s = A_{st} - A_{sb},$$

where A<sub>s</sub> is the absorbance of sample; A<sub>st</sub> is the absorbance of test sample solution with DPPH; A<sub>sb</sub> is the absorbance of blank sample solution without DPPH.

The IC<sub>50</sub> value, defined as the concentration of the tested compounds required to scavenge 50 % of DPPH free radicals, was calculated by non-linear regression using GraphPad Prism 8 (GraphPad Software Inc., La Jolla, USA).

#### *Nitric Oxide (NO) Free Radical Scavenging Assay*

Sodium nitroprusside was used for nitric oxide production in aqueous solution at 7.4 pH which combine with oxygen to give nitrite ion which one determined by using Griess reagent. For this aim to 2 mL of various concentration (5, 10, 15, 20 and 25 µg/ml) of sample solution in DMSO, 2 mL of 10 mL sodium

nitroprusside in PBS (phosphate buffer saline) solution was added and incubated at 25 °C for 4 hours. After incubation to 2 mL of reaction solution containing nitrate ion 2 mL of Griess reagent (1 % sulphanilamide in 5 % phosphoric acid (1 mL) and 0.1 % N-(1-naphthyl)ethylenediamine dihydrochloride (1 mL) was added and again incubated at 25 °C for 30 minutes. Same reaction mixture instead test compound having 2 mL DMSO served as blank. The absorbance of chromophore formed was measured at 546 nm using Optima SP300-spectrophotometer. The experiment was done in triplicate and % scavenging was calculated by using formula:

$$\% \text{Scavenging} = ((A_o - A_s)/A_o) \times 100,$$

where  $A_o$  is the absorbance of blank;  $A_s$  is the absorbance of sample.

Absorbance of sample was calculated by using formula:

$$A_s = A_{st} - A_{sb},$$

where  $A_s$  is the absorbance of sample;  $A_{st}$  is the absorbance of test sample solution with DPPH;  $A_{sb}$  is the absorbance of blank sample solution without DPPH.

The  $IC_{50}$  value, defined as the concentration of the tested compounds required to scavenge 50 % of NO free radicals, was calculated by non-linear regression using GraphPad Prism 8 (GraphPad Software Inc., La Jolla, USA).

#### Anti-Bacterial Activities

The synthesized compounds were studied for the antibacterial activity against the bacterial species. All the synthesized ligands (ZL11-ZL16) and their metal complexes with (Mn(II), Zn(II)) (Figures S1–S18). The Zone of inhibitions of synthesized compounds was carried out by disc diffusion method [24]. The antibacterial activity of all the synthesized ligands was evaluated against 24 hr culture of various selected bacteria. The gram-negative bacteria used were *E. Coli* and *Pseudomonas aeruginosa* while gram-positive bacteria were *Staphylococcus Pyogenes* and *Bacillus*. Amikacin was used as standard drug for the evaluation of antibacterial activity. Activity was reported by zone of inhibition (mm) [25].

#### Molecular Docking Protocol

In this study, we aimed to investigate the binding interactions between newly synthesized coumarin derivatives and two enzymes, namely Mannosyl-oligosaccharide glucosidase and Oligo-1,6-glucosidase. To initiate, we obtained the 3D crystal structures of these enzymes from the Protein Data Bank (www.rcsb.com) with the Mannosyl-oligosaccharide glucosidase structure having a resolution of 2.04 Å (PDB ID: 4J5T) and the Oligo-1,6-glucosidase structure having a resolution of 1.30 Å (PDB ID: 3AJ7). Before conducting the docking analysis, we prepared the structures of the target proteins using MGL tools. Heteroatoms and water molecules present in protein structures were removed. Additionally, polar hydrogen atoms and Kollman charges were added to ensure the accurate representation of the protein structures. Furthermore, any missing amino acid residues were rendered in the structures to ensure their structures. Furthermore, we generated the 3D structures of the synthesized coumarin derivatives (ZL11-ZL16) using ChemDraw 3D [26]. These structures were then subjected to energy minimization to obtain their most stable conformations. For the docking analysis, we utilized AutoDock, employing its default genetic algorithm as the scoring function. The compounds (ZL11-ZL16) were docked into the active pockets of Mannosyl-oligosaccharide glucosidase and Oligo-1,6-glucosidase. The dimensions of grid box were set as  $x$ : 21.306612;  $y$ : -0.461484;  $z$ : 18.843785 for Mannosyl-oligosaccharide glucosidase and  $x$ : -18.523631;  $y$ : -20.732132;  $z$ : 8.202425 for Oligo-1,6-glucosidase to define the search space for docking respectively. Multiple docking configurations were generated for each compound and enzyme, resulting in approximately 100 different configurations. Finally, to attain a deeper insight of the binding interactions occurring within the active sites of Mannosyl-oligosaccharide glucosidase and Oligo-1,6-glucosidase, the most stable configurations were selected for further analysis and development of 2D and 3D models to understand the binding interactions among the derivatives within the active sites of Mannosyl-oligosaccharide glucosidase and Oligo-1,6-glucosidase.

#### Results and Discussion

Coumarin derivatives were synthesized utilizing a previously documented procedure, resulting in a remarkable yield. The confirmation of these derivatives was accomplished by analyzing their physical spectroscopic parameters. Subsequently, complexes of transition metals ( $Mn^{+2}$ ,  $Zn^{+2}$ ) with these coumarin derivatives were synthesized and subjected to characterization based on various physical properties, including solubility, melting point, as well as spectroscopic techniques such as UV-visible spectroscopy, FTIR spectroscopy.

copy, X-ray diffraction, and Thermal gravimetric analysis. To ensure conformity with existing literature regarding the synthesis of metal complexes, the coordination of ligands with metal ions was investigated. Initially, Job's method was employed to determine the optimal stoichiometric ratio, and it was observed that a 2:1 ratio of ligands to metals yielded the highest absorbance [27]. Consequently, the metal complexes were synthesized utilizing this specific stoichiometric ratio of ligands and metal salts [28]. Regarding the thermal stability of these metal complexes, it was observed that Mn(II) and Zn(II) complexes exhibited melting points exceeding 300 °C, while the coumarin derivatives themselves displayed a melting point range of 150–300 °C. This discrepancy indicates that the metal coordination compounds of the derivatives exhibit significantly enhanced stability due to the smaller size and higher charge of the Mn and Zn complexes [29]. Furthermore, all complexes demonstrated solubility in DMSO.

### Spectroscopic Characterization

#### FTIR Characterization of Synthesized Coumarin Derivatives

FTIR spectra of all synthesized coumarin derivatives were recorded in 400–6000  $\text{cm}^{-1}$  region which gave valuable information about formation and structure of all the synthesized coumarin ligand. The FTIR spectra showed prominent peaks of functional groups like O–H, C–H, C=O, C=N, N=N, C=C, C–N and C–O which confirms the formation of coumarin derivatives [30]. The appearance of a broad peak of O–H stretch near 3650–3200  $\text{cm}^{-1}$ , N–H stretch appeared around 3600–3400  $\text{cm}^{-1}$ . Appearance of a distinctive peak of N=N of diazinyl group at around 1700–1400  $\text{cm}^{-1}$  were observed in FTIR spectra of ligands confirmed the presence of these functional groups. The vibrational frequency for  $\text{sp}^2$  CH stretch was observed around 3000–2800  $\text{cm}^{-1}$  which is region according to literature. Since O–H has a broad peak so it overlapped with aromatic C–H stretch. Another peak C=C stretch was observed near 1520–1400  $\text{cm}^{-1}$  and aromatic C–N stretch was seen at 1390–1180  $\text{cm}^{-1}$ . While C–O stretch was observed in 1320–900  $\text{cm}^{-1}$ , it was seen that all the above-mentioned peaks are in IR region according to literature. For all the metal complexes M–O stretch was shifted towards lower frequency in complexes because nitrogen was involved in complex formation. For exemplary, FTIR spectra of ligand ZL14 (Fig. 2) with its complexes ( $\text{Zn}^{+2}$ ,  $\text{Mn}^{+2}$ ) were discussed for comparative study.

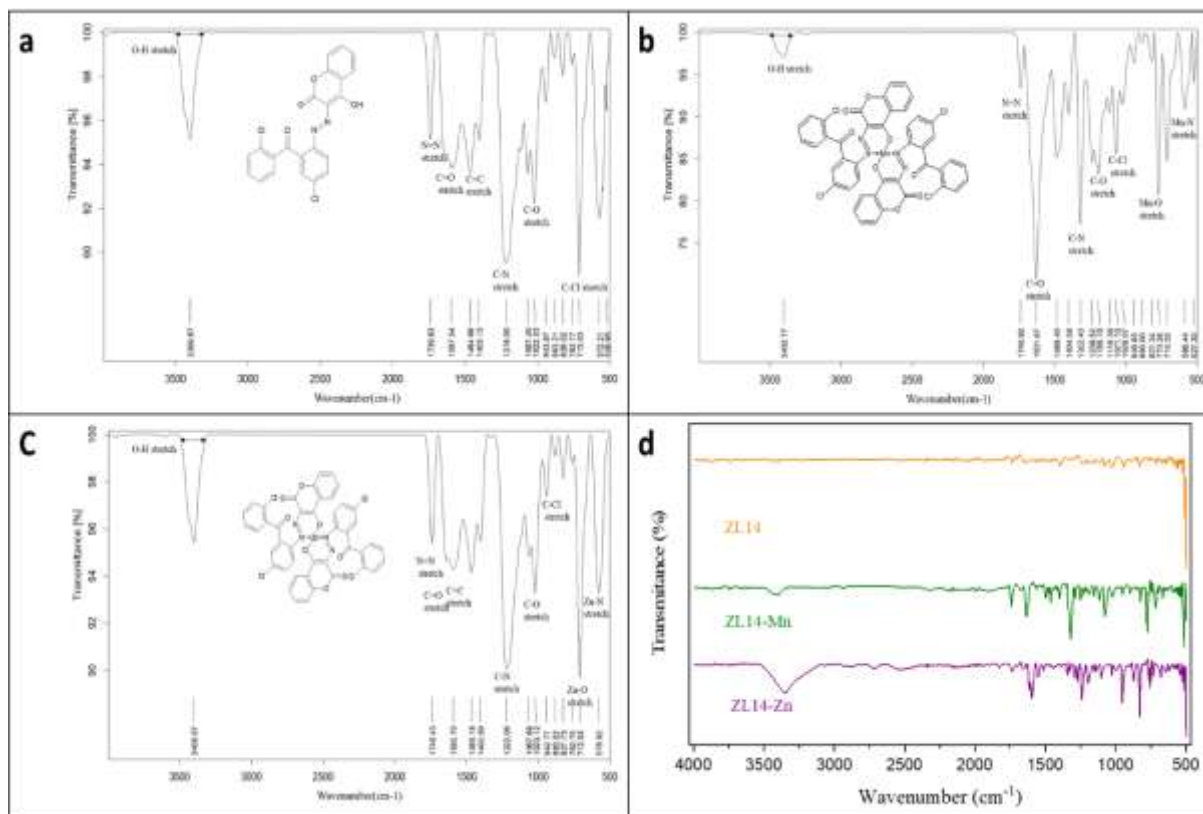
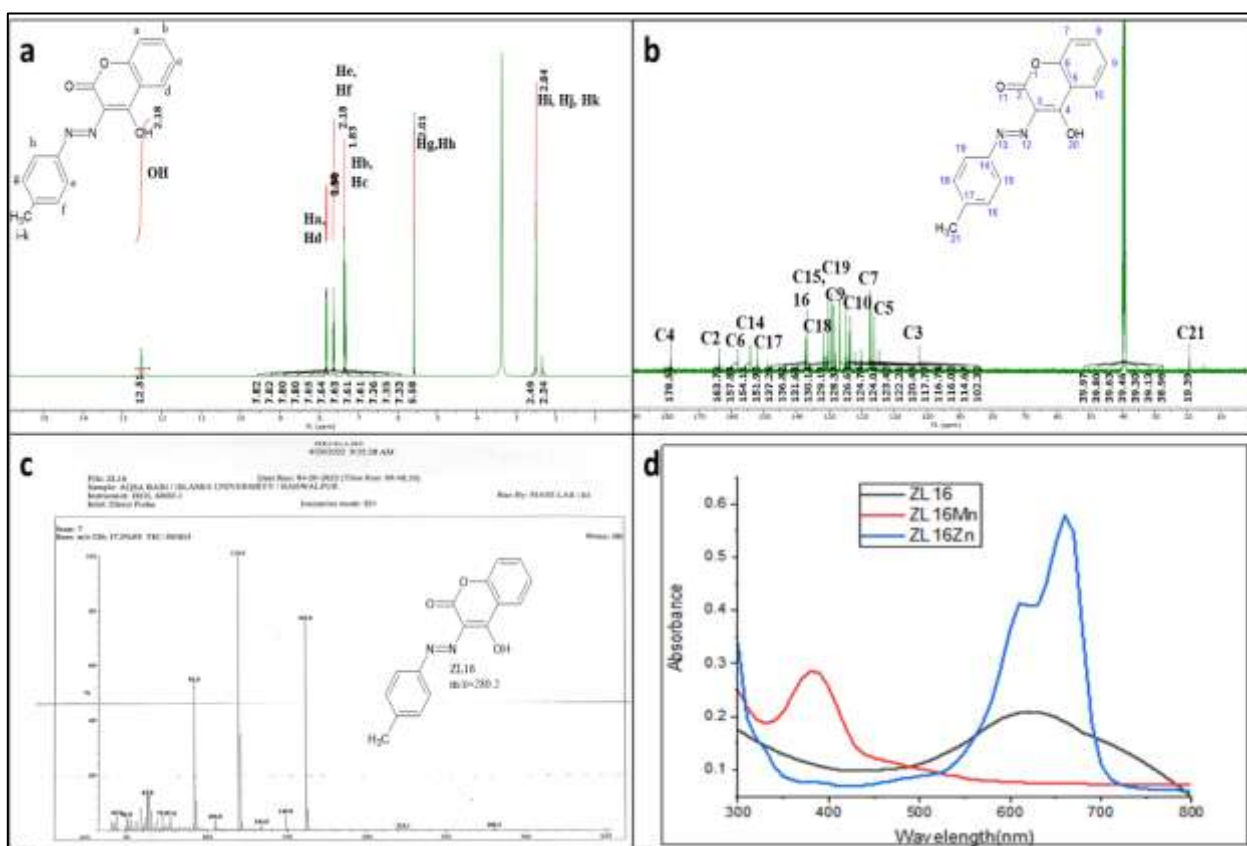


Figure 2. FTIR spectra of (a) ZL14 (b) ZL14Mn (c) ZL14Zn (d) comparative FTIR spectra of ZL14 and its transition metal complexes

The stretching frequency for dizenyl group N=N was observed at  $1596.09\text{ cm}^{-1}$ , a broad and sharp peak of OH was seen at  $3399.49\text{ cm}^{-1}$ . The Aromatic =C–H stretch was observed near  $3251.09\text{ cm}^{-1}$ . The vibrational frequency of C=O was observed at  $1739.99\text{ cm}^{-1}$ , C–N and C–O stretch were seen at  $1403.68$  and  $1022.88\text{ cm}^{-1}$  respectively while  $\text{sp}^2$  C–H stretch were observed near  $3251.09\text{ cm}^{-1}$ . The C=O peak appeared near  $1739.99\text{ cm}^{-1}$ . M–O stretch for all metal complexes appeared below  $591.63$  and  $712.08\text{ cm}^{-1}$  for Mn(II) and Zn(II) respectively. Similarly, Mn(II) and Zn(II) stretch at  $516.99$  and  $577.64\text{ cm}^{-1}$  respectively. FTIR spectra of all other coumarin derivatives (ZL11–ZL16) is given in supplementary material (Figures S1–S18).

### <sup>1</sup>H NMR Study

Proton NMR spectroscopy is an important analytical method for determining the structure of substances associated with the hydrogen-1 nucleus in the molecule of the analyzed product. In the NMR spectra of all azo groups, peaks of aldehyde protons are observed at 9.5–10.3 ppm. The phenolic proton concentration of coumarin compounds is 11.0 to 1.5 ppm, but in these studies this value varies from 13 to 15 ppm for coumarin compounds [31]. <sup>1</sup>H NMR spectra of all synthesized compounds (ZL11–ZL16) were studied. All signals confirming the structure corresponding to the proton nucleus were evaluated by chemical shift values (ppm). The experimental spectrum is almost identical to the theoretical spectrum obtained using ChemSketch. <sup>1</sup>H NMR spectra allow us to identify the different chemical shifts of protons within a compound. The synthesis of compound ZL16 was confirmed through proton nuclear magnetic resonance (NMR) analysis, as illustrated in Figure 3. The spectrum revealed a sharp peak at 15.51 ppm, indicating the presence of exchangeable protons (OH). The analysis also identified multiple peaks at 7.82–7.80 ppm, corresponding to the proton (Hd, Ha) in the CH group. Another multiple peaks at 7.65–7.63 ppm were observed for protons (He, Hf) in the CH group, while doublet peak at 7.36 ppm indicated the presence of protons (Hb, Hc) in another CH group. Furthermore, singlet peak at 5.58 ppm were attributed to protons (Hg, Hh) in the CH group, and peaks at 2.49 ppm were associated with protons (Hi, Hj, Hk) in the CH group. This detailed analysis confirms the structural characteristics of compound ZL16 based on its proton NMR spectrum. <sup>1</sup>H NMR data of all other coumarin derivatives (ZL11–ZL16) is given in supplementary material (Figures S19–S24).





*<sup>13</sup>C NMR Study*

The <sup>13</sup>C NMR spectra of compounds ZL11–ZL16 show a clear resonance in the direction of the carbon nucleus. NMR spectra of the new compounds were obtained on a Bruker AM400 MHz NMR spectrometer. All compounds were dissolved in DMSO-D6. The structures of all new compounds were confirmed by <sup>1</sup>H NMR data. Direct signals of carbon for azo groups are detected at 136 and 152 ppm, and nitro, hydroxyl, and nitro groups are detected at 153, 125, and 142 ppm. The confirmation of the synthesis of ZL16 derivative of coumarin compounds was established through the observation of distinct peaks in the <sup>1</sup>H NMR spectrum. A sharp singlet peak was observed at a chemical shift at 178.5 ppm, indicating the presence of the C–OH (C4) group. The carbon atoms (C2, C6) attached to the nitrile group were evident in the region of 163.7 and 154.1 ppm. Peaks corresponding to the carbon atoms 151.9 (C14), 137.2 (C17), 130.1 (C15, C16), 129.1 (C19), 128.7 (C18), 124.7 (C9), 124.0 (C10), 117.7 (C7), 116.7 (C5), 102.3 (C3), 19.3 (C21) in the aromatic ring were observed. <sup>13</sup>C NMR data of all other coumarin derivatives (ZL11–ZL15) is given in supplementary material (Figures S25–S30).

*UV-Visible Characterization of Synthesized Compounds*

Coumarin derivatives ZL11–ZL16 and their metal complexes analyzed by UV-Visible spectroscopy and their spectra were recorded in DMSO solvent using 250 μL solution in the range of 200–800 nm. All the recorded UV-Vis spectra of coumarin derivatives ZL11–ZL16 and their metal complexes are illustrated in Figures S31–36 (Supporting file). The ultraviolet-visible (UV-Vis) spectra of the synthesized coumarin derivatives and their Mn(II) and Zn(II) complexes were recorded using 50 ppm solution of each compound in dimethyl sulfoxide (DMSO), and the measurements were conducted at room temperature within the wavelength range of 300–800 nm. The outcomes have been visually showed through comparative UV-Vis spectra, showed the  $\lambda_{\text{max}}$  peak in the range of 320–660. Interestingly, the synthesized coumarin derivatives exhibited significant absorbance in this region. In stark contrast, all the metal complexes demonstrated absorption maxima with weak absorbance peaks in the range of 380–670 nm. The Mn(II) complexes showcased intense absorption within the 390–660 nm region, whereas the Zn(II) complexes exhibited absorption within range 400–660 nm. These findings unequivocally indicate the successful synthesis of these metal complexes, as their absorption in the visible region strongly suggests their formation.

*XRD Characterization of Synthesized Compounds*

The XRD analysis of ligand ZL16 revealed distinct, sharp peaks at  $2\theta$  positions of 10.74°, 11.54°, 12.29°, 22.94°, and 29.26°, indicating a crystalline structure with an average crystal size of 4.092 nm. In contrast, the XRD pattern of its manganese complex (ZL16 Mn) showed the disappearance of these peaks and the emergence of new ones at  $2\theta$  positions of 17.27°, 26.69°, 31.54°, 34.75°, 38.69°, and 55.70°, with a slightly larger average crystal size of 4.34 nm, confirming the coordination of ZL16 with manganese. Similarly, the zinc complex exhibited peak shifts to 14.56°, 36.06°, 56.82°, 58.82°, and 61.30°, with an average crystal size of 1.574 nm, indicating successful complex formation with zinc. The sharpness of the peaks across all samples suggested their small size and crystalline nature, providing clear evidence of ligand coordination with both manganese and zinc metals. The crystallite sizes were calculated using the Scherrer equation, ( $D = 0.9\lambda/\beta \cos \theta$ ). The particle size of ligand ZL16, ZL16Mn and ZL16Zn complexes are found to be 4.092 nm, 4.341 nm and 1.574 nm respectively.

*Thermo Analytical Results (TG and DTG) of Ligands and Metal Complex*

The thermogravimetric analysis (TGA) of ZL14 reveals distinct decomposition stages across different metal variants. For ZL14, three decomposition stages occur between 45–500 °C: the first stage (45–150 °C) involves moisture and CO<sub>2</sub> evolution with a mass loss of 3.17 %; the second stage (150–350 °C) corresponds to the elimination of the azo group and Cl, resulting in a 20.39 % mass loss; the final stage (350–500 °C) leads to complete decomposition, leaving carbon as a residue with an 11.18 % mass loss. The total mass loss across these stages is 34.74 %, with an endothermic peak observed at 310 °C. In contrast, ZL14 Zn shows four decomposition stages from 32–500 °C: the first stage (32–150 °C) accounts for a 2.18 % mass loss due to water and CO<sub>2</sub>; the second stage (150–200 °C) results in a 1.14 % mass loss from azo group elimination; the third stage (200–350 °C) involves the loss of heterocycles; and the final stage (350–450 °C) leads to carbon and ZnO formation with a 3.13 % mass loss. The total mass loss here is 9.59 %, with an endothermic peak at 180 °C. For ZL14 Mn, two decomposition stages are noted between 20–600 °C: the first stage (20–100 °C) results in an 8.76 % mass loss from moisture and CO<sub>2</sub>, while the second stage (200–600 °C) corresponds to azo group elimination and yields an 8.77 % mass loss, culminating in carbon and MnO as final products. The total mass loss is 17.53 %, with an endothermic peak at 110 °C.

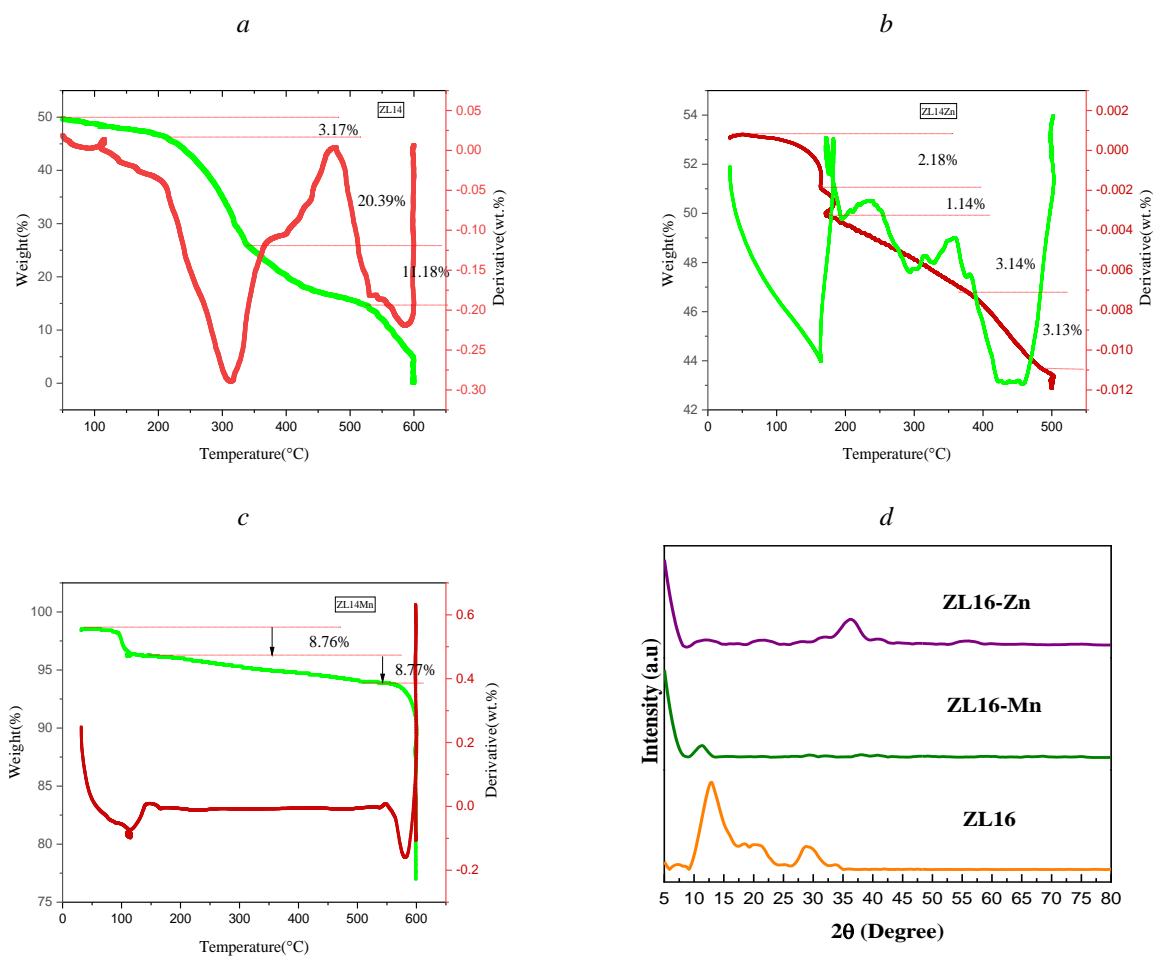


Figure 4. (a) TGA spectra of ZL14; (b) TGA spectra of ZL14Mn; (c) TGA spectra of ZL14Zn; (d) XRD of ZL16

### Mass Spectrometric Study

Mass spectrometry is a method of determining the molecular mass of a substance [7]. Using this method, not only the peak information of the molecular ion but also information on the scattering pattern can be obtained, allowing the characteristics of the compound to be determined [8]. The quality of a compound can be determined using mass spectrometry methods. Information on molecular ion peaks, fragmentation patterns, and structural annotations were obtained through mass spectrometry. Therefore, in this study, we fixed the size of the coumarin ligand in the reaction model [4]. Mass spectra of synthesized compounds (ZL11–ZL16) are described in Figures S37–S42 (Supporting file). The molecular masses of the ZL11–ZL16 ligands are 282.25, 404.0, 280.8, 438.3, 300.1 and 280.2 which were confirmed in mass spectrometry studies, respectively. In the mass spectra of compound ZL16 (Fig. 5) the molecular ion peak appears at  $m/z$  value of 280.2 which is exact to the molecular mass of ZL16 (215.1) which is also the (most intense) base peak for this ligand. The possible modes of fragmentation for ZL16 ligand are given in Figure 5. Another important peak appeared at  $m/z$  value 119.1 by the removal of  $C_9H_5O_3$  group from parent compound then the other important peak was seen at  $m/z$  value 91.0 by the removal of  $N_2$  groups from the 1st fragments (Route 1). The next important peak appeared at  $m/z$  value 104.0 by the removal  $CH_3$  from the 1st fragment. Two peaks appeared at  $m/z$  value 76.0 and 49.9 from the 2nd and the 3rd fragment by the removal of  $N_2$  and  $C_2H_2$  respectively (Route 2). The next peaks appeared at  $m/z$  value 120.0, 92.0 and 64.0 by the removal of  $C_9H_8N_2O$ , CO and CO radical from parent, the 1st and the 2nd fragment respectively (Route 3). The next important peak appeared at  $m/z$  value 162.0 and 134.0 by the removal  $C_7H_2O_2$  and CHO from parent and the 1st fragment. Another important peak was observed at  $m/z$  119.1 value by the removal of  $CH_3$  group from the 2nd fragment then other peak appeared at  $m/z$  value 93.0 by removal of  $N_2$  from the 3rd fragment. The peak of another important fragment was observed at  $m/z$  value 65.0 and 49.9 by the removal of  $N_2$  and  $CH_3$  radical from the 4th and the 5th fragment (Route 4).

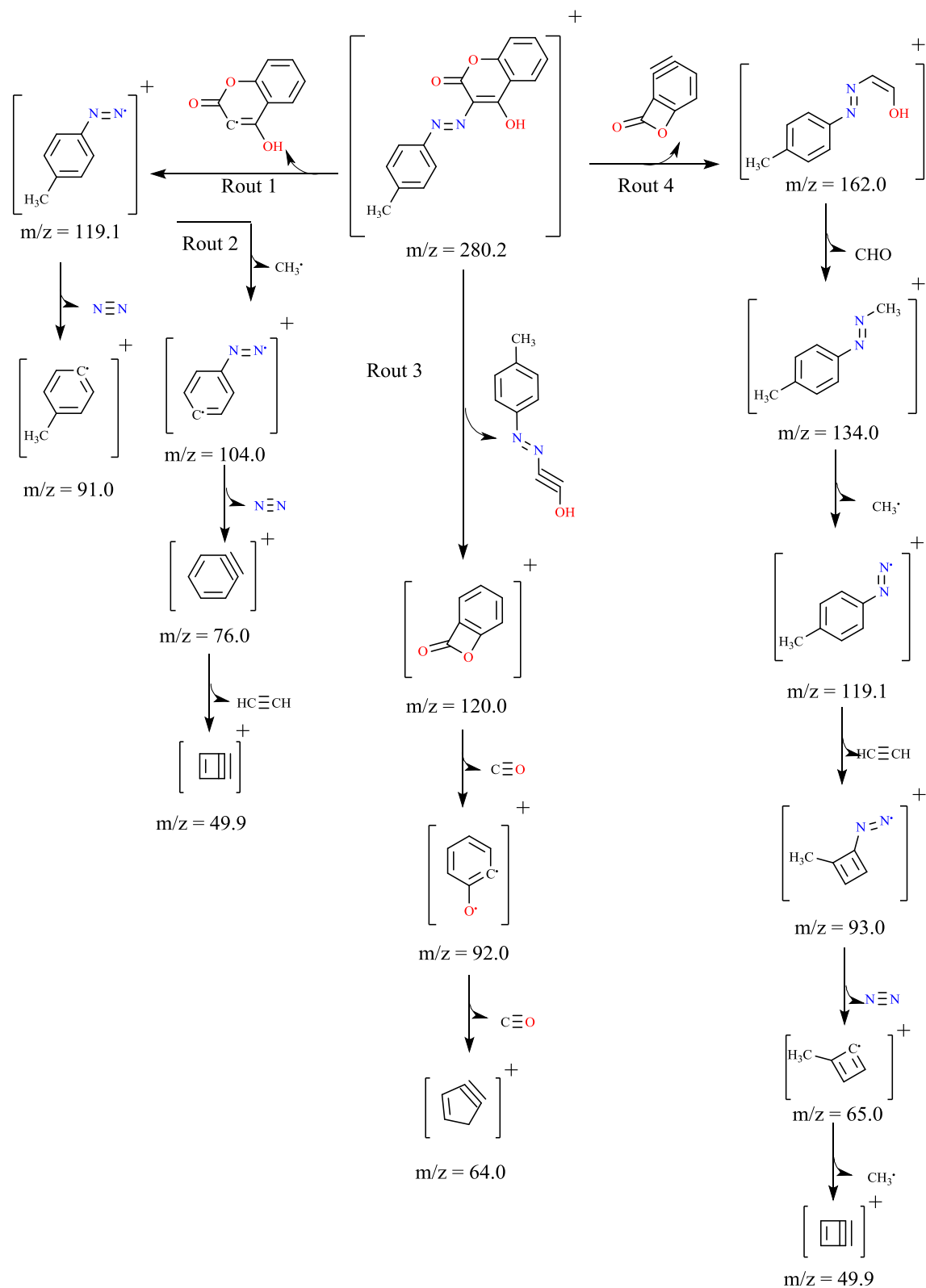


Figure 5. Mass spectrum fragmentation spectra ZL16

*Free Radical Scavenging Potential of Coumarin Derivatives and Their Metal Complexes (ZL11-ZL16)**DPPH Radical Scavenging Assay*

DPPH radical scavenging potential is a simple, efficient and relatively stable free radical method in which hydrogen or an electron is accepted by the reduction of free radical with the help of antioxidant mole-

cule. The solution of DPPH has purple color which is in reduced form changes to yellow. When more color change reduced more DPPH, radical enhance antioxidant activity. 579 nm absorbance is used for their calculation [32]. The DPPH radical scavenging activity of five concentrations (5, 10, 15, 20 and 25 µg/mL) of coumarin derivatives (ZL11–ZL16) and their manganese complexes (ZL11Mn–ZL16Mn) and zinc complexes (ZL11Zn–ZL16Zn) has been approved by ascorbic acid (AA) as standard. The results of antioxidant potential of prepared compounds are expressed in IC<sub>50</sub> as given in Table 1.

Table 1

**IC<sub>50</sub> values of DPPH assay of coumarin derivatives and their metal complexes (ZL11–ZL16)**

Compound	Scavenging of DPPH IC <sub>50</sub> * (µg/mL)		
	ZL (Ligands)	Mn(II) Complex	Zn(II) Complex
ZL11	7.62±0.04	6.45±0.07	8.31±0.051
ZL12	6.93±0.05	11.84±0.01	6.10±0.048
ZL13	7.6±0.04	7.09±0.010	8.49±0.046
ZL14	7.78±0.03	11.04±0.01	5.65±0.080
ZL15	6.94±0.06	11.84±0.04	8.32±0.060
ZL16	6.57±0.03	6.62±0.02	7.14±0.075
AA**	7.066±0.06	7.066±0.06	7.066±0.06

Notes: \* IC<sub>50</sub> is the concentration of compounds for 50 % inhibition of DPPH calculated by non-linear regression; \*\* AA is the ascorbic acid (standard compound)

All the prepared compounds display excellent inhibition potential as compared to standard (ascorbic acid) (7.06 µg/mL). Compounds ZL16, ZL11Mn and ZL14Zn, are more potent than that of ascorbic acid with IC<sub>50</sub> = 6.57, 6.45 and 5.65 µg/m.

#### *Nitric Oxide (NO) Radical Scavenging Assay*

Nitric oxide (NO) is regarded as free radicals as they have unpaired electrons. NO is very reactive oxidant that can decompose to form OH and NO by the reaction with superoxide to form peroxynitrite anion. All the synthesized compounds displayed inhibition effect on nitrite ion generated from sodium nitroprusside in aqueous solution by reaction of oxygen with nitric oxide at biological pH. Griess reagent is used for calculating scavenging effect at decreased absorbance of 546 nm. All the prepared coumarin ligands and their metal complexes display better nitric oxide radical scavenging potential as compared to DPPH radical scavenging activity. The NO radical scavenging activity of five concentrations (5, 10, 15, 20 and 25 µg/mL) of coumarin derivatives (ZL11–ZL16) and their zinc complexes (ZL11Zn–ZL16Zn) has been approved by ascorbic acid (AA) (7.06 µg/mL) as standard. The results of antioxidant potential of prepared compounds are expressed in IC<sub>50</sub> as given in Table 2.

Table 2

**IC<sub>50</sub> values of NO assays of coumarin derivatives and their metal complexes (ZL6–ZL10)**

Compound	Scavenging of NO IC <sub>50</sub> * (µg/mL)		
	ZL(Ligands)	Mn(II) (Complex)	Zn(II) (Complex)
ZL11	6.46±0.046	7.29±0.021	7.32±0.044
ZL12	6.38±0.095	5.99±0.060	6.77±0.078
ZL13	5.89±0.038	6.56±0.070	6.63±0.034
ZL14	7.015±0.068	6.98±0.024	6.07±0.09
ZL15	6.47±0.052	6.35±0.096	6.59±0.060
ZL16	11.2±0.053	7.10±0.670	6.30±0.065
AA**	6.79±0.026	6.79±0.026	6.79±0.026

Notes: \* IC<sub>50</sub> is the concentration of compounds for 50 % inhibition of NO calculated by non-linear regression; \*\* AA is the ascorbic acid (standard compound)

All the prepared compounds display excellent inhibition potential as compared to standard (ascorbic acid). Compounds ZL12, ZL12Mn and ZL14Zn, are more potent than that of ascorbic acid with IC<sub>50</sub> = 6.38, 5.99 and 6.07 µg/mL respectively.

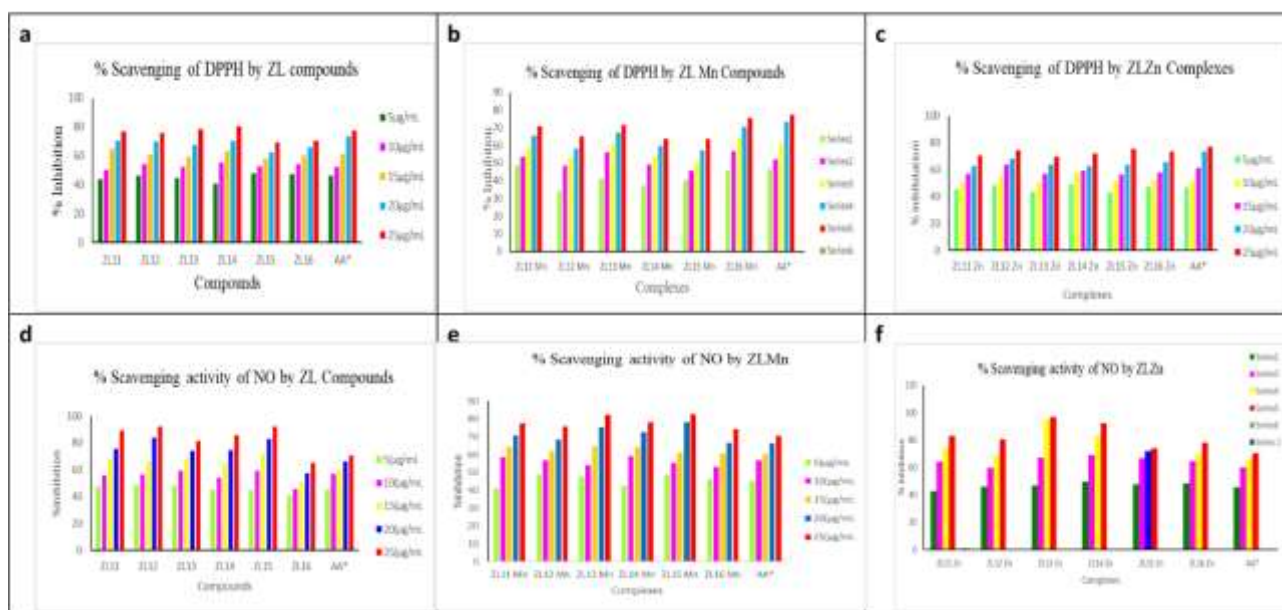


Figure 6. (a) Comparative graphical representation of DPPH scavenging activity by ZL compounds; (b) ZL Mn; (c) ZL Zn; (d) Comparative graphical representation of NO scavenging activity by ZL compounds; (e) ZL Mn; (f) ZL Zn

#### Antibacterial Activity

The in vitro antibacterial activity of coumarin compounds was screened against *Staphylococcus Pyogenes* and *Bacillus* (gram positive bacteria) and *Escherichia Coli* and *Pseudomonas aeruginosa* (gram negative bacteria) using the minimum inhibitory concentration (MIC) method. Amikacin was used as epy standard drug for the evaluation of antibacterial activity. Activity was also reported as zones of inhibition (mm) [25]. The Zinc(II) complex exhibited higher activity than the other tested compounds due to the interaction of the metal ions with nitrogen. Biological screening results of coumarin ligands showed that compounds ZL13, ZL13Mn and ZL15Zn exhibited good antibacterial activity against *E. Coli*, with zones of inhibition of 15 mm, 31 mm, and 28 mm, respectively, while all other compounds showed zones of inhibition in the range 9–28 mm. Ligands ZL11, ZL16, ZL11Mn, and ZL12Zn showed excellent activity against *Bacillus*, with zones of inhibition of 18 mm, 18 mm, 18 mm and 23 mm, respectively, while all other compounds exhibited zones in the range 12–22 mm. Ligands ZL14, ZL12Mn, and ZL16Zn showed good antibacterial activity against *Pseudomonas*, with zones of inhibition of 15, 18, and 23 mm, respectively, while all other derivatives exhibited zones in the range of 9–22 mm. Ligands ZL12, ZL12Mn, and ZL11Zn showed activity against *Staphylococcus Pyogenes*, with zones of inhibition of 16 mm, 20 mm and 20 mm, respectively, while all other compounds exhibited zones in the range of 9–16 mm. For comparison, the standard drug Amikacin exhibited a zone of inhibition of 15 mm. Overall, the biological screening of coumarin ligands revealed promising results. Against *E. Coli*, compound ZL16 demonstrated good antibacterial activity, resulting in a zone of inhibition of 16 mm as shown in Table 3–5.

Table 3

#### Antibacterial activity of coumarin derivatives ZL11-ZL16

Compound	Zone of Inhibition (mm)			
	Gram-negative bacteria		Gram-positive bacteria	
	<i>E. coli</i>	<i>Pseudomonas</i>	<i>S. Pyogenes</i>	<i>Bacillus</i>
ZL11	9	12	15	18
ZL12	11	8	16	18
ZL13	15	12	9	14
ZL14	12	15	10	16
ZL15	13	8	14	17
ZL16	14	22	16	18
Amikacin	15	13	16	15

Table 4

**Antibacterial activity of metal complexes ZL11Mn-ZL16Mn**

Compound No.	Zone of Inhibition (mm)			
	Gram-negative bacteria		Gram-positive bacteria	
	<i>E. coli</i>	<i>Pseudomonas</i>	<i>S. Pyogenes</i>	<i>Bacillus</i>
ZL11Mn	18	14	13	18
ZL12 Mn	20	18	20	10
ZL13 Mn	31	10	8	12
ZL14 Mn	8	8	9	14
ZL15 Mn	11	11	9	16
ZL16 Mn	12	9	7	18
Amikacin	14	16	15	13

Table 5

**Antibacterial activity of metal complexes ZL11Zn-ZL16Zn**

Compound No.	Zone of Inhibition (mm)			
	Gram-negative bacteria		Gram-positive bacteria	
	<i>E. coli</i>	<i>Pseudomonas</i>	<i>S. Pyogenes</i>	<i>Bacillus</i>
ZL11 Zn	12	9	20	20
ZL12 Zn	14	15	15	23
ZL13 Zn	12	11	14	21
ZL14 Zn	13	12	16	18
ZL15 Zn	28	13	15	17
ZL16 Zn	22	23	13	22
Amikacin	16	14	16	14

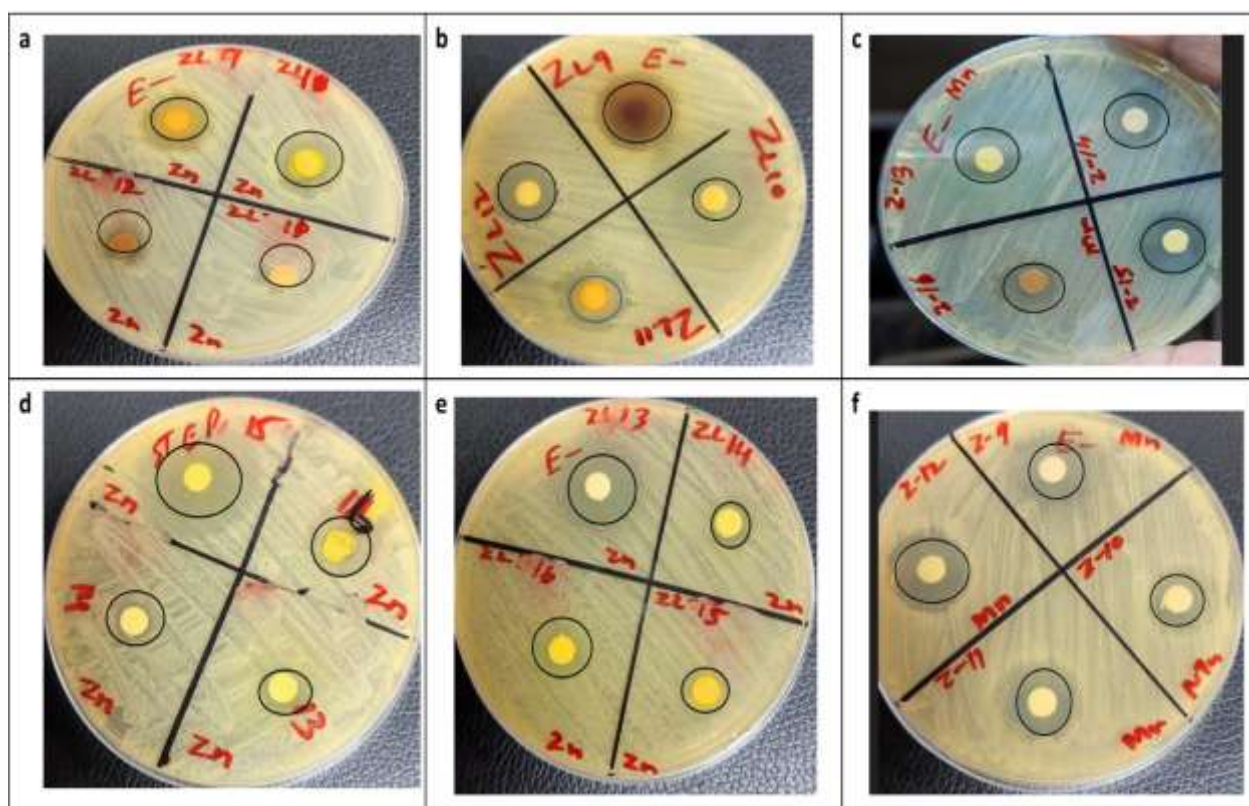


Figure 7. Anti-Bacterial activities of coumarin derivatives and their metal complexes (ZL11–ZL16)



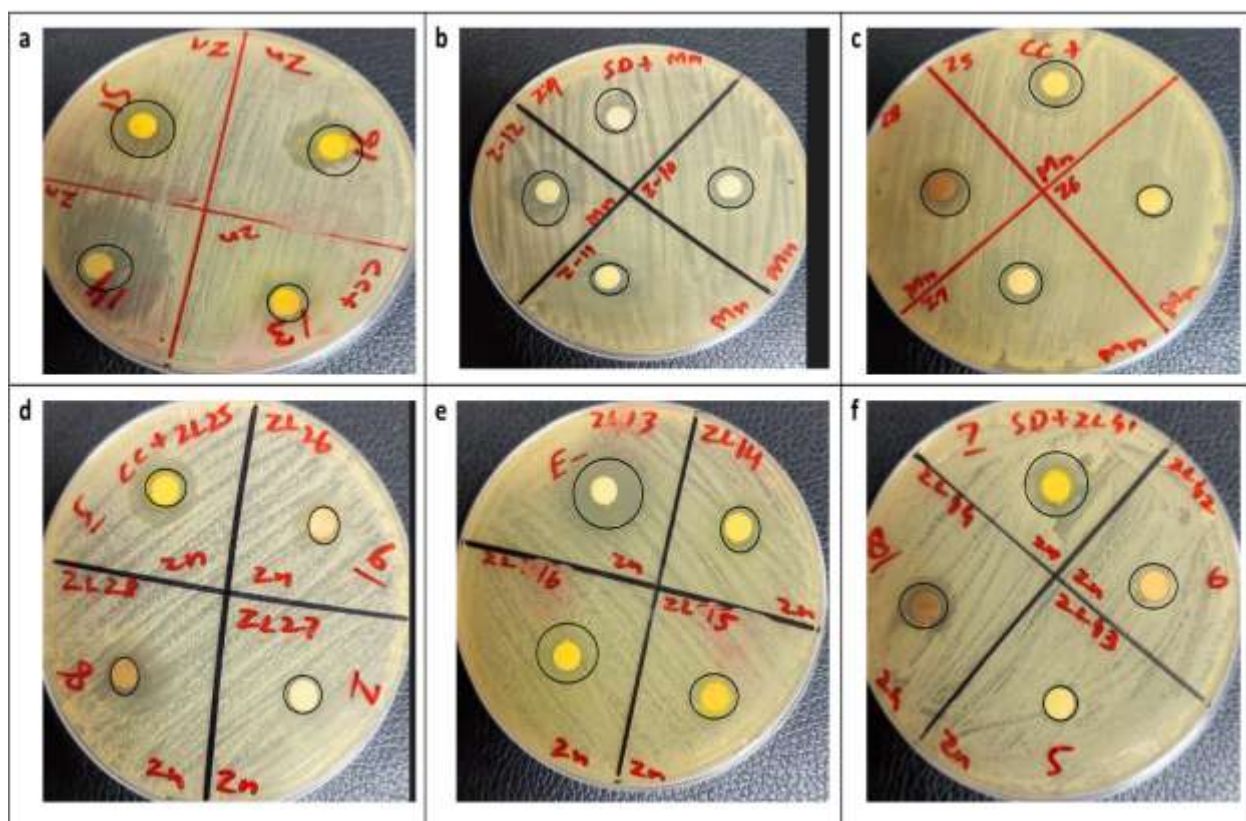


Figure 8. Anti-Bacterial activities of coumarin derivatives and their metal complexes (ZL11–ZL16)

#### Molecular Docking Analysis

In order to understand the mechanism of action, the molecular interaction between the synthesized ligands and two specific enzymes, Oligo-1,6-glucosidase (PDB ID: 3AJ7) and Mannosyl-oligosaccharide glucosidase (PDB ID: 4J5T), was studied. The resolution of the Oligo-1,6-glucosidase structure was 1.30Å, while the resolution of the Mannosyl-oligosaccharide glucosidase structure was 2.04Å. The results of the study revealed that hydrogen bonds were formed when a hydrogen atom interacted with an electronegative atom, such as oxygen or nitrogen. To investigate the binding interactions between the ligands (ZL11–ZL16) and their metal complexes with the binding pocket of Mannosyl-oligosaccharide and Oligo-1,6-glucosidase, molecular docking analysis was conducted. The docking analysis yielded highly convincing results, indicating strong binding interactions between several amino acid residues within the binding pocket of Mannosyl-oligosaccharide glucosidase and Oligo-1,6-glucosidase. These findings provide valuable insights into potential lead compounds for drug development targeting mannosyl-oligosaccharide glucosidase and Oligo-1,6-glucosidase. The docking analysis of Oligo-1,6-glucosidase also produced convincing results, indicating strong interactions between several amino acid residues within its binding pocket and the ZL16, ZL16Mn, and ZL16Zn compounds as shown in Figure 9. The binding energies for these interactions were determined to be –9.8, –10.9 and –10.8 kcal/mol, respectively as given in Table 6.

Similarly, the docking analysis yielded highly convincing results, indicating strong binding interactions between several amino acid residues within the binding pocket of Mannosyl-oligosaccharide glucosidase and the ZL15, ZL15Mn, and ZL15Zn compounds as shown in Figure 8. The binding energies for these interactions were determined to be –10.1, –10.3, and –10.6 kcal/mol, respectively as given in Table 7. These findings suggest that the synthesized ligands have the potential to interact strongly with the binding pockets of both Mannosyl-oligosaccharide glucosidase and Oligo-1,6-glucosidase.

Table 6

**Molecular Docking of compounds (ZL11-ZL16) with Oligo-1,6-glucosidase  
and mannosyl-oligosaccharide glucosidase**

Ligand Codes	PDB ID	Binding energy, kcal/mol	Hydrogen bonds interactions	Hydrophobic interactions
ZL11	3AJ7	-8.6	LYS156	LEU313, ALA418, PHE314, ILE419, ASP233
	4J5T	-9.0	HIS803, ARG799, ASP724	GLU463, GLU402, ARG727, MET401
ZL12	3AJ7	-8.6	No	LYS156, TYR158, PHE303
	4J5T	-9.7	ARG428	ASP392, GLU771, ASP568, TYR709, LEU563, PHE444
ZL13	3AJ7	-8.7	HIS295, ASN259, ILE272	VAL266, ALA292, ARG263
	4J5T	-9.4	HIS803, ARG799, ASP724	ARG727, ARG467
ZL14	3AJ7	-10.1	No	LYS156, TYR158, PHE303
	4J5T	-8.3	ARG428	GLU771, ASP392, ASP568, TYR709, LEU563, PHE444
ZL15	3AJ7	-10.1	HIS295, ASN259, ILE272	VAL266, ALA292, ARG263
	4J5T	-9.3	HIS803, ARG799, ASP724	ARG727, ARG467
ZL16	3AJ7	-8.8	ASN317, LYS156	LEU313, ASP233, ALA418, PHE314, ILE419
	4J5T	-9.8	NO	ARG727, GLU402, GLU463, SER802, MET401, PRO731, ILE734

Table 7

**Molecular Docking metal complexes (ZL11-ZL16) with Oligo-1,6-glucosidase  
and mannosyl-oligosaccharide glucosidase**

Ligand Codes	PDB ID	Binding energy, kcal/mol	Hydrogen bonds interactions	Hydrophobic interactions
ZL11Mn	3AJ7	-9.1	PHE321	LEU439
	4J5T	-9.8	TYR709	PHE444, PHE389, PHE385, PRO441
ZL11Zn	3AJ7	-9.7	PHE543, LEU323, LYS523	PHE321
	4J5T	-8.9	MET493, ARG304	PHE7, LYS98
ZL12Mn	3AJ7	-8.1	NO	GLU332, ALA329, ILE328, PRO312, HIS280
	4J5T	-8.6	LYS597, LYS669	HIS601, TYR728, GLU616
ZL12Zn	3AJ7	-9.4	ASP363	PHE321, LEU439, ASP362
	4J5T	-8.9	HIS561, ARG428	PHE444, PRO441, PHE385, TYR709, LEU563
ZL13Mn	3AJ7	-9.1	PHE321	LEU439
	4J5T	-9.5	ARG387	PHE444, ALA783, PHE385, PHE384
ZL13Zn	3AJ7	-9.1	NO	
	4J5T	-10.2	HIS561	LEU563, ARG428, GLU707
ZL14Mn	3AJ7	-8.7	SER545	ASP362, LEU439, LYS524
	4J5T	-10.4	TYR709, ARG387	GLU771, PHE444
ZL14Zn	3AJ7	-10.2	NO	
	4J5T	-9.6	NO	TYR709, PHE385, PHE444, PRO441
ZL15Mn	3AJ7	-10.3	NO	PRO312
	4J5T	-12.2	NO	PHE444, ILE362, ILE451, LYS363
ZL15Zn	3AJ7	-10.6	LYS523, LEU323	LEU439
	4J5T	-12.7	ASP568, TRP710	ARG428, TYR709, PHE385
ZL16Mn	3AJ7	-8.9	NO	LYS523, PHE360, LEU323, LEU439
	4J5T	-10.9	NO	LYS98, PHE7, ARG304, GLU10, LYS6
ZL16Zn	3AJ7	-9.1	ASP363	LEU439, PHE321
	4J5T	-10.8	HIS561, ARG428	TRP710, LEU563, PHE389, PHE385, GLU707

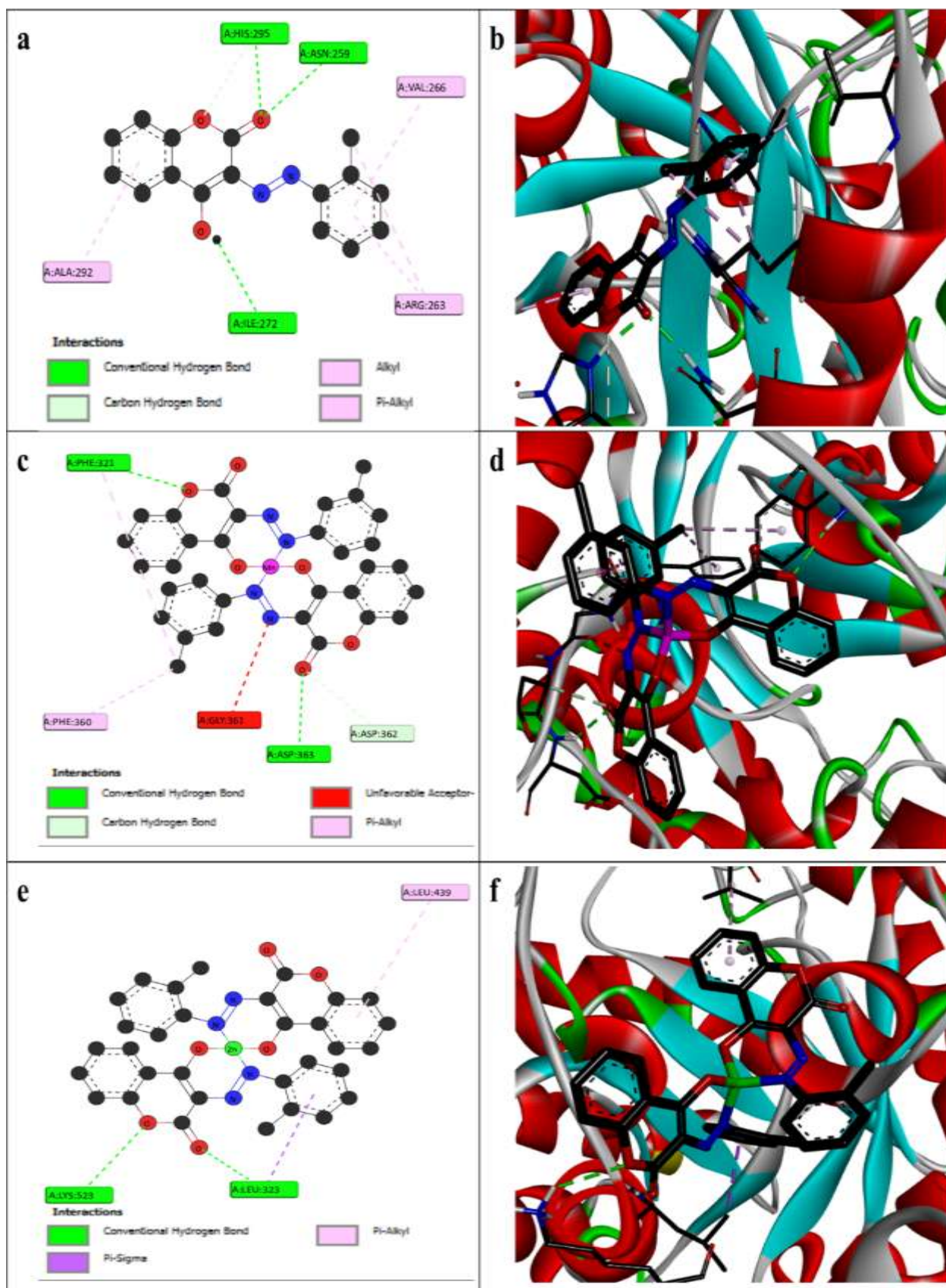


Figure 9. (a) Most probable 2D and (b) 3D binding modes of ZL15; (c) 2D ZL15Mn; (d) 3D ZL15Mn; (e) 2D ZL15Zn; (f) 3D ZL15Zn



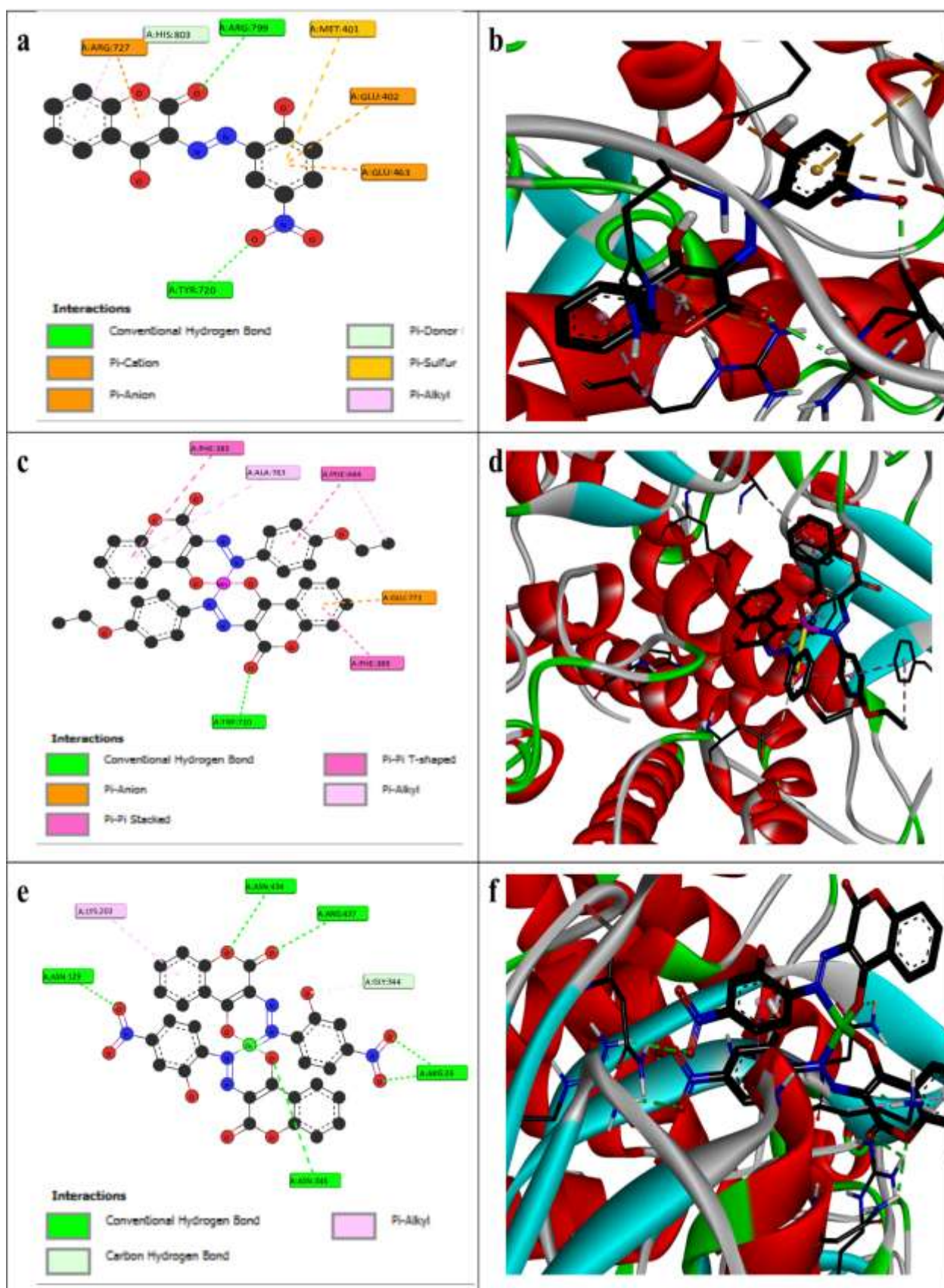


Figure 10. (a) Most probable 2D and (b) 3D binding modes of ZL16; (c) 2D ZL16Mn; (d) 3D ZL16Mn; (e) 2D ZL16Zn; (f) 3D ZL16Zn

### Conclusions

In a recent study, researchers successfully synthesized several new medicinal coumarin derivatives using a synthesis process that is both environmentally friendly and efficient. The compounds synthesized include 4-hydroxycoumarin, 2-aminophenol, 2-amino-5-chlorobenzophenone, o-toluidine, 2'-amino-2,5-dichlorophenylphenone, 2-chloroaniline, p-toluidine. The synthesis process achieved excellent yields ranging from 70 % to 87 % at temperatures between 0–5 °C. To determine the structure of the synthesized compounds, various characterization methods were employed, including FTIR, <sup>1</sup>H NMR, <sup>13</sup>C NMR, UV/VIS, XRD, and TGA. Mass spectroscopy was also used to confirm the mass of the synthesized compounds. The FTIR spectra analysis revealed the presence of functional groups such as O–H stretch, N–H stretch, and N=N group, which confirmed the successful synthesis of the ligands. The spectra also showed peaks corresponding to sp<sup>3</sup> CH<sub>3</sub> stretch, aromatic C–H stretch, carbonyl group C=O stretch, C=C stretch, and aromatic C–N stretch. Interestingly, the phenolic proton concentration of most coumarin compounds typically falls within the range of 11.0 to 1.5 ppm. However, in this study, the values varied from 13 to 15 ppm for the coumarin compounds, indicating some structural differences. The <sup>13</sup>C NMR analysis of the coumarin derivatives revealed specific peaks corresponding to the 6 signals of carbon for azo- groups and nitro-, hydroxyl-, and nitro- groups were also detected. To further characterize the synthesized compounds and their metal complexes, UV-Visible analysis was conducted in the 300–600 nm range, and powder XRD analysis was performed. The XRD results indicated crystal sizes for ZL16, ZL16Mn, and ZL16Zn as 4.092 nm, 4.341 nm, and 1.574 nm, respectively. Thermal stability was assessed through TGA analysis, which demonstrated that the synthesized compounds exhibited thermal stability up to 800 °C. The synthesized ligands and their metal complexes were then subjected to screening for antibacterial, molecular docking, and antioxidant activities.

Antibacterial activity was assessed against gram-negative bacteria (*E. coli* and *Pseudomonas*) and gram-positive bacteria (*Staphylococcus pyogenes* and *Bacillus*), with inhibition zones ranging from 7–31 mm, while Amikacin showed a zone of inhibition of 15 mm. In terms of DPPH antioxidant activity, compounds ZL16, ZL11Mn, and ZL14Zn demonstrate greater potency than ascorbic acid, with IC<sub>50</sub> values 6.57, 6.45 and 5.65 µg/mL respectively. In the same way DPPH antioxidant activity, compounds ZL12, ZL12Mn, and ZL14Zn demonstrate greater potency than ascorbic acid, with IC<sub>50</sub> values 6.38, 5.99 and 6.07 µg/mL respectively. The docking analysis revealed strong binding interactions between the Mannosyl-oligosaccharide glucosidase binding pocket and ZL15, ZL15Mn, and ZL15Zn compounds, with binding energies of –10.1, –10.3, and –10.6 kcal/mol, respectively. Similarly, Oligo-1,6-glucosidase showed strong interactions with the ZL16, ZL16Mn, and ZL16Zn compounds, with binding energies of –9.8, –10.9, and –10.8 kcal/mol, respectively. In conclusion, this study successfully synthesized new medicinal coumarin derivatives and their metal complexes using an environmentally friendly synthesis process. The compounds exhibited significant antibacterial and antioxidant activities, as well as promising results in molecular docking studies. These findings contribute to the field of medicinal chemistry and hold promise for the development of potential therapeutic agents. Further investigations are warranted to explore their full potential.

### Supporting Information

The Supporting Information is available free at <https://ejc.buketov.edu.kz/ejc/article/view/479/322>

### Author Information\*

\*The authors' names are presented in the following order: First Name, Middle Name and Last Name

**Zulfiqar Ali Shahid** — PhD Scholar; Institute of Chemistry, Islamia University of Bahawalpur, 63100, Bahawalpur, Pakistan; e-mail: [zulfiqar.ali.shahid1980@gmail.com](mailto:zulfiqar.ali.shahid1980@gmail.com); <https://orcid.org/0009-0004-0722-7563>

**Rukhsana Tabassum** (corresponding author) — Assistant Professor; Institute of Chemistry, Islamia University of Bahawalpur, 63100, Bahawalpur, Pakistan; e-mail: [rukhsana.tabassum@iub.edu.pk](mailto:rukhsana.tabassum@iub.edu.pk); <https://orcid.org/0000-0002-9483-254X>

### Author Contributions

The manuscript was written through contributions of all authors. All authors have given approval to the final version of the manuscript. **CRedit**: **Zulfiqar Ali Shahid** — investigation, validation, formal analysis, — writing-original draft, writing-review & editing; **Rukhsana Tabassum** — design, conceptualization, methodology, supervision.

### Acknowledgments

Authors are grateful to the Institute of Chemistry-IUB for providing essential facilities. Authors also acknowledge the Higher Education Commission for providing analyses facility via ASIP.

### Declaration of Generative AI and AI-Assisted Technologies in the Writing Process

During the preparation of this work the authors used Grammarly in order to refine the language of the manuscript. After using this service, the authors reviewed and edited the content as needed and take full responsibility for the content of the publication.

### Conflicts of Interest

The authors declare no conflict of interest.

### References

- 1 Abdel-Latif, S. A., & Moustafa, H. (2018). Synthesis, spectroscopic properties, density functional theory calculations, and nonlinear optical properties of novel complexes of 5-hydroxy-4,7-dimethyl-6-(phenylazo) coumarin with Mn(II), Co(II), Ni(II), Cu(II), and Zn(II) metal ions. *Applied Organometallic Chemistry*, 32(4), e4269. <https://doi.org/10.1002/aoc.4269>
- 2 Adimule, V. M., Nandi, S. S., Kerur, S., Khadapure, S. A., & Chinnam, S. (2022). Recent advances in the one-pot synthesis of coumarin derivatives from different starting materials using nanoparticles: A review. *Topics in Catalysis*, 1–31. <https://doi.org/10.1007/s11244-022-01554-0>
- 3 Anderson, N. C., Hendricks, M. P., Choi, J. J., & Owen, J. S. (2013). Ligand exchange and the stoichiometry of metal chalcogenide nanocrystals: Spectroscopic observation of facile metal-carboxylate displacement and binding. *Journal of the American Chemical Society*, 135(49), 18536–18548. <https://doi.org/10.1021/ja4091298>
- 4 Attaullah, H. M., Ejaz, S. A., Channar, P. A., Saeed, A., Ujan, R., Zargar, S., Channar, S. A., Sahito, R., Wani, T. A., & Abbas, Q. (2024). Exploration of newly synthesized azo-thiohydantoins as potential alkaline phosphatase inhibitors via advanced biochemical characterization and molecular modeling approaches. *BMC Chemistry*, 18(1), 47. <https://doi.org/10.1186/s13065-024-00472-3>
- 5 Balewski, L., Szulta, S., Jalińska, A., & Kornicka, A. (2021). A mini-review: Recent advances in coumarin-metal complexes with biological properties. *Frontiers in Chemistry*, 9, 781779. <https://doi.org/10.3389/fchem.2021.781779>
- 6 Bazargani, M. M., & Rohloff, J. (2016). Antibiofilm activity of essential oils and plant extracts against *Staphylococcus aureus* and *Escherichia coli* biofilms. *Food Control*, 61, 156–164. <https://doi.org/10.1016/j.foodcont.2015.09.036>
- 7 Catapano, M. C., Karlíčková, J., Tvrdý, V., Sharma, S., Prasad, A. K., Saso, L., Chhillar, A. K., Kuneš, J., Pour, M., & Parmar, V. S. (2018). Mono and dihydroxy coumarin derivatives: Copper chelation and reduction ability. *Journal of Trace Elements in Medicine and Biology*, 46, 88–95. <https://doi.org/10.1016/j.jtemb.2017.10.003>
- 8 Filipisky, T., Riha, M., Macakova, K., Anzenbacherová, E., Karlickova, J., & Mladenka, P. (2015). Antioxidant effects of coumarins include direct radical scavenging, metal chelation, and inhibition of ROS-producing enzymes. *Current Topics in Medicinal Chemistry*, 15(5), 415–431. <https://doi.org/10.2174/1568026614666150407124745>
- 9 Garg, S. S., Gupta, J., Sharma, S., & Sahu, D. (2020). An insight into the therapeutic applications of coumarin compounds and their mechanisms of action. *European Journal of Pharmaceutical Sciences*, 152, 105424. <https://doi.org/10.1016/j.ejps.2020.105424>
- 10 Ghanghas, P., Choudhary, A., Kumar, D., & Poonia, K. (2021). Coordination metal complexes with Schiff bases: Useful pharmacophores with comprehensive biological applications. *Inorganic Chemistry Communications*, 130, 108710. <https://doi.org/10.1016/j.inoche.2021.108710>
- 11 Gupta, A., Mumtaz, S., Li, C.-H., Hussain, I., & Rotello, V. M. (2019). Combatting antibiotic-resistant bacteria using nanomaterials. *Chemical Society Reviews*, 48(2), 415–427. <https://doi.org/10.1039/C7CS00857J>
- 12 Houas, N., Chafaa, S., Chafai, N., Ghedjati, S., Djenane, M., & Kitouni, S. (2022). Synthesis, characterization, DFT study, and antioxidant activity of (2-hydroxynaphthalen-1-yl)methyl-2-hydroxyphenylamino phosphonic acid. *Journal of Molecular Structure*, 1247, 131322. <https://doi.org/10.1016/j.molstruc.2021.131322>
- 13 Kadhum, A. A. H., Al-Amiery, A. A., Musa, A. Y., & Mohamad, A. B. (2011). The antioxidant activity of new coumarin derivatives. *International Journal of Molecular Sciences*, 12(9), 5747–5761. <https://doi.org/10.3390/ijms12095747>
- 14 Kapur, A., Hasković, A., Čopra-Janićijević, A., Klepo, L., Topčagić, A., Tahirović, I., & Sofić, E. (2012). Spectrophotometric analysis of total ascorbic acid content in various fruits and vegetables. *Bulletin of the Chemists and Technologists of Bosnia and Herzegovina*, 38(4), 39–42. <https://doi.org/10.35773/bctb.2012.38.4.39>
- 15 Kaur, H., Lim, S. M., Ramasamy, K., Vasudevan, M., Shah, S. A. A., & Narasimhan, B. (2020). Diazenyl Schiff bases: Synthesis, spectral analysis, antimicrobial studies, and cytotoxic activity on human colorectal carcinoma cell line (HCT-116). *Arabian Journal of Chemistry*, 13(1), 377–392. <https://doi.org/10.1016/j.arabjc.2016.08.004>



- 16 Keri, R. S., Sasidhar, B., Nagaraja, B. M., & Santos, M. A. (2015). Recent progress in the drug development of coumarin derivatives as potent antituberculosis agents. *European Journal of Medicinal Chemistry*, 100, 257–269. <https://doi.org/10.1016/j.ejmech.2015.06.037>
- 17 Kharadi, G. (2012). Thermal decomposition and mass spectra of mixed ligand copper (II) complexes of 1,10-phenanthroline and coumarin derivatives. *Journal of Thermal Analysis and Calorimetry*, 107(2), 651–659. <https://doi.org/10.1007/s10973-011-1760-2>
- 18 Lončarić, M., Gašo-Sokač, D., Jokić, S., & Molnar, M. (2020). Recent advances in the synthesis of coumarin derivatives from different starting materials. *Biomolecules*, 10(1), 151. <https://doi.org/10.3390/biom10010151>
- 19 Maobe, M. A., & Nyarango, R. M. (2013). Fourier transformer infra-red spectrophotometer analysis of *Urtica dioica* medicinal herb used for the treatment of diabetes, malaria, and pneumonia in Kisii region, Southwest Kenya. *World Applied Sciences Journal*, 21(8), 1128–1135. <https://doi.org/10.5829/idosi.wasj.2013.21.8.1898>
- 20 Marchi, R. C., Campos, I. A., Santana, V. T., & Carlos, R. M. (2022). Chemical implications and considerations on techniques used to assess the in vitro antioxidant activity of coordination compounds. *Coordination Chemistry Reviews*, 451, 214275. <https://doi.org/10.1016/j.ccr.2022.214275>
- 21 Ndagi, U., Mhlongo, N., & Soliman, M. E. (2017). Metal complexes in cancer therapy—an update from a drug design perspective. *Drug Design, Development and Therapy*, 599–616. <https://doi.org/10.2147/DDDT.S134156>
- 22 Olson, E. J., & Bühlmann, P. (2011). Getting more out of a Job plot: Determination of reactant to product stoichiometry in cases of displacement reactions and n:n complex formation. *The Journal of Organic Chemistry*, 76(20), 8406–8412. <https://doi.org/10.1021/jo2015719>
- 23 Patil, S. A., Unki, S. N., & Badami, P. S. (2013). Synthesis, characterization, biological and thermal behavior of Co(II), Ni(II), and Cu(II) complexes with Schiff bases having coumarin moieties. *Journal of Thermal Analysis and Calorimetry*, 111, 1281–1289. <https://doi.org/10.1007/s10973-012-2809-2>
- 24 Peng, X.-M., LV Damu, G., & Zhou, H. (2013). Current developments of coumarin compounds in medicinal chemistry. *Current Pharmaceutical Design*, 19(21), 3884–3930. <https://doi.org/10.2174/1381612811319210010>
- 25 Retnam, C. G., Rose, S. V., & Kumari, B. S. (2023). Synthesis, characterization, biological activity, and molecular docking study of transition metal complexes from heterocyclic ligand system. *Journal of Molecular Structure*, 1282, 135162. <https://doi.org/10.1016/j.molstruc.2023.135162>
- 26 Sharma, T., Singh, D., Mahapatra, A., Mahapatra, P., Sahoo, S., & Sahoo, S. K. (2022). Advancements in clinical translation of flavonoid nanoparticles for cancer treatment. *OpenNano*, 100074. <https://doi.org/10.1016/j.opnano.2022.100074>
- 27 Sohrabi, M., Binaeizadeh, M. R., Iraj, A., Larijani, B., Saeedi, M., & Mahdavi, M. (2022). A review on  $\alpha$ -glucosidase inhibitory activity of first-row transition metal complexes: A futuristic strategy for the treatment of type 2 diabetes. *RSC Advances*, 12(19), 12011–12052. <https://doi.org/10.1039/D2RA02383A>
- 28 Souhangir, M., Bidoki, S. M., & Gharanjig, K. (2022). Synthesis of a novel fluorescent reactive dye based on coumarin-benzimidazole for high visibility dyeing of cotton. *Progress in Color, Colorants and Coatings*, 15(4), 327–340. <https://doi.org/10.1515/pccc-2022-0024>
- 29 Sunitha, N., Raj, C. I. S., & Kumari, B. S. (2023). Synthesis, spectral studies, biological evaluation, and molecular docking studies of metal complexes from coumarin derivative. *Journal of Molecular Structure*, 1285, 135443. <https://doi.org/10.1016/j.molstruc.2023.135443>
- 30 Wiester, M. J., Ulmann, P. A., & Mirkin, C. A. (2011). Enzyme mimics based upon supramolecular coordination chemistry. *Angewandte Chemie International Edition*, 50(1), 114–137. <https://doi.org/10.1002/anie.201004563>
- 31 Zaidan, M., Noor Rain, A., Badrul, A., Adlin, A., Norazah, A., & Zakiah, I. (2005). In vitro screening of five local medicinal plants for antibacterial activity using disc diffusion method. *Trop Biomed*, 22(2), 165–170.
- 32 Zhang, G., Zheng, H., Guo, M., Du, L., Liu, G., & Wang, P. (2016). Synthesis of polymeric fluorescent brightener based on coumarin and its performances on paper as light stabilizer, fluorescent brightener, and surface sizing agent. *Applied Surface Science*, 367, 167–173. <https://doi.org/10.1016/j.apsusc.2016.01.031>

## CHEMICAL TECHNOLOGY

### Article

Received: 24 September 2024 | Revised: 30 October 2025 |

Accepted: 3 November 2025 | Published online: 3 December 2025

UDC 541.128.13

<https://doi.org/10.31489/2959-0663/4-25-14>

Irada G. Melikova<sup>1\*</sup>, Arif J. Efendi<sup>1</sup>, Manaf R. Manafov<sup>1</sup>, Natavan F. Aykan<sup>1</sup>,  
Guseyn M. Faradjev<sup>1</sup>, Ceyran T. Rustamova<sup>1</sup>, Nizami I. Shikhaliyev<sup>2</sup>

<sup>1</sup>*Institute of Catalysis and Inorganic Chemistry named after acad. M. Nagiyev,*

*Ministry of Science and Education of Republic of Azerbaijan, Baku, Azerbaijan;*

<sup>2</sup>*Azerbaijan Technical University, Ministry of Education of the Republic of Azerbaijan, Baku, Azerbaijan*

(\*Corresponding author's e-mail: [iradam@rambler.ru](mailto:iradam@rambler.ru))

### Kinetics and Mechanism of the Oxidation Reaction of Chlorine-Containing Hydrocarbons on a Vanadium Phosphorus Catalyst

The kinetic regularities of oxidation reactions of 1,2,4-trichlorobutene-2, 2,3,3-trichlorobutene-1, 1,2,3-trichlorobutene-2 and pentachlorobutene-1 on vanadium phosphorus catalyst exhibiting high activity and selectivity were studied. The presence of parallel-sequential pathways of XY oxidation with the formation of the main organochlorine compounds and deep oxidation products was established. It was shown that presence and location of the double bond and the number of chlorine atoms affected the direction of the oxidation reaction. The rate of XY consumption in a fixed catalyst bed exceeds that in a fluidized bed, although the rate of formation of the target product is higher in a fluidized bed. Hypotheses reflecting the possibility of a staged reaction mechanism taking into account the modification of the surface of the vanadium-phosphorus oxide system by the main and by-products of the oxidation reactions of chlorobutenes, as well as the competition of substances for active centers were investigated. Discrimination of these hypotheses was carried out on the basis of the Bartlett's criterion and Powell's method, and the mechanism that most fully explains the experimental results was selected. The calculated hardness values were obtained according to the proposed kinetic model by the Kutta-Meyerson and Runge-Kutta methods. A more detailed study of the mechanism of the oxidation reaction of chlorinated hydrocarbons will allow for effective control of its course and the achievement of selective oxidation of chlorinated hydrocarbons.

**Keywords:** kinetic regularities, mechanism, vanadium-phosphorus catalyst, oxidation reactions, chlorinated hydrocarbons, product formation rate, fluidized bed, fixed catalyst bed, Bartlett's criterion

#### Abbreviations

chlorohydrocarbons	—	CH
1,1,3-dichlorobutene-2	—	1,3-DCB-2
1,2,4-trichlorobutene-2	—	1,2,4-TCB-2
1,2,3,4-pentachlorobutene-1	—	PCB-1
chloropropanoic acid	—	CPA
chloroacetic acid	—	CAA
chloroacrylic acid	—	CA
monochloromaleic anhydride	—	m-ChMA
dichloromaleic anhydride	—	d-ChMA
acetic acid	—	AA
fixed bed	—	F
fluidized bed	—	Fl

### Introduction

The study of the kinetics and mechanism of the oxidation reaction of chlorinated hydrocarbons on a vanadium phosphorus catalyst is important both for understanding the mechanism of interactions and for developing more efficient processes in the chemical industry, such as obtaining valuable products from hydrocarbons.

Numerous scientific papers are devoted to the oxidation of hydrocarbons on various catalysts and identifying their mechanism [1–6]. However, there are few works devoted to the oxidation of their chlorinated derivatives. In this regard, the study of the kinetic patterns of oxidation reactions of chlorinated hydrocarbons (CH) is important for establishing the directions and mechanism of their oxidation, as well as for constructing kinetic models.

It is known that for process calculations it is necessary to determine the yields of products, reaction rates, the amount and composition of material flows, raw material consumption, heat, etc. A special place in this is occupied by the analysis of the kinetics of a chemical reaction on a selected catalytic system to identify the kinetic equation of the reaction rate and construct a mathematical model of the process [7–8]. In the presented work, when studying the heterogeneous catalytic oxidation of chlorohydrocarbons (CH), it was noted that it is expedient to study the kinetic patterns of the oxidation reaction using the example of various chlorine-containing hydrocarbons  $C_4$  as the most pronounced representatives of CH on V–P–O/SiO<sub>2</sub>, V–P–O/SiO<sub>2</sub> + MoO<sub>3</sub>, V–Mo–O/Al<sub>2</sub>O<sub>3</sub> + P<sub>2</sub>O<sub>5</sub> catalysts, exhibiting high activity and selectivity [9–11].

Another factor influencing the oxidation process is the concentration of O<sub>2</sub>. The results obtained showed that high oxygen concentrations provide high selectivity.

The results of the oxidation process in a stationary and fluidized bed catalyst are, of course, not the same. This is of great importance in the oxidation of CH, especially in the case of the need to utilize them [12]. The description of the rates of heterogeneous catalytic processes occurring in flow systems in a fluidized bed of catalyst has some difficulties associated with their hydrodynamics. These problems are reflected in the works [13], where an analysis of the kinetic description of heterogeneous catalytic reactions occurring in a fluidized bed of catalyst is carried out, and various models of their implementation are proposed [14–16].

The purpose of the conducted studies is to establish the kinetic patterns of the oxidation process of various chlorohydrocarbons in a stationary and fluidized bed of catalyst, as well as to propose a relatively simplified mechanism that includes the key stages of chlorohydrocarbon oxidation.

### Experimental

Carrying out heterogeneous catalytic oxidation of HC in a fluidized bed of V–P–O/SiO<sub>2</sub>, V–P–O/SiO<sub>2</sub> + MoO<sub>3</sub>, V–Mo–O/Al<sub>2</sub>O<sub>3</sub> + P<sub>2</sub>O<sub>5</sub> catalysts is characterized by a number of advantages: high heat transfer, low intra-diffusion resistance due to the use of small grains (0.4–0.8 mm) of the catalyst, simple reactor design, ease of input and output of particles and products, ease of regeneration, etc. A series of special experiments established the necessary fluidization rates, selected catalyst granules of certain sizes and linear velocity of the gas flow. Another series of experiments showed the oxidation reaction in the kinetic region [17–20].

It should be noted that chlorohydrocarbons without catalysts are not subject to selective oxidation, and at very high temperatures of 600–700 °C they decompose or are completely oxidized to CO<sub>2</sub>. The used V–P–O/SiO<sub>2</sub>, V–P–O/SiO<sub>2</sub> + MoO<sub>3</sub>, V–Mo–O/Al<sub>2</sub>O<sub>3</sub> + P<sub>2</sub>O<sub>5</sub> catalysts were synthesized by the known method of co-precipitation from the corresponding nitrate salts and supported on SiO<sub>2</sub> and Al<sub>2</sub>O<sub>3</sub> [6]. Only in the presence of these catalysts at relatively low temperatures of 673–793 K (400–500 °C) chlorohydrocarbons are selectively oxidized to valuable petrochemical products such as monochloromaleic and dichloromaleic anhydrides. The effect of the catalyst granule size on the degree of HC conversion at temperatures of 673–773 K was studied by varying the catalyst particle size from 0.25÷0.5 to 0.6÷0.8 mm. The degree of HC conversion, as well as the selectivity of the process at the same temperature, remain virtually unchanged, indicating the absence of diffusion complications. Changing the feed rate of the initial gas flow also does not affect the process parameters, which indicates the absence of external diffusion inhibition, i.e. the oxidation reaction occurs in the kinetic region. The data obtained during the study in the gradient-free flow-circulation and flow-through installations are consistent with each other and with the results of [4, 5, 21–24].

In order to identify the kinetic patterns of oxidation reactions of chlorine-containing hydrocarbons  $C_4$  and to construct kinetic models that make it possible to control the oxidation process, the effect of various parameters on its course was studied in a wide range of their change:  $T = 673–793$  K,  $C_{O_2} = 1 \cdot 10^{-4}–20 \cdot 10^{-5}$ ,

$C_{XY} = 1 \cdot 10^{-4} - 20 \cdot 10^{-3}$  mol/l,  $\tau = 0.1 - 1.0$  s using examples of oxidation reactions of 12-DCButene, 1,3-dichlorobutene-2 (1,3-DCB-2), 1,2,4-trichlorobutene-2 (1,2,4-TCB-2), 2,3,3-trichlorobutene-1 (2,3,3-TCB-1), 1,2,3-trichlorobutene-2 (1,2,3-TCB-2), 1,2,3,4-pentachlorobutene-1 (PCB-1). The oxidation products of Ch-Butenes are chloropropanoic acid (CPA), chloroacetic acid (CAC), HCl, CO<sub>2</sub>, CO, H<sub>2</sub>O; 1,2-DCB-2 — chloroacrylic acid (CA), monochloromaleic anhydride (m-ChMA), dichloromaleic anhydride (d-ChMA), acetic acid (AA), CO, CO<sub>2</sub>, HCl, H<sub>2</sub>O, Cl<sub>2</sub>.

The statistical manipulation of the experimental results was ultimately aimed at determining the confidence interval boundary:

$$\left[ M - t_{n,p} \frac{S}{\sqrt{n}}; M + t_{n,p} \frac{S}{\sqrt{n}} \right],$$

where  $M$  is the average value of the data extraction;  $S$  is the standard deviation;  $t_{n,p}$  is a table value of Student's distribution with a number of degrees of freedom ( $n$ ) and confidence factor ( $P$ );  $n$  is a number of elements in taken extraction of corresponding experiments.

The calculation was carried out using the Excel software package with a confidence probability of  $P = 95\%$  and a preliminary calculation of the standard deviation ( $S$ ), with a sample size of  $n = 4 - 12$ . To find the confidence interval of all curves on graphs 1–4, given in the work, we use the “descriptive statistics” of the Excel program.

### Results and Discussion

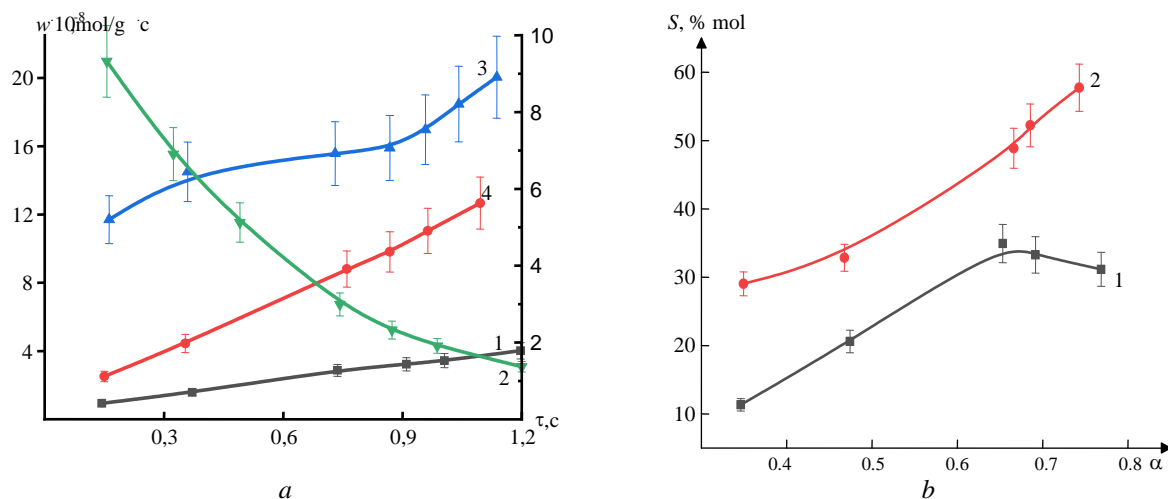
Catalysts containing vanadium and phosphorus oxides were previously used in the oxidation of four-carbon chlorohydrocarbons, such as *n*-butane, *n*-butene, 1,3-butadiene chlorides, or their mixtures with molecular oxygen or oxygen-containing gas to produce chloromaleic anhydrides. Conventional methods for preparing such catalysts involve reducing a pentavalent vanadium compound and combining it with a phosphorus compound and, optionally, promoter compounds under conditions where the valence of vanadium is below +5 to form catalyst precursors capable of being converted to vanadium phosphorus oxide. The oxide catalyst precursor is then isolated and converted to the active catalyst before or after forming suitable catalyst particles for either a fixed bed or a fluidized bed.

In the experimental work, catalytic systems were synthesized from water-soluble salts of vanadium and phosphorus (also molybdenum as a promoter) by impregnation on a carrier (SiO<sub>2</sub>) and subsequent annealing at various temperatures, and were studied in both fluidized and fixed-bed oxidation processes in an open-flow reactor. From the study of the nature of active centers on the surface of synthesized V–P–O/SiO<sub>2</sub>, V–P–O/SiO<sub>2</sub>+MoO<sub>3</sub>, V–Mo–O/Al<sub>2</sub>O<sub>3</sub>/P<sub>2</sub>O<sub>5</sub>, etc. catalysts by derivatographic method with acetone, phenol, butylamine, CO<sub>2</sub> and in pure form, it was found that there are a number of weak, medium, strong, very strong electron-acceptor, oxidizing and acid-base centers on the surface of the catalysts, which differ in energy and concentration. It has been proven by the X-ray phase method that during the activation of catalytic systems in air, O<sub>2</sub>, and chlorohydrocarbons, the phase formation processes continue and the phases that provide activity and selectivity are V<sub>2</sub>MoO<sub>8</sub> and V<sub>9</sub>Mo<sub>6</sub>O<sub>40</sub>. Here, the main oxidizing components are considered to be V and Mo. According to our previous studies (EPR), the catalyst is more active in the oxidation states of V<sup>+4</sup> and V<sup>+5</sup>, Mo<sup>+6</sup> and Mo<sup>+5</sup>. The ratio of V<sup>+4</sup>/V<sup>+5</sup>, Mo<sup>+6</sup>/Mo<sup>+5</sup> plays a decisive role. At the same time, the role of phosphorus is to regulate the ratios of V<sup>+4</sup>/V<sup>+5</sup>, Mo<sup>+6</sup>/Mo<sup>+5</sup> and the amount of weakly adsorbed oxygen, which causes deep oxidation. The fact that the amount of oxygen required for the oxidation reaction of chlorohydrocarbons exceeds stoichiometry is due to the consumption of oxygen in several directions: the creation of catalyst-environment equilibrium, prevention of the transition of reduced active components to a lower oxidation state (V<sup>+5</sup>→V<sup>+4</sup>→V<sup>+3</sup>), oxidation of active centers. At the beginning of the oxidation process, oxidation occurs due to oxygen escaping from the crystal lattice of the catalyst to the surface. Exposure of the surface of the catalysts to the oxidation-reduction process affects the nature of the active centers on the surface and directs the process in a selective direction.

The objects of the study were 1,2,4-trichlorobutene-2 (1,2,4-TCB-2), 1,2,3-trichlorobutene-1 (1,2,3-TCB-1), 2,3,3-trichlorobutene-1 (2,3,3-TCB-1), 1,1,2,3,4-pentachlorobutene-1 (PCB-1). It was of interest to study the kinetic patterns of tri- and pentachlorobutenes from the point of view of clarifying the role of the double bond and chlorine atoms in the formation of monochloromaleic (*m*-ChMA) and dichloromaleic (*d*-ChMA) anhydride. It was also important to clarify the conditions for the deep oxidation reaction and compare its rate with the rate of the reaction of formation of the target product. The kinetic curves of the oxidation reaction of 1,2,4-TCB-2 are shown in Figure 1. As can be seen from Figure 1, the rate of consumption

of the initial 1,2,4-TCB-2 gradually increases, while the rates of formation of *m*-ChMA, CO<sub>2</sub> and freely splitting chlorine increase simultaneously. The rate of the deep oxidation reaction exceeds the rate of the main reaction of *m*-ChMA formation by more than an order of magnitude, however, some parallelism of the graphs of these rates is observed up to  $\tau = 0.6$  s, after which  $w_{\text{CO}_2}$  increases sharply. Description of the results in  $w_i - C_i$  coordinates for the corresponding substances shows that they comply with a linear dependence (Fig. 1, *a*, *b*).

Comparison of the rates of the main reaction of *m*-ChMA formation and the deep oxidation reaction shows that CO<sub>2</sub> is formed in a parallel-sequential scheme both from the initial raw material and from the target product under certain conditions, which follows from the analysis of the curve of the selectivity dependence on the degree of conversion (Fig. 1 *b*).



*a* — Kinetic curves of the dependences of the oxidation reaction rate of 1,2,4-TCB-2 on the contact time.  
 1 — the rate of consumption of TCButene,  $w_{1,2,4\text{-TCB-2}}$ ; 2 — the rate of formation of *m*-ChMA— $w_{m\text{-ChMA}}$ ,  
 3 —  $w_{\text{CO}_2}$ ; 4 —  $w_{\text{Cl}_2}$ ; *b* — The dependence of selectivity on the degree of conversion of 1,2,4-TCB-2:  
 1 — *m*-ChMA; 2 — CO<sub>2</sub>. Confidence level  $P = 95\%$

Figure 1

The results of statistical processing of the experimental data in Figures 1–4 and the confidence intervals of the curves are shown in Table 1.

Table 1

Statistical analysis of experimental data and confidence intervals for the kinetic and selectivity curves presented in Figures 1–4 (confidence level  $P = 95\%$ )

Figure	Curve No.	$\bar{y} \pm \Delta$ ( $P = 0.95$ )	Range	Sample size, $n$
Figure 1a	1	$10.3 \pm 4.4$	(5.9; 14.7)	8
	2	$16.9 \pm 1.6$	(15.3; 18.5)	6
	3	$8.2 \pm 3.2$	(5.0; 11.4)	6
	4	$2.55 \pm 0.95$	(1.6; 3.5)	6
Figure 1b	1	$44 \pm 11$	(33; 55)	5
	2	$26.1 \pm 8.8$	(17.3; 34.9)	5
Figure 2	1	$14.8 \pm 7.0$	(7.8; 21.8)	7
	2	$5.7 \pm 3.1$	(2.6; 8.8)	5
	3	$12.9 \pm 6.6$	(6.3; 19.5)	7
	4	$5.7 \pm 3.8$	(1.9; 9.5)	6
Figure 3	1	$3.35 \pm 0.64$	(2.71; 3.99)	8
	1'	$2.91 \pm 0.88$	(2.03; 3.79)	8
	2	$0.59 \pm 0.20$	(0.39; 0.79)	12
	2'	$0.46 \pm 0.27$	(0.19; 0.73)	8
	3	$8.13 \pm 0.45$	(7.68; 8.58)	4



Continuation of Table 1

Figure	Curve No.	$\bar{y} \pm \Delta$ ( $P = 0.95$ )	Range	Sample size, $n$
Figure 3	3'	$7.84 \pm 0.64$	(7.20; 8.48)	4
	4	$5.88 \pm 0.17$	(5.71; 6.05)	6
	4'	$5.76 \pm 0.23$	(5.53; 5.99)	4
Figure 4	1	$3.5 \pm 2.1$	(2.4; 5.6)	4
	2	$5.29 \pm 0.87$	(4.42; 6.16)	4
	3	$8.0 \pm 2.6$	(5.4; 10.6)	4

The results of the study of the kinetic patterns of the oxidation reaction of 2,3,3-TCB-1 are shown in Figure 2.

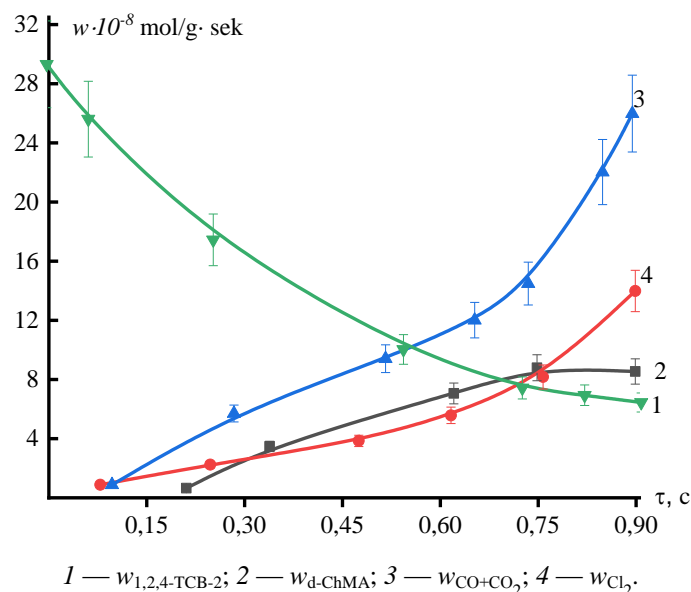


Figure 2. Results of kinetic studies of the oxidation reaction of 2,3,3-TCB-1, dependence of the accumulation rate on the contact time. Confidence level  $P = 95\%$

As can be seen from the presented dependencies (Fig. 2), the oxidation rate of the original 2,3,3-TCB-1 exceeds the rate of formation of d-ChMA and is comparable with the rate of formation of  $\text{CO}_2$ . Carbon dioxide is formed from the beginning of the reaction and then at small  $\tau$  as well, but after the value  $\tau = 0.7$  s, a sharp jump in the rate of formation of  $\text{CO}_2$  is observed. The curve of the rate of formation of chlorine (4) behaves similarly to the curve of the rate of formation of  $\text{CO}_2$  (3), which confirms the idea of the presence of an additional path of formation of  $\text{CO}_2$  (3) and a chlorine-containing compound. This is also evident from Figure 2, where the dependences of the rates of formation of  $\text{CO}_2$  and  $\text{Cl}_2$  on their concentrations grow in parallel at close values.

The study of the kinetics of 1,2,3-TCB-2, the results of which are presented in Figure 3, also confirmed the stated assumption about the formation of  $\text{CO}_2$ . The patterns revealed for 1,2,4-TCB-2 and 2,3,3-TCB-1 are also preserved in this case. Comparison of the rates of the main reaction and the deep oxidation reaction here more expressively indicates the presence of a parallel-sequential path of  $\text{CO}_2$  formation.

To clarify the role of the location of chlorine atoms in pentachlor-containing hydrocarbons, a detailed study of the kinetic regularities was carried out using 1,1,2,3,4-PCB-1 as an example.

The results of the influence of various parameters on the rates of the PCB-1 oxidation reaction in both fixed and fluidized beds of V-P-O/SiO<sub>2</sub> catalyst at different ratios of 1,1,2,3,4-PCB-1:O<sub>2</sub> (1:6 and 1:35) are shown in Figures 3 and 4. Comparison of the rate of total PCB-1 consumption in a fixed bed (Fig. 3) with the rate in a fluidized bed (Fig. 4) showed that  $w_{\text{PCB}}^F = 7.4 \cdot 10^{-8}$  mol/g is almost 2.0 times higher than  $w_{\text{PCB}}^{FI} = 3.58 \cdot 10^{-8}$  mol/g under the same reaction conditions ( $\tau = 0.6$  s). In this case, the rates of formation  $w_{\text{DCMA}}^{FI}$  are higher, and the rate of deep oxidation reaction decreases almost 2.0 times.

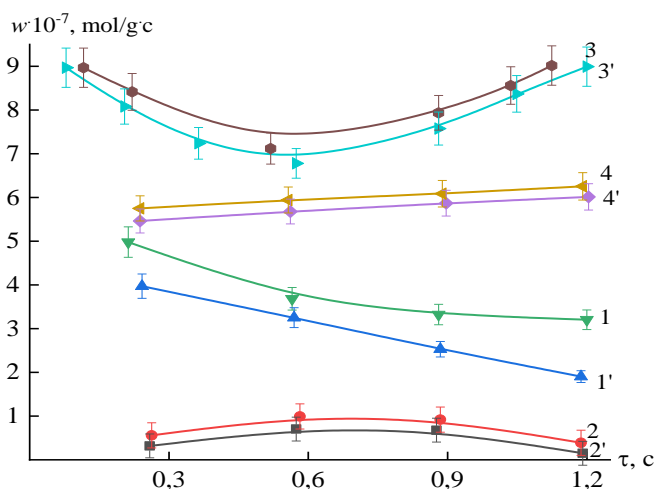


Figure 3. Results of the study of kinetic regularities of the oxidation reaction of 1,1,2,3,4-PCB-1, dependence of the reaction rate on the contact time in a fixed catalyst bed with PCB:O<sub>2</sub>. Confidence level  $P = 95\%$

And if the latter in the case of a fixed bed passes through a minimum, then in the case of a fluidized bed it is almost constant (at  $\tau = 0.15$  s,  $w_{\text{CO}_2} = 4.04 \cdot 10^{-7}$  mol/g s,  $\tau = 0.7$  s,  $w_{\text{CO}_2} = 4.33 \cdot 10^{-7}$  mol/g s — the increase is insignificant). When analyzing the obtained results, attention is drawn to the fact that in a fixed bed at a molar ratio of PCB:O<sub>2</sub> = 1:6 and  $\tau = 0.6$  s, the PCB consumption rate  $w_{\text{PCB}} = 3.85 \cdot 10^{-8}$  mol/g s, and at a ratio of PCB:O<sub>2</sub> = 1:35  $w_{\text{PCB}} = 3.52 \cdot 10^{-8}$  mol/g s. In the fluidized bed, the  $w_{\text{PCB}}$  values are  $7.68 \cdot 10^{-8}$  and  $7.44 \cdot 10^{-8}$  mol/g, respectively. The rates of d-ChMA formation are also higher, which confirms the correctness of the transition to studying reactions in the fluidized bed. The study of the effect of oxygen concentration at different temperatures on the oxidation rate of PCB and the rates of formation of reaction products in the fluidized bed is shown in Figure 4.

Here, a somewhat strange behavior of the dependence of  $w_{\text{PCB}}$  on CO<sub>2</sub> is also observed (Fig. 4), namely, at very low concentrations of O<sub>2</sub> — in the range from  $0.08 \cdot 10^{-3}$  mol/l to  $0.8 \cdot 10^{-3}$  mol/l, a decrease in the rate of PCB consumption is observed.

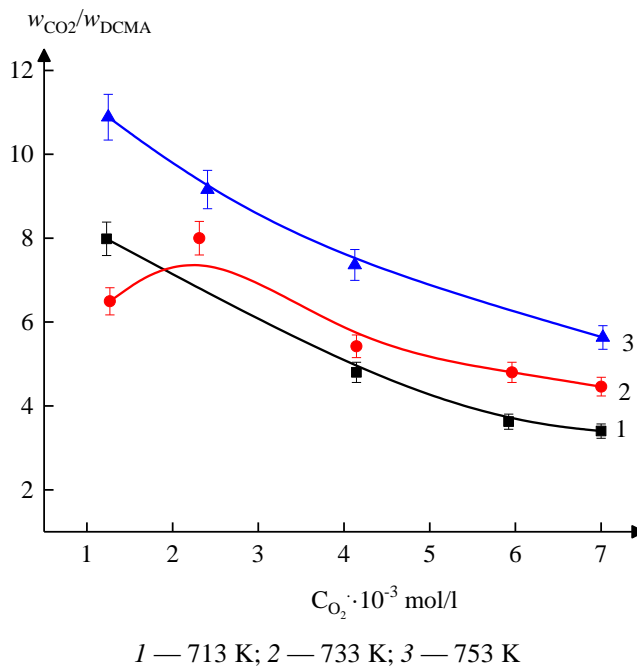
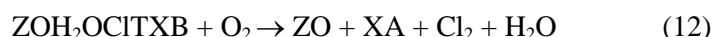
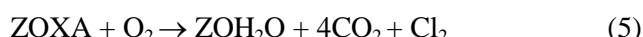
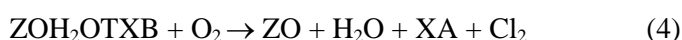


Figure 4. Results of the study of the kinetics of PCB-1 oxidation in a fluidized bed of catalyst at different temperatures. Confidence level  $P = 95\%$

A further increase in  $\text{CO}_2$  to  $7.15 \cdot 10^{-3}$  has almost no effect on the PCB oxidation rate. Only with an increase in temperature does the latter increase slightly (Fig. 4). The rate of d-ChMA formation at an initial  $\text{CO}_2$  concentration of up to  $5.36 \cdot 10^{-3}$  mol/l reaches a maximum. With an increase in temperature after 713 K, it decreases slightly. The rate of deep oxidation at initial oxygen concentrations is low and increases with an increase in  $\text{CO}_2$ , reaching its maximum at a value of  $\text{CO}_2 = 0.858 \cdot 10^{-3}$  mol/l, and then decreases slightly and becomes constant with a further increase in  $\text{CO}_2$ . However, with an increase in temperature, the rate of formation of freely cleaved chlorine increases. Comparison of the rates of the d-ChMA formation reaction and the deep oxidation reaction showed that when the reaction is carried out in a fixed catalyst bed, the  $w_{\text{CO}_2}/w_{\text{d-ChMA}}$  ratio changes more sharply than in the case of a fluidized bed (Fig. 4). With increasing temperature and with changing  $\text{CO}_2$ , this ratio increases [5, 7]. The reaction mechanism describes the step-by-step process of transforming reagents into products. For oxidation reactions involving chlorine-containing hydrocarbons and vanadium-phosphorus catalysts, the mechanism may include stages of oxygen activation on the catalyst surface, its interaction with the hydrocarbon, and the formation of intermediate products.

One of the main decisive and central places in the development of mathematical models of the process, which is important for the design and management of chemical technological processes, is occupied by the kinetic model of processes. The development of the kinetic model of processes, in turn, proceeds from the reaction mechanisms based on the experimental results of the study of the kinetic regularities of chemical reactions. Based on the proposed mechanisms of heterogeneous catalytic oxidation reactions of hydrocarbons and their chlorinated derivatives and the results of the oxidation reactions of chlorobutenes, we will consider a number of their stage mechanisms based on the results of the oxidation reactions of trichlorobutenes, which we studied. It should be noted that the discrimination of kinetic equations based on the proposed mechanisms and the calculation of the parameters of the kinetic model are based on known methods.

It is assumed that all active centers on the surface of the catalyst are in an oxidized state and modified by reaction products. Also, the process is quasi-stationary, the initial TXBs and the oxidation reaction occur according to the oxidation-reduction mechanism, and the main and by-products of the reaction are obtained according to the sequential-parallel reaction scheme. The oxidation reaction of TXB, which occurs in the "hot" layer of the catalyst, is more complex and occurs in more than 30 stages. Since solving the kinetic equation of this step-by-step reaction requires too much computer time and memory, and since it is necessary to solve a complex kinetic equation, it is possible to propose a relatively simplified mechanism that includes the main stages. Such a step-by-step mechanism can be written as follows:



where ZO is the means adsorbed oxygen on the surface of the active centers of the catalyst.

Based on this mechanism, we can write the kinetic equations of individual stages as follows:

$$W_1 = K_1 C_{\text{ZO}} P_{\text{TXB}} - K_{-1} C_{\text{ZOTXB}}$$

$$W_2 = K_2 C_{\text{ZOTXB}} P_{\text{O}_2}$$

$$W_3 = K_3 C_{\text{ZOH}_2\text{O}} P_{\text{TXB}} - K_{-3} C_{\text{ZOH}_2\text{OTXB}}$$

$$W_4 = K_4 C_{\text{ZOH}_2\text{OTXB}} P_{\text{O}_2}$$

$$W_5 = K_5 C_{\text{ZOXA}} P_{\text{O}_2}$$

$$W_6 = K_6 C_{\text{ZOXA}} P_{\text{TXB}}$$

$$W_7 = K_7 C_{\text{ZOH}_2\text{O}} P_{\text{XA}} - K_{-7} C_{\text{ZOH}_2\text{OXA}}$$

$$W_8 = K_8 C_{\text{ZOH}_2\text{OXA}} P_{\text{TXB}} - K_{-8} C_{\text{ZOH}_2\text{OTXB}}$$

$$W_9 = K_9 C_{\text{ZOH}_2\text{OXATXB}} P_{\text{O}_2}$$

$$W_{10} = K_{10} C_{\text{ZOH}_2\text{O}} P_{\text{O}_2} - K_{-10} C_{\text{ZOH}_2\text{OCl}}$$

$$W_{11} = K_{11} C_{\text{ZOH}_2\text{OCl}} P_{\text{TXB}} - K_{-11} C_{\text{ZOH}_2\text{OCITXB}}$$

$$W_{12} = K_{12} C_{\text{ZOH}_2\text{OCITXB}} P_{\text{O}_2}.$$

The results of the calculations showed that the kinetic model that more accurately reflects the experimental results is the one based on the mechanism put forward in the hypothesis. Based on the kinetic model, we found the parameters of the kinetic equations for three temperatures (693, 713 and 733 K) with the “OptimMe” software application [24, 25]. Here the experimental and calculated values coincided. The calculated values of stiffness’s were found from that system of equations by the Kutta-Meyerson and Runge-Kutta method, and the values of the obtained parameters were initially taken for function minimization.

$$F = \sum_{i=1}^n \sum_{j=1}^m \left( \frac{Y_{ij}^t - Y_{ij}^N}{Y_{ij}} \right)^2;$$

$$F(K_1, \dots, K_{12}) = \sum_{k=1}^{12} [C_{ip}(K_1, \dots, K_{12}) - C_{ip}]^2.$$

Here,  $C_{ip}(K_1, \dots, K_{12})$   $i = 1 \div 2$  minimization was carried out based on Powell’s method, and the values of  $\ln K_0$  and activation energy were calculated by substituting the obtained rate constants in the Arrhenius equation. It should be noted that the experimental results accurately corresponded with the calculated values (10–15 %) of the concentrations obtained as a result of minimization, which indicates that the mechanisms of the oxidation reactions of TCHbutenes were correctly deduced.

Table 2

**Parameters and rate constants of the kinetic model of the oxidation process of 1,2,4-TXButene-2 to m-ChMA**

$k_i$	Temperature, K			$\ln K_0$	$E$ , kC/mol
	693 K	713 K	733 K		
$K_1$	0.3861	0.3712	0.3142	–6.4731	32.45
$K_{-1}$	$0.6742 \cdot 10^{-10}$	$0.6240 \cdot 10^{-9}$	$0.5036 \cdot 10^{-8}$	–5.4873	28.06
$K_2$	5.4623	5.8751	7.0221	14.3221	96.34
$K_3$	74.2702	68.7254	64.3104	1.0436	27.02
$K_{-3}$	$0.4823 \cdot 10^{-9}$	$0.4062 \cdot 10^{-8}$	$0.26 \cdot 10^{-7}$	–3.1435	36.78
$K_4$	1.5245	1.6113	2.1402	4.3768	58.43
$K_5$	$0.1024 \cdot 10^{-4}$	$0.56 \cdot 10^{-4}$	$0.632 \cdot 10^{-4}$	2.89	70.19
$K_6$	$0.091 \cdot 10^{-7}$	$0.041 \cdot 10^{-7}$	$0.018 \cdot 10^{-7}$	–14.41	23.54
$K_7$	71.2024	65.423	61.671	–3.172	19.22
$K_{-7}$	$0.23 \cdot 10^{-10}$	$0.56 \cdot 10^{-9}$	$0.12 \cdot 10^{-8}$	–2.01	20.46
$K_8$	$62.136 \cdot 10^{-8}$	$58.712 \cdot 10^{-8}$	$56.4 \cdot 10^{-8}$	–2.45	21.36
$K_{-8}$	$10.21 \cdot 10^{-9}$	$9.43 \cdot 10^{-9}$	$7.45 \cdot 10^{-6}$	–4.02	20.71
$K_{-9}$	33.56	38.42	41.76	13.84	80.68
$K_{10}$	$4.1 \cdot 10^{-2}$	$3.2 \cdot 10^{-2}$	$2.8 \cdot 10^{-2}$	4.25	26.93
$K_{11}$	52.12	46.38	41.82	–5.32	24.02
$K_{-11}$	54.21	57.01	62.36	–1.21	15.27
$K_{-12}$	29.37	42.38	68.70	+11.20	68.74

Based on the obtained model, rate constants and parameters of the model were calculated for the kinetic equations of the mechanism of oxidation reactions in the hot bed of 1,2,3-TXB-1; 2,3,3-TXB-1; 1,2,3-TXB-2 and PXB V–P–O/SiO<sub>2</sub> catalysts. The obtained results are shown in Table 2.

### Conclusions

Thus, the study of the kinetic regularities of the oxidation reactions of tri- and pentachloro-containing non-limiting hydrocarbons C<sub>4</sub> on vanadium-phosphorus catalysts showed that they have the same character. The comparison of the rates of formation of products of selective and deep oxidation indicates the presence of parallel-consequential pathways of their formation, and the presence of an additional path of formation of CO<sub>2</sub> from chlorine-containing target compounds. It is shown that the amount, as well as the location of chlorine atoms and the double bond, have an effect on the direction of the oxidation reaction. The comparison of the rates of formation of the target products confirms the correctness of the choice of the fluidized bed of the catalyst for the implementation of selective oxidation. It is also shown that the initial end products of the reaction do not have an inhibitory effect on the rate of oxidation reactions. On the basis of kinetic conditions, a staged mechanism, kinetic model and oxidation reaction of chlorine-containing hydrocarbons were compiled and the parameters of this model were calculated.

### Author Information\*

*\*The authors' names are presented in the following order: First Name, Middle Name and Last Name*

**Irada Gasan Melikova** (*corresponding author*) — Leading Researcher, Associate Professor, Institute of Catalysis and Inorganic Chemistry named after acad. M. Nagiyev of Ministry of Science and Education of the Republic of Azerbaijan, H. Javid Ave. 113, Az-1143, Baku, Azerbaijan; e-mail: [iradam@rambler.ru](mailto:iradam@rambler.ru); <https://orcid.org/0000-0002-7906-1556>

**Arif Javanshir Efendi** — Doctor of Chemical Sciences, Professor, Institute of Catalysis and Inorganic Chemistry named after acad. M. Nagiyev, Ministry of Science and Education of the Republic of Azerbaijan, H. Javid Ave. 113, Az-1143, Baku, Azerbaijan; e-mail: [efendi-arif@mail.ru](mailto:efendi-arif@mail.ru); <https://orcid.org/0000-0002-5529-980X>

**Manaf Rizvan Manafov** — Leading Researcher, Associate Professor, Institute of Catalysis and Inorganic Chemistry named after acad. M. Nagiyev, Ministry of Science and Education of the Republic of Azerbaijan, H. Javid Ave. 113, Az-1143, Baku, Azerbaijan; e-mail: [mmanafov@gmail.com](mailto:mmanafov@gmail.com); <https://orcid.org/0000-0002-9965-4850>

**Natavan Fakhraddin Aykan** — Senior Researcher, Assistant Professor, Institute of Catalysis and Inorganic Chemistry named after acad. M. Nagiyev, Ministry of Science and Education of the Republic of Azerbaijan, H. Javid Ave. 113, Az-1143, Baku, Azerbaijan; e-mail: [ntvn\\_78@hotmail.com](mailto:ntvn_78@hotmail.com); <https://orcid.org/0000-0003-2245-7047>

**Guseyn Mammad Faradjev** — Leading Researcher, Associate Professor, Institute of Catalysis and Inorganic Chemistry named after acad. M. Nagiyev, Ministry of Science and Education of the Republic of Azerbaijan, H. Javid Ave. 113, Az-1143, Baku, Azerbaijan; e-mail: [huseynfaracov13@gmail.com](mailto:huseynfaracov13@gmail.com)

**Ceyran Teymur Rustamova** — Senior Researcher, Assistant Professor, Institute of Catalysis and Inorganic Chemistry named after acad. M. Nagiyev of Ministry of Science and Education of the Republic of Azerbaijan, H. Javid Ave. 113, Az-1143, Baku, Azerbaijan; e-mail: [rustamovac63@gmail.com](mailto:rustamovac63@gmail.com); <https://orcid.org/0000-0003-2300-8120>

**Nizami Ismail Shikhaliyev** — PhD, Assistant Professor, Azerbaijan Technical University, Ministry of Education of the Republic of Azerbaijan, G. Javid Ave. 25, Az-1073, Baku, Azerbaijan; e-mail: [nizamishihaliyev54@gmail.com](mailto:nizamishihaliyev54@gmail.com); <https://orcid.org/0009-0008-0381-8912>

### Conflict of Interest

The authors declare no conflict of interest.



### Author Contributions

The manuscript was written through contributions of all authors. All authors have given approval to the final version of the manuscript. CRediT: **Irada Gasan Melikova** conceptualization, data curation, methodology; writing — review and editing; **Arif Javanshir Efendi** writing — original draft, writing-review and editing, investigation, data curation; **Manaf Rizvan Manafov** data curation, writing — review and editing; **Natavan Fakhreddin Aykan** and **Nizami Ismail Shikhaliyev** investigation, resources; **Guseyn Mammad Faradjov** and **Ceyran Teymur Rustamova** investigation.

### References

- Shaoqi, Chu, Enlai, Wang, Fushan, Feng, Changsheng, Zhang, Jie, Jiang, Qinqin, Zhang, Fang, Wang, Liancheng, Bing, Guangjian, & Wang, Dezhi, Han (2022). A Review of Noble Metal Catalysts for Catalytic Removal of VOCs. *Catalysts*, 12(12), 1543. <https://doi.org/10.3390/catal12121543>
- Muhammad, Faizan, Ruirui, Zhang, & Ruixia, Liu (2022). Vanadium phosphorus oxide catalyst: Progress, development and applications. *Journal of Industrial and Engineering Chemistry*, 110, 27–67. <https://doi.org/10.1016/j.jiec.2022.02.049>
- Wang, J., Zhang, Y., Guo, X., Tang, J., Chen, Z., Ha, M. N., Cui, P., & Ke, Q. (2024). Manganese oxide-based catalysts for the sustainable synthesis of value-added chemicals through oxidation processes: A critical review and perspectives for the future. *Green Chemistry*, 26, 2365–2383. doi: <https://doi.org/10.1039/d3gc04117d>
- Ziran, Ma, Jiali, Zhou, Jing, Lin, Gongjin, Yang, Shuang, Liu, & Ge, Li (2024). Catalytic combustion of light hydrocarbons over Pd – Pt/Al<sub>2</sub>O<sub>3</sub>: The hidden PtI active sites. *Fuel*, 374, 132437. <https://doi.org/10.1016/j.fuel.2024.132437>
- Bagirzade, G. A., Tagiyev, D. B., & Manafov, M. R. (2016). Kinetics of vapor phase ammoxidation of o-xylene on V-Sb-Bi-Cr/γ-Al<sub>2</sub>O<sub>3</sub> oxide catalyst II. Development of kinetic reaction model. *Elixir Appl. Chem.*, 94, 40096–40099.
- Melikova, I. G., Efendi, A. D., Ismailova, B. A., Faradzhev, G. M., Magerramova, L. G., & Gadzhieva, K. I. (2018). Study of the Kinetics of Esterification of Dichloromaleic Anhydride with Methanol in the Presence of Zeolitic Catalysts. *Russian Journal of General Chemistry*, 88(12), 2480–2485. <https://doi.org/10.1134/s1070363218120058>
- Le, M. D., Warth, V., Giarracca, L., Moine, E., Bounaceur, R., Privat, R., Jaubert, J.-N., Fournet, R., Glaude, P.-A., & Sirjean, B. (2021). Development of a Detailed Kinetic Model for the Oxidation of n-Butane in the Liquid Phase. *The Journal of Physical Chemistry B*, 125(25), 6955–6967. <https://doi.org/10.1021/acs.jpcc.1c02988>
- Blanco-Bonilla, F., Estevez, R., López-Tenllado, F. J., Luna, D., & Bautista, F. M. (2024). Selective oxidation of methanol to green oxygenates on vanadium-aluminum phosphate-based catalysts. *Catalysis Today*, 430, 114517. <https://doi.org/10.1016/j.cattod.2024.114517>
- Sepideh, Badehkhsh, Nooshin, Saadatkhah, Mohammad, Jaber, Darabi, Mahboub, Olga, Guerrero-Pérez, & Gregory, S. Patience (2023). Morphological changes of vanadyl pyrophosphate due to thermal excursions. *Catalysis Today*, 407, 301–311. <https://doi.org/10.1016/j.cattod.2021.12.008>
- Zha, X., Yang, C., Huang, X., Ding, J., & Ding, Z. (2024). Recent progress and perspectives on metal oxide catalysts for thermocatalytic and photocatalytic oxidation of VOCs: a review. *Environmental Pollutants and Bioavailability*, 36(1), 1–16. <https://doi.org/10.1080/26395940.2024.2376827>
- Xueming, Zhang & Zhongkui, Zhao (2024). An efficient vanadium phosphorus oxide catalyst prepared by tuning vanadium precursor for selective oxidation of n-butane to maleic anhydride. *Materials Letters*, 357, 135679. <https://doi.org/10.1016/j.matlet.2023.135679>
- Emilio, Ritoré, José, Morillo, Carmen, Arnaiz, Bruno, Coquelet, José, Usero (2023). Chemical oxidation of hydrocarbon-contaminated soil: oxidant comparison study and soil influencing factors. *Environmental Engineering Research*, 28(6), 220610. <https://doi.org/10.4491/eer.2022.610>
- Andrushkevich, T. V. & Chesalov, Yu. A. (2018). Mechanism of heterogeneous catalytic oxidation of organic compounds to carboxylic acids. *Russian Chemical Reviews*, 87(6), 586–603. <https://doi.org/10.1070/RCR4779>
- Kai, Li & Xiaoqing, Luo (2023). Research Progress on Catalytic Combustion of Volatile Organic Compounds in Industrial Waste Gas. *Catalysts*, 13(2), 68. <https://doi.org/10.3390/catal13020268>
- Shakhtakinsky, T. N., Efendi, A. J., Salehli, N. F., Malikova, I. H., Manafov, M. R. et al. (2004). Study of oxidation reactions of o-Dichlorobenzene on oxide catalysts. *Azerbaijan Chemistry Journal*, 3, 13–17.
- Fazeli, A., Naseri, A., & Eslamjamal, F. (2020). Review of kinetic models of ethylene oxide production processes on silver catalysts. *Kinetics and catalysis*, 61, 4, 549–549. <https://doi.org/10.31857/s0453881120040073>
- Fei, Dai, Zihang, Li, Xuejing, Chen, Bin, He, Ruixia, Liu and Suojia, Zhang (2018). Synthesis of vanadium phosphorus oxide catalysts promoted by iron-based ionic liquids and their catalytic performance in selective oxidation of n-butane. *Catal. Sci. Technol.*, 8, 4515–4525. <https://doi.org/10.1039/C8CY01023D>
- Pillai, U. R. & Sahle-Demessie, E. (2003). Vanadium phosphorus oxide as an efficient catalyst for hydrocarbon oxidations using hydrogen peroxide. *New Journal of Chemistry*, 27(3), 525–528. <https://doi.org/10.1039/b209268a>

- 19 Bin, He, Zihang, Li, Huiling, Zhang, Fei, Dai, Kang, Li, Ruixia, Liu, & Suojia, Zhang. (2019). Synthesis of Vanadium Phosphorus Oxide Catalysts Assisted by Deep-Eutectic Solvents for *n*-Butane Selective Oxidation. *Industrial & Engineering Chemistry Research*, 58(8), S1–S5. <https://doi.org/10.1021/acs.iecr.8b06010>
- 20 He, B., Li, Z., Zhang, H., Dai, F., Li, K., Liu, R., & Zhang, S. (2019). Synthesis of Vanadium Phosphorus Oxide Catalysts Assisted by Deep-Eutectic Solvents for *n*-Butane Selective Oxidation. *Industrial & Engineering Chemistry Research*, 58(8), 2857–2867. <https://doi.org/10.1021/acs.iecr.8b06010>
- 21 Ban, H., Yang, S., Cheng, Y., Wang, L., & Li, X. (2019). Kinetics and Mechanism of Catalytic Oxidation of 2,6-Dimethylnaphthalene to 2,6-Naphthalenedicarboxylic Acid. *Industrial & Engineering Chemistry Research*, 58(8), 2704–2716. <https://doi.org/10.1021/acs.iecr.8b05630>
- 22 Nathaniel, Oladunni, Suleiman, Ola Idris, Ameh, David Onu, Gideon, & Adamu Shallangwa (2021). Kinetics and Mechanism of Oxidation of Catechol by Oxygenated  $[\text{Co}_2(\text{O}_2)(\text{NH}_3)_{10}]^{5+}$  Complex. *Science Frontiers*, 2(1), 1–7. <https://doi.org/10.11648/j.sf.20210201.11>
- 23 Bagirzade, G. A., Tagiyev, D. B., Guliyev, F. A., & Manafov, M. R. (2018). Preparation of Phthalimide and Kinetics of Vapour Phase Ammoxidation of *o*-Xylene on V-Sb-Bi-Cr/g- $\text{Al}_2\text{O}_3$  Oxide Catalyst-III. *Asian Journal of Chemistry*, 30(2), 305–308. <https://doi.org/10.14233/ajchem.2018.20915>
- 24 Manafov, M.R. (2015). Development of a Software Application for Solving of Problems of Chemical Kinetics and its Implementation in a C#. *Int. J. Eng. Appl. Sci.*, 2(10), 33–37.
- 25 Manafov, M.R. (2016). Software application for solving some typical problems of chemical technology. *Azerbaijan Chemical Journal*, 4, 89–94.

Savita Kumari<sup>1</sup> , Praveen K. Gupta<sup>1\*</sup> , Amit Kumar<sup>2</sup> , Ramesh Kumar<sup>3</sup> 

<sup>1</sup>Department of Chemistry, Maharishi Markandeshwar (Deemed to be University), Haryana, India;

<sup>2</sup>Department of Chemistry, Indira Gandhi National College, Haryana, India;

<sup>3</sup>Department of Chemistry, Kurukshetra University, Haryana, India

(\*Corresponding author's e-mail: [praveenguptachem@gmail.com](mailto:praveenguptachem@gmail.com); [parveen.gupta@mmumullana.org](mailto:parveen.gupta@mmumullana.org))

## Oxidative Transformation of Ethylbenzene Utilizing Metal Bound Immobilized Catalysts

In the present contribution, we have investigated the catalytic potential of immobilized metal catalysts for the oxidation of ethylbenzene. Chloromethylated polystyrene was initially converted to aldehydopolystyrene followed by its functionalization with 2-aminothiophenol to get functionalized resin. This resin was successfully binded with appropriate metal (Mn(II), Fe(III), Ni(II), Cu(II), VO(II)) salts to prepare different heterogeneous catalysts which were characterized using CHNS, energy dispersive X-ray spectroscopy (EDX), diffuse reflectance spectra (DRS), fourier transform infrared spectra (FTIR), atomic absorption spectrophotometry (AAS) and electron paramagnetic resonance (EPR) spectra techniques. Metal binding in mmol per gram of resin for different catalysts was found in the range 0.96–1.24. The catalytic potential of these supported catalysts was assessed for the oxidation of ethylbenzene, utilizing hydrogen peroxide (H<sub>2</sub>O<sub>2</sub>) and tert-butyl hydroperoxide (TBHP) as the oxidants. The effects of various reaction parameters, such as temperature, reaction duration, type of oxidant, and the amount of catalyst used were examined for the oxidation reaction. Under optimized milder conditions, the results showed that H<sub>2</sub>O<sub>2</sub> as oxidants resulted in 53.8 % conversion rates with the copper catalyst. The nickel catalyst, when used with H<sub>2</sub>O<sub>2</sub>, showed the highest selectivity for acetophenone, reaching 83 %. The recovered catalysts retained its original structure, as established by a comparative analysis of DRS and FT-IR spectra of both the original and reused catalysts. Moreover, the catalysts can be employed repeatedly up to five times under optimum conditions without any noticeable reduction in activity.

**Keywords:** immobilization, catalyst, nickel, copper, recycle, oxidation, ethylbenzene, polymer

### Introduction

Catalysis indeed plays a crucial role in modern chemistry, serving as a cornerstone for sustainable and efficient chemical transformations. By accelerating reactions, catalysts allow the synthesis of valuable products under milder conditions [1]. Transition metal based catalysts are indeed powerful, widely used in a variety of chemical transformations like hydrocarboxylation and hydroesterification reaction, olefin polymerization, carbonylation of propargylic and allylic compounds, isomerization of olefin, cross-coupling reactions, C–N and C–O bond-forming reactions, olefinations of aryl halides, olefin metathesis and many other key reactions in industry [2, 3]. Their adaptability and high efficiency make them indispensable in modern synthetic chemistry. Polystyrene-anchored transition metal complexes represent an important class of heterogeneous catalysts due to their stability and versatility in catalyzing a range of organic transformations [4]. These complexes are often chemically inert, preventing unwanted side reactions, and can be reused in multiple reaction cycles without significant loss of activity, making them both economically and environmentally favorable [5]. Unlike homogeneous catalysts that are dissolved in the reaction medium, supported catalysts are often heterogeneous (insoluble), which allows them to be separated by simple filtration or centrifugation. This significantly simplifies the post-reaction purification process [6]. Polystyrene supports can be chemically modified into other functional supports, such as aldehyde, carboxylic acid, acid chloride, aminomethylated and azidomethyl resins [7]. This adaptability allows fine-tuning of the polymer's reactivity and its ability to bind different metal catalysts, broadening its application to various catalytic processes [8–10]. These catalysts not only enhance the reaction's stability and selectivity but also make the process more sustainable due to their reusability and the use of eco-friendly oxidants. The oxidation of ethylbenzene in the presence of polymer-anchored catalysts can produce a range of products, including acetophenone, benzaldehyde, and benzoic acid. In a similar manner, acetophenone, an important product derived from the selective oxidation of ethylbenzene [11], has attracted significant interest. It is widely used as an intermediate in pharmaceuticals, aldehydes, resins, alcohols, esters, tear gas formulations, and also finds applications in perfumery and sleep-

inducing drugs [12–16]. Benzaldehyde's versatility makes it an important compound in various sectors, from flavors and fragrances to pharmaceuticals and industrial applications. Its distinctive odor and chemical reactivity contribute to its broad range of uses [17–20]. Benzoic acid and its salts, such as sodium benzoate, are widely used as preservatives in food and beverages, cosmetics, intermediate, dyes and pigments etc. [21, 22].

Several studies have reported efficient catalytic systems for the oxidation of ethylbenzene using various oxidants. Faraji et al. achieved 88.1 % conversion and 98 % selectivity to acetophenone with reusable amino propyl trimethoxysilane immobilized metformin-cobalt nanocatalyst  $[\text{Fe}_3\text{O}_4@\text{SiO}_2\text{-APTMS/CC/Met@Co(II)}]$  using  $\text{O}_2/\text{N-hydroxyphthalimide}$  (NHPI) as an oxidant at 100 °C [23]. Gao et al. employed  $\text{Co}_3\text{O}_4$  nanoparticles supported on reduced graphene oxide (Co/rGO) with  $\text{O}_2/\text{NHPI}$ , affording 84.1 % conversion and 96.2 % selectivity in 2 h at 120 °C [24]. Li et al. developed a Co-based single-atom black powdered catalyst anchored on a graphitic carbon nitride ( $\text{SACo@g-C}_3\text{N}_4$ ) with peroxy monosulfate (PMS) as oxidant, yielded over 95 % conversion and selectivity under mild conditions [25]. Yang et al. reported Mn(II) complexes bearing bis(pyridin-2-ylmethyl)amine ligands that oxidized ethylbenzene with ozone ( $\text{O}_3$ ) in an acetonitrile-water (1:1) medium to give 91 % conversion and 89 % selectivity [26]. Similarly, Yamazaki et al. demonstrated complete conversion (100 %) using  $\text{CrO}_3$  and periodic acid ( $\text{H}_5\text{IO}_6$ ) as oxidant at room temperature, affording 49 % acetophenone selectivity within 1 h [27]. The aim of this study was to describe the series of new immobilized catalysts, provide their structural characterization, and demonstrate their application for the selective oxidation of ethylbenzene using  $\text{H}_2\text{O}_2$  and TBHP as oxidants.

### Experimental

#### Materials and Methods

2-aminothiophenol (99 % purity, Sigma-Aldrich), chloromethylated polystyrene (2 % divinylbenzene cross-linked, 4.5 mmol Cl/g of resin, mesh 200–400) was generously gifted by Thermax Ltd, Pune, India. All other reagents were purchased from Central Drug House (CDH). Nickel(II) chloride hexahydrate ( $\text{NiCl}_2 \cdot 6\text{H}_2\text{O}$ ,  $\geq 98$  %, AR grade), iron(III) chloride hexahydrate ( $\text{FeCl}_3 \cdot 6\text{H}_2\text{O}$ , 98 %, AR grade), copper(II) chloride dihydrate ( $\text{CuCl}_2 \cdot 2\text{H}_2\text{O}$ , 99 %, AR grade), manganese(II) acetate tetrahydrate [ $\text{Mn}(\text{CH}_3\text{COO})_2 \cdot 4\text{H}_2\text{O}$ , 99.5 %, AR grade], vanadyl sulphate pentahydrate ( $\text{VO}_2\text{SO}_4 \cdot 6\text{H}_2\text{O}$ , 97 %, AR grade), 2,4-dinitrophenylhydrazine reagent (99 %, AR grade), hydrogen peroxide ( $\text{H}_2\text{O}_2$ , 30 % in water), *t*-butyl hydroperoxide [ $(\text{CH}_3)_3\text{COOH}$ , 70 % in water], ethylbenzene (98 %, synthesis grade), acetonitrile ( $\text{CH}_3\text{CN}$ , 99 %, AR grade), methanol ( $\text{CH}_3\text{OH}$ , 99 %, synthesis grade), ethanol ( $\text{C}_2\text{H}_5\text{OH}$ , 99 %, synthesis grade) and acetone [ $(\text{CH}_3)_2\text{O}$ , 99 %, synthesis grade] were used for the synthesis. Analytical-grade reagents were dried according to the standard procedures without any further purification.

The synthesized compounds were analyzed using a range of techniques, including FT-IR, DRS, ESR, EDS, AAS, and CHNS elemental analysis. FT-IR spectra were recorded from 400 to 4000  $\text{cm}^{-1}$  on a Shimadzu IR Spirit Fourier transform infrared spectrophotometer. Diffuse reflectance spectra (DRS) were obtained using a Shimadzu UV-2600 double beam spectrophotometer with  $\text{BaSO}_4$  as the standard. CHNS analysis was conducted using a Thermo Scientific Flash 2000 analyzer. Metal content in the polymer-anchored catalysts was measured titrimetrically and gravimetrically as well as with a Shimadzu ASC-6880 atomic absorption spectrophotometer (AAS). Energy dispersive X-ray (EDX) spectra were captured with a Hitachi SU8010 Series FEG scanning electron microscope. Electron paramagnetic resonance (EPR) spectra were recorded on JES-FA200 X-band (9.45 GHz) spectrometer with a modulation frequency of 100 kHz and modulation amplitude of 2.0 Gauss. Gas Chromatography-Mass Spectrometry (GC-MS) analysis was performed using an Agilent 7000 GC/TQ system. The gas chromatograph used was equipped with GsBP-624 column and FID detector.

#### Synthesis of Aldehydopolystyrene (PS-CHO)

Chloromethylated polystyrene beads (6 g) were swollen in 100 mL of DMSO for an hour. Sodium hydrogen carbonate (7.5 g) was then added, and the mixture was stirred and refluxed at 150 °C for 6 hours. The resulting aldehyde-functionalized polymer was isolated by vacuum filtration, washed with ethanol, and dried in a vacuum desiccator at 25 °C.

#### Functionalization of Aldehydopolystyrene with 2-Aminothiophenol [PS-ATP]

PS-CHO beads (6 g) were first allowed to swell in 30 mL of methanol for an hour. Separately, 2-aminothiophenol (ATP) (30 mmol) was dissolved in 50 mL of methanol and then introduced into the polymer suspension. The reaction mixture was stirred and refluxed at 80 °C in a water bath for 18 hours. After completion, the solid was collected by vacuum filtration and repeatedly washed with hot ethanol, hot metha-

nol, and acetone. The final product was dried in an air oven at 70 °C. The addition of the ligand to the polymer was periodically monitored using the 2,4-DNP test.

#### Loading of Metal to Functionalized Aldehydopolystyrene Resin

The functionalized resin PS-ATP (4.5 mmol) was initially swollen in 15 mL of methanol for an hour. A metal salt solution was prepared by dissolving  $\text{VOSO}_4 \cdot 5\text{H}_2\text{O}$ ,  $\text{Mn}(\text{CH}_3\text{COO})_2 \cdot 4\text{H}_2\text{O}$ ,  $\text{FeCl}_3 \cdot 6\text{H}_2\text{O}$ ,  $\text{NiCl}_2 \cdot 6\text{H}_2\text{O}$  or  $\text{CuCl}_2 \cdot 2\text{H}_2\text{O}$  (4.5–9.0 mmol) in methanol, which was then introduced into the resin suspension. As the reaction proceeded, a noticeable color change was observed in the resin. The mixture was subjected to reflux for 6–18 hours, and then allowed to cool to room temperature. The solid was collected via vacuum filtration and thoroughly washed with hot methanol, ethanol, and acetone. Finally, the resin was dried in an oven at 80 °C.

#### Experiment on Catalytic Performance

Ethylbenzene oxidation using catalysts was performed in a thermostatted oil bath. The reaction was carried out with *tert*-butyl hydroperoxide/or hydrogen peroxide as oxidants at 60 °C for 3–8 hours, using catalyst amounts of 0.1 and 0.15 g. The catalyst was pre-swollen in 20 mL of acetonitrile for 30 minutes before adding ethylbenzene (10 mmol) and the oxidant (20 mmol). The reaction was monitored via TLC, and product formation was confirmed by GC-MS. A control experiment without the catalyst was also conducted. The catalyst was recovered, washed, dried under vacuum, and reused.

#### Results and Discussion

The aldehydopolystyrene was modified with 2-aminothiophenol to form the functionalized resin [PS-ATP] (Fig. 1). Ligands at the para position of the polymer backbone facilitated metal binding (Fig. 3). The formation of immobilized metal catalysts (Fig. 2) was initially observed through a change in colour of the beads and later confirmed by characterization techniques. The ligand attachment was verified by the DNP test, where the disappearance of the orange color indicated aldehyde group replacement (Fig. 4(a)). Real images of the functionalized resin and its metal catalysts are shown in (Fig. 4(b-g)).

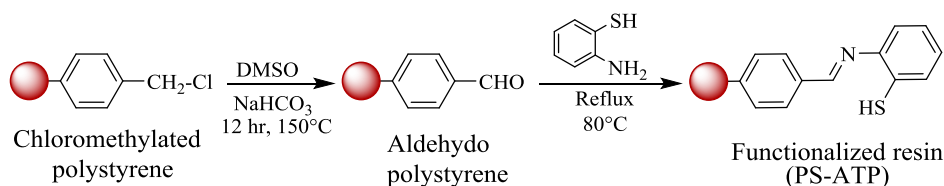


Figure 1. Synthesis of polystyrene-anchored ligand

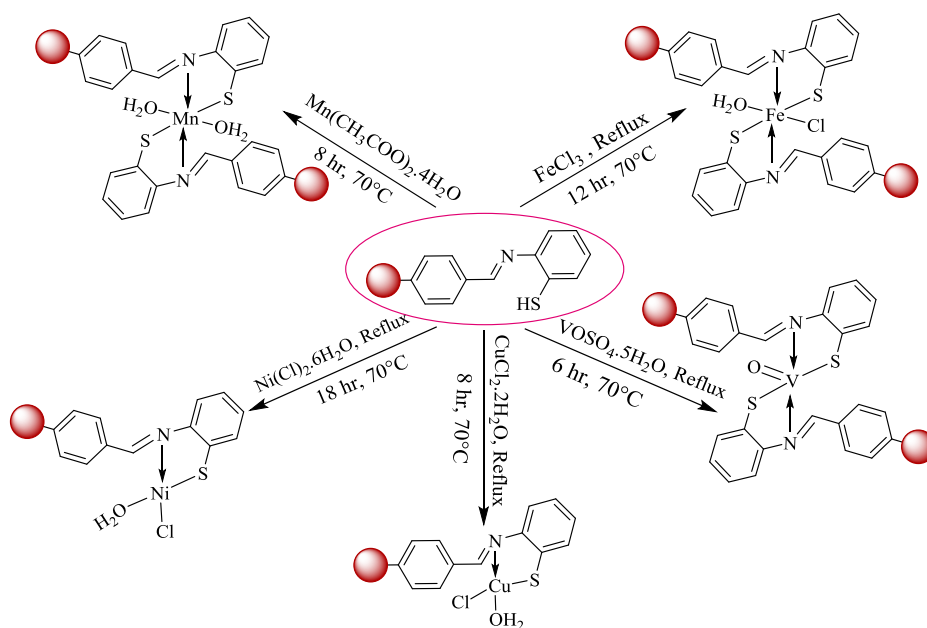


Figure 2. Synthesis of metal incorporated functionalized resin

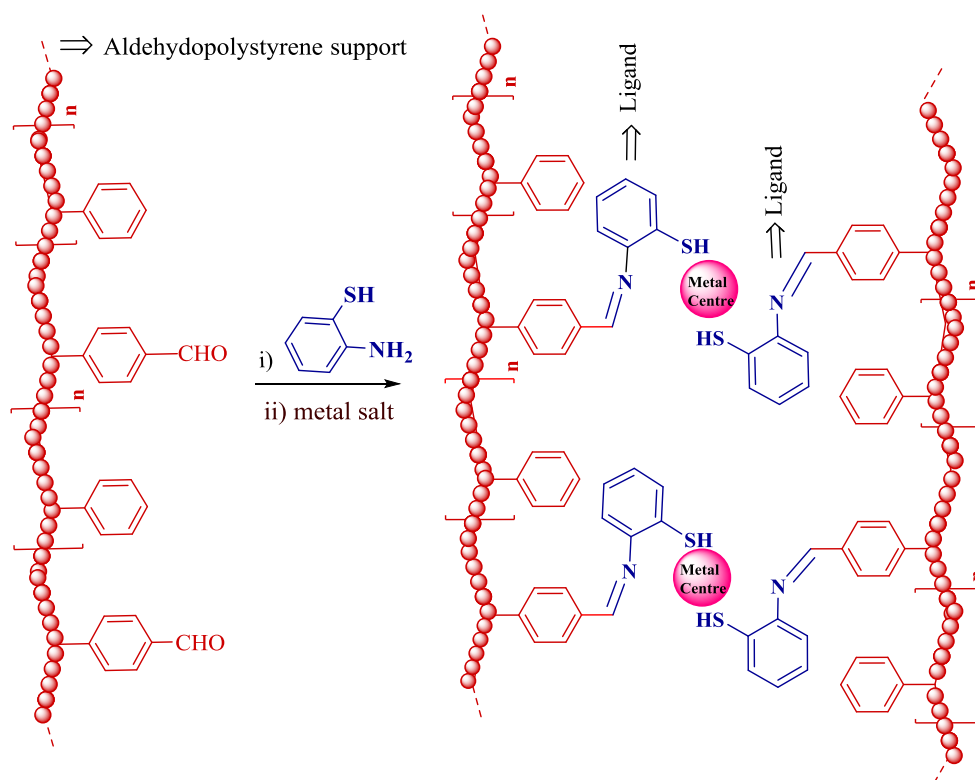


Figure 3. Incorporated metal ions onto functionalized aldehydopolystyrene

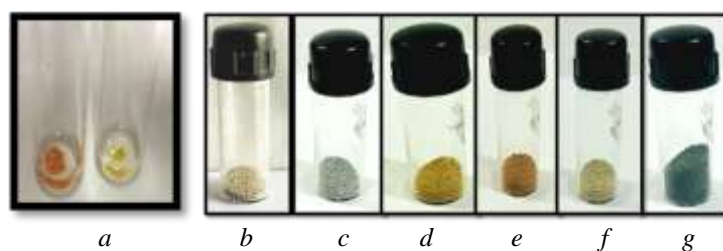


Figure 4. DNP test of [PS-CHO] &amp; [PS-ATP] (a); Sample pictures of [PS-ATP] (b), [PS-ATP-V] (c), [PS-ATP-Mn] (d), [PS-ATP-Fe] (e), [PS-ATP-Ni] (f), [PS-ATP-Cu] (g)

### Characterization

The incorporation of the organic ligand onto the polymer backbone was confirmed by CHNS analysis through the measurement of carbon, hydrogen, nitrogen, and sulfur content. Metal loading in the catalysts was determined using atomic absorption spectroscopy (AAS) indicating the metal bounded onto the functionalized resin (Table 1), providing insights into the ligand: metal stoichiometry within the polymer structure.

Table 1

Analytical data of functionalized resin and its catalyst

Compound	Colour	Elemental analysis, %					Ligand attachment (mmol per gram of resin)	Metal binding (mmol per gram of resin)	Ligand/ Metal ratio
		C	H	N	S	M			
[PS-ATP]	Cream	80.95	6.92	3.89	8.42	-	2.78	-	-
[PS-ATP-V]	Olive green	72.54	6.71	3.20	8.82	5.9	2.29	1.16	1.97:1
[PS-ATP-Mn]	Mustard	72.91	6.96	2.74	8.99	5.3	1.96	0.96	2:1
[PS-ATP-Fe]	Dark brown	71.65	6.49	3.20	5.89	6.7	2.29	1.19	1.92:1
[PS-ATP-Ni]	Off-white	66.73	6.20	2.05	8.73	7.1	1.46	1.18	1.2:1
[PS-ATP-Cu]	Dark green	65.98	6.19	2.01	8.70	7.9	1.44	1.24	1.2:1



### EDX Investigation

EDX analysis confirmed the successful binding of metal ions in all catalysts by detecting their respective ion signals. The spectra for Cu, Fe, and Ni catalysts displayed Cl signals, while the V catalyst exhibited an S signal, indicating coordination with chlorine and sulfur atoms, respectively (Fig. 5).

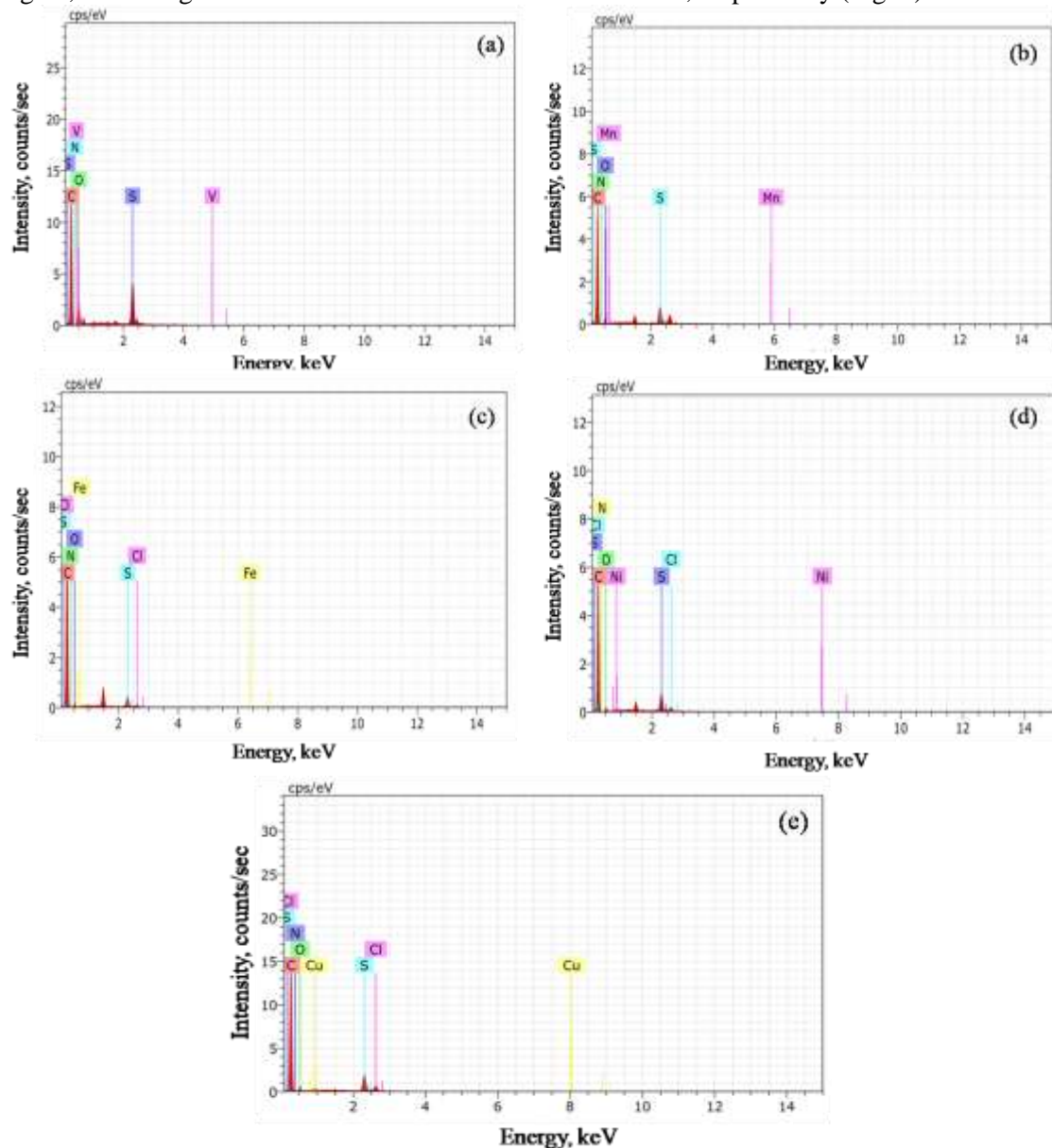


Figure 5. EDX plot of [PS-ATP-V] (a), [PS-ATP-Mn] (b), [PS-ATP-Fe] (c), [PS-ATP-Ni] (d) and [PS-ATP-Cu] (e)

### FTIR Investigation

The binding of metal ions to the polymer support was analysed by FTIR spectra (Fig. 6 and Table 2) of the functionalized resin and its metal catalysts. PS-ATP exhibits a distinct band at  $1659\text{ cm}^{-1}$ , corresponding to the  $\nu(\text{C}=\text{N})$  stretch. A shift of  $11\text{--}21\text{ cm}^{-1}$  to lower wavenumber in this band indicates the coordination of the azomethine nitrogen to the metal ions [28]. The IR spectrum of the functionalized resin shows a weak band at  $2571\text{ cm}^{-1}$  which is assigned to the SH group respectively. The disappearance of this band in the spectra of the catalysts indicates the deprotonation of the thiol groups upon chelation [29]. The vanadium catalyst displays a prominent band at  $952\text{ cm}^{-1}$  assigned to  $(\text{V}=\text{O})$  stretch [30]. The interaction of metal ions with [PS-ATP] was confirmed by the appearance of M–N, M–O, and M–S bands in the regions of  $486\text{--}531\text{ cm}^{-1}$ ,  $564\text{--}572\text{ cm}^{-1}$ , and  $423\text{--}449\text{ cm}^{-1}$ , respectively [31]. A band in the region  $3312\text{--}3415\text{ cm}^{-1}$  in the metal catalysts indicates the coordination of a water molecule [32].

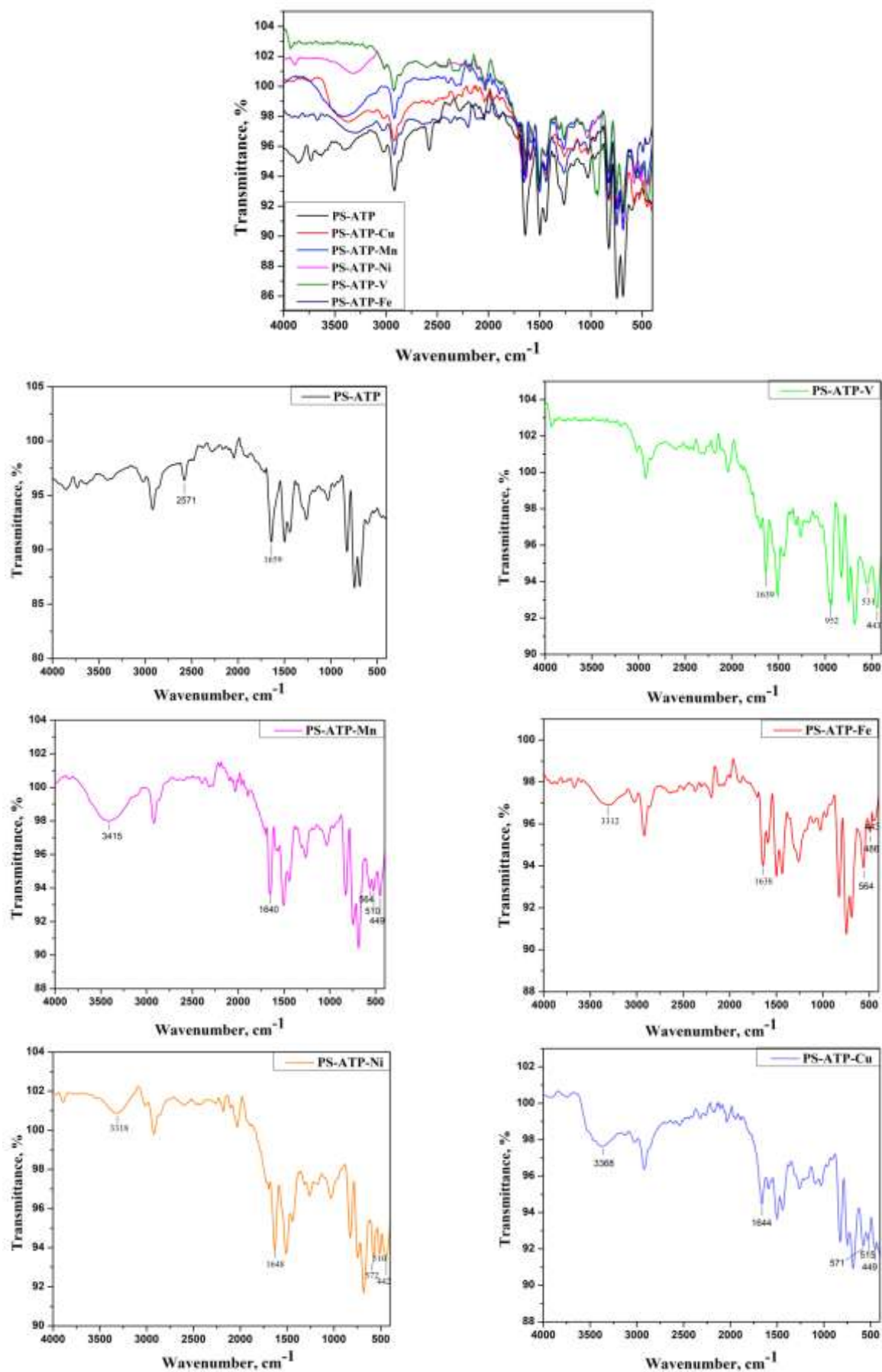


Figure 6. Overlap and individual FTIR spectra of functionalized resin and its metal catalysts

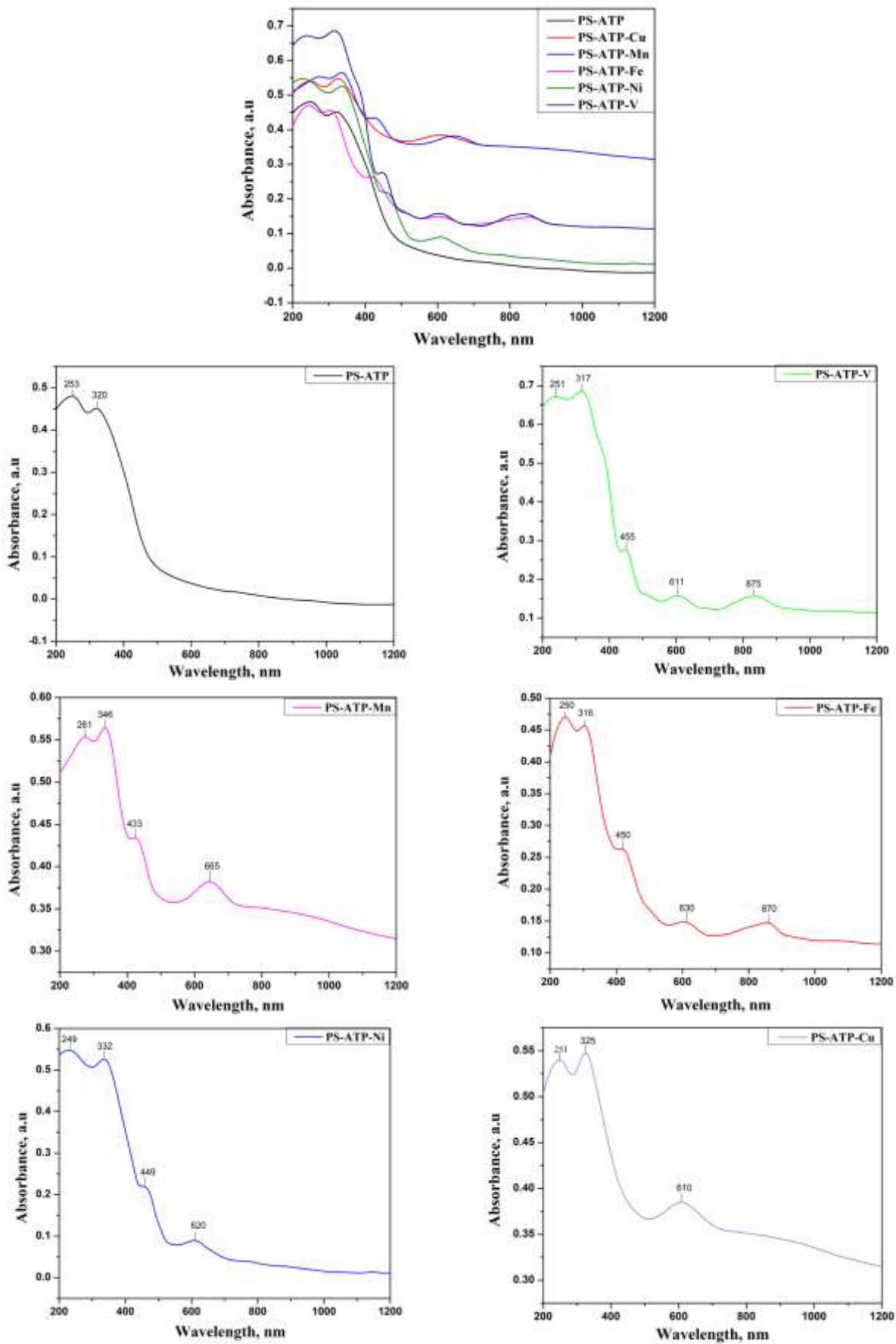


Figure 7. Overlap and individual DRS spectra of metal catalysts

### DRS Investigation

Diffuse reflectance spectral studies (Fig. 7, Table 2) were performed to examine the structure of the solid, insoluble catalysts. The [PS-ATP] spectrum shows intraligand absorption transitions and 30303 and 39062  $\text{cm}^{-1}$ , corresponding to  $n \rightarrow \pi^*$  and  $\pi \rightarrow \pi^*$  transitions, respectively. The [PS-ATP-V] spectrum displays three well-resolved transitions at 11428, 16366, and 21978  $\text{cm}^{-1}$ , consistent with the spectral characteristics of five-coordinate oxovanadium(IV) complexes possessing  $C_{4v}$  symmetry. These three observed transitions can be attributed to  ${}^2B_{2g} \rightarrow {}^2E_g$ ,  ${}^2B_{2g} \rightarrow {}^2B_{1g}$  and  ${}^2B_{2g} \rightarrow {}^2A_{1g}$  in increasing energy [33]. Manganese shows two bands at 15037 and 23094  $\text{cm}^{-1}$ , corresponding to  ${}^6A_{1g} \rightarrow {}^4T_{1g}(G)$  and  ${}^6A_{1g} \rightarrow {}^4T_{2g}(G)$  transitions, suggesting an octahedral geometry [34]. Iron catalyst displays distinct bands at 11494, 15873, and 22222  $\text{cm}^{-1}$  due to  ${}^6A_{1g} \rightarrow {}^4T_{1g}(G)(v_1)$ ;  ${}^6A_{1g} \rightarrow {}^4T_{2g}(F)(v_2)$  and  ${}^6A_{1g} \rightarrow {}^4T_{1g}(P)(v_3)$  transitions respectively [35]. [PS-ATP-Ni] exhibits spin-allowed transitions at 16129 and 22,271  $\text{cm}^{-1}$ , which correspond to  ${}^3A_{2g} \rightarrow {}^3T_{2g}(G)(v_1)$  and  ${}^3A_{2g} \rightarrow {}^3T_{1g}(F)(v_2)$  transitions, respectively, indicating Ni(II) in an octahedral environment [36]. The reflectance spectrum of copper catalyst shows d  $\rightarrow$  d transitions at 16393  $\text{cm}^{-1}$ , which can be attributed to  ${}^2B_{1g} \rightarrow {}^2A_{1g}$ ;  ${}^2B_{1g} \rightarrow {}^2B_{2g}$ ;  ${}^2B_{1g} \rightarrow {}^2E_g$  transitions, indicative of a square planar geometry [37].

Table 2

FTIR and DRS spectral data for functionalized resin and its metal catalysts

Polymer-anchored compounds	$\nu(\text{C}=\text{N})$	$\nu(\text{S}-\text{H})$	$\nu(\text{V}=\text{O})$	$\nu(\text{M}-\text{Cl})$	$\nu(\text{H}_2\text{O})$	d-d band position ( $\text{cm}^{-1}$ )	d-d band assignment
[PS-ATP]	1659	2571	—	—	—	—	—
[PS-ATP-V]	1639	—	952	—	—	11428; 16366; 21978	${}^2B_{2g} \rightarrow {}^2E_g$ ; ${}^2B_{1g}$ ; ${}^2A_{1g}$
[PS-ATP-Mn]	1640	—	—	—	3415	15037; 23094	${}^6A_{1g} \rightarrow {}^4T_{1g}(G)$ ; ${}^4T_{2g}(G)$
[PS-ATP-Fe]	1638	—	—	351	3312	11494; 15873; 22222	${}^6A_{1g} \rightarrow {}^4T_{1g}(G)(v_1)$ ; ${}^4T_{2g}(F)(v_2)$ ; ${}^4T_{1g}(P)(v_3)$
[PS-ATP-Ni]	1648	—	—	357	3318	16129; 22271	${}^3A_{2g} \rightarrow {}^3T_{2g}(G)(v_1)$ ; ${}^3T_{1g}(F)(v_2)$
[PS-ATP-Cu]	1644	—	—	355	3368	16393	${}^2B_{1g} \rightarrow {}^2A_{1g}$ ; ${}^2B_{2g}$ ; ${}^2E_g$

### EPR Studies

At ambient conditions, EPR spectroscopy was employed to examine vanadium, manganese, and copper catalysts, as illustrated in Figure 8. The EPR spectrum of the vanadium catalyst [PS-ATP-V] exhibits an axially symmetric signal, a characteristic feature of V(IV) ions. This suggests that the electron distribution around the vanadium ion is anisotropic, favoring a specific orientation. Signals appear in both the perpendicular and parallel regions, highlighting the anisotropic nature of the V(IV) ion's electronic structure. The well-defined hyperfine splitting indicates that vanadium ions are uniformly incorporated into the polystyrene support, with no interactions. The spectrum displays anisotropy, with Hamiltonian parameters:  $A_{\parallel} > A_{\perp}$  ( $A_{\perp} = 86$  and  $A_{\parallel} = 193$ );  $g_{\perp} > g_{\parallel}$  ( $g_{\perp} = 1.99$  and  $g_{\parallel} = 1.93$ ). This suggests a square pyramidal coordination geometry, with the V=O bond aligned along the z axis and exhibiting  $C_{4v}$  symmetry [38]. The EPR spectrum of [PS-ATP-Mn] exhibits six hyperfine lines, resulting from the interaction between the electron spin and the nuclear spin of  ${}^{55}\text{Mn}$  ( $I = 5/2$ ,  $2nI + 1 = 6$ ). The Hamiltonian parameters,  $A = 74$  G and  $g = 2.03$ , are indicative of Mn(II) species with axial symmetry and an octahedral coordination environment [39]. The copper catalyst displays a characteristic axial spectrum with  $g_{\parallel} > g_{\perp}$  ( $g_{\parallel} = 2.27$ ), along with hyperfine splitting in the parallel region due to  ${}^{63}\text{Cu}$  ( $I = 3/2$ ,  $2nI + 1 = 4$ ). The hyperfine lines divide the parallel component, maintaining an average separation of 122 G. The spectrum suggests that Cu(II) species are uniformly incorporated within the polymer matrix, with no evidence of Cu–Cu interactions. However, the perpendicular region of the spectrum appears unresolved. The observed g value implies that the unpaired electron in copper resides in the  $d_{x^2-y^2}$  orbital. The EPR spectra of the other catalysts were not well resolved, so their EPR parameters could not be determined [40].

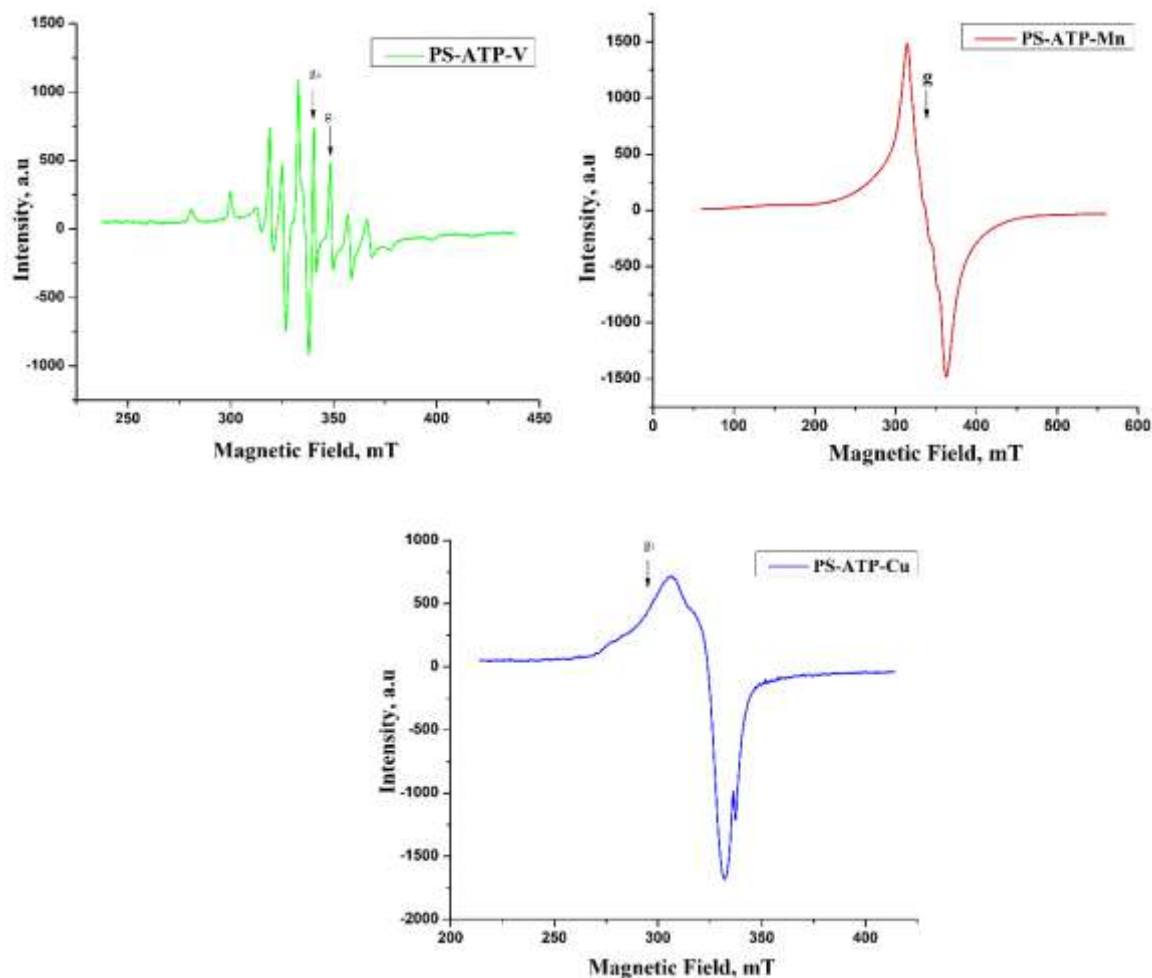


Figure 8. EPR spectra of [PS-ATP-V], [PS-ATP-Mn] and [PS-ATP -Cu]

### Catalytic Performance

The catalytic performance of the synthesized materials was evaluated through the oxidation of ethylbenzene using TBHP and  $\text{H}_2\text{O}_2$  as oxidizing agents. Control experiments confirmed that both the catalyst and the oxidant were essential for the reaction to proceed. The primary oxidation products obtained were acetophenone, benzaldehyde, and benzoic acid. To optimize the product yield, we investigated the influence of several reaction parameters, including the choice of oxidant, duration of the reaction, temperature, and catalyst dosage.

#### Influence of Catalyst Dosage

Figure 9 illustrates the impact of catalyst dosage on the oxidation of ethylbenzene. The data reveal that with 0.1 g of catalyst, the reaction proceeded at a slower rate, resulting in lower conversion under the given conditions. An increase in catalyst loading to 0.15 g led to a noticeable enhancement in conversion. However, further increasing the catalyst amount beyond this point did not yield any significant improvement in the oxidation process.

#### Influence of Oxidant

In the present work,  $\text{H}_2\text{O}_2$  and TBHP were chosen as oxidants as they are green and environmentally benign, producing only water or tert-butanol as by-products and avoiding the use of halogenated or toxic oxidants. Preliminary trials with molecular oxygen under similar conditions resulted in very low conversion. The investigation examined how TBHP and  $\text{H}_2\text{O}_2$  influenced the catalytic performance of polystyrene-supported catalysts in ethylbenzene oxidation. As shown in Tables 3 and 4, both oxidants facilitated a conversion rate of 53.8 % when used with the copper catalyst. Notably, the highest selectivity for acetophenone, reaching 83.9 %, was observed when  $\text{H}_2\text{O}_2$  served as the oxidizing agent in combination with the copper catalyst.



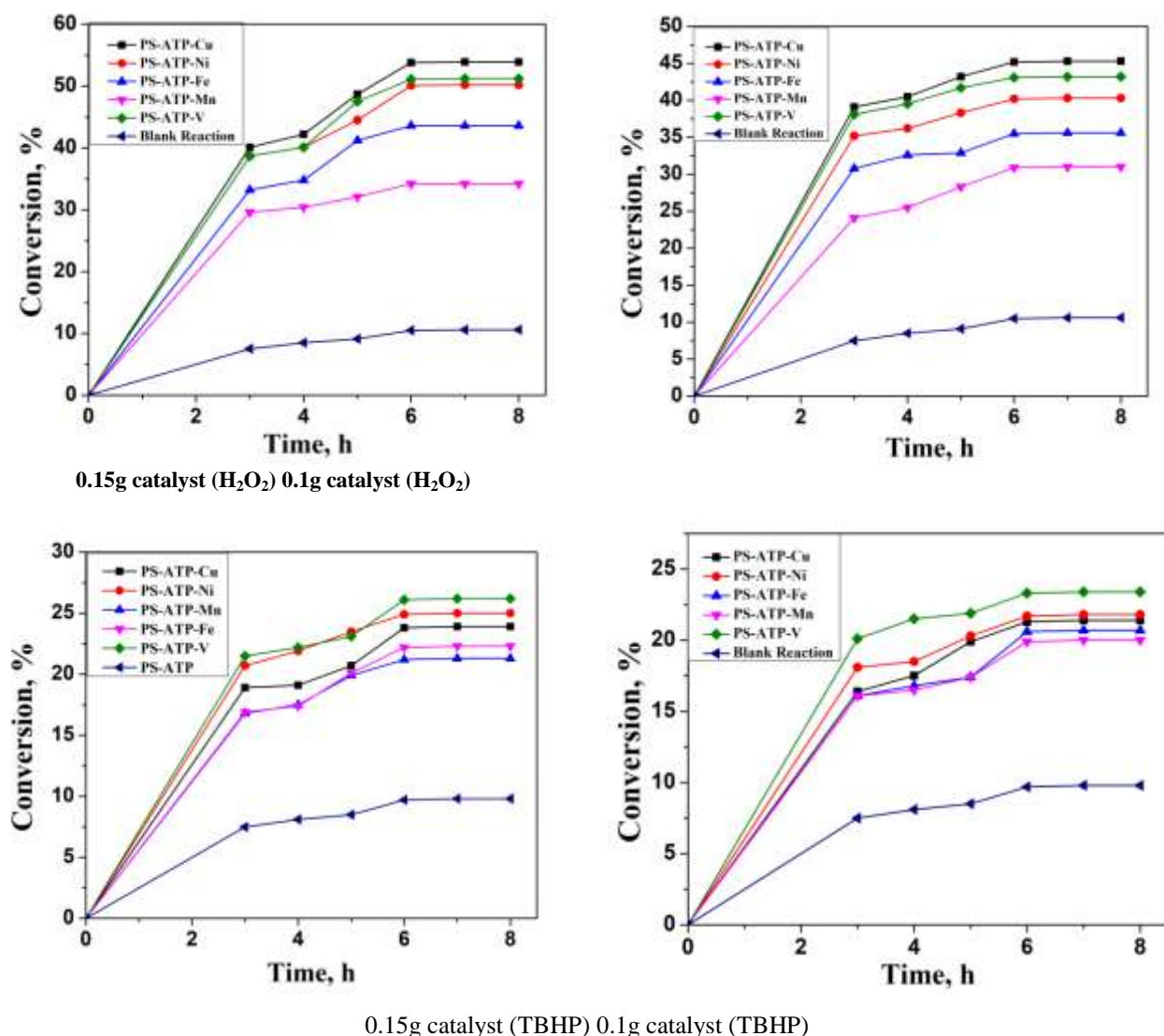


Figure 9. Influence of time on the oxidation of ethylbenzene in presence of different catalysts

#### *Influence of Time*

The reaction progress was tracked by performing ethylbenzene oxidation using a 1:2 ratio of TBHP/ $\text{H}_2\text{O}_2$ , with 0.1 g / 0.15 g of catalyst at an optimized temperature (60 °C). During the first two hours, minimal conversion was observed, suggesting an induction phase. As the reaction proceeded, ethylbenzene conversion gradually increased across all catalysts. As illustrated in Figure 9, a comparison between 3–8 hours indicated that the maximum conversion occurred at the 6-hour mark. Furthermore, product selectivity remained relatively stable despite extended reaction times.

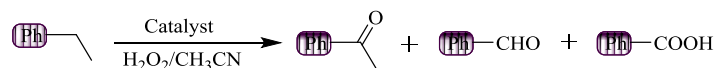
#### *Influence of Temperature*

At room temperature, no detectable products were formed. As the temperature was increased to 60 °C, ethylbenzene conversion improved significantly. However, beyond 60 °C, no significant improvement in conversion was observed at 70 °C and 80 °C. Therefore, 60 °C was identified as the optimal temperature for maintaining both selectivity and conversion efficiency.



Table 3

## Conversion of ethylbenzene and product selectivity

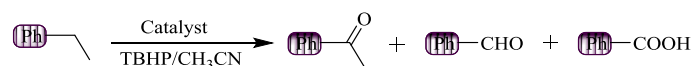


Catalysts	Catalyst concentration, g	Time, hr	Conversion, %	Selectivity, %			
							Others
Blank Reaction		3	7.5	75.8	18.1	2.5	3.6
		4	8.5	76.1	18.3	2.6	3.0
		5	9.1	77.2	18.3	2.6	1.9
		6	10.5	77.2	18.4	2.7	1.7
[PS-ATP-V]	0.1	3	38.1	66.5	21.3	2.9	9.3
		4	39.5	66.9	21.2	2.1	9.8
		5	41.7	67.1	19.8	1.9	11.2
		6	43.1	67.5	19.7	1.7	11.1
	0.15	3	38.7	66.8	19.3	2.5	11.4
		4	40.1	67.5	19.2	2.4	10.9
		5	47.5	68.3	18.9	2.1	10.7
		6	51.1	69.2	18.8	1.9	10.1
[PS-ATP-Mn]	0.1	3	24.1	62.1	22.5	3.9	11.5
		4	25.5	62.8	22.4	3.7	11.1
		5	28.3	63.1	22.1	3.7	11.1
		6	30.9	64.3	21.9	3.6	10.2
	0.15	3	29.6	62.3	21.9	3.5	12.3
		4	30.4	63.5	21.8	3.3	11.4
		5	32.1	63.9	21.5	3.2	11.4
		6	34.2	65.4	21.4	3.1	10.2
[PS-ATP-Fe]	0.1	3	30.8	68.1	21.1	3.2	7.6
		4	32.6	69.3	20.9	3.1	6.7
		5	32.9	69.7	20.7	2.9	6.7
		6	35.5	70.2	20.6	2.8	6.4
	0.15	3	33.2	69.2	20.6	2.5	7.7
		4	34.8	69.9	20.5	2.3	7.3
		5	41.2	70.9	19.9	2.3	6.9
		6	43.6	71.3	19.8	2.2	6.4
[PS-ATP-Ni]	0.1	3	35.1	78.3	17.2	1.1	3.4
		4	36.2	79.2	17.1	1.1	2.6
		5	38.3	80.3	17.1	1.2	1.4
		6	40.2	80.8	16.9	1.2	1.1
	0.15	3	38.7	78.9	14.9	1.4	4.8
		4	40.1	80.7	15.1	1.3	2.9
		5	44.5	82.4	15.1	1.3	2.9
		6	50.1	83.9	14.8	1.1	0.2
PS-ATP-Cu	0.1	3	39.1	71.2	15.6	2.7	10.5
		4	40.5	72.3	16.8	2.1	8.8
		5	43.2	72.9	16.8	2.1	8.8
		6	45.2	73.1	16.7	1.9	8.3
	0.15	3	40.1	72.5	19.1	1.5	6.9
		4	42.2	73.8	19.3	1.6	5.3
		5	48.7	74.4	19.5	1.6	4.5
		6	53.8	75.1	19.3	1.4	4.2

Reaction Condition: Acetonitrile (20 mL), ethylbenzene (10 mmol), and H<sub>2</sub>O<sub>2</sub> (20 mmol) at 60 °C.

Table 4

## Conversion of ethylbenzene and product selectivity



Catalysts	Catalyst concentration, g	Time, hr	Conversion, %	Selectivity, %			
							Others
Blank Reaction		3	7.5	59.1	17.2	5.1	18.6
		4	8.1	59.2	17.5	5.2	18.1
		5	8.5	59.2	17.6	5.2	18.0
		6	9.7	59.3	17.6	5.3	17.8
[PS-ATP-V]	0.1	3	20.1	65.5	18.3	4.9	11.3
		4	21.5	65.6	18.5	5.1	10.8
		5	21.9	65.6	18.5	5.2	10.7
		6	23.3	65.7	18.6	5.3	10.4
	0.15	3	21.5	65.6	18.5	5.4	10.5
		4	22.2	65.8	18.6	5.6	10.0
		5	23.1	65.9	18.9	5.3	9.9
		6	26.1	66.1	19.1	5.1	9.7
[PS-ATP-Mn]	0.1	3	16.1	58.7	21.4	3.9	16.0
		4	16.5	58.9	21.4	3.5	16.2
		5	17.4	58.9	21.5	3.3	16.3
		6	19.9	59.1	21.6	3.2	16.1
	0.15	3	16.8	58.3	21.5	4.5	15.7
		4	17.5	58.9	21.6	4.5	15.0
		5	19.9	59.2	21.8	4.7	14.3
		6	21.2	59.4	21.9	4.8	13.9
[PS-ATP-Fe]	0.1	3	16.1	68.1	21.1	3.2	7.6
		4	16.8	69.3	20.9	3.1	6.7
		5	17.4	69.7	20.7	2.9	6.7
		6	20.6	70.2	20.6	2.8	6.4
	0.15	3	16.9	69.2	20.6	2.5	7.7
		4	17.6	69.9	20.5	2.3	7.3
		5	20.1	70.9	19.9	2.3	6.9
		6	22.2	71.3	19.8	2.2	6.4
[PS-ATP-Ni]	0.1	3	16.1	67.3	16.9	6.1	9.7
		4	17.5	67.6	17.1	6.3	9.3
		5	20.3	68.1	17.2	6.4	8.3
		6	24.2	68.8	17.2	6.4	7.6
	0.15	3	20.7	67.7	14.5	3.3	14.5
		4	21.9	67.7	14.7	3.2	14.4
		5	23.5	68.9	14.7	3.2	13.2
		6	24.9	69.1	14.8	3.1	13.0
PS-ATP-Cu	0.1	3	18.1	62.1	16.5	3.7	17.7
		4	18.5	63.2	16.6	3.6	16.6
		5	19.9	63.2	16.6	3.6	16.6
		6	21.3	63.7	16.7	3.1	16.5
	0.15	3	18.9	62.3	18.1	2.6	17.0
		4	19.1	63.8	18.2	2.5	15.5
		5	20.7	63.9	18.5	2.6	15.0
		6	23.8	64.1	18.5	2.3	15.1

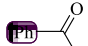


Reaction Condition: Acetonitrile (20 mL), ethylbenzene (10 mmol), and TBHP (20 mmol) at 60 °C.

### Reusability Evaluation

The reusability of polymer-supported metal complexes in ethylbenzene oxidation was assessed. Each cycle was followed by filtration, washing, drying, and reusing of the catalysts under the same conditions. Product yields and selectivity remained stable, though a slight decline in conversion was noted after five cycles (Table 5, Figure 10). IR and DRS spectra showed no significant structural changes, indicating catalyst integrity. AAS analysis detected minor metal leaching in the fifth cycle, but overall stability ensured effective reuse, making the catalysts cost-efficient and environmentally friendly.

Table 5

Recyclability Test

Catalyst	Cycle	Conversion, %	Selectivity, %			
						Others
[PS-ATP-V]	1	51.1	69.2	18.8	1.9	10.1
	2	51.1	69.2	18.8	1.9	10.1
	3	50.0	69.2	18.8	1.9	10.1
	4	49.9	69.2	18.8	1.9	10.1
	5	49.9	69.2	18.8	1.9	10.1
[PS-ATP-Mn]	1	34.2	65.4	21.4	3.1	10.2
	2	34.1	65.4	21.4	3.1	10.2
	3	34.0	65.4	21.4	3.1	10.2
	4	33.9	65.4	21.4	3.1	10.2
	5	33.9	65.4	21.4	3.1	10.2
[PS-ATP-Fe]	1	43.6	71.3	19.8	2.2	6.4
	2	43.5	71.3	19.8	2.2	6.4
	3	43.4	71.3	19.8	2.2	6.4
	4	43.3	71.3	19.8	2.2	6.4
	5	43.3	71.3	19.8	2.2	6.4
[PS-ATP-Ni]	1	50.1	83.9	14.8	1.1	0.2
	2	50.1	83.9	14.8	1.1	0.2
	3	50.0	83.9	14.8	1.1	0.2
	4	49.9	83.9	14.8	1.1	0.2
	5	49.9	83.9	14.8	1.1	0.2
[PS-ATP-Cu]	1	53.8	75.1	19.3	1.4	4.2
	2	53.8	75.1	19.3	1.4	4.2
	3	53.7	75.1	19.3	1.4	4.2
	4	53.6	75.1	19.3	1.4	4.2
	5	53.6	75.0	19.3	1.4	4.2

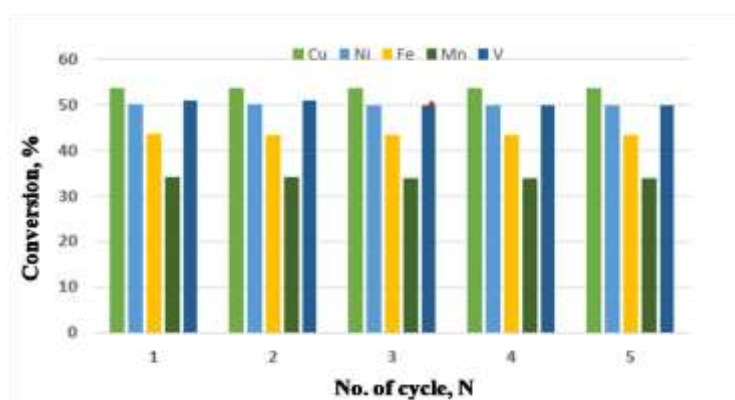


Figure 10. Recyclability test of polystyrene-anchored metal catalyst

### Probable Mechanism for Oxidation of Ethylbenzene

Figure 11 illustrates a proposed pathway for the oxidation of ethylbenzene using peroxides such as hydrogen peroxide or *tert*-butyl hydroperoxide (TBHP) in the presence of a metal-based catalyst. Initially, the metal catalyst interacts with the oxidant to produce a reactive hydroperoxide intermediate, accompanied by the release of counterions like chloride or acetate. This is followed by the formation of a resonance-stabilized benzylic carbocation, which undergoes a nucleophilic attack by the *tert*-butylperoxide anion. The resulting phenylethanol intermediate subsequently rearranges and experiences bond cleavage within the peroxide moiety, ultimately producing benzaldehyde and acetophenone as final oxidation products [41].

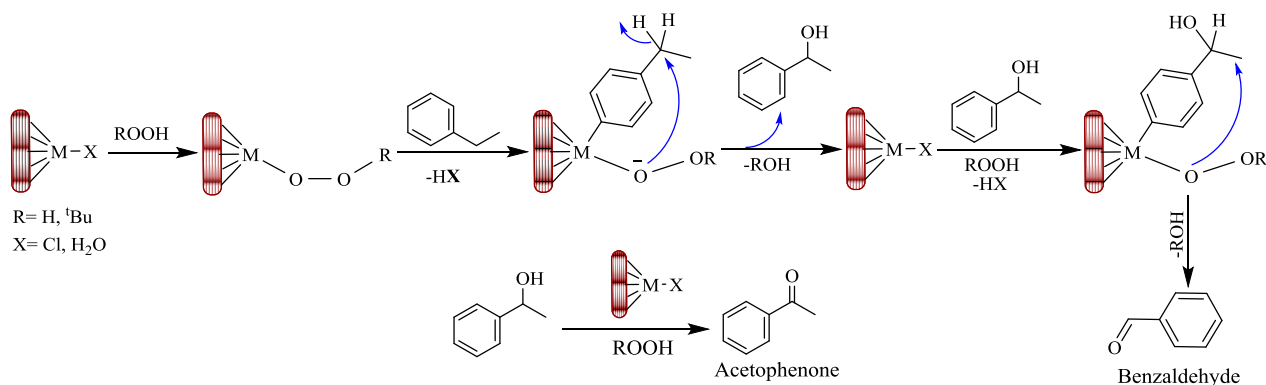


Figure 11. Proposed mechanism for the  $\text{H}_2\text{O}_2$ /TBHP facilitated oxidation of ethylbenzene catalyzed by supported catalyst

### Conclusions

In summary, new catalytic systems {[PS-ATP-V], [PS-ATP-Mn], [PS-ATP-Fe], [PS-ATP-Ni], and [PS-ATP-Cu]} were developed and characterized. Their catalytic efficiency was assessed using ethylbenzene as a model substrate. Oxidation reactions were performed under optimized conditions (0.15 g catalyst, 6-hour reaction time, 60 °C) with  $\text{H}_2\text{O}_2$  or TBHP as oxidants. Among the catalysts, [PS-ATP-Cu] exhibited the highest ethylbenzene conversion (53.8 %) with  $\text{H}_2\text{O}_2$ , whereas [PS-ATP-Mn] showed the lowest conversion (21.2 %) with TBHP. The best selectivity for acetophenone (83.9 %) was achieved using [PS-ATP-Ni] with  $\text{H}_2\text{O}_2$ , while [PS-ATP-Mn] had the lowest selectivity (59.4 %) with TBHP. These catalysts demonstrated excellent stability, maintaining their activity over five reuse cycles with minimal loss, indicating their potential for broader applications in heterogeneous catalysis.

### Author Information\*

\*The authors' names are presented in the following order: First Name, Middle Name and Last Name

**Savita Kumari** — Research Scholar, Department of Chemistry, Maharishi Markandeshwar (Deemed to be University), Mullana, Haryana, 133207, India; e-mail: [sheoransavita4@gmail.com](mailto:sheoransavita4@gmail.com); <https://orcid.org/0009-0005-9438-2445>

**Praveen Kumar Gupta** (corresponding author) — Professor, Department of Chemistry, Maharishi Markandeshwar (Deemed to be University), 133207, Mullana, Haryana, India; e-mail: [praveenguptachem@gmail.com](mailto:praveenguptachem@gmail.com); [parveen.gupta@mmumullana.org](mailto:parveen.gupta@mmumullana.org); <https://orcid.org/0000-0002-2718-1310>

**Amit Kumar** — Assistant Professor, Department of Chemistry, Indira Gandhi National College, Ladwa, Kurukshetra-136132, Haryana, India; e-mail: [amitvash76@gmail.com](mailto:amitvash76@gmail.com); <https://orcid.org/0009-0000-2748-1543>

**Ramesh Kumar** — Associate Professor, Department of Chemistry, Kurukshetra University, Kurukshetra-136119, Haryana, India; e-mail: [rameshkumarkuk@gmail.com](mailto:rameshkumarkuk@gmail.com); <https://orcid.org/0000-0003-2089-2213>

### Author Contributions

The manuscript was written through contributions of all authors. All authors have given approval to the final version of the manuscript. **CRedit: Savita Kumari** writing original draft, experimentation; **Praveen Kumar Gupta** writing, review, editing, supervision; **Amit Kumar** methodology, validation, visualization; **Ramesh Kumar** software, formal analysis, supervision, validation.

### Acknowledgments

The authors are thankful to the Maharishi Markandeshwar (Deemed to be University), Mullana, Haryana, India.

### Conflicts of Interest

The authors declare no conflict of interest.

### References

- 1 Nørskov, J. K., Studt, F., Abild-Pedersen, F., & Bligaard, T. (2014). *Fundamental concepts in heterogeneous catalysis*. John Wiley & Sons. <https://doi.org/10.1002/9781118892114>
- 2 Spargo, P. L. (2005). *Transition Metals for Organic Synthesis: Building Blocks and Fine Chemicals*. Second Revised and Enlarged Edition. (2-Volume Set.) Edited by Matthias Beller and Carsten Bolm. Wiley-VCH: Weinheim. 2004. 662 pp. (Vol. 1), 652 pp. (Vol. 2). £270. ISBN 3-527-30613-7. *Organic Process Research & Development*, 9(6), 1017–1018. <https://doi.org/10.1021/op050145w>
- 3 Ayogu, J. I., & Onoabedje, E. A. (2019). Recent advances in transition metal-catalysed cross-coupling of (hetero)aryl halides and analogues under ligand-free conditions. *Catalysis Science & Technology*, 9(19), 5233–5255. <https://doi.org/10.1039/C9CY01331H>
- 4 Maharana, T., Nath, N., Pradhan, H. C., Mantri, S., Routaray, A., & Sutar, A. K. (2022). Polymer-supported first-row transition metal schiff base complexes: Efficient catalysts for epoxidation of alkenes. *Reactive and Functional Polymers*, 171, 105142. <https://doi.org/10.1016/j.reactfunctpolym.2021.105142>
- 5 Sharma, A. S., Sharma, V. S., Yadav, P., Kaur, H., & Varma, R. S. (2023). Polystyrene Resins: Versatile and Economical Support for Heterogeneous Nanocatalysts in Sustainable Organic Reactions. *ChemCatChem*, 15(8), e202201493. <https://doi.org/10.1002/cctc.202201493>
- 6 Wang, K., Horlyck, J., An, N., & Voutchkova-Kostal, A. (2024). Homogeneous vs. heterogeneous catalysts for acceptorless dehydrogenation of biomass-derived glycerol and ethanol towards circular chemistry. *Green Chemistry*, 26(7), 3546–3564. <https://doi.org/10.1039/D3GC04378A>
- 7 Kumari, S., Kumar, S., Karan, R., Bhatia, R., Kumar, A., Rawal, R. K., & Gupta, P. K. (2024). Synthetic and catalytic perspectives of polystyrene supported metal catalyst. *Journal of the Iranian Chemical Society*, 21(4), 951–1010. <https://doi.org/10.1007/s13738-024-02970-7>
- 8 Corain, B., Zecca, M., Canton, P., & Centomo, P. (2010). Synthesis and catalytic activity of metal nanoclusters inside functional resins: an endeavour lasting 15 years. *Philosophical Transactions of the Royal Society A: Mathematical, Physical and Engineering Sciences*, 368(1915), 1495–1507. <https://doi.org/10.1098/rsta.2009.0278>
- 9 Sharma, A. S., Sharma, V. S., Yadav, P., Kaur, H., & Varma, R. S. (2023). Polystyrene Resins: Versatile and Economical Support for Heterogeneous Nanocatalysts in Sustainable Organic Reactions. *ChemCatChem*, 15(8), e202201493. <https://doi.org/10.1002/cctc.202201493>
- 10 Králík, M., & Biffis, A. (2001). Catalysis by metal nanoparticles supported on functional organic polymers. *Journal of Molecular Catalysis A: Chemical*, 177(1), 113–138. [https://doi.org/10.1016/s1381-1169\(01\)00313-2](https://doi.org/10.1016/s1381-1169(01)00313-2)
- 11 Azeez, M. O., Nafiu, S. A., Olarewaju, T. A., Olabintan, A. B., Tanimu, A., Gambo, Y., & Aitani, A. (2023). Selective catalytic oxidation of ethylbenzene to acetophenone: a review of catalyst systems and reaction mechanisms. *Industrial & Engineering Chemistry Research*, 62(33), 12795–12828. <https://doi.org/10.1021/acs.iecr.3c01588>
- 12 Siddiqi, I., & Pitre, K. S. (2003). Determination of phenones in a perfume composition. *Reviews in Analytical Chemistry*, 22(1), 9–18. <https://doi.org/10.1515/REVAC.2003.22.1.9>
- 13 Kizilcan, N., Galioğlu, O., & Akar, A. (1993). Modified cyclohexanone – formaldehyde and acetophenone – formaldehyde resins. *Journal of applied polymer science*, 50(4), 577–584. <https://doi.org/10.1002/app.1993.070500402>
- 14 Zubkov, F. I., & Kouznetsov, V. V. (2023). Traveling across life sciences with acetophenone — a simple ketone that has special multipurpose missions. *Molecules*, 28(1), 370. <https://doi.org/10.3390/molecules28010370>
- 15 Soucy, N. V. (2014). Acetophenone. *Encyclopedia of Toxicology*, 43–45. <https://doi.org/10.1016/b978-0-12-386454-3.01157-x>
- 16 Mohammadi Ziarani, G., Kheilkordi, Z., & Mohajer, F. (2020). Recent advances in the application of acetophenone in heterocyclic compounds synthesis. *Journal of the Iranian Chemical Society*, 17, 247–282. <https://doi.org/10.1007/s13738-019-01774-4>

- 17 Loch, C., Reusch, H., Ruge, I., Godelmann, R., Pflaum, T., Kuballa, T., & Lachenmeier, D. W. (2016). Benzaldehyde in cherry flavour as a precursor of benzene formation in beverages. *Food Chemistry*, 206, 74–77. <https://doi.org/10.1016/j.foodchem.2016.03.034>
- 18 Opgrande, J. L., Dobratz, C. J., Brown, E., Liang, J., Conn, G. S., Shelton, F. J., & With, J. (2000). *Benzaldehyde*. Kirk-Othmer Encyclopedia of Chemical Technology. <https://doi.org/10.1002/0471238961.0205142615160718.a01>
- 19 Mohammadi, A., Mohammadi, S., Bayandori Moghaddam, A., Masoumi, V., & Walker, R. B. (2014). Electropolymerized fluorinated aniline-based fiber for headspace solid-phase microextraction and gas chromatographic determination of benzaldehyde in injectable pharmaceutical formulations. *Journal of chromatographic science*, 52(9), 971–976. <https://doi.org/10.1093/chromsci/bmt152>
- 20 Theodoropoulou, M. A., Nikitas, N. F., & Kokotos, C. G. (2020). Aldehydes as powerful initiators for photochemical transformations. *Beilstein Journal of Organic Chemistry*, 16(1), 833–857. <https://doi.org/10.3762/bjoc.16.76>
- 21 Sieber, R., Bütikofer, U., & Bosset, J. O. (1995). Benzoic acid as a natural compound in cultured dairy products and cheese. *International Dairy Journal*, 5(3), 227–246. [https://doi.org/10.1016/0958-6946\(94\)00005-A](https://doi.org/10.1016/0958-6946(94)00005-A)
- 22 Londry, K. L., & Fedorak, P. M. (1992). Benzoic acid intermediates in the anaerobic biodegradation of phenols. *Canadian Journal of Microbiology*, 38(1), 1–11. <https://doi.org/10.1139/m92-001>
- 23 Faraji, A. R., Mosazadeh, S., & Ashouri, F. (2017). Synthesis and characterization of cobalt-supported catalysts on modified magnetic nanoparticle: green and highly efficient heterogeneous nanocatalyst for selective oxidation of ethylbenzene, cyclohexene and oximes with molecular oxygen. *Journal of Colloid and Interface Science*, 506, 10–26. <https://doi.org/10.1016/J.JCIS.2017.06.100>
- 24 Gao, L., Zhuge, W., Feng, X., Sun, W., Sun, X., & Zheng, G. (2019). Co/rgo synthesized via the alcohol-thermal method as a heterogeneous catalyst for the highly efficient oxidation of ethylbenzene with oxygen. *New Journal of Chemistry*, 43(21), 8189–8194. <https://doi.org/10.1039/C9NJ00470J>
- 25 Li, J., Zhao, S., Yang, S., Wang, S., Sun, H., Jiang, S. P., Johannessen, B., & Liu, S. (2021). Atomically dispersed cobalt on graphitic carbon nitride as a robust catalyst for selective oxidation of ethylbenzene by peroxymonosulfate. *Journal of Materials Chemistry A*, 9, 3029–3035. <https://doi.org/10.1039/d0ta11503g>
- 26 Yamazaki, S. (1999). Chromium (VI) oxide-catalyzed benzylic oxidation with periodic acid. *Organic Letters*, 13(1), 2129–2132. <https://doi.org/10.1021/ol991175k>
- 27 Yang, Y., Zhong, W., Nie, B., Chen, J., Wei, Z., & Liu, X. (2017). Synergetic oxidation of ethylbenzene to acetophenone catalyzed by manganese(II) complexes bearing pendant iodophenyl groups. *Journal of Organometallic Chemistry*, 853, 136–142. <https://doi.org/10.1016/J.JORGACHEM.2017.10.034>
- 28 Venkatesh, G., Vennila, P., Kaya, S., Ahmed, S. B., Sumathi, P., Siva, V., & Kamal, C. (2024). Synthesis and spectroscopic characterization of Schiff base metal complexes, biological activity, and molecular docking studies. *ACS omega*, 9(7), 8123–8138. <https://doi.org/10.1021/acsomega.3c08526>
- 29 Raman, N., Kulandaisamy, A., & Jeyasubramanian, K. (2001). Synthesis, spectroscopic characterization, redox, and biological screening studies of some Schiff base transition metal (II) complexes derived from salicylidene-4-aminoantipyrine and 2-aminophenol/2-aminothiophenol. *Synthesis and Reactivity in Inorganic and Metal-Organic Chemistry*, 31(7), 1249–1270. <https://doi.org/10.1081/SIM-100106862>
- 30 Islam, M. T., Bitu, M. N. A., Ali, M. A., Hossen, M. F., & Kudrat, M. (2024). Oxovanadium (IV) complexes of  $\alpha$ -Amino acid schiff bases and 2,2'-Bipyridine ligands: Synthesis, characterization and investigation of their biological potency. <http://dx.doi.org/10.52711/0974-4150.2024.00020>
- 31 Aly, A. A., Ghandour, M., & Alfakeh, M. S. (2012). Synthesis and characterization of transition metal coordination polymers derived from 1,4-benzenedicarboxylate and certain azoles. *Turkish Journal of Chemistry*, 36(1), 69–79. <https://doi.org/10.3906/kim-1106-61>
- 32 Al-Fakeh, M. S. (2020). Synthesis, thermal stability and kinetic studies of copper (II) and cobalt (II) complexes derived from 4-aminobenzohydrazide and 2-mercaptobenzothiazole. *European Chemical Bulletin*, 9(12), 403–409. <http://dx.doi.org/10.17628/ecb.2020.9.403-409>
- 33 Maurya, M. R., Chauhan, A., Arora, S., & Gupta, P. (2022). Triazole based oxidovanadium (V) complex supported on chloromethylated polymer and its catalytic activity for the synthesis of dihydropyrimidinones (DHPMs). *Catalysis Today*, 397, 3–15. <https://doi.org/10.1016/j.cattod.2022.03.006>
- 34 Gomathi, V., & Selvameena, R. (2022). Synthesis, structural analysis and antimicrobial screening of Mn (II) complexes of Schiff bases. *Journal of the Mexican Chemical Society*, 66(1), 70–78. <https://doi.org/10.29356/jmcs.v66i1.1621>
- 35 Buldurun, K., Turan, N., Savci, A., Alan, Y., & Colak, N. (2022). Synthesis, characterization, X-ray diffraction analysis of a tridentate Schiff base ligand and its complexes with Co (II), Fe (II), Pd (II) and Ru (II): Bioactivity studies. *Iran. J. Chem. Chem. Eng.*, 41(8). <https://doi.org/10.30492/ijcce.2021.531629.4775>
- 36 Dinku, D., Demissie, T. B., Beas, I. N., Eswaramoorthy, R., Abdi, B., & Desalegn, T. (2024). Antimicrobial activities and docking studies of new Schiff base ligand and its Cu (II), Zn (II) and Ni (II) Complexes: Synthesis and Characterization. *Inorganic Chemistry Communications*, 160, 111903. <https://doi.org/10.1016/j.inoche.2023.111903>
- 37 Chellaian, J. D., & SS, S. R. (2021). Co (II), Ni (II), Cu (II), and Zn (II) complexes of 4-aminoantipyrine-derived Schiff base. Synthesis, structural elucidation, thermal, biological studies, and photocatalytic activity. *Journal of Heterocyclic Chemistry*, 58(4), 928–941. <https://doi.org/10.1002/jhet.4209>



- 38 Vijayan, J. G. (2022). Synthesis, Characterization, Magnetic, Thermal and Electrochemical Studies of Oxovanadium (IV) Complex of 2-thiophenecarba Benzhydrazone. In *Advanced Polymeric Materials* (pp. 59–72). River Publishers. <https://doi.org/10.1201/9781003337041-3>
- 39 Mureseanu, M., Filip, M., Bleotu, I., Spinu, C. I., Marin, A. H., Matei, I., & Parvulescu, V. (2023). Cu (II) and Mn (II) Anchored on Functionalized Mesoporous Silica with Schiff Bases: Effects of Supports and Metal–Ligand Interactions on Catalytic Activity. *Nanomaterials*, 13(12), 1884. <https://doi.org/10.3390/nano13121884>
- 40 Howsau, H. B., Sharfalddin, A. A., Abdellattif, M. H., Basaleh, A. S., & Hussien, M. A. (2021). Synthesis, spectroscopic characterization and biological studies of Mn (II), Cu (II), Ni (II), Co (II) and Zn (II) complexes with new schiff base of 2-((pyrazine-2-ylimino)methyl) phenol. *Applied Sciences*, 11(19), 9067. <https://doi.org/10.3390/app11199067>
- 41 Azeez, M. O., Nafiu, S. A., Olarewaju, T. A., Olabintan, A. B., Tanimu, A., Gambo, Y., & Aitani, A. (2023). Selective catalytic oxidation of ethylbenzene to acetophenone: a review of catalyst systems and reaction mechanisms. *Industrial & Engineering*, 62(33), 12795–12828. <https://doi.org/10.1021/acs.iecr.3c01588>

Arina G. Kicheeva<sup>1\*</sup>, Ekaterina S. Sushko<sup>1</sup>, Artur A. Dzeranov<sup>2,3,4</sup>,  
Lyubov S. Bondarenko<sup>2,3</sup>, Natalya S. Tropkaya<sup>2,3</sup>, Kamila A. Kydralieva<sup>2</sup>,  
Nadezhda S. Kudryasheva<sup>1,5</sup>

<sup>1</sup>*Institute of Biophysics SB RAS, Federal Research Center “Krasnoyarsk Science Center SB RAS”, Krasnoyarsk, Russia;*

<sup>2</sup>*Moscow Aviation Institute (National Research University), Moscow, Russia;*

<sup>3</sup>*Sklifosovsky Research Institute for Emergency Medicine, Moscow, Russia;*

<sup>4</sup>*Federal Research Center of Problems of Chemical Physics and Medicinal Chemistry,  
Russian Academy of Sciences, Chernogolovka, Moscow region, Russia;*

<sup>5</sup>*School of Fundamental Biology and Biotechnology, Siberian Federal University, Krasnoyarsk, Russia*

(\*Corresponding author's e-mail: [khyzylsy@mail.ru](mailto:khyzylsy@mail.ru))

## A Bacterial Enzymatic System Neutralizes the Impact of Silica-Magnetite Nanocomposites on ROS Levels

This study investigates the reactive oxygen species (ROS) generation and biological activity of novel silica-magnetite nanocomposites, TA-AA-Fe<sub>3</sub>O<sub>4</sub> and TA-HA-Fe<sub>3</sub>O<sub>4</sub>, where TA is a silicon dioxide copolymer, AA is ascorbic acid, and HA is humic acids. A key challenge in nanotoxicology is the contradictory data from complex biological systems. To address this, we employed a standardized bioluminescent enzymatic assay (bacterial luciferase/oxidoreductase) as a simple, rapid biosensor system to evaluate the nanocomposites' effects under controlled conditions. We compared ROS activity in both non-biological (enzyme-free aqueous solutions) and biological (enzymatic system) environments, with and without model oxidative stress induced by 1,4-benzoquinone. The enzymatic system exerted a pronounced neutralizing effect on ROS content, suppressing the significant ROS fluctuations and synergistic ROS generation (up to 300%) observed in non-biological media in the presence of the oxidizer. Additionally, the nanocomposites showed no effect on the bioluminescence intensity of the enzymatic system. This disparity between the higher reactivity in simple aqueous solutions and the neutral effect in the enzymatic system highlights the critical role of biological matrices. The findings suggest that enzymatic environments can mitigate the radical processes driven by iron-based nanocomposites, which is crucial for predicting their biological activity and potential for applications like ferroptosis-based tumor therapy.

**Keywords:** iron-based nanocomposite, magnetite, silica, ascorbic acid, humic acids, bacterial enzymatic assay, reactive oxygen species, bioluminescence, chemiluminescence

### Introduction

The biological activity of nanoparticles is a highly promising field of study, and the number of articles and reviews in this field is growing rapidly [1–3]. However, the results of these studies are often contradictory due to the variety of experimental conditions and the use of complex biological systems. This makes it difficult to compare and predict the properties of nanoparticles.

Superparamagnetic iron oxide nanoparticles (Fe<sub>3</sub>O<sub>4</sub>) are widely used for adsorption [4], enzyme immobilization [5], Fenton reaction catalysis [6–8], drug delivery [9], and energy storage [10–11]. To prevent the aggregation of these nanoparticles [12], their surfaces are modified with various organic and inorganic ligands, including humic acids (HA), ascorbic acid (AA) and polymer derivatives of silicon dioxide—tetraethoxysilane and 3-aminopropyltriethoxysilane (TA) [13–15].

Nanocomposites based on silica-magnetite nanoparticles (TA-Fe<sub>3</sub>O<sub>4</sub>) are promising for biomedical applications due to their biocompatibility, magnetic properties and easy surface functionalization [16–17]. Mesoporous silica nanoparticles enable flexible tuning of their structure for efficient drug loading and targeted delivery. They also serve as substrates for other nanomaterials, forming multifunctional composites.

AA and HA act as surface modifiers, preventing aggregation and influencing Fenton reaction-driven ROS generation by iron-containing nanoparticles [18–21], resulting in iron-programmed cell death—ferroptosis. AA maintains magnetite stoichiometry and has both antioxidant and prooxidant effects, while

HA enhance the catalytic activity of  $\text{Fe}_3\text{O}_4$  in Fenton reactions. On the other hand, magnetite can provide magnetically-controlled delivery of AA and HA in organisms.

Previous research showed that nanocomposite  $\text{Fe}_3\text{O}_4$ -AA-MOF (where MOF is a metal-organic framework) retained the antibacterial and prooxidant properties of AA [22]. In this system, MOF- $\text{Fe}_3\text{O}_4$  acts as an inert magnetic carrier.

Despite the fact that some silica-based nanostructures have passed clinical trials, concerns about their safety persist. The key challenges include conducting toxicity studies, designing simple but effective nanoplateforms, and understanding their *in vivo* mechanisms. The toxicity of mesoporous silica nanoparticles depends on their size, morphology [23-24], surface charge [25], degree of crystallinity [26–30], and concentration [31]. Studies report that membrane damage, cytotoxicity, hemolysis [32-33], and immune activation [34] depend on nanoparticle properties and cell type.

However, the available data pertain to various aspects of the biological activity of nanomaterials and are typically obtained under non-comparable conditions. The standardization of experimental protocols remains an urgent task. For this purpose, the authors selected a simple and rapid biosensor system—a bioluminescent enzymatic assay.

The bacterial luminescence bioassay is widely used in ecological studies. This technique exploits the fact that luminous marine bacteria naturally produce light; thus, a decrease in luminescence intensity directly indicates the presence of toxic substances. High sensitivity, speed, and simplicity have made this bioassay a standard tool for toxicity monitoring for more than six decades [35–38]. The long-term application of this bioassay has contributed to a broad understanding of the effects of various compounds on bacterial cells, their enzymes, and cellular membranes [39–41]. Patterns of the effects of toxicants on enzymatic reactions contribute to understanding the mechanisms of toxic effects on living organisms.

A newer approach involves using the isolated enzymes responsible for the luminescence. In 1990, a toxicity bioassay was developed based on a coupled enzyme system including bacterial luciferase and NAD(P)H:FMN-oxidoreductase [42]:



This enzyme system is sensitive to redox-active compounds; its bioluminescence depends on concentration and redox parameters of these compounds [39-40, 43]. Both enzymatic and bacterial bioluminescence assays have been used to study the prooxidant [20, 44] and antioxidant [45–49] properties of bioactive compounds, and to detect the involvement of reactive oxygen species (ROS) in these effects.

ROS are oxygen-containing molecules with unpaired electrons, such as superoxide anion ( $\text{O}_2^-$ ), hydrogen peroxide ( $\text{H}_2\text{O}_2$ ), hydroxyl radical ( $\cdot\text{OH}$ ), etc. They are constantly present at physiological levels and play key roles in cellular signaling [50] and apoptosis [51–54]. While essential for normal metabolism, excessive ROS levels produce toxic effects, damaging DNA, proteins, and lipids [55]. Maintaining ROS balance is, therefore, vital for cellular function.

In bioluminescence systems, ROS are both generated and utilized in the coupled redox reactions. Therefore, the role of ROS in these enzymatic systems (Reactions R.1 and R.2) is crucial.

Iron's ability to generate ROS is directly due to its unique chemical properties: partially filled *d*-orbitals, variable oxidation states, and involvement in electron transfer processes. Investigating the ROS-related activity of iron nanoparticles, such as magnetite-silica nanocomposites, is crucial for developing their biomedical applications.

Our study aims to characterize silica-based nanocomposites (TA-AA- $\text{Fe}_3\text{O}_4$  and TA-HA- $\text{Fe}_3\text{O}_4$ ). We investigated ROS generation and the biological activity of these compounds, comparing their ROS activity in a non-biological system and the simplest biological system (an enzymatic reaction). The results will contribute to predicting the biological activity of iron nanoparticles, which is important for the development of ferroptosis-based tumor treatments.

## Experimental

### Preparation of a Copolymer of Tetraethoxysilane and 3-Aminopropyltriethoxysilane (TA)

To prepare the copolymer, 150 mL of deionized water (DI) was added to a mixture of 10 mL of tetraethoxysilane (T) and 4.2 mL of 3-aminopropyltriethoxysilane (A) (molar ratio T:A = 1:0.5) under constant stirring on an overhead mixer (600 rpm, 10 min). The mixture was then stirred on an orbital shaker

(150 rpm, 24 h) at room temperature. The resulting precipitate was collected and washed with DI water until the supernatant reached pH~8. The final product was dried and lyophilized in a freeze dryer at  $-37^{\circ}\text{C}$ .

#### *Preparation of TA-HA-Fe<sub>3</sub>O<sub>4</sub> Composite*

To obtain the TA-HA-Fe<sub>3</sub>O<sub>4</sub> composite (1:0.1:1 wt.%), 2 g of TA and 0.2 g of HA were dispersed in 200 mL of DI in an argon atmosphere on an overhead agitator (1400–1500 rpm, 30 min). The concentrations of magnetite nanoparticles, as a source of iron ions, were determined by calculating a 20-fold excess of Fe<sup>3+</sup> (HA-Fe = 1:20) based on the content of HA functional groups (5 mmol/g of the COOH and OH groups), in order to obtain water-soluble humic preparations with a high iron content. As a result, salt mixtures of 5.4 g of FeCl<sub>3</sub>·6H<sub>2</sub>O, 1.98 g of FeCl<sub>2</sub>·4H<sub>2</sub>O and 12 mL of 25 % NH<sub>4</sub>OH were added. The formed precipitate was separated on a paper filter, washed with DI and dried in a dynamic vacuum. Wt.% Fe: 37.7.

#### *Preparation of TA-AA-Fe<sub>3</sub>O<sub>4</sub> Composite*

To obtain the TA-AA-Fe<sub>3</sub>O<sub>4</sub> composite (1:0.1:1 wt.%), iron salt samples were dissolved in DI in an argon atmosphere and 12 mL of 25 % NH<sub>4</sub>OH was added with constant stirring (1400–1500 rpm, 30 min). The formed Fe<sub>3</sub>O<sub>4</sub> precipitate was separated using a magnet (0.3 T) and washed once with 200 mL of DI. Then 0.2 g of AA was dissolved in 70 mL of suspension containing Fe<sub>3</sub>O<sub>4</sub>, 200 mL of 96 % C<sub>2</sub>H<sub>5</sub>OH (pH = 7–8) was added with constant stirring (1200 rpm) and 2 g of TA. The solution was stirred on an overhead mixer (1000 rpm) for 60 minutes. The formed precipitate was separated on a paper filter, washed with DI and dried in a dynamic vacuum. Wt.% Fe: 51.8.

#### *Characterization of Nanocomposites*

Samples of the nanocomposites TA-AA-Fe<sub>3</sub>O<sub>4</sub> and TA-HA-Fe<sub>3</sub>O<sub>4</sub> were characterized using X-ray diffraction, transmission electron microscopy, and low-temperature nitrogen adsorption (Supplementary Materials A, B).

#### *Luminol Chemiluminescence Assay System*

ROS levels were quantified using a luminol-based chemiluminescence method. Measurements were performed both in distilled water (enzyme-free solutions) and within the enzymatic system, across a range of composite concentrations [56]. The chemiluminescence reaction was initiated by adding an alkaline luminol solution ( $3 \times 10^{-5}$  M). The concentration of K<sub>3</sub>[Fe(CN)<sub>6</sub>] in all samples was maintained at  $1.2 \times 10^{-4}$  M.

#### *Bioluminescence Enzymatic Assay System*

The effects of the silica-based composites on an enzyme system were evaluated using a bioluminescence enzymatic assay. The composition of this bioluminescence enzyme system is described in [56].

#### *Measurements of Bioluminescence/Chemiluminescence Intensities*

The preparation of nanocomposite suspensions for bioluminescent and chemiluminescent analyses was the same as described in [56].

##### *a) Luminol Chemiluminescence Assay*

To assess a role of ROS in the biological effects of the nanocomposites, the chemiluminescence intensity was measured in the enzyme-free and enzymatic solutions.

The relative ROS content ( $ROS^{rel}$ ) was defined as follows:

$$ROS^{rel} = ROS_{NC} / ROS_{contr}, \quad (1)$$

where  $ROS_{contr}$  and  $ROS_{NC}$  are the ROS contents in the absence and presence of nanocomposites, respectively.

Additionally, ROS contents were determined under conditions of model oxidative stress. To model oxidative stress, we employed the organic oxidizer 1,4-benzoquinone (Sigma-Aldrich, St. Louis, MO, USA). For the experiments, a benzoquinone concentration that inhibits the bioluminescence intensity by 50 % ( $IC_{50} = 10^{-6}$  M) was selected. The relative ROS content ( $ROS_{Bq}^{rel}$ ) was defined as follows:

$$ROS_{Bq}^{rel} = ROS_{NC+Bq} / ROS_{Bq},$$

where  $ROS_{NC+Bq}$  and  $ROS_{Bq}$  are the ROS contents in 1,4-benzoquinone solutions in the presence and absence of nanocomposites, respectively.

##### *b) Bioluminescence Enzyme System*

The inhibitory effects of the nanocomposites on the enzymatic activity were quantified using the relative bioluminescence intensity,  $I^{rel}$ :

$$I^{rel} = I_{NC}/I_{contr}, \quad (3)$$

where  $I_{contr}$  and  $I_{NC}$  are the maximum bioluminescence intensities in the absence and presence of nanocomposites, respectively.

The effects of the nanocomposites in the enzymatic bioluminescent system under model oxidative stress were evaluated using relative bioluminescence intensity,  $I_{Bq}^{rel}$ :

$$I_{Bq}^{rel} = I_{NC+Bq}/I_{Bq}, \quad (4)$$

where  $I_{NC+Bq}$  and  $I_{Bq}$  are the maximum bioluminescence intensities in 1,4-benzoquinone solutions in the presence and absence of nanocomposites, respectively.

### Statistical Processing

Bio/chemi-luminescence measurements were performed in 5–10 replicates at 25 °C using a Luminoskan Ascent bioluminometer (Thermo Electron Corporation, USA) with an integrated injector. The maximum chemiluminescence and bioluminescence intensities were determined. Standard deviations (SD) for  $I^{rel}$  and  $ROS^{rel}$ ,  $I_{Bq}^{rel}$  and  $ROS_{Bq}^{rel}$  were analyzed with GraphPad Prism 8 (GraphPad Software, Inc., USA); all SD were less than 20 %. To evaluate quantitatively the spread of data across experimental curves, we compared the coefficients of determination ( $R^2$ ) for the exponential dependences of  $I^{rel}$ ,  $ROS^{rel}$ ,  $I_{Bq}^{rel}$  and  $ROS_{Bq}^{rel}$  on nanocomposite concentrations.

## Results and Discussion

### A. ROS Content in Water Suspensions of TA-AA-Fe<sub>3</sub>O<sub>4</sub> and TA-HA-Fe<sub>3</sub>O<sub>4</sub>. Enzyme-Free and Enzyme Solutions

Preliminarily, we studied the effects of the triple nanocomposites TA-AA-Fe<sub>3</sub>O<sub>4</sub> and TA-HA-Fe<sub>3</sub>O<sub>4</sub> on ROS content in distilled water (Fig. 1A). The figure shows no significant effects ( $p > 0.05$ ) at nanocomposite concentrations  $<10^{-2}$  mg/L and a minor suppression of ROS content at concentrations  $>10^{-2}$  mg/L.

We simulated a biological medium in the nanocomposite suspensions by adding the enzyme system. The ROS content was measured during the enzymatic bioluminescence process. Figure 1C shows that the addition of the enzymes did not notably change the ROS content at low nanocomposite concentrations ( $< 10^{-2}$  mg/L) and mitigated the minor ROS suppression observed at higher concentrations ( $> 10^{-2}$  mg/L).

However, the data scatter across the curves reduced compared to the enzyme-free medium (Fig. 1A). The values of the coefficients of determination ( $R^2$ ) for the exponential dependences of  $ROS^{rel}$  on nanocomposite concentration increased from 0.02 to 0.14 for TA-AA-Fe<sub>3</sub>O<sub>4</sub> and from 0.02 to 0.34 for TA-HA-Fe<sub>3</sub>O<sub>4</sub>. This increase quantitatively confirms the reduced variation in ROS content when replacing the enzyme-free medium with the enzymatic one.

Additionally, we conducted similar experiments in the presence of a model oxidizer—1,4-benzoquinone. In our previous research [20, 22, 44, 56], we used this compound to model oxidative stress in bacterial suspensions and enzymatic solutions. This approach is based on the assumption that such model oxidative stress stimulates the additional formation of active oxygen radicals (in accordance with the Fenton reaction [6–8]) and, consequently, may induce antitumor activity.

Figure 1B shows the ROS content in aqueous solutions at different concentrations of TA-AA-Fe<sub>3</sub>O<sub>4</sub> and TA-HA-Fe<sub>3</sub>O<sub>4</sub> nanocomposites in the presence of 1,4-benzoquinone. The difference from the medium containing no benzoquinone (Fig. 1A) is pronounced: the presence of 1,4-benzoquinone increased the ROS content by up to 150 % for TA-HA-Fe<sub>3</sub>O<sub>4</sub> and by up to 300 % for TA-AA-Fe<sub>3</sub>O<sub>4</sub> across the entire concentration range studied (Fig. 1B). The 300 % increase in ROS content in TA-AA-Fe<sub>3</sub>O<sub>4</sub> suspensions (Fig. 1B) can be explained by synergistic effects on ROS generation via a process known as redox cycling [57]. According to the authors' findings, quinones, ascorbic acid, and iron interact in redox cycles involving semiquinone radical intermediates, iron participation, and OH generation through Fenton reactions. The more moderate increase in ROS content observed in TA-HA-Fe<sub>3</sub>O<sub>4</sub> suspensions (Fig. 1B) may be related to processes discussed in [58–59]: humic acids (HA) and quinones can accelerate Fe(III) reduction by electron shuttling, and the subsequent ROS generation via the Fenton reaction may result from this acceleration.

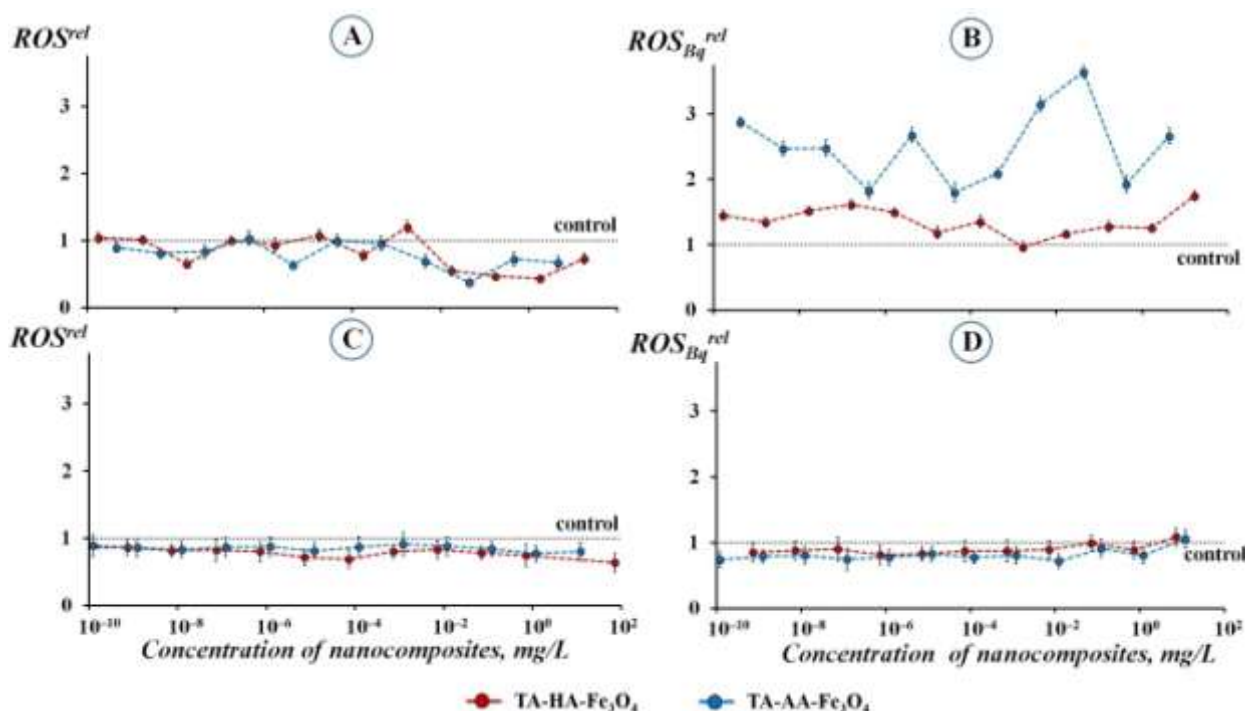


Figure 1. Relative ROS content: (A) in enzyme-free water solutions,  $ROS^{rel}$ ; (B) under conditions of oxidative stress in enzyme-free water solutions,  $ROS_{Bq}^{rel}$ ; (C) in the enzyme system,  $ROS^{rel}$ ; (D) under conditions of oxidative stress in the enzyme system,  $ROS_{Bq}^{rel}$ . Control suspension — in the absence of nanocomposites. Conditions of oxidative stress — in the presence of 1,4-benzoquinone ( $IC_{50Bq} = 10^{-6}$  M).

Figure 1D presents the ROS content in the enzymatic system in the presence of 1,4-benzoquinone ( $10^{-6}$  M) at different concentrations of the nanocomposites. A comparison of Figures 1B and 1D reveals a neutralizing effect of the enzymes on the ROS content: the addition of nanocomposites TA-AA- $Fe_3O_4$  and TA-HA- $Fe_3O_4$  did not alter the ROS content compared to the control solution under conditions of model oxidative stress.

Additionally, the data spread across the curves in Figure 1D decreased compared to the enzyme-free medium (Fig. 1B), similar to the trend observed in benzoquinone-free media (Figures 1A and 1C). The values of the coefficients of determination ( $R^2$ ) for the exponential dependencies of  $ROS^{rel}$  on nanocomposite concentration increased from 0.01 to 0.40 for TA-AA- $Fe_3O_4$  and from 0.10 to 0.38 for TA-HA- $Fe_3O_4$ . This increase again quantitatively confirms the reduced variation in ROS content when replacing the enzyme-free medium with the enzymatic one.

The fluctuations in ROS levels observed in Figures 1A and 1B show a non-random pattern, reminiscent of effects discussed in the literature [60]. In any case, the effect noted in our study (Fig. 1B) is interesting and warrants further investigation. Importantly, we have observed similar ROS fluctuations for other types of magnetite-based nanocomposites, specifically  $Fe_3O_4$ -AA-MOF and  $Fe_3O_4$ -HA-MOF, in an aquatic non-biological environment (Supplementary Materials C, Figures S5A, S5B).

Hence, we observed a neutralizing effect of the enzymatic system on the ROS content in suspensions of the TA-AA- $Fe_3O_4$  and TA-HA- $Fe_3O_4$  nanocomposites. This effect was observed both in the absence and presence of 1,4-benzoquinone (Figures 1B and 1D), i.e., independent of the initial oxidative characteristics of the aqueous media. We assume possible mechanisms for enzymatic neutralization: 1) The enzyme proteins (via the variety of chemical groups) may act as radical scavengers, quenching ROS; 2) Components of the assay (NADH, FMN) might compete in redox cycling reactions, effectively “shunting” electrons away from the nanocomposite-driven pathways; 3) The proteins could chelate iron ions, sequestering them from participating in Fenton chemistry. The neutralization of ROS variations by bacterial enzymes was previously observed in suspensions of other magnetite-based nanocomposites (Supplementary Materials C, Figures S5C, S5D).



Moreover, consistent with our current observations in the enzyme solutions (Fig. 1), authors [20, 56] reported an alteration of ROS levels in a bacterial environment compared to non-biological aqueous media. This effect was attributed to the metabolic ability of bacteria to balance the external ROS level, adapting it to an optimum for bacterial physiology—a phenomenon known as a protective regulatory function of bacteria.

#### B. Effects of Nanocomposites TA-AA-Fe<sub>3</sub>O<sub>4</sub> and TA-HA-Fe<sub>3</sub>O<sub>4</sub> on Bioluminescence Intensity of Enzyme System

We studied the efficiency of enzymatic process in the presence of the nanocomposites. Bioluminescence intensity was used as an indicator of the enzymatic efficiency. The experiments were carried out in the absence and presence of the model oxidizer 1,4-benzoquinone (Figures 2A, 2B). The results show that the values of  $I^{rel}$  were close to the control, indicating no significant effects of the nanocomposites on the enzymatic process.

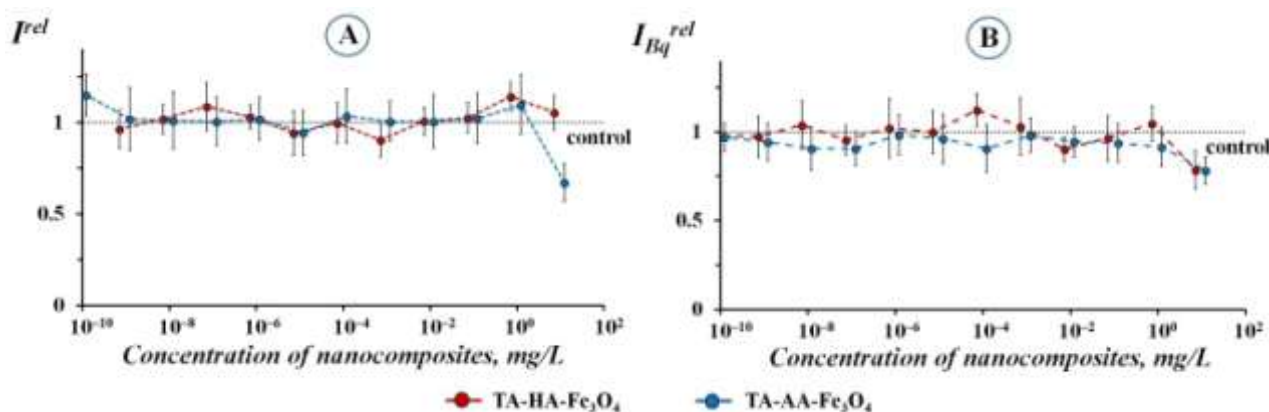


Figure 2. Relative bioluminescence intensity: (A) in the enzyme system,  $I^{rel}$ ; (B) under conditions of oxidative stress in the enzyme system,  $I_{Bq}^{rel}$ . Control suspension — in the absence of nanocomposites. Conditions of oxidative stress — in the presence of 1,4-benzoquinone ( $IC_{50Bq} = 10^{-6}$  M)

This result is likely related to the absence of nanocomposite effects on the ROS level in the enzymatic solutions (Figures 1C and 1D). As discussed previously [61–63], the bioluminescence oxidative reaction—involving its intermediate (peroxyhemiacetal)—and competing dark side reactions are sensitive to ROS levels.

Furthermore, the low sensitivity of the bioluminescence enzyme system to magnetite-based nanocomposites was demonstrated in prior work [20, 56] and Supplementary Materials D (Figures S6A, S6B), using nanocomposites such as Fe<sub>3</sub>O<sub>4</sub>-MOF, Fe<sub>3</sub>O<sub>4</sub>-HA, Fe<sub>3</sub>O<sub>4</sub>-APTES, Fe<sub>3</sub>O<sub>4</sub>-AA-MOF, and Fe<sub>3</sub>O<sub>4</sub>-HA-MOF as examples.

However, our previous studies have shown that triple nanocomposites of similar structure, specifically Fe<sub>3</sub>O<sub>4</sub>-AA-MOF [56] and Fe<sub>3</sub>O<sub>4</sub>-HA-MOF, did affect luminescent bacterial cells, demonstrating both toxicity and pro-oxidant activity. Furthermore, Fe<sub>3</sub>O<sub>4</sub>-AA-MOF retained the antibacterial properties of AA. Hence, the effects of these compounds on whole cells and isolated enzymes differed. This suggests that our current investigation should continue toward cellular processes, with special attention given to the role of the cellular membrane.

### Conclusions

This study investigated the reactive oxygen species (ROS) generation and biological activity of silica-based nanocomposites, TA-AA-Fe<sub>3</sub>O<sub>4</sub> and TA-HA-Fe<sub>3</sub>O<sub>4</sub>, in both non-biological (aqueous) and simple biological (enzymatic) systems. The key findings are as follows:

1. Neutralizing Effect of the Enzymatic System: The enzymatic bioluminescence system effectively neutralized the impact of the nanocomposites on ROS levels. In enzyme-free water, the nanocomposites caused significant and variable increases in ROS content (up to 300 % for TA-AA-Fe<sub>3</sub>O<sub>4</sub>, in the presence of the model oxidant 1,4-benzoquinone. However, in the enzymatic solution, these effects were abolished, and the ROS content remained stable and close to control levels, regardless of the presence of benzoquinone.

2. Reduced Data Variability in Biological Media: The presence of the enzymatic system significantly reduced the data spread and fluctuations in ROS measurements observed in non-biological aqueous suspen-

sions. The increase in the determination coefficients ( $R^2$ ) quantitatively confirms a more predictable and stable behavior of the nanocomposites in the biological environment.

3. No Direct Effect on Enzyme Function: The nanocomposites did not exhibit any significant inhibitory or activating effects on the bioluminescence enzymatic process itself, as indicated by the stable relative bioluminescence intensity ( $I^{rel}$ ). This suggests that the enzymes are not a primary target for these specific nanocomposites.

4. Divergence from Cellular Effects: Previous findings of bacterial toxicity and pro-oxidant activity suggest that the cellular context, particularly membrane interactions, is crucial for understanding nanoparticle bioactivity. The lack of effect on the isolated enzyme system contrasts with previous findings on bacterial cells, where similar nanocomposites (e.g.,  $\text{Fe}_3\text{O}_4$ -AA-MOF) demonstrated toxicity and pro-oxidant activity. This highlights a critical difference: the cellular membrane and internal metabolic processes likely play a decisive role in the biological activity and toxicity of these nanocomposites, which is not captured by acellular enzymatic assays. Hence, our current investigation should continue toward cellular processes using cells of luminous bacteria as example.

In summary, while the silica-magnetite nanocomposites can change ROS level in simple aqueous environments, their activity is effectively modulated and neutralized in an enzymatic system. The results suggest that for an accurate prediction of *in vivo* biological activity, particularly for applications like ferroptosis-based therapy, further investigation must focus on cellular models where membrane interactions and complex metabolic pathways determine the final biological outcome.

### Supporting Information

The Supporting Information is available free at <https://ejc.buketov.edu.kz/index.php/ejc/article/view/500/308>

### Funding

This research was funded by the Russian Science Foundation (Grant No. 25-25-20098, <https://rscf.ru/project/25-25-20098/>) and Krasnoyarsk Regional Fund of Science.

### Author Information\*

\*The authors' names are presented in the following order: First Name, Middle Name and Last Name

**Arina Gennadijevna Kicheeva** (*corresponding author*) — Engineer, Laboratory of Photobiology, Institute of Biophysics SB RAS, Federal Research Center “Krasnoyarsk Science Center SB RAS”, Akademgorodok Street, 50/50, 660036, Krasnoyarsk, Russia; e-mail: [khyzylsyg@mail.ru](mailto:khyzylsyg@mail.ru); <https://orcid.org/0000-0001-7816-4644>

**Ekaterina Sergeevna Sushko** — PhD in Biological Sciences, Junior Research Fellow, Laboratory of Photobiology, Institute of Biophysics SB RAS, Federal Research Center “Krasnoyarsk Science Center SB RAS”, Akademgorodok Street, 50/50, 660036, Krasnoyarsk, Russia; e-mail: [kkovel@yandex.ru](mailto:kkovel@yandex.ru); <https://orcid.org/0000-0002-4524-6413>

**Artur Albertovich Dzeranov** — Assistant Professor, Department 903 “Advanced Materials and Technologies for Aerospace Applications”, Moscow Aviation Institute (National Research University), Volokolamskoe shosse, 4, 125080, Moscow, Russia; Laboratory Research Assistant of Laboratory of Experimental Pathology, Sklifosovsky Research Institute for Emergency Medicine, Bolshaya Sukharevskaya Square, 3/21, 107045, Moscow, Russia; Junior Research Fellow of Laboratory of Metal Polymers, Federal Research Center of Problems of Chemical Physics and Medicinal Chemistry, Russian Academy of Sciences, Semenov avenue, 1, 142432, Chernogolovka, Moscow region, Russia; e-mail: [arturdzeranov99@gmail.com](mailto:arturdzeranov99@gmail.com); <https://orcid.org/0000-0003-3240-9321>

**Lyubov Sergeevna Bondarenko** — PhD in Chemical Sciences, Professor, Department 903 “Advanced Materials and Technologies for Aerospace Applications” Moscow Aviation Institute (National Research University), Volokolamskoe shosse, 4, 125080, Moscow, Russia; Sklifosovsky Research Institute for Emergency Medicine, Bolshaya Sukharevskaya Square, 3/21, 107045, Moscow, Russia; e-mail: [l.s.bondarenko92@gmail.com](mailto:l.s.bondarenko92@gmail.com); <https://orcid.org/0000-0002-3107-0648>

**Natalya Sergeevna Tropkaya** — PhD in Biological Sciences, Professor, Moscow Aviation Institute (National Research University), Volokolamskoe shosse, 4, 125080, Moscow, Russia; Leading Scientist of

Sklifosovsky Research Institute for Emergency Medicine, Bolshaya Sukharevskaya Square, 3/21, 107045, Moscow, Russia; Moscow Aviation Institute (National Research University), Volokolamskoe shosse, 4, 125080, Moscow, Russia; e-mail: [tropskayans@gmail.com](mailto:tropskayans@gmail.com); <https://orcid.org/0000-0001-5870-9483>

**Kamila Asylbekovna Kydralieva** — PhD in Chemical Sciences, Professor of Moscow Aviation Institute (National Research University), Volokolamskoe shosse, 4, 125080, Moscow, Russia; e-mail: [kydralievaka@mai.ru](mailto:kydralievaka@mai.ru); <https://orcid.org/0000-0002-4596-4140>

**Nadezhda Stepanovna Kudryasheva** — PhD in Physics and Mathematical Sciences, Leading Researcher, Laboratory of Photobiology, Institute of Biophysics SB RAS, Federal Research Center “Krasnoyarsk Science Center SB RAS”, Akademgorodok Street, 50/50, 660036, Krasnoyarsk, Russia; Professor of Department of Biophysics, School of Fundamental Biology and Biotechnology, Siberian Federal University, Svobodny Avenue, 79, 660041, Krasnoyarsk, Russia; e-mail: [n-qdr@yandex.ru](mailto:n-qdr@yandex.ru); <https://orcid.org/0000-0001-5315-8002>

#### Author Contributions

The manuscript was written through contributions of all authors. All authors have given approval to the final version of the manuscript. **CRedit**: **Arina Gennadievna Kicheeva** and **Ekaterina Sergeevna Sushko** investigation, formal analysis, visualization, writing — original draft, writing-review & editing; **Artur Albertovich Dzeranov** and **Lyubov Sergeevna Bondarenko** investigation, formal analysis, visualization, writing-review & editing; **Natalya Sergeevna Tropskaya** — validation, **Kamila Asylbekovna Kydralieva** and **Nadezhda Stepanovna Kudryasheva** conceptualization, formal analysis, project administration, supervision, validation, writing-original draft, writing-review & editing.

#### Conflicts of Interest

The authors have no conflicts of interest to declare.

#### References

- 1 Castro, E., Garcia, A.H., Gerardo, Z., & Echegoyen, L. (2017). Fullerenes in biology and medicine. *Journal of Materials Chemistry B*, 5(32), 6523–6535. <https://doi.org/10.1039/C7TB00855D>
- 2 Ghazanfari, M.R., Kashefi, M., Shams, S.F., & Jaafari, M.R. (2016). Perspective of Fe<sub>3</sub>O<sub>4</sub> nanoparticles role in biomedical applications. *Biochemistry Research International*, 2016, 7840161. <https://doi.org/10.1155/2016/7840161>
- 3 Kahru, A. & Mortimer, M. (2021). Advances in nanotoxicology: Towards enhanced environmental and physiological relevance and molecular mechanisms. *Nanomaterials*, 11(4), 919. <https://doi.org/10.3390/nano11040919>
- 4 Fraga García, P., Brammen, M., Wolf, M., Reinlein, S., Freiherr von Roman, M., & Berensmeier, S. (2015). High-gradient magnetic separation for technical scale protein recovery using low cost magnetic nanoparticles. *Separation and Purification Technology*, 150, 29–36. <https://doi.org/10.1016/j.seppur.2015.06.024>
- 5 Bauer, L.M., Situ, S.F., Griswold, M.A., & Samia, A.C. (2016). High-performance iron oxide nanoparticles for magnetic particle imaging — guided hyperthermia (hMPI). *Nanoscale*, 8(24), 12162–12169. <https://doi.org/10.1039/c6nr01877g>
- 6 An, Q., Sun, C., Li, D., Xu, K., Guo, J., & Wang, C. (2013). Peroxidase-like activity of Fe<sub>3</sub>O<sub>4</sub>@carbon nanoparticles enhances ascorbic acid-induced oxidative stress and selective damage to PC-3 prostate cancer cells. *ACS Applied Materials & Interfaces*, 5(24), 13248–13257. <https://doi.org/10.1021/am4042367>
- 7 Dixon, S.J., Lemberg, K.M., Lamprecht, M.R., Skouta, R., Zaitsev, E.M., Gleason, C.E., Patel, D.N., Bauer, A.J., Cantley, A.M., Yang, W.S., Morrison, B. 3rd., & Stockwell, B.R. (2012). Ferroptosis: an iron-dependent form of nonapoptotic cell death. *Cell*, 149(5), 1060–1072. <https://doi.org/10.1016/j.cell.2012.03.042>
- 8 He, Y.-J., Liu, X.-Y., Xing, L., Wan, X., Chang, X., & Jiang, H.-L. (2020). Fenton reaction-independent ferroptosis therapy via Glutathione and iron redox couple sequentially triggered lipid peroxide generator. *Biomaterials*, 241, 119911. <https://doi.org/10.1016/j.biomaterials.2020.119911>
- 9 Feng, L., Xie, R., Wang, C., Gai, S., He, F., Yang, D., Yang, P., & Lin, J. (2018). Magnetic targeting, tumor microenvironment-responsive intelligent nanocatalysts for enhanced tumor ablation. *ACS Nano*, 12(11), 11000–11012. <https://doi.org/10.1021/acsnano.8b05042>
- 10 Rossi, L.M., Costa, N.J.S., Silva, F.P., & Wojcieszak, R. (2014). Magnetic nanomaterials in catalysis: advanced catalysts for magnetic separation and beyond. *Green Chemistry*, 16(6), 2906. <https://doi.org/10.1039/C4GC00164H>
- 11 Wu, Y., Zhu, W.-H., Zakeeruddin, S.M., & Grätzel, M. (2015). Insight into D-A- $\pi$ -A structured sensitizers: A promising route to highly efficient and stable dye-sensitized solar cells. *ACS Applied Materials & Interfaces*, 7(18), 9307–9318. <https://doi.org/10.1021/acsaami.5b02475>









- 12 Carlos, L., Cipollone, M., Soria, D.B., Moreno, M.S., Ogilby, P.R., García Einschlag, F.S., & Mártire D.O. (2012). The effect of humic acid binding to magnetite nanoparticles on the photogeneration of reactive oxygen species. *Separation and Purification Technology*, 91, 23–29. <https://doi.org/10.1016/j.seppur.2011.08.028>
- 13 Nuzhina, J.V., Shtil, A.A., Prilepskii, A.Y., & Vinogradov, V.V. (2019). Preclinical evaluation and clinical translation of magnetite-based nanomedicines. *Journal of Drug Delivery Science and Technology*, 54, 101282. <https://doi.org/10.1016/j.jddst.2019.101282>
- 14 Brollo, M.E.F., Orozco-Henao, J.M., López-Ruiz, R., Muraca, D., Dias, C.S.B., Pirola, K.R., & Knobel, M. (2016). Magnetic hyperthermia in brick-like Ag@Fe<sub>3</sub>O<sub>4</sub> core-shell nanoparticles. *Journal of Magnetism and Magnetic Materials*, 397, 20–27. <https://doi.org/10.1016/j.jmmm.2015.08.081>
- 15 Kydralieva, K.A., Dzhardimalieva, G.I., Yurishcheva, A.A., & Jorobekova, S.J. (2016). Nanoparticles of magnetite in polymer matrices: synthesis and properties. *Journal of Inorganic and Organometallic Polymers and Materials*, 26, 1212–1230. <https://doi.org/10.1007/s10904-016-0436-1>
- 16 Ansari, L. & Malaekheh-Nikouei, B. (2017). Magnetic silica nanocomposites for magnetic hyperthermia applications. *International Journal of Hyperthermia*, 33(3), 354–363. <https://doi.org/10.1080/02656736.2016.1243736>
- 17 Taufiq, A., Nikmah, A., Hidayat, A., Sunaryono, S., Mufti, N., Hidayat, N., & Susanto, H. (2020). Synthesis of magnetite/silica nanocomposites from natural sand to create a drug delivery vehicle. *Heliyon*, 6(4), e03784. <https://doi.org/10.1016/j.heliyon.2020.e03784>
- 18 Sun, H., Xie, G., He, D., & Zhang, L. (2020). Ascorbic acid promoted magnetite Fenton degradation of alachlor: Mechanistic insights and kinetic modeling. *Applied Catalysis B: Environmental*, 267, 118383. <https://doi.org/10.1016/j.apcatb.2019.118383>
- 19 Jiang, W., Cai, Q., Xu, W., Yang, M., Cai, Y., Dionysiou, D.D., & O'Shea, K.E. (2014). Cr(VI) adsorption and reduction by humic acid coated on magnetite. *Environmental Science & Technology*, 48(14), 8078–8085. <https://doi.org/10.1021/es405804m>
- 20 Kicheeva, A.G., Sushko, E.S., Bondarenko, L.S., Kydralieva, K.A., Pankratov, D.A., Tropkaya, N.S., Dzeranov, A.A., Dzhardimalieva, G.I., Zarrelli, M., & Kudryasheva, N.S. (2023). Functionalized magnetite nanoparticles: characterization, bioeffects, and role of reactive oxygen species in unicellular and enzymatic systems. *International Journal of Molecular Sciences*, 24(2), 1133. <https://doi.org/10.3390/ijms24021133>
- 21 Rusdianso, B., & Basuki, R. (2020). Stability improvement of humic acid as sorbent through magnetite and chitin modification. *Jurnal Kimia Sains & Aplikasi*, 23(5), 152–159. <https://doi.org/10.14710/jksa.23.5.152-159>
- 22 Bondarenko, L., Baimuratova, R., Dzeranov, A., Pankratov, D., Kicheeva, A., Sushko, E., Kudryasheva, N., Valeev, R., Tropkaya, N., Dzhardimalieva, G., & Kydralieva, K. (2024). Fenton reaction-driven pro-oxidant synergy of ascorbic acid and iron oxide nanoparticles in MIL-88B(Fe). *New Journal of Chemistry*, 48(22), 10142–10160. <https://doi.org/10.1039/D4NJ00963K>
- 23 Joglekar, M., Rogers, R.A., Zhao, Y., & Trewyn, B.G. (2013). Interaction effects of mesoporous silica nanoparticles with different morphologies on human red blood cells. *RSC Advances*, 3(7), 2454–2461. <https://doi.org/10.1039/C2RA22264G>
- 24 Teng, W., Yang, Z., Wang, S., Xiong, D., Chen, Y., & Wu, Z. (2021). Toxicity evaluation of mesoporous silica particles Santa Barbara No. 15 amorphous in human umbilical vein endothelial cells: influence of particle morphology. *Journal of Applied Toxicology*, 41(9), 1467–1478. <https://doi.org/10.1002/jat.4137>
- 25 Yu, T., Malugin, A., & Ghandehari, H. (2011). Impact of silica nanoparticle design on cellular toxicity and hemolytic activity. *ACS Nano*, 5(7), 5717–5728. <https://doi.org/10.1021/nn2013904>
- 26 Ahmad, J., Ahamed, M., Akhtar, M.J., Alrokayan, S.A., Siddiqui, M.A., Musarrat, J., & Al-Khedhairi, A.A. (2012). Apoptosis induction by silica nanoparticles mediated through reactive oxygen species in human liver cell line HepG2. *Toxicology and Applied Pharmacology*, 259(2), 160–168. <https://doi.org/10.1016/j.taap.2011.12.020>
- 27 Hegde, B., Bodduluri, S.R., Satpathy, S.R., Alghsham, R.S., Jala, V.R., Uriarte, S.M., Chung, D.H., Lawrenz, M.B., & Haribabu, B. (2018). Inflammasome-independent leukotriene B<sub>4</sub> production drives crystalline silica-induced sterile inflammation. *The Journal of Immunology*, 200(10), 3556–3567. <https://doi.org/10.4049/jimmunol.1701504>
- 28 Hornung, V., Bauernfeind, F., Halle, A., Samstad, E.O., Kono, H., Rock, K.L., Fitzgerald, K.A., & Latz, E. (2008). Silica crystals and aluminum salts activate the NALP3 inflammasome through phagosomal destabilization. *Nature Immunology*, 9(8), 847–856. <https://doi.org/10.1038/ni.1631>
- 29 Muñoz-Planillo, R., Kuffa, P., Martínez-Colón, G., Smith, B.L., Rajendiran, T.M., & Núñez, G. (2013). K<sup>+</sup> efflux is the common trigger of NLRP3 inflammasome activation by bacterial toxins and particulate matter. *Immunity*, 38(6), 1142–1153. <https://doi.org/10.1016/j.immuni.2013.05.016>
- 30 Rossol, M., Pierer, M., Raulien, N., Quandt, D., Meusch, U., Rothe, K., Schubert, K., Schöneberg, T., Schaefer, M., Krügel, U., Smajilovic, S., Bräuner-Osborne, H., Baerwald, C., & Wagner, U. (2012). Extracellular Ca<sup>2+</sup> is a danger signal activating the NLRP3 inflammasome through G protein-coupled calcium sensing receptors. *Nature Communications*, 3, 1329. <https://doi.org/10.1038/ncomms2339>
- 31 Decan, N., Wu, D., Williams, A., Bernatchez, S., Johnston, M., Hill, M., & Halappanavar, S. (2016). Characterization of *in vitro* genotoxic, cytotoxic and transcriptomic responses following exposures to amorphous silica of different sizes. *Mutation Research/Genetic Toxicology and Environmental Mutagenesis*, 796, 8–22. <https://doi.org/10.1016/j.mrgentox.2015.11.011>
- 32 Jiang, L., Yu, Y., Li, Y., Yu, Y., Duan, J., Zou, Y., Li, Q., & Sun, Z. (2016). Oxidative damage and energy metabolism disorder contribute to the hemolytic effect of amorphous silica nanoparticles. *Nanoscale Research Letters*, 11(1), 57. <https://doi.org/10.1186/s11671-016-1280-5>



- 33 Nemmar, A., Beegam, S., Yuvaraju, P., Yasin, J., Shahin, A., & Ali, B.H. (2014). Interaction of amorphous silica nanoparticles with erythrocytes *in vitro*: role of oxidative stress. *Cellular Physiology and Biochemistry*, 34(2), 255–265. <https://doi.org/10.1159/000362996>
- 34 Vis, B., Hewitt, R.E., Faria, N., Bastos, C., Chappell, H., Pele, L., Jugdaohsingh, R., Kinrade, S.D., & Powell, J.J. (2018). Non-functionalized ultrasmall silica nanoparticles directly and size-selectively activate T cells. *ACS Nano*, 12(11), 10843–10854. <https://doi.org/10.1021/acsnano.8b03363>
- 35 Bulich, A.A., & Isenberg, D.L. (1981). Use of the luminescent bacterial system for the rapid assessment of aquatic toxicity. *ISA transactions*, 20(1), 29–33.
- 36 Girotti, S., Ferri, E.N., Fumo, M.G., & Maiolini, E. (2008). Monitoring of environmental pollutants by bioluminescent bacteria. *Analytica Chimica Acta*, 608(1), 2–29. <https://doi.org/10.1016/j.aca.2007.12.008>
- 37 Roda, A., Pasini, P., Mirasoli, M., Michelini, E., & Guardigli, M. (2004). Biotechnological application of bioluminescence and chemiluminescence. *Trends in Biotechnology*, 22(6), 295–303. <https://doi.org/10.1016/j.tibtech.2004.03.011>
- 38 Abbas, M., Adil, M., Ehtisham-ul-Haque, S., Munir, B., Yameen, M., Ghaffar, A., Shar, G.A., Tahir, M.A., & Iqbal, M. (2018). *Vibrio fischeri* bioluminescence inhibition assay for ecotoxicity assessment: A review. *Science of the Total Environment*, 626, 1295–1309. <https://doi.org/10.1016/j.scitotenv.2018.01.066>
- 39 Kudryasheva, N.S. (2006). Bioluminescence and exogenous compounds: Physico-chemical basis for bioluminescent assay. *Journal of Photochemistry and Photobiology B: Biology*, 83(1), 77–86. <https://doi.org/10.1016/j.jphotobiol.2005.10.003>
- 40 Kudryasheva, N., Vetrova, E., Kuznetsov, A., Kratasyuk, V., & Stom, D. (2002). Bioluminescence assays: Effects of quinones and phenols. *Ecotoxicology and Environmental Safety*, 53(2), 221–225. <https://doi.org/10.1006/eesa.2002.2214>
- 41 Kudryasheva, N., Kratasyuk, V., Esimbekova, E., Vetrova, E., Nemtseva, E., & Kudinova, I. (1998). Development of bioluminescent bioindicators for analysis of environmental pollution. *Field Analytical Chemistry & Technology*, 2(5), 277–280. [https://doi.org/10.1002/\(SICI\)1520-6521\(1998\)2:5%3C277::AID-FACT4%3E3.0.CO;2-P](https://doi.org/10.1002/(SICI)1520-6521(1998)2:5%3C277::AID-FACT4%3E3.0.CO;2-P)
- 42 Kratasyuk, V.A. (1990). Principles of luciferase biotesting. In B. Jezowska-Trzebiatowska, B. Kochel, J. Stawinski, & I. Strek (Eds.). *Biological Luminescence* (pp. 550–558). World Scientific, Singapore.
- 43 Vetrova, E.V., Kudryasheva, N.S., & Kratasyuk, V.A. (2007). Redox compounds influence on the NAD(P)H:FMN–oxidoreductase–luciferase bioluminescent system. *Photochemical & Photobiological Sciences*, 6(1), 35–40. <https://doi.org/10.1039/b608152e>
- 44 Bondarenko, L.S., Kovel, E.S., Kydraliev, K.A., Dzhardimalieva, G.I., Illés, E., Tombácz, E., Kicheeva, A.G., & Kudryasheva, N.S. (2020). Effects of modified magnetite nanoparticles on bacterial cells and enzyme reactions. *Nanomaterials*, 10(8), 1499. <https://doi.org/10.3390/nano10081499>
- 45 Kudryasheva, N.S., Kovel, E.S., Sachkova, A.S., Vorobeva, A.A., Isakova, V.G., & Churilov, G.N. (2017). Bioluminescent enzymatic assay as a tool for studying antioxidant activity and toxicity of bioactive compounds. *Photochemistry and Photobiology*, 93(2), 536–540. <https://doi.org/10.1111/php.12639>
- 46 Sachkova, A.S., Kovel, E.S., Churilov, G.N., Stom, D.I., & Kudryasheva, N.S. (2019). Biological activity of carbonic nanostructures—Comparison via enzymatic bioassay. *Journal of Soils and Sediments*, 19, 2689–2696. <https://doi.org/10.1007/s11368-018-2134-9>
- 47 Kovel, E.S., Kicheeva, A.G., Vnukova, N.G., Churilov, G.N., Stepin, E.A., & Kudryasheva, N.S. (2021). Toxicity and antioxidant activity of fullereneol C<sub>60,70</sub> with low number of oxygen substituents. *International Journal of Molecular Sciences*, 22(12), 6382. <https://doi.org/10.3390/ijms22126382>
- 48 Sushko, E.S., Vnukova, N.G., Churilov, G.N., & Kudryasheva, N.S. (2022). Endohedral Gd-containing fullereneol: Toxicity, antioxidant activity, and regulation of reactive oxygen species in cellular and enzymatic systems. *International Journal of Molecular Sciences*, 23(9), 5152. <https://doi.org/10.3390/ijms23095152>
- 49 Stepin, E.A., Sushko, E.S., Vnukova, N.G., Churilov, G.N., Rogova, A.V., Tomilin, F.N., & Kudryasheva, N.S. (2024). Effects of Endohedral Gd-containing fullereneols with a different number of oxygen substituents on bacterial bioluminescence. *International Journal of Molecular Sciences*, 25(2), 708. <https://doi.org/10.3390/ijms25020708>
- 50 Sies, H., & Jones, D.P. (2020). Reactive oxygen species (ROS) as pleiotropic physiological signalling agents. *Nature Reviews Molecular Cell Biology*, 21(7), 363–383. <https://doi.org/10.1038/s41580-020-0230-3>
- 51 Fan, J., Ren, D., Wang, J., Liu, X., Zhang, H., Wu, M., & Yang, G. (2020). Bruceine D induces lung cancer cell apoptosis and autophagy via the ROS/MAPK signaling pathway *in vitro* and *in vivo*. *Cell Death & Disease*, 11(2), 126. <https://doi.org/10.1038/s41419-020-2317-3>
- 52 Su, L.-J., Zhang, J.-H., Gomez, H., Murugan, R., Hong, X., Xu, D., Jiang, F., & Peng, Z.-Y. (2019). Reactive oxygen species-induced lipid peroxidation in apoptosis, autophagy, and ferroptosis. *Oxidative Medicine and Cellular Longevity*, 2019, 5080843. <https://doi.org/10.1155/2019/5080843>
- 53 Tavsán, Z., & Kayali, H.A. (2019). Flavonoids showed anticancer effects on the ovarian cancer cells: Involvement of reactive oxygen species, apoptosis, cell cycle and invasion. *Biomedicine & Pharmacotherapy*, 116, 109004. <https://doi.org/10.1016/j.biopha.2019.109004>
- 54 Fleury, C., Mignotte, B., & Vayssi  re, J.-L. (2002). Mitochondrial reactive oxygen species in cell death signaling. *Biochimie*, 84, 131–141. [https://doi.org/10.1016/S0300-9084\(02\)01369-X](https://doi.org/10.1016/S0300-9084(02)01369-X)
- 55 Hasanuzzaman, M., Bhuyan, M.H.M.B., Parvin, K., Bhuiyan, T.F., Anee, T.I., Nahar, K., Hossen, M.S., Zulfiqar, F., Alam, M.M., & Fujita, M. (2020). Regulation of ROS metabolism in plants under environmental stress: A review of recent experimental evidence. *International Journal of Molecular Sciences*, 21(22), 8695. <https://doi.org/10.3390/ijms21228695>

- 56 Kicheeva, A.G., Sushko, E.S., Bondarenko, L.S., Baimuratova, R.K., Kydralieva, K.A., Schwaminger, S.P., Prassl, R., Tropkaya, N.S., Dzhardimalieva, G.I., Smirnykh, D.V., Martynova, A.A., & Kudryasheva, N.S. (2024). Cytotoxic and radical activities of metal-organic framework modified with iron oxide: Biological and physico-chemical analyses. *Chemico-Biological Interactions*, 399, 111150. <https://doi.org/10.1016/j.cbi.2024.111150>
- 57 Li, Y., Zhu, T., Zhao, J., & Xu, B. (2012). Interactive enhancements of ascorbic acid and iron in hydroxyl radical generation in quinone redox cycling. *Environmental Science & Technology*, 46(18), 10302–10309. <https://doi.org/10.1021/es301834r>
- 58 Wolf, M., Kappler, A., Jiang, J., & Meckenstock, R.U. (2009). Effects of humic substances and quinones at low concentrations on ferrihydrite reduction by *Geobacter metallireducens*. *Environmental Science & Technology*, 43(15), 5679–5685. <https://doi.org/10.1021/es803647r>
- 59 Visser, S.A. (1964). Oxidation-reduction potentials and capillary activities of humic acids. *Nature*, 204, 581. <https://doi.org/10.1038/204581a0>
- 60 Shnoll S.E. (2009). *Cosmophysical factors in random processes*. Svenska fysikarkivat. [https://digitalphysics.ru/pdf/Kaminskii\\_A\\_V/shnoll2009ru.pdf](https://digitalphysics.ru/pdf/Kaminskii_A_V/shnoll2009ru.pdf) [in Russian].
- 61 Trachootham, D., Alexandre, J., & Huang, P. (2009). Targeting cancer cells by ROS-mediated mechanisms: a radical therapeutic approach? *Nature Reviews Drug Discovery*, 8(7), 579–591. <https://doi.org/10.1038/nrd2803>
- 62 Hastings, J.W., & Gibson, Q.H. (1963). Intermediates in the bioluminescent oxidation of reduced flavin mononucleotide. *Journal of Biological Chemistry*, 238(7), 2537–2554. [https://doi.org/10.1016/S0021-9258\(19\)68004-X](https://doi.org/10.1016/S0021-9258(19)68004-X)
- 63 Lee, J., Müller, F., & Visser, A.J.W.G. (2018). The sensitized bioluminescence mechanism of bacterial luciferase. *Photochemistry and Photobiology*, 95(3), 679–704. <https://doi.org/10.1111/php.13063>



Makhliyo M. Kuzieva<sup>1</sup> , Fayruza M. Urishova<sup>1</sup> , Abdumutolib A. Atakhanov<sup>1\*</sup> ,  
Nurbek Sh. Ashurov<sup>1</sup> , Sayyora Sh. Rashidova<sup>1</sup> , Dmitriy I. Shiman<sup>2</sup> ,  
Sergei V. Kostjuk<sup>3</sup> , Saewon Kang<sup>4</sup> 

<sup>1</sup>*Institute of Polymer Chemistry and Physics, Tashkent, Uzbekistan;*

<sup>2</sup>*Research Institute for Physical Chemical Problems of the Belarusian State University, Minsk, Belarus;*

<sup>3</sup>*Sorbonne Universite, CNRS, Institut Parisien de Chimie Moleculaire, Sorbonne, France;*

<sup>4</sup>*Korea Research Institute of Chemical Technology, Daejeon, South Korea*

(\*Corresponding author's e-mail: [a-atakhonov@yandex.com](mailto:a-atakhonov@yandex.com))

## Potassium Permanganate–Oxidized Nanocellulose: Structural Features and Rheological Performance for Advanced Applications

The development of environmentally friendly strategies for nanocellulose modification is crucial for advancing biomedical materials. Traditional oxidation methods often involve costly or toxic reagents, limiting large-scale use. This study addresses this by preparing oxidized nanocellulose (ONC) from microcrystalline cellulose using an eco-friendly acidic potassium permanganate (KMnO<sub>4</sub>) oxidation method to introduce surface carboxyl groups. Structural and morphological changes were characterized through FTIR, XRD, SEM, and DLS analyses, which confirmed successful oxidation, retained fibrillar morphology, and altered crystallinity and surface charge. Hydrogel formulations were developed from ONC suspensions, and their rheological properties were assessed through frequency and amplitude sweeps. FTIR spectra confirmed the introduction of carboxyl groups, while XRD revealed reduced crystallinity and lattice expansion with oxidation. DLS demonstrated narrower size distributions at intermediate oxidation times, indicating improved dispersion stability. SEM images confirmed retention of fibrous morphology with reduced fibril widths. Rheological tests showed that ONC hydrogels exhibited shear-thinning and gel-like behavior ( $G' > G''$ ), displaying the highest storage modulus and broadest linear viscoelastic region, consistent with a strong and stable gel network. ONC-based hydrogels show significant promise for biomedical applications, including mucoadhesive drug delivery, wound healing, and tissue engineering.

**Keywords:** oxidized nanocellulose, microcrystalline cellulose, permanganate oxidation, carboxyl functionalization, structural characterization, hydrogel, rheological properties, drug delivery systems

### Introduction

Cellulose, the most abundant biopolymer on Earth, has attracted considerable attention in recent years due to its renewable origin, biodegradability, and versatility in designing advanced functional materials [1]. Chemical modification of cellulose, particularly microcrystalline cellulose (MCC), offers powerful opportunities to tailor its physicochemical properties and expand its applications in biomedicine, drug delivery, and environmental technologies [2, 3]. Among various modification strategies, oxidation is especially important because it introduces functional groups such as carboxyl and aldehyde, thereby enhancing the reactivity, dispersibility, and binding capacity of cellulose derivatives [4, 5].

Conventional oxidants, including 2,2,6,6-tetramethylpiperidine-1-oxyl (TEMPO) [6], sodium periodate (NaIO<sub>4</sub>) [7], potassium dichromate [8], and ammonium persulfate (APS) [9], have been widely employed to prepare carboxylated and dialdehyde nanocellulose. Despite their effectiveness, these methods often involve expensive reagents and environmentally unfriendly processes.

Consequently, attention has shifted toward greener oxidation routes to obtain oxidized nanocellulose (ONC), which has shown great promise for tissue engineering, wound healing [10], mucoadhesive drug delivery [11, 12], and biosensing applications [13]. The structural and functional properties of ONC are highly dependent on the oxidation pathway, and different oxidizing systems have been explored to tailor these features [14].

In this context, potassium permanganate (KMnO<sub>4</sub>) in acidic conditions represents a strong yet relatively eco-friendly oxidizing agent. It selectively oxidizes the C6-hydroxyl group of anhydroglucose units, generating carboxyl and carbonyl functionalities [15]. This method is attractive because it is cost-effective, simple to

perform, and produces less toxic by-products compared to chromium-based oxidations [16].  $\text{KMnO}_4$  oxidation has been reported to yield surface-functionalized cellulose with improved dispersibility and higher negative surface charge, properties that are crucial for electrostatic interactions in biomedical formulations.

Furthermore, ONC produced by  $\text{KMnO}_4$  oxidation has been evaluated for its rheological behavior, which is essential for designing injectable hydrogels, thickeners, and bioinks for 3D printing. The entanglement of nanofibrils or nanocrystals governs the flow properties, typically resulting in shear-thinning and viscoelastic responses depending on the oxidation degree and concentration [17, 18]. However, while TEMPO- or periodate-based methods have been extensively studied, the use of acidic  $\text{KMnO}_4$  oxidation remains underexplored for producing ONC with controlled rheological and structural characteristics [19–21].

Although  $\text{KMnO}_4$  oxidation of cellulose has been reported previously, studies at the nanoscale level remain scarce. The present findings highlight the significance of acidic  $\text{KMnO}_4$  oxidation as a cost-effective and environmentally benign pathway for introducing functional groups into nanocellulose. This strategy opens promising opportunities for designing functional cellulose-based materials with tailored structural and rheological properties, particularly in the fields of biomedicine, environmental remediation, and advanced industrial applications.

Therefore, the aim of this work was to synthesize oxidized nanocellulose via acidic potassium permanganate oxidation and to investigate its structural features and rheological properties.

## Experimental

### *Chemicals and Materials*

This study used MCC (DP = 240, CrI = 72 %) was produced from cotton cellulose according to the protocol described previously [22]. Potassium permanganate ( $\text{KMnO}_4$ , 99.5 wt%) and sulfuric acid ( $\text{H}_2\text{SO}_4$ , 98.0 wt%) were purchased from Sigma-Aldrich Chemical Co. Ltd. (Tianjin, China). Hydrogen peroxide ( $\text{H}_2\text{O}_2$ ) and sodium hydroxide ( $\text{NaOH}$ , 98.0 %) were obtained from Daejung Chemicals (South Korea). All reagents were of analytical grade and used without further purification. Deionized water was employed throughout all experiments unless otherwise stated.

### *Preparation of Oxidized Nanocellulose (ONC)*

ONC was synthesised in an aqueous medium using potassium permanganate under acidic conditions, following a published method with slight modifications [8]. In a three-neck flask, 3.0 g MCC was dispersed in 50 mL of deionized water and sonicated for 20 min. The suspension pH was adjusted to 2.0 with sulphuric acid, after which 2.34 g  $\text{KMnO}_4$  was added under continuous magnetic stirring at 50 °C in a glycerin bath. The reaction was carried out for 2 h (sample ONC-2), 3 h (sample ONC-3) and 4 h (sample ONC-4) under nitrogen bubbling. After completion, the reaction was quenched with hydrogen peroxide. The product was centrifuged (8000 rpm, 15 min) and repeatedly washed with deionized water until the pH reached 5. The ONC suspension was then dialyzed against 4.5 L deionised water with 6 water changes over 72 h. The final product was freeze-dried using HetoPowerDry LL3000 Freeze Dryer (Thermo Scientific, UK).

### *Preparation of ONC-Based Hydrogels*

Hydrogels were prepared from oxidized nanocellulose formulations (ONC-2, ONC-3, ONC-4). A 2 %  $\text{NaOH}$  solution (30 mL) was placed in a three-neck flask covered with aluminum foil, and 3 g ONC was added. The mixture was kept under controlled thawing for 4 h. The samples were subsequently subjected to repeated freeze–thaw cycles until gelation occurred. The resulting gels were washed with distilled water, centrifuged four times (10 min each), and stored at 4 °C prior to use.

### *Characterization Methods*

#### *FTIR*

The FTIR spectrometer “Inventio-S” (Bruker) was used and FTIR spectra were recorded in 400–4000  $\text{cm}^{-1}$  wavenumber range with a resolution of 2  $\text{cm}^{-1}$  and 32 scans at a temperature of 25 °C. All samples were finely ground, dried at 60 °C for 12 h, and pressed into KBr pellets (1 wt%) before analysis. Software of OPUS was applied to determine the peaks at specific points.

#### *Ultraviolet (UV) Spectroscopy*

UV spectra of samples were recorded with a Specord 210 UV-spectrophotometer (Analytic Jena, Germany) by using quartz cells 1 cm in diameter and 1 nm slit; the scanning range of measurement was 190–

1000 nm, a scanning speed was 5 nm/s. The aqueous ONC suspensions (0.05 wt%) were ultrasonically dispersed for 15 min prior to measurement.

#### *Atomic force microscopy (AFM)*

Morphological studies of ONC were performed by using AFM Agilent 5500 (Agilent, USA). The silicon cantilevers with a stiffness of  $9.5 \text{ N/m}^2$  were used and the frequency was 262 kHz. The AFM scan area ( $x-y-z$ ) was  $3.0-3.0-1 \text{ }\mu\text{m}$ .

#### *Wide-Angle X-ray diffraction*

XRD studies were carried out using XRD Miniflex 600 (Rigaku, Japan) with monochromatic  $\text{CuK}\alpha$  radiation isolated by a nickel filter with a wavelength of  $1.5418 \text{ }\text{\AA}$  at 40 kV and the current strength of 15 mA. The spectrum was recorded in the interval  $2\theta = 5^\circ-40^\circ$ . The air-dried ONC powders were gently ground, mounted on zero-background glass slides, and analyzed under identical sample thickness and humidity conditions. The data processing of experimental diffraction patterns, peak deconvolution, describing the peaks used by Miller indices, peak shape, and the basis for the amorphous contribution were conducted using the software "SmartLab Studio II" and data base PDF-2 (2020 Powder diffraction file, ICDD).

#### *Scanning Electron Microscopy (SEM)*

Scanning electron microscopy studies were performed using SEM equipment Veritas-3100 (Korea). Magnification of the device  $\times 10-300000$ , voltage 200–300 V, maximum scanning area ( $x-y-z$ ) is  $120\div 120\div 65 \text{ }\mu\text{m}$ . ONC powder samples obtained by freeze-drying were mounted on double-sided conductive carbon tape and subsequently coated with a thin carbon layer (15–20 nm) using a vacuum sputter coater. SEM images were obtained at an accelerating voltage of 10 kV and a working distance of 10.6 mm.

#### *Dynamic Light Scattering (DLS)*

Particle size distribution was measured on a Photocor Compact (Photocor, Russia) at 298 K, using a 635.6 nm semiconductor laser (25 mW). The ONC suspensions were prepared at 0.01 wt%, sonicated for 10 min to disperse aggregates, and filtered through a  $0.45 \text{ }\mu\text{m}$  PTFE membrane before measurement at  $25^\circ\text{C}$ .

#### *Determination of Carboxyl Group Content*

The content of carboxyl groups (mmol/g) was determined by conductometric titration on a Mettler Toledo conductometer (Switzerland). 50 mg ONC was dispersed in 20 mL of 0.01M HCl solution for 15 minutes by using magnetic stirring. Then, the suspension was titrated with a 0.01 M NaOH solution. The number of carboxyl groups was calculated using an equation [23] and expressed in mmol/g. Each batch was titrated three times.

#### *Rheological Measurements*

Rheological tests of the hydrogels were carried out using a rotational Rheometer MCR-92 (AntonPaar) equipped with a "cone-plane" type measuring unit (25 mm diameter /  $2^\circ$  angle) at a temperature of  $25^\circ\text{C}$ , shear rate of  $0.1-4400 \text{ s}^{-1}$ , with 20 s exposure at each step.

#### *Statistical Analysis*

All experimental data were collected in triplicates and data expressed as average  $\pm$  standard deviation. Data were compared using a one-way ANOVA with post-Bonferroni test using GraphPad Prism 5.04 (GraphPad Software Inc.)

### *Results and Discussion*

The ONCs were successfully obtained through acidic potassium permanganate oxidation combined with mild mechanical treatment. The reaction pathway suggests that  $\text{MnO}_4^-$  ions are initially reduced to  $\text{Mn}^{2+}$  via oxidation of the C6-OH groups of cellulose. Excess  $\text{MnO}_4^-$  is subsequently reduced to colloidal  $\text{MnO}_2$ , which acts as a self-catalyst, thereby enhancing the oxidative capacity of the system (Fig. 1).

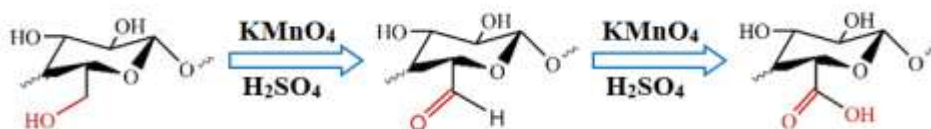


Figure 1. Schematic representation of ONC preparation via potassium permanganate oxidation

Upon completion, the reaction was quenched with hydrogen peroxide, which reduced  $\text{MnO}_2$  back to colorless  $\text{Mn}^{2+}$ . At this stage, the suspension of cellulose nanostructures rapidly turned white, indicating the end of oxidation. The  $\text{Mn}^{2+}$  ions were efficiently removed during the repeated washing steps. A comparable carboxylation mechanism has been described for oxidation of cellulose nanofibrils [24]. The oxidation of MCC under these conditions proceeds heterogeneously, with the supramolecular organization of cellulose strongly influencing the reaction course [8]. In particular, the C6–OH groups were selectively converted into C6–COOH functionalities, involving electron transfer, proton abstraction, and dehydration steps. This transformation substantially modifies the surface chemistry, charge density, and dispersibility of nanocellulose.

Conductometric titration confirmed that the oxidized samples contained 1.11 mmol/g of carboxyl groups. The successful introduction of these functionalities was further verified by FTIR spectroscopy (Fig. 2).

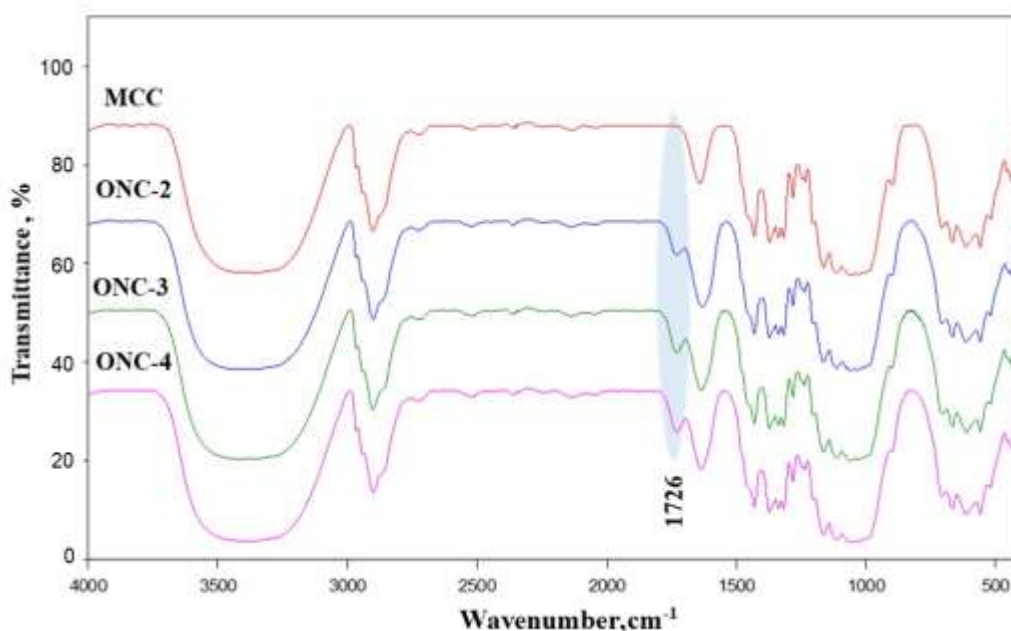


Figure 2. FTIR spectra of MCC, ONC-2, ONC-3 and ONC-4

Comparison of MCC and ONC spectra revealed a broad absorption band near  $3415\text{ cm}^{-1}$ , attributed to O–H stretching vibrations. In ONC, this band became sharper and more intense, reflecting a decrease in the number of hydroxyl groups engaged in hydrogen bonding. Stretching vibrations of C–H bonds from methylene and methine groups were detected in the  $2800\text{--}2900\text{ cm}^{-1}$  region, while a band at  $1632\text{ cm}^{-1}$  corresponded to absorbed water, which cannot be fully removed due to strong cellulose–water interactions.

Additional peaks at  $1430\text{ cm}^{-1}$ ,  $1335\text{--}1375\text{ cm}^{-1}$ ,  $1202\text{ cm}^{-1}$ , and  $1075\text{--}1113\text{ cm}^{-1}$  were assigned to bending vibrations of  $-\text{CH}-$ ,  $-\text{CH}_2-$ ,  $-\text{OH}$ , and  $-\text{CO}$  groups, together with stretching vibrations of C–O bonds and pyranose rings. Importantly, a new and distinct absorption band at  $1726\text{ cm}^{-1}$  was observed in the ONC spectrum, corresponding to C=O stretching vibrations of carboxyl groups, confirming that the primary hydroxyls at the C6 position were oxidized into carboxyl functionalities [25].

The intensity of the C=O band increased with oxidation time: ONC-4 displayed a stronger peak compared to ONC-2, indicating a higher degree of oxidation. Concurrently, the  $1425\text{ cm}^{-1}$  band ( $-\text{CH}_2-$  bending) decreased, while the  $1372\text{ cm}^{-1}$  band (out-of-plane  $-\text{CH}_2-$  vibrations) became more pronounced. These spectral changes suggest a reduction in crystallinity, which was further corroborated by XRD analysis (Fig. 4).

Nevertheless, the persistence of characteristic pyranose ring vibrations confirms that the cellulose backbone remained intact, and oxidation occurred predominantly at the C6 hydroxyl position.

UV–Vis spectroscopic analysis (Fig. 3) revealed characteristic absorption bands for ONC in the 196–202 nm region, associated with electronic transitions of carbonyl-containing groups (aldehydes and carboxyls). A weak shoulder near 230 nm is attributed specifically to C=O transitions of aldehyde functionalities.

The spectra of ONC-2 displayed significantly lower absorbance compared to ONC-3 and ONC-4 across the investigated wavelength range, indicating a lower degree of oxidation and incomplete nanofibrillation. In contrast, ONC-3 and ONC-4 exhibited nearly overlapping spectra with the highest absorbance intensities, consistent with a greater oxidation extent, higher surface charge density, and enhanced colloidal stability. The stronger short-wavelength absorbance in these samples also suggests finer dispersion and reduced particle size, due to increased light scattering in the colloidal state.

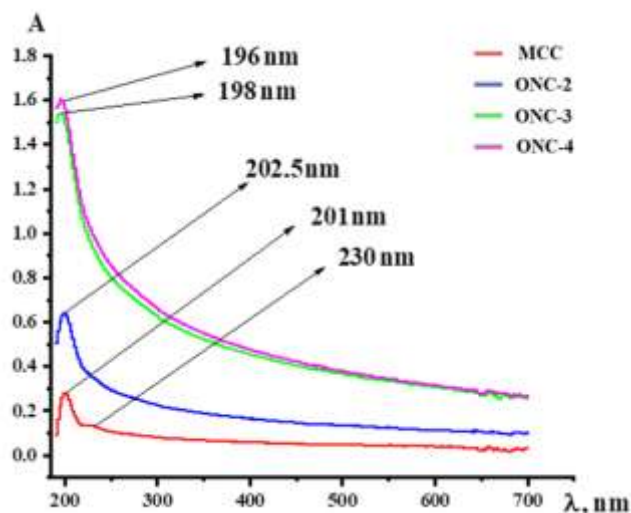


Figure 3. UV spectra of MCC, ONC-2, ONC-3 and ONC-4

For comparison, MCC showed the weakest absorption response, as expected, owing to the absence of UV-active carbonyl groups and the tendency to form larger aggregates, which exhibit limited Rayleigh scattering and lower overall absorbance.

X-ray diffraction (XRD) analysis was performed to evaluate the effect of potassium permanganate oxidation on the crystallinity of MCC (Fig. 4). The diffractograms of MCC and oxidized nanocellulose samples (ONC-2, ONC-3, ONC-4) all exhibited the characteristic reflections of cellulose I $\beta$ , with prominent peaks at  $2\theta \approx 14\text{--}16^\circ$  (1–10, 110),  $22\text{--}23^\circ$  (200), and  $34\text{--}35^\circ$  (004). The preservation of these reflections indicates that the native cellulose I lattice was retained after oxidation, consistent with previous reports on TEMPO- and periodate-oxidized cellulose nanostructures [26].

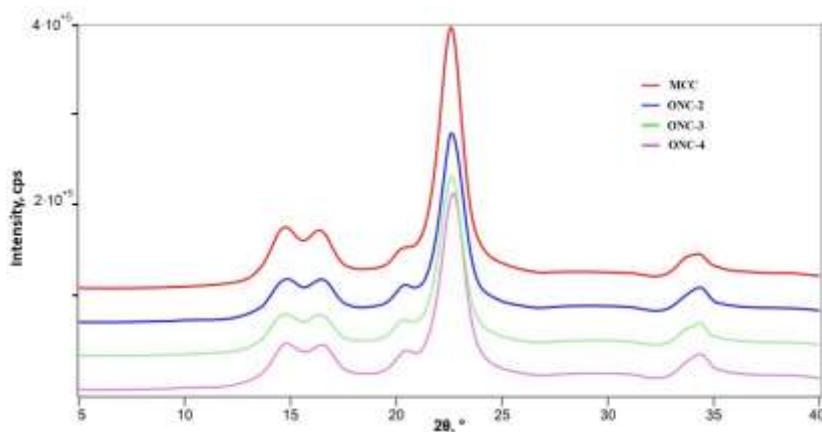


Figure 4. X-ray diffraction patterns of MCC, ONC-2, ONC-3 and ONC-4

MCC displayed the most intense and sharp (200) reflection, indicative of a high degree of crystalline order. With increasing oxidation time, the intensity of the crystalline peaks decreased progressively (ONC-2>ONC-3>ONC-4) and reflections became broader, confirming a gradual reduction in crystallinity and disruption of long-range order. This loss of crystallinity is attributed to the incorporation of carboxyl and aldehyde groups, which disturb inter- and intramolecular hydrogen bonding within the native lattice [27].

The (200) reflection shifted slightly toward lower  $2\theta$  values with increasing oxidation time. Calculated d-spacings expanded from  $\sim 3.90$  Å (MCC) to  $\sim 4.00$  Å (ONC-4), suggesting that bulky, hydrophilic groups introduced at the C6 hydroxyl (and partially at C2/C3) increase the intersheet separation along the a-axis of the monoclinic unit cell. This expansion is consistent with electrostatic repulsion and hydration effects previously reported in carboxylated cellulose nanofibers [28].

Analysis of the full width at half maximum (FWHM) of the (200) peak revealed progressive broadening, corresponding to reduced crystallite dimensions. Scherrer analysis showed a decrease in crystallite size from  $\sim 7$ – $8$  nm (MCC) to  $\sim 4$  nm (ONC-4), consistent with fragmentation of crystalline domains. Such reduction reflects enhanced lattice disorder and partial depolymerization, phenomena also observed in TEMPO-oxidized cellulose fibrils [29].

Overall, the data indicate that oxidation produces two concurrent structural effects: (i) expansion of the cellulose lattice, due to functional group substitution and hydration, and (ii) reduction of crystallite size, due to chain scission and disorder. At higher oxidation levels (ONC-4), these effects accumulate, yielding a material with predominantly amorphous character and only residual crystalline order.

Importantly, the progressive decline in crystallinity correlates with the rheological performance of ONC-based hydrogels. MCC, although highly crystalline, exhibited weak gel strength due to poor interparticle interactions. ONC-3, with moderate crystallinity and sufficient functionalization, provided the best balance between structural order and surface activity, resulting in optimal network interactions and enhanced mechanical resilience. In contrast, ONC-4 showed extensive lattice disruption, consistent with its reduced storage modulus and premature yielding. These findings highlight that an intermediate oxidation state (ONC-3) achieves the most favorable structural balance for hydrogel performance.

Dynamic light scattering (DLS) analysis revealed clear differences in the particle size distribution of MCC and ONC samples as a function of oxidation time (Fig. 5). Native MCC exhibited a broad and polydisperse profile, with a main population in the 100–500 nm range and a secondary fraction extending into the micron scale. This heterogeneity reflects the tendency of MCC to agglomerate due to limited dispersibility.

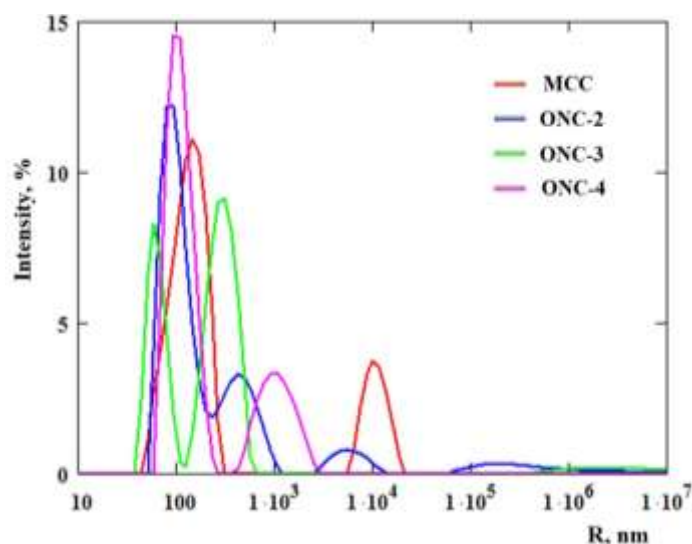


Figure 5. DLS size distributions of MCC, ONC-2, ONC-3 and ONC-4

Oxidation induced a pronounced shift toward smaller and narrower particle size distributions, confirming that the introduction of carboxyl groups enhanced electrostatic stabilization. ONC-2 showed two populations: a dominant peak near  $\sim 200$  nm and a minor fraction above  $1$   $\mu\text{m}$ , indicating partial fibril disintegration with residual aggregates. ONC-3 displayed the sharpest and most intense peak at 100–150 nm, with minimal larger fractions, signifying efficient oxidation, high colloidal stability, and uniform dispersion.



In contrast, ONC-4 exhibited a bimodal distribution with a primary peak near 100 nm and a secondary fraction above 500 nm. This suggests that prolonged oxidation induced partial re-aggregation, likely due to excessive chain scission and weakening of the fibrillar framework, which compromised steric stabilization. Such behavior is consistent with FTIR and XRD data, where ONC-4 showed pronounced lattice disruption and higher densities of oxidized groups.

These results underscore the close link between oxidation degree and colloidal stability. Moderate oxidation (ONC-3) produced the most homogeneous nanoparticle distribution, while insufficient oxidation (ONC-2) left aggregates intact and over-oxidation (ONC-4) introduced heterogeneity through structural degradation. These trends align with previous reports on oxidized nanocellulose dispersions, where carboxylation improves stability up to an optimal level, beyond which colloidal uniformity decreases [28].

It should be noted that the dynamic light scattering (DLS) technique has certain limitations when applied to anisotropic nanocellulose systems. As emphasized by Filippov et al. [30], the DLS method assumes that particles are spherical and isotropic scatterers. In the case of fibrillar materials such as ONS, this assumption may lead to an overestimation of the hydrodynamic diameter and an inaccurate interpretation of the size distribution. Moreover, the presence of polydisperse populations, inter-fibrillar interactions, and orientation effects can significantly influence the intensity-weighted size values obtained by DLS. Therefore, the DLS data in this study should be interpreted as providing a relative measure of colloidal dispersion quality rather than an absolute representation of particle dimensions.

The morphological characteristics of ONC were investigated by SEM, which provided detailed visualization of particle shape, size distribution, and surface structure. Due to their high surface energy, ONC particles exhibited a marked tendency to agglomerate, forming clusters at both the nano- and microscale.

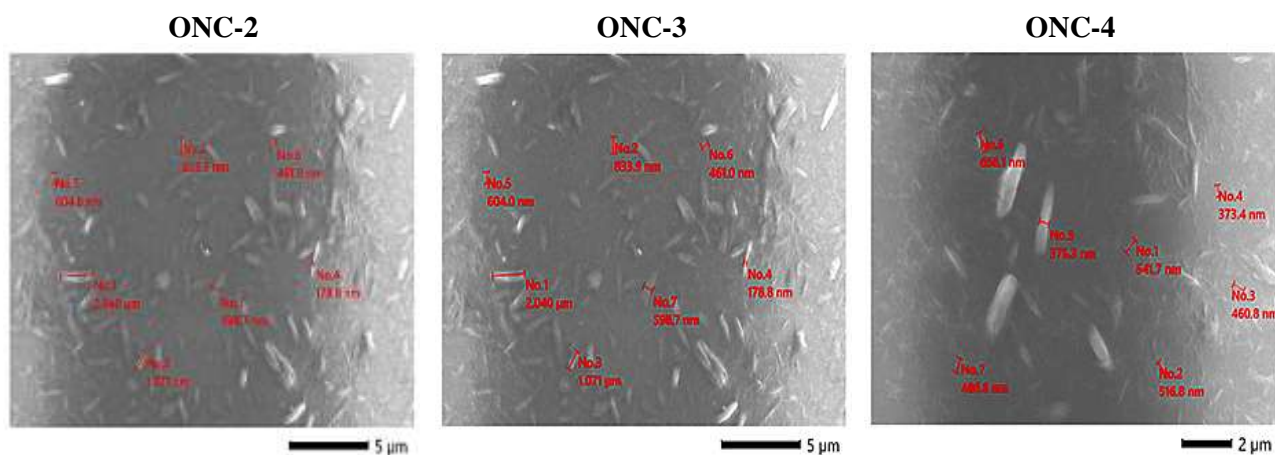


Figure 6. SEM images of ONC-2, ONC-3 and ONC-4

SEM analysis demonstrated a clear relationship between oxidation time and particle dimensions. With prolonged reaction duration, the average width of ONC fibrils progressively decreased from ~12–20 nm to ~3–5 nm, while maintaining a fibrous morphology. The fibril lengths were in the range of 200–500 nm (Fig. 6). Extended oxidation led to the formation of finer and more uniform nanofibers, resulting in a more homogeneous nanoscale network.

The successful fabrication of hydrogels and cryogels from ONC highlights its versatility as a functional biopolymer for biomedical applications. As illustrated in Figure 7, ONC was dissolved in an alkaline medium (2 % NaOH), followed by controlled freezing and freeze-drying, yielding three-dimensional porous cryogels. This behavior parallels earlier findings on TEMPO-oxidized cellulose, which also forms robust and morphologically controlled hydrogels and films [27].

The freezing-induced ice-templating process generated a distinctive porous architecture, ideal for water uptake, solute diffusion and etc. The introduction of carboxyl and carbonyl groups in ONC enhanced solubility. Hydrogen bonding plays a central role in stabilization: intermolecular bonds contribute elasticity and resilience, while intramolecular bonds ensure structural integrity. This dual mechanism yields scaffolds with high porosity, and tunable swelling capacity. SEM image confirmed a sponge-like porous network (Fig. 7), consistent with previous reports on nanocellulose-based aerogels and hydrogels [31].

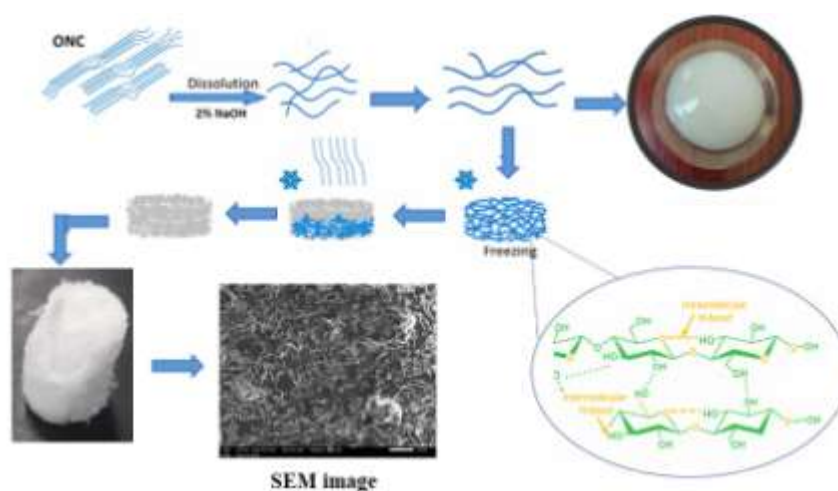


Figure 7. Schematic illustration of the preparation of ONC-based hydrogels and cryogels

Importantly, these ONC-based hydrogels were fabricated without synthetic crosslinkers, providing an eco-friendly and inherently biocompatible route to advanced biomaterials [32].

Rheological characterization provides essential insights into the mechanical integrity and stability of hydrogels [33]. Both frequency sweep and amplitude sweep experiments were conducted to evaluate the viscoelastic performance of ONC hydrogels. These tests allow differentiation between solid-like and liquid-like behaviour, determination of the linear viscoelastic region (LVE), and identification of the yield point, where the internal network collapses (Fig. 8).

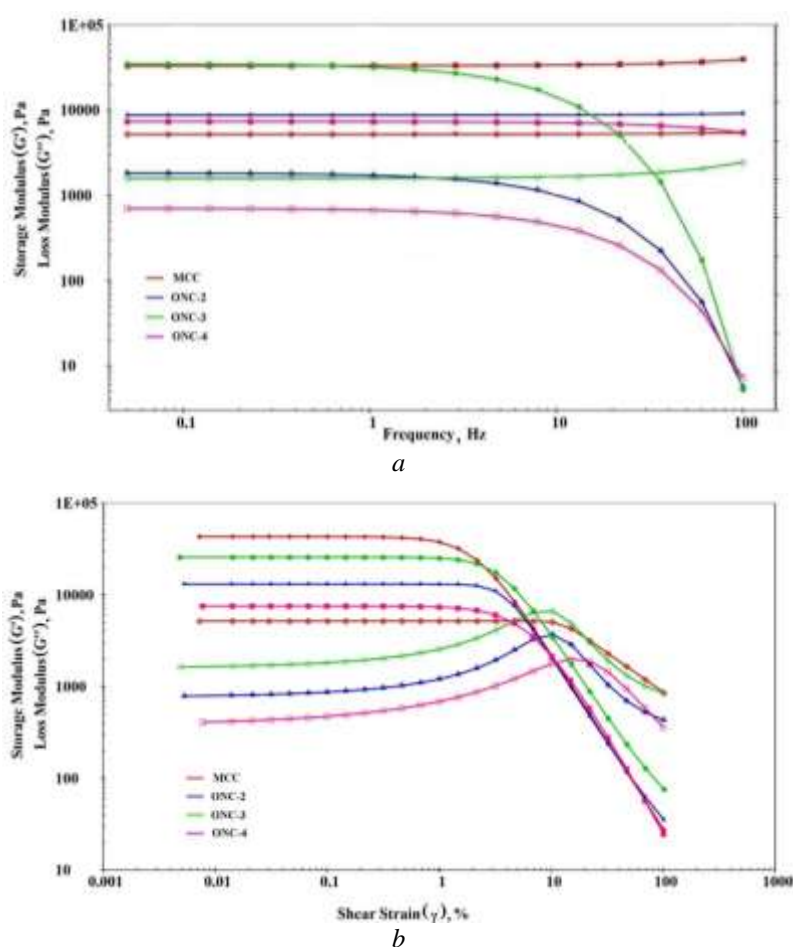


Figure 8. Frequency- (a) and amplitude- (b) sweep curves of ONC hydrogels

In frequency sweeps, a stable gel is defined by a frequency-independent storage modulus ( $G'$ ) dominating over the loss modulus ( $G''$ ). All ONC hydrogels exhibited  $G' > G''$  throughout the frequency range, confirming their predominantly elastic character. In contrast, MCC showed a relatively high damping factor ( $\tan \delta \approx 0.9$ ), consistent with weak elasticity and viscous predominance. Oxidation markedly enhanced network strength: ONC-2 displayed improved elasticity, while ONC-3h achieved the highest  $G'$  values ( $10^4$ – $10^5$  Pa) and the lowest  $\tan \delta$  ( $\sim 0.1$ – $0.2$ ), characteristic of a strong, stable gel network stabilized by carboxyl groups. ONC-4, however, exhibited declining  $G'$  at higher frequencies, indicative of network fatigue and partial breakdown caused by cellulose chain scission during prolonged oxidation.

Amplitude sweeps further clarified the strain-dependent stability of gels. Within the LVE, both  $G'$  and  $G''$  remained constant, reflecting intact networks; beyond this region,  $G'$  decreased and eventually crossed  $G''$  at the yield point. MCC hydrogels displayed a narrow LVE and early yielding ( $\gamma \approx 15$ – $20$  %), highlighting poor resistance to deformation. ONC-2 extended the LVE slightly ( $\sim 20$ – $25$  %), whereas ONC-3 showed the broadest LVE ( $\sim 25$ – $30$  %) and the highest  $G'$  plateau, exemplifying a “true gel” with excellent stability under deformation and strong cohesive forces. ONC-4 again yielded earlier ( $\sim 15$ – $20$  %) with reduced moduli, confirming the detrimental effects of excessive oxidation.

Taken together, both rheological tests demonstrate that ONC-3 hydrogels strike the optimal balance between functionalization and structural integrity. They combine frequency-independent elasticity, a broad LVE, and high yield strain — hallmarks of robust gel networks. In contrast, ONC-2 and ONC-4 deviate from this profile due to insufficient and excessive oxidation, respectively. These findings are highly relevant for the design of nanocellulose-based hydrogels tailored to biomedical applications such as mucoadhesion, drug delivery, and wound healing.

### Conclusions

In this study, microcrystalline cellulose was successfully oxidized with potassium permanganate to produce oxidized nanocellulose with tunable structural and functional properties. Systematic characterization revealed that the oxidation time critically governed crystallinity, surface chemistry, particle size distribution, and rheological performance of the resulting materials.

FTIR analysis confirmed the introduction of carboxyl groups at the C6 hydroxyl position, while XRD indicated progressive loss of crystallinity, lattice expansion, and crystallite size reduction with increasing oxidation. DLS measurements showed enhanced colloidal stability and narrower size distributions at intermediate oxidation, whereas prolonged treatment led to partial re-aggregation. Rheological studies identified ONC-3 hydrogels as the strongest and most stable, displaying high storage modulus, a broad linear viscoelastic region, and superior deformation resistance compared with under- or over-oxidized samples.

Taken together, the results demonstrate that intermediate oxidation (3 h) offers the optimal balance between functionalization and structural preservation, yielding nanocellulose with enhanced dispersion stability, crystallinity, and mechanical robustness. This work advances the understanding of structure–property relationships in oxidized nanocellulose and identifies ONC-3 as a promising platform for biomedical hydrogels, particularly in mucoadhesive drug delivery, wound healing, and tissue engineering.

### Funding

This research was supported by the Basic Fundamental Program of the Academy of Sciences of the Republic of Uzbekistan, and the Uzbekistan–Belarus joint project funded by the Ministry of Higher Education, Science and Innovation of the Republic of Uzbekistan (Grant No. FL-8824063315, X25UZB-126).

### Author Information\*

\*The authors' names are presented in the following order: First Name, Middle Name and Last Name

**Makhliyo Mukhammadiyeva Kuzieva** — PhD, Junior Researcher, Institute of Polymer Chemistry and Physics, Abdulla Kadiri street, 7-b, 100128, Tashkent, Uzbekistan; e-mail: [makhliyokuziyeva92@gmail.com](mailto:makhliyokuziyeva92@gmail.com); <https://orcid.org/0000-0003-2552-6941>

**Fayruza Murod qizi Urishova** — Junior Researcher, Institute of Polymer Chemistry and Physics, Abdulla Kadiri street, 7-b, 100128, Tashkent, Uzbekistan; e-mail: [urishovafayruza600@gmail.com](mailto:urishovafayruza600@gmail.com); <https://orcid.org/0009-0001-8798-9522>

**Abdumutolib Abdupatto o'g'li Atakhanov** (*corresponding author*) — Doctor of Technical Sciences, Professor, Director of Institute of Polymer Chemistry and Physics, Abdulla Kadiri street, 7-b, 100128, Tashkent, Uzbekistan; e-mail: [a-atakhanov@yandex.com](mailto:a-atakhanov@yandex.com); <https://orcid.org/0000-0002-4975-3658>

**Nurbek Shodieovich Ashurov** — Candidate of Physical and Mathematical Sciences, Senior Researcher, Institute of Polymer Chemistry and Physics, Abdulla Kadiri street, 7-b, 100128, Tashkent, Uzbekistan; e-mail: [ansss72@mail.ru](mailto:ansss72@mail.ru); <https://orcid.org/0000-0001-5246-434X>

**Sayyora Sharafovna Rashidova** — Doctor of Science, Professor, Academician, Consultant of Director, Institute of Polymer Chemistry and Physics, Abdulla Kadiri street, 7-b, 100128, Tashkent, Uzbekistan; e-mail: [polymer@academy.uz](mailto:polymer@academy.uz); <https://orcid.org/0000-0003-1667-4619>

**Dmitriy Ivanovich Shiman** — Senior Researcher, Research Institute for Physical Chemical Problems of the Belarusian State University, Leningradskaya str., 14, 220006, Minsk, Belarus; e-mail: [ShimanD@bsu.by](mailto:ShimanD@bsu.by); <https://orcid.org/0000-0001-8810-9825>

**Sergei Viktorovich Kostjuk** — Research Director, Sorbonne Universite, CNRS, Institut Parisien de Chimie Moleculaire, 4 Pl. Jussieu, 75005, Paris, France; e-mail: [Kostjuks@bsu.by](mailto:Kostjuks@bsu.by), [sergei.kostjuk@sprbonne-universite.fr](mailto:sergei.kostjuk@sprbonne-universite.fr); <https://orcid.org/0000-0002-7466-3662>

**Saewon Kang** — Professor, Korea Research Institute of Chemical Technology, 141 Gajeong-ro, Yuseong District, 34114, Daejeon, South Korea; e-mail: [skang@kriect.re.kr](mailto:skang@kriect.re.kr); <https://orcid.org/0000-0001-5932-6636>

#### Author Contributions

The manuscript was written through contributions of all authors. All authors have given approval to the final version of the manuscript. **CRedit**: **Kuzieva Makhliyo Mukhammadievna** investigation, validation, writing-original draft; **Urishova Fayruza Murod qizi** investigation, methodology, formal analysis; **Abdumutolib Abdupatto o'g'li Atakhanov** conceptualization, data curation, formal analysis, validation, writing-review & editing; **Nurbek Shodieovich Ashurov** conceptualization, data curation, investigation, methodology, visualization, writing-original draft, writing-review & editing; **Sayyora Sharafovna Rashidova** conceptualization, supervision, editing; **Dmitriy Ivanovich Shiman** formal analysis, editing; **Sergei Viktorovich Kostjuk** formal analysis, editing; **Saewon Kang** formal analysis, editing.

#### Declaration of Generative AI and AI-Assisted Technologies in the Writing Process

During the preparation of this work the authors used Grammarly in order to refine the language of the manuscript. After using this service, the authors reviewed and edited the content as needed and take full responsibility for the content of the publication.

#### Conflicts of Interest

The authors declare no conflict of interest.

#### References

- 1 Seddiqi, H., Oliaei, E., Honarkar, H., Jin, J., Geonzon, L. C., Bacabac, R. G., & Klein-Nulend, J. (2021). Cellulose and its derivatives: towards biomedical applications. *Cellulose*, 28(4), 1893–1931. <https://doi.org/10.1007/s10570-020-03674-w>
- 2 Lupidi, G., Pastore, G., Marcantoni, E., & Gabrielli, S. (2023). Recent developments in chemical derivatization of microcrystalline cellulose (mcc): pre-treatments, functionalization, and applications. *Molecules*, 28(5), 2009. <https://doi.org/10.3390/molecules28052009>
- 3 Shakhabutdinov, S.Sh., Yugay, S.M., Ashurov, N.Sh., Ergashev, D.J., Atakhanov, A.A., & Rashidova, S.Sh. (2024). Characterization electrospun nanofibers based on cellulose triacetate synthesized from licorice root cellulose. *Eurasian Journal of Chemistry*, 2(114), 21–31. <https://doi.org/10.31489/2959-0663/2-24-2>
- 4 Aziz, T., Farid, A., Haq, F., Kiran, M., Ullah, A., Zhang, K., Li, C., Ghazanfar, S., Sun, H., Ullah, R., Ali, A., Muzammal, M., Shah, M., Akhtar, N., Selim, S., Hagagy, N., Samy, M., & Al Jaouni, S. K. (2022). A review on the modification of cellulose and its applications. *Polymers*, 14(15), 3206. <https://doi.org/10.3390/polym14153206>
- 5 Goyibnazarov, I. S., Yuldoshov, S. A., Sarymsakov, A. A., Yunusov, K. E., Yarmatov, S. S., Shukurov, A. I. & Wan, Y. (2025). Obtaining dialdehyde carboxymethylcellulose through microwave treatment. *Advances in Polymer Technology*, 1, 9917563. <https://doi.org/10.1155/adv/9917563>



- 6 Abraham, E., Deepa, B., Pothan, L. A., Jacob, M., Thomas, S., Cvelbar, U., & Anandjiwala, R. (2011). Extraction of nanocellulose fibrils from lignocellulosic fibres: A novel approach. *Carbohydrate Polymers*, 86(4), 1468–1475. <https://doi.org/10.1016/j.carbpol.2011.06.034> [Get rights and content](#)
- 7 Choi, H. N., Yang, H. S., Chae, J. H., Choi, T. L., & Lee, I. H. (2020). Synthesis of conjugated rod-coil block copolymers by RuPhos Pd-catalyzed Suzuki–Miyaura catalyst-transfer polycondensation: initiation from coil-type polymers. *Macromolecules*, 53(13), 5497–5503. <https://doi.org/10.1021/acs.macromol.0c00949>
- 8 Kuzieva, M., Atakhanov, A.A., Shahobutdinov, S., Ashurov, N.S., Yunusov, K.E., & Guohua, J. (2023). Preparation of oxidized nanocellulose by using potassium dichromate. *Cellulose*, 30, 5657–5668. <https://doi.org/10.1007/s10570-023-05222-8>
- 9 Saba, F., Mohammad, H.N., Navid, R., & Siavash, I. (2023). *ACS Biomaterials Science & Engineering*, 9(6), 2949–2969. <https://doi.org/10.1021/acsbiomaterials.3c00300>
- 10 Bayer, I.S. (2021). A review of sustained drug release studies from nanofiber hydrogels. *Biomedicines*, 9(11), 1612. <https://doi.org/10.3390/biomedicines9111612>
- 11 Atakhanov, A.A., Ashurov, N.Sh., Kuzieva, M.M., Mamadiyrov, B.N., Ergashev, D.J., Rashidova, S.S., & Khutoryanskiy, V.V. (2024). Novel acryloylated and methacryloylated nanocellulose derivatives with improved mucoadhesive properties. *Macromolecular Bioscience*, 2400183 (1–10). <https://doi.org/10.1002/mabi.202400183>
- 12 Balcerak-Woźniak, A., Dzwonkowska-Zarzycka, M., & Kabatc-Borcz, J. (2024). A Comprehensive Review of Stimuli-Responsive Smart Polymer Materials — Recent Advances and Future Perspectives. *Materials*, 17(17), 4255. <https://doi.org/10.3390/ma17174255>
- 13 Tortorella, S., Vetri Buratti, V., Maturi, M., Sambri, L., Comes Franchini, M., & Locatelli, E. (2020). Surface-modified nanocellulose for application in biomedical engineering and nanomedicine: A review. *International journal of nanomedicine*, 9909–9937. <https://doi.org/10.2147/IJN.S266103>
- 14 Mehwish, H. M., Liu, G., Rajoka, M. S. R., Cai, H., Zhong, J., Song, X., & He, Z. (2021). Therapeutic potential of Moringa oleifera seed polysaccharide embedded silver nanoparticles in wound healing. *International Journal of Biological Macromolecules*, 184, 144–158. <https://doi.org/10.1016/j.ijbiomac.2024.138116>
- 15 Hassan, R. M., & Ibrahim, S. M. (2024). Review on synthesis of novel carbonyl derivatives of biological macromolecules by oxidation of polysaccharides with permanganate ion in alkaline media. *Journal of Umm Al-Qura University for Applied Sciences*, 10(2), 348–366. <https://doi.org/10.1007/s43994-023-00098-7>
- 16 Guan, X., He, D., Ma, J., & Chen, G. (2010). Application of permanganate in the oxidation of micropollutants: a mini review. *Frontiers of Environmental Science & Engineering in China*, 4(4), 405–413. <https://doi.org/10.1007/s11783-010-0252-8>
- 17 Zhou, S., Han, C., Ni, Z., Yang, C., Ni, Y., & Lv, Y. (2022). Gelatin-oxidized nanocellulose hydrogels suitable for extrusion-based 3D bioprinting. *Processes*, 10(11), 2216. <https://www.mdpi.com/2227-9717/10/11/2216>
- 18 Won, T., Goh, M., Lim, C., Moon, J., Lee, K., Park, J., & Gwon, K. (2025). Recent Progress in Cellulose Nanofibril Hydrogels for Biomedical Applications. *Polymers*, 17(17), 2272. <https://doi.org/10.3390/polym17172272>
- 19 Jaffar, S. S., Saallah, S., Misson, M., Siddiquee, S., Roslan, J., Saalah, S., & Lenggoro, W. (2022). Recent development and environmental applications of nanocellulose-based membranes. *Membranes*, 12(3), 287. <https://doi.org/10.3390/membranes12030287>
- 20 Liu, S., Tian, Z., & Ji, X.X. (2024). Preparation and modification of nanocellulose using deep eutectic solvents and their applications. *Cellulose*, 31, 2175–2205. <https://doi.org/10.1007/s10570-024-05738-7>
- 21 Rouhi, M., Garavand, F., Heydari, M., Mohammadi, R., Sarlak, Z., Cacciotti, I., & Parandi, E. (2024). Fabrication of novel antimicrobial nanocomposite films based on polyvinyl alcohol, bacterial cellulose nanocrystals, and boric acid for food packaging. *Journal of Food Measurement and Characterization*, 18(3), 2146–2161. <https://doi.org/10.1007/s11694-023-02325-5>
- 22 Atakhanov, A. A., Kholmuminov, A. A., Mamadierov, B. N., Turdikulov, I. Kh., & Ashurov, N. Sh. (2020). Rheological Behavior of Nanocellulose Aqueous Suspensions. *Polym. Sci. Series A*, 62(3), 213–217. <https://doi.org/10.1134/S0965545X20030013>
- 23 Habibi, Y., Chanzy, H., & Vignon, M. R. (2006). TEMPO-mediated surface oxidation of cellulose whiskers. *Cellulose*, 13(6), 679–687. <https://doi.org/10.1007/s10570-006-9075-y>
- 24 Pan, R., Cheng, Y., Pei, Y., Liu, J., Tian, W., Jiang, Y., & Zheng, X. (2023). Cellulose materials with high light transmittance and high haze: a review. *Cellulose*, 30(8), 4813–4826. <https://doi.org/10.21203/rs.3.rs-1310113/v1>
- 25 Yusuf, M. O. (2023). Bond characterization in cementitious material binders using Fourier-transform infrared spectroscopy. *Applied Sciences*, 13(5), 3353.25. <https://doi.org/10.3390/app13053353>
- 26 Yang, B., Zhang, M., Lu, Z., Tan, J., Luo, J., Song, S., & Zhang, Q. (2019). Comparative study of aramid nanofiber (ANF) and cellulose nanofiber (CNF). *Carbohydrate polymers*, 208, 372–381. <https://doi.org/10.3390/app13053353>
- 27 Isogai, A., Saito, T., & Fukuzumi, H. (2011). TEMPO-oxidized cellulose nanofibers. *Nanoscale*, 3(1), 71–85. <https://doi.org/10.1039/C0NR00583E>
- 28 Saito, T., Nishiyama, Y., Putaux, J. L., Vignon, M., & Isogai, A. (2006). Homogeneous suspensions of individualized microfibrils from TEMPO-catalyzed oxidation of native cellulose. *Biomacromolecules*, 7(6), 1687–1691. <https://doi.org/10.1021/bm060154s>
- 29 Alexander, S. P., Mathie, A., Peters, J. A., Veale, E. L., Striessnig, J., Kelly, E., & Zhu, M. (2021). The concise guide to pharmacology 2021/22: Ion channels. *British Journal of Pharmacology*, 178, S157–S245. <https://doi.org/10.1111/bph.15539>

- 30 Filippov S.K., Khusnutdinov R., Murmiliuk A., Inam W., Zakharova L.Ya., Zhang H., & Khutoryanskiy V.V. (2023). Dynamic light scattering and transmission electron microscopy in drug delivery: a roadmap for correct characterization of nanoparticles and interpretation of results. *Materials Horizons*, 10, 5354–5370. <https://doi.org/10.1039/D3MH00717K>
- 31 Huo, Y., Liu, Y., Xia, M., Du, H., Lin, Z., Li, B., & Liu, H. (2022). Nanocellulose-Based Composite Materials Used in Drug Delivery Systems. *Polymers*, 14(13), 2648. <https://doi.org/10.3390/polym14132648>
- 32 Zhang, H. (2018). *Ice templating and freeze-drying for porous materials and their applications*. John Wiley & Sons. <https://doi.org/10.1002/9783527807390.ch10>
- 33 Mezger, T. (2020). *The rheology handbook: for users of rotational and oscillatory rheometers*. European Coatings. <https://doi.org/10.1515/arh-2002-0029>



**Index of articles published in  
“Eurasian Journal of Chemistry”  
in 2025**

№      p.

**CHEMICAL TECHNOLOGY**

<i>Borsynbayev, A.S., Mustafin, Ye.S., Omarov, Kh.B. Muratbekova, A.A., Kaykenov, D.A., Sadyrbekov, D.T., Aynabayev, A.A., Bolatbay A.N, Turovets, M.A.</i> Study of the Phase Composition and Kinetics of the Metal Leaching Process Using Electrohydropulse Discharge on the Waste from the Zhezkazgan Concentrating Plants .....	2	119
<i>Galiyeva, A.R., Yessentayeva, N.A., Marsel, D.T., Daribay, A.T., Sadyrbekov, D.T., Moustafine, R.I., &amp; Kutulutsкая, T.V.</i> Polylactide Acid-Based Nanoparticles for Controlled Delivery of Isoniazid and Rifampicin: Synthesis, Characterization, and <i>In Vitro</i> Release Study .....	2	95
<i>Hasanov, R.M., Mammadova, R.E., Amirov, S.Q., Aliyeva, Z.D.</i> Effect of Sunflower Oil-Based Metal Soaps on the Thermal Stability of Polyvinyl Chloride .....	1	89
<i>Kicheeva, A.G., Sushko, E.S., Dzeranov, A.A., Bondarenko, L.S., Tropkaya N.S., Kydralieva, K.A., &amp; Kudryasheva N.S.</i> A Bacterial Enzymatic System Neutralizes the Impact of Silica-Magnetite Nanocomposites on ROS Levels .....	4	137
<i>Kumari, S., Gupta, P.K., Kumar, A., &amp; Kumar, R.</i> Oxidative Transformation of Ethylbenzene Utilizing Metal Bound Immobilized Catalysts .....	4	120
<i>Kuzieva, M.M., Urishova, F.M., Atakhanov, A.A., Ashurov, N.Sh., Rashidova, S.Sh., Shiman, D.I., Kostjuk, S.V. &amp; Kang, S.</i> Potassium Permanganate–Oxidized Nanocellulose: Structural Features and Rheological Performance for Advanced Applications.....	4	148
<i>Mammadov, E.S., Kerimli, F.Sh., Akhmedova, N.F., Mammadov, S.E., &amp; Mirzaliyeva, S.E.</i> Effect of Solid-Phase Modification of High-Modulus Zeolite TsVM with Cerium Oxide in Conversion of Bioethanol to Hydrocarbons .....	2	109
<i>Melikova, I.G., Efendi, A.J., Manafov, M.R., Aykan, N.F., Faradjev, G.M., Rustamova, C.T., &amp; Shikhaliyev, N.I.</i> Kinetics and Mechanism of the Oxidation Reaction of Chlorine-Containing Hydrocarbons on a Vanadium Phosphorus Catalyst.....	4	109
<i>Turarbek, A.M., Abilkanova, F.Zh., Uali, A.S.</i> Development of Novel Wheat Waste-Derived Biochar and Its Potential in Pharmaceutical Wastewater Treatment .....	1	76

**INORGANIC CHEMISTRY**

<i>Badaoui, M., Sehil, H., &amp; Lamouri, C.</i> Synthesis, Characterization, and Photocatalytic Activity of CeBiO <sub>3</sub> and FeBiO <sub>3</sub> Nanoparticles Prepared via the Sol-Gel Process .....	2	85
<i>Ismayilova, S.Z., Guliyeva, L.Sh., Ismayilov, R.H., Tagiyev, D.B., Valiyev, F.F., Yalcin, B., Medjidov, A.A., Huseynova, M.T., Chien, S.Y., Lee, G.H., &amp; Peng, Sh.M.</i> Synthesis and Structure of the Novel Mononuclear Copper(II) Complex of the Unsymmetrical Pyrimidine-Modulated Long-Chain Hexapyridylpentaamine Ligand.....	4	79
<i>Ivanova, N.M., Muldakhmetov, Z.M., Vissurkhanova, Ya.A., Soboleva Ye.A., &amp; Borsynbayev A.S.</i> N-Containing Graphene Preparation Using Melamine as a Nitrogen Source .....	2	74
<i>Shahid, Z.A., &amp; Tabassum, R.</i> Mn(II) and Zn(II) Complexes of a Coumarin Derivative: Synthesis, Characterization and Biological Potential .....	4	88
<i>Soualmi, S., Henni, M., Djahnit, L., &amp; Bouzegaou, M.</i> Structural, Photocatalytic, and Antibacterial Evaluation of Cu-Doped ZnMn <sub>2</sub> O <sub>4</sub> Nanoparticles.....	4	66

**ORGANIC CHEMISTRY**

<i>Alzhapparova, N.A., Panshina, S.Yu., Ibrayev, M.K., &amp; Babaev, E.V.</i> Features on the Way to the Synthesis of 1-Benzoyl-2-Phenyl-3a,6a-Diazapentalene and 1-Pivaloyl-2-Tert-Butyl-3a,6a-Diazapentalene.	4	14
<i>Awad, A.A., Maged, M.N., Abed, D.A., Wennas, O.N., Kbah, N.Z., Disher, A.A.</i> Synthesis, Docking Study and Biological Evaluation of Naproxen-Based Heterocyclic Derivatives .....	1	15

<i>Dubovskaia, P.I., Saeidi, A., Pronchenko, A.A., Drannikova, A.I., Lukoyanov, I.A., Aripova, F.K., Savenko, M.E., Veretennikova, E.A., Pestov, A.V., Litvinova, E.A., &amp; Drannikov, A.A.</i> Gel-Phase Synthesis and pH-Sensitive Swelling-Structure Relationships of N-Carboxyethylchitosan .....	2	19
<i>Filina, M.P., Bakibaev, A.A., &amp; Baiguzin, F.A.</i> Cyclopentane as an Eco-Friendly Alternative: A Review of its Properties, Industrial Applications, and Production Methods .....	4	4
<i>Kukushkin, A.A., Kudashova, E.V., Root, E.V., Kositsyna, A.S., Ponomarev, I.S., Lyubyashkin, A.V., &amp; Pustolaikina, I.A.</i> Synthesis, Characterization and Computational Study of Novel Copper(II) Chelate Complexes Ligated by Pyridyl-Containing Beta-Diketonates .....	2	4
<i>Palamarchuk, I.V., Kulakov, I.V. &amp; Volkova, S.S.</i> Synthesis and Optical Properties of Substituted Derivatives of Oxazolo[5,4-b]Pyridine .....	4	23
<i>Rana, A.J., Bisht, S., Upadhyaya, K., Singh, P., Rana, M., Singh, Sh.</i> Benzodioxole Scaffold Incorporating Compound with Promising Anti-Fungal Potential: An Overview .....	1	27
<i>Sarwade, K.N., Sakhare, K.B., Sakhare, M.A., Thakur, Sh.V.</i> Neuroprotective, Anticancer and Antimicrobial Activities of Azo-Schiff Base Ligand and Its Metal Complexes .....	1	4
<i>Verekar, R.R., Shaikh, Sh.B.M., Rebelo, S., &amp; Gurav, Sh.S.</i> Double-Loaded Liposomes Encasing Umbelliferone in Hydroxypropyl- $\beta$ -Cyclodextrin Inclusion Complexes: Formulation, Characterisation and Investigation of Photoprotective Activity .....	2	34

### PHYSICAL AND ANALYTICAL CHEMISTRY

<i>Abdulsattar, M.A.</i> WO <sub>3</sub> Doped SnS <sub>2</sub> Gas Sensor Response to NO <sub>2</sub> : Effect of Temperature and Humidity Using Transition State Theory Formalism.....	4	34
<i>Abdulsattar, M.A., Almaroof, S.M.</i> H <sub>2</sub> S Properties and Temperature Effects on the Response of Pristine and Al-Doped ZnO Gas Sensor .....	1	40
<i>Burkeyeva, G.K., Kovaleva, A.K., Muslimova, D.M., Havlicek, D., Zhumabek, N.M. &amp; Nukin, N.A.</i> Investigation of Physical and Chemical Properties of Thermosetting Copolymers of Polyethylene Glycol Maleate with Acrylic Acid During their “Cold” Curing .....	2	52
<i>Milusheva, R.Yu., Nurgaliev, I.N., Abilkasimov, A.B., &amp; Rashidova, S.Sh.</i> Bioactive Chitosan/ $\beta$ -Tricalcium Phosphate Coatings on Titanium: Experimental Optimization and DFT Insight .....	4	45
<i>Mukhametgazy, N., Temirkulova, K.M., Balgabayeva, B., Khamzin, B.G., Azat, S., Supiyeva, Zh.A., &amp; Abbas, Q.</i> Effect of Activating Agent and Temperature Conditions on the Electrochemical Performance of Rice Husk-Based Activated Carbon in Supercapacitors .....	2	62
<i>Ramasamy, M., Velayutham, G., Pitchaipillai, R.</i> A Novel Mannich Based Metal II Complexes: Synthesis and Characterization of Magnetic, Conductivity and Antimicrobial Properties .....	1	60
<i>Shcherban', M.G., Ivanchina, E.A., Sedusov, I.V., Sosunova, V.V. Novosyolov, K.P.</i> Study of the Effect of Potassium Chloride on the Coagulation of PTFE Dispersion by Optical Methods .....	1	50

### PREFACE

<i>Mashentseva, A.A., Nechaev, A.N., Barsbay, M., &amp; Apel, P.Yu.</i> Preface to the Special Issue “Track-Etched Membranes: Future Prospects, Opportunities and Challenges” .....	3	5
---	---	---

### ADVANCED REVIEWS ON TEMs

<i>Rossouw, A., Petrik, L.F., Nechaev, A.N., &amp; Apel, P.Yu.</i> Advancing Functionalized Track-Etched Membranes: Composite and Hybrid Materials through the JINR–South Africa Partnership .....	3	23
<i>Sütekin, S.D., Rakisheva, S.R., Mashentseva, A.A., &amp; Barsbay, M.</i> A Mini Review on Track-etched Membranes Potential for Sensors Development .....	3	7

### MODIFICATION AND DEVELOPMENT OF NEW TYPES OF TEMs

<i>Kryukova-Seliverstova, A.V., Orelovich, O.L., Altynov, V.A., Akimov, A.V., Shmakov, A.S., Nikolskaya, D.V., Kirilkin, N.S., &amp; Pinaeva, U.V.</i> Radiation Grafting of PVDF Track-Etched Membranes: A Study for Nanoscale Pore Functionalization.....	3	40
---	---	----

<i>Ponomar, M.A., Sarapulova, V.V., Guliaeva, V.V., Apel, P.Yu., &amp; Pismenskaya, N.D.</i> Transport Properties of Cation-Exchange Membranes Obtained by Pore Filling of Track-Etched Membranes with Perfluorosulfonic Acid Polymer .....	3	65
<i>Shakayeva, A.Kh., Omertasov, D.D., Zhatkanbayeva, Zh.K., Zhumazhanova, A.T., Zdorovets, M.V., &amp; Korolkov, I.V.</i> Graft Polymerization of Allylamine for the Modification of PET Track-Etched Membrane .....	3	85
<i>Yeszhanov, A.B., Korolkov, I.V., &amp; Zdorovets, M.V.</i> Graft Polymerization of Octadecyl Acrylate on PET Track-Etched Membranes for Direct Contact Membrane Distillation .....	3	56

#### PROSPECTIVE APPLICATIONS OF TEMs

<i>Balyasin, M.V., Serpionov, G.V., Krashenninnikov, M.E., Lyundup, A.V., &amp; Nechaev, A.N.</i> Biological Compatibility of Polyethylene Terephthalate Track Membranes: Growth, Proliferation, and Viability of Cells in Culture Systems .....	3	99
<i>Bedin, S.A., Kozhina, E.P., Doludenko, I.M., &amp; Drachev, V.P.</i> Track-Etched Membranes for Gold Nanowire SERS Substrates .....	3	110
<i>Mitrofanov, A.V., Apel, P.Yu., Ivanov, O.M., &amp; Pudonin, F.A.</i> A New Application of Track-Etched Membranes in X-Ray and Vacuum Ultraviolet Optics .....	3	93

#### TEMs BASED COMPOSITES AND ITS PRACTICAL APPLICATIONS

<i>Andreev, E.V., Fadeikina, I.N., Mutali, A.K., &amp; Kukushkin, V.I.</i> Comparison of SERS Effect on Composite Track-Etched Membranes with Silver Nanostructures Obtained by Vacuum Deposition and Chemical Synthesis .....	3	143
<i>Drozhzhin, N.A., Ponomareva, O.Yu., Vinogradov, I.I., Serpionov, G.V., Kanet, A., Nikolskaya, D.V., &amp; Vershinina, T.N.</i> Nickel (II) Based Metal-Organic Framework Consolidated on Nanofibers Modified Track-Etched Membrane for Dye Removal .....	3	118
<i>Rakisheva, S.R., Nurpeisova, D.T., Zhumabayev, A.M., Parmanbek, N., Barsbay, M. &amp; Mashentseva, A.A.</i> Galvanic Replacement-Assisted Synthesis of Cu–Ag Composite Membrane Catalysts for Potassium Ferricyanide Reduction .....	3	129